LAWRENCE
LIVERMORE
NATIONAL
LABORATORY

UCRL-TR-234787

HIGH-PERFORMANCE CORROSION-RESISTANT MATERIALS: IRON-BASED AMORPHOUS-METAL THERMAL-SPRAY COATINGS

SAM HPCRM Program – FY04 Annual Report – Rev. 0
DARPA DSO & DOE OCRWM Co-Sponsored Advanced Materials Program

Authors: J. C. Farmer, J. J. Haslam, F. Wong, X. Ji, S. D. Day, Lawrence Livermore National Laboratory, D. J. Branagan, M. C. Marshall, B. E. Meacham, E. J. Buffa, NanoSteel Company, C. A. Blue, J. D. K. Rivard, Oak Ridge National Laboratory, M. B. Beardsley, D. T. Weaver Caterpillar, L. F. Aprigliano, L. Kohler, Naval Surface Warfare Center, R. Bayles, E. J. Lemieux, T. M. Wolejsza, F. J. Martin, Naval Research Laboratory & Geo-Centers Corporation, N. Yang, G. Lucadamo Sandia National Laboratory California, J. H. Perepezko, K. Hildal University of Wisconsin Madison, L. Kaufman, Massachusetts Institute of Technology, A. H. Heuer, F. Ernst, G. M. Michal, H. Kahn Case Western Reserve University, E. J. Lavernia, University of California Davis

This work was performed under the auspices of the U.S. Department of Energy by University of California Lawrence Livermore National Laboratory under contract No. W-7405-Eng-48.

HIGH-PERFORMANCE CORROSION-RESISTANT MATERIALS: IRON-BASED AMORPHOUS-METAL THERMAL-SPRAY COATINGS

J. C. Farmer, J. J. Haslam, F. Wong, X. Ji & S. D. Day
Lawrence Livermore National Laboratory

D. J. Branagan, M. C. Marshall, B. E. Meacham & E. J. Buffa
NanoSteel Company

C. A. Blue & J. D. K. Rivard
Oak Ridge National Laboratory

M. B. Beardsley & D. T. Weaver
Caterpillar

L. F. Aprigliano & L. Kohler
Naval Surface Warfare Center

R. Bayles, E. J. Lemieux, T. M. Wolejsza & F. J. Martin
Naval Research Laboratory & Geo-Centers Corporation

N. Yang & G. Lucadamo
Sandia National Laboratory California

J. H. Perepezko & K. Hildal
University of Wisconsin Madison

L. Kaufman
Massachusetts Institute of Technology

A. H. Heuer, F. Ernst, G. M. Michal & H. Kahn
Case Western Reserve University

E. J. Lavernia
University of California Davis

TABLE OF CONTENTS

LISTING OF TABLES

LISTING OF FIGURES

HIGH-PERFORMANCE CORROSION-RESISTANT MATERIALS: IRON-BASED AMORPHOUS-METAL THERMAL-SPRAY COATINGS

J. C. Farmer[1], J. J. Haslam[1], F. Wong[1], X. Ji[1], S. D. Day[1], D. J. Branagan[2], M. C. Marshall[2], B. E. Mecham[2], E. J. Buffa[2], C. A. Blue[3], J. D. K. Rivard[3], D. C. Harper[3], M. B. Beardsley[4], D. T. Weaver[4], L. F. Aprigliano[5], L. Kohler[5], R. Bayles[6], E. J. Lemieux[6], T. M. Wolejsza[6], N. Yang[7], G. Lucadamo[7], J. H. Perepezko[8], K. Hildal[8], L. Kaufman[9], A. H. Heuer[10], F. Ernst[10], G. M. Michal[10], H. Kahn[10]and E. J. Lavernia[11]

Lawrence Livermore National Laboratory[1], NanoSteel Company[2], Oak Ridge National Laboratory[3], Caterpillar[4], Naval Surface Warfare Center[5], Naval Research Laboratory & Geo-Center Corporation[6], Sandia National Laboratory California[7], University of Wisconsin Madison[8], Massachusetts Institute of Technology[9], Case Western Reserve University[10] and University of California Davis[11]

ABSTRACT

The multi-institutional High Performance Corrosion Resistant Materials (HPCRM) Team is co-sponsored by the Defense Advanced Projects Agency (DARPA) Defense Science Office (DSO) and the Department of Energy (DOE) Office of Civilian Radioactive Waste Management (OCRWM), and has developed new corrosion-resistant, iron-based amorphous metals that can be applied as coatings with advanced thermal spray technology. Two compositions have corrosion resistance superior to wrought nickel-based Alloy C-22 (UNS # N06022) in very aggressive environments, including concentrated calcium-chloride brines at elevated temperature.

Corrosion costs the Department of Defense billions of dollars every year, with an immense quantity of material in various structures undergoing corrosion. For example, in addition to fluid and seawater piping, ballast tanks, and propulsions systems, approximately 345 million square feet of structure aboard naval ships and crafts require costly corrosion control measures. The use of advanced corrosion-resistant materials to prevent the continuous degradation of this massive surface area would be extremely beneficial. The Fe-based corrosion-resistant, amorphous-metal coatings under development may prove of importance for applications on ships.

Such coatings could be used as an “integral drip shield” on spent fuel containers, as well as protective coatings that could be applied over welds, thereby preventing exposure to environments that might cause stress corrosion cracking. In the future, such new high-performance iron-based materials could be substituted for more-expensive nickel-based alloys, thereby enabling a reduction in the $58-billion life cycle cost for the long-term storage of the Nation’s spent nuclear fuel by tens of percent.

INTRODUCTION

Value of HVOF Amorphous-Metal Coatings to Department of Defense

The HPCRM Program is a pro-active response to corrosion problems within the Department of Defense (DOD). A recent Government Office (GAO) Accounting Report prepared for the United States Congress and available to the public has made the impact of such corrosion clear. [Defense Management, Opportunities to Reduce Corrosion Costs and Increase Readiness, United States General Accounting Office, Report to Congress, GAO-03-753, July 2003]. The preface letter in this report was written by The Honorable John Ensign, Chairman, and The Honorable Daniel Akaka, Ranking Minority Member, Armed Services, Subcommittee on Readiness and Management Support, United States Senate; and The Honorable Joel Hefley, Chairman, and The Honorable Solomon Oritz, Ranking Minority Member, Committee on Armed Services, Subcommittee on Readiness, House of Representatives. This report makes several important points. For example, Department of Defense maintains equipment and infrastructure worth billions of dollars in many environments where corrosion, in one form or another, is causing these assets to deteriorate, shortening their useful lives. The resulting increase in needed repairs and replacements drives up costs and takes valuable systems out of action.. Because numerous advanced in products and technologies have been found to enhance efforts to prevent and mitigate corrosion, it is critical that Department of Defense, as the steward of an enormous investment, ensure that all appropriate measures are implemented to reduce corrosion costs to the greatest extent possible. The Congress, recognizing corrosion as a serious military concern, enacted legislation as part of the Bob Stump National Defense Authorization Act for Fiscal Year 2003 which requires Department of Defense to designate a senior official or organization responsible for preventing and mitigating the effects of corrosion. The act requires the designated official or organization to oversee and coordinate efforts throughout DOD, recommend policy guidance, and review proposed funding levels. The Secretary of Defense is required to develop and implement a long-term strategy to reduce the effects of corrosion.

Another report for the United States Congress was prepared by the Principal Deputy Under Secretary of Defense, Acquisition, Technology & Logistics (Long-Term Strategy to Reduce Corrosion and the Effects of Corrosion on the Military Equipment and Infrastructure of the Department of Defense, Report to Congress, Department of Defense, December 2003). This report addressed the impacts of corrosion on safety, readiness and operational costs. In Section I, entitled Strategic Direction, The Honorable Michael W. Wynne, the DOD Corrosion Executive, writes: “It is simply good sense and good management to prevent corrosion through better design and selection of materials, and to reduce treatment costs by detecting corrosion earlier and more precisely.”

Corrosion is a distraction for the Department of Defense. Maintenance, including corrosion control activities, involves nearly 700,000 personnel (active and reserve military, and civilian employees), as well as several thousand contractors worldwide.

The quantity of material undergoing corrosion is immense. In addition to fluid and seawater piping, ballast tanks, and propulsions systems, approximately 345 million square feet of structure aboard naval ships and crafts require costly corrosion control measures. The use of advanced corrosion-resistant materials to prevent the continuous degradation of this massive surface area would be extremely beneficial. The Fe-based corrosion-resistant, amorphous-metal coatings under development are also non-magnetic, and may prove of importance for applications on naval vessels (Figure 1).

Value of HVOF Amorphous-Metal Coatings to Department of Energy

Man-made materials with unusually service lives are needed for the construction of containers and associated structures for the long-term storage or disposal of spent nuclear fuel (SNF) and high-level waste (HLW) in underground repositories. Man has never designed and constructed any structure or system with the service life required by a SNF and HLW repository. Such systems will be required to contain these radioactive materials for a period as short as 10,000 years, and possible as long as 300,000 years. The most robust engineering materials known are challenged by such long times. Thus, the ongoing investigation of newer, more advanced materials such as the corrosion-resistant amorphous metals reported here is prudent.

A conceptual drawing of a proposed repository for SNF and HLW is shown in Figure 2, with large horizontal containers, support pallets, drip shields, ground support, and invert. In this particular case, Alloy C-22 & Type 316NG stainless steel are envisioned as the materials for container fabrication, due to their strength, ability to be welded, and corrosion resistance.

The United States needs a repository for the emplacement of 70,000 MTHM. Such a repository, designed as shown in Figure 2, would require: 11,000-15,000 SNF containers (21 PWR type) costing $4-6 billion; 11,000-15,000 support pallets costing $600-800 million; and 10,000-13,000 titanium drips that would cost $3-4 billion. The total estimated cost for this engineered barrier system would then be $8-11 billion dollars (Tables 1 and 2). The overall life cycle for the repository, including excavation, has been estimated to be $58 billion. Thus, savings through the use of less-expensive, corrosion and wear resistant materials for containers and excavation equipment could be substantial.

OBJECTIVE OF WORK

Tasks

The High-Performance Corrosion-Resistant Materials (HPCRM) Program is co-funded by DARPA DSO and DOE OCRWM, and utilizes both theoretical and experimental materials science to develop corrosion-resistant, amorphous-metal, thermal-spray coatings suitable for the desired applications. The formal memorandum of agreement between DARPA and DOE that has enabled DOE to leverage advances in materials science achieved by DARPA, while DARPA has leveraged expertise in corrosion science and nuclear applications within the DOE complex. Specific tasks include those necessary for the synthesis and enhancement of the coatings, as well as tasks for the full characterization of performance in relevant environments. By including work on computational materials performance as shown in Figure 3, a level of insight will be gained that will enable dramatic improvements in capability over those that are possible today. This project promises to satisfy the need for new, more corrosion resistant materials within both the Department of Energy, and the Department of Defense.

Task 1

- Development/Deposition of HVOF Coatings
    - Coating with 316L Performance (Formula A)
    - Coating with Alloy 22 Performance (Formula B)
    - Coating with Titanium Performance (Formula C)

Task 2

- High-Density Infrared Fusing
    - Coating with 316L Performance (Formula A)
    - Coating with Alloy 22 Performance (Formula B)
    - Coating with Titanium Performance (Formula C)

Task 3

- General/Localized Corrosion Quantification
    - Corrosion, Threshold & Repassivation Potentials
    - Corrosion & Passive Current Densities
    - General Corrosion Rates from Weight Loss
    - Localized Corrosion Rates from Microscopy

Task 4

- Passive Film Characterization
    - SEM, TEM, EDS, XPS, AES and/or AFM

Task 5

- Stress Corrosion Cracking (SCC)
  - Environments & Conditions Causing Susceptibility
  - Threshold Stress Intensity Factor
  - Crack Propagation Rate

Task 6

- Hydrogen Induced Cracking (HIC)
  - Environments & Conditions Causing Susceptibility
  - Threshold Stress Intensity Factor
  - Crack Propagation Rate

Task 7

- Thermochemical Equilibria & Reaction Kinetics
  - Phase Diagrams
  - Pourbaix Diagrams
  - Time Temperature Transformation (TTT) Diagrams

Task 8

- Mechanical & Physical Property Determination
  - Stress vs. Strain Curves
  - Melting Point & Glass Transition Temperature
  - Heat Capacity & Thermal Conductivity
  - Coefficient of Thermal Expansion

During FY04, the HPCRM Team has addressed Task 1 (Formulae A and B), Task 2 (Formula A), Task 2 (Formula A), Task 3 (Formulae A and B), Task 4 (SEM and EDS), Task 7 (Phase, Pourbaix, and TTT Diagrams), and Task 8 (except for Stress vs. Strain Curves). No substantial work has yet been done on Task 5 and 6, which has been deferred until FY05. Another team member with expertise in stress analysis will be added in FY05 and directed to address Task 8, with particular emphasis on interfacial stresses that might cause failure at the coating-substrate bond.

MILESTIONES & DELIVERABLES

A well-integrated research program has been established and promises to meet the following milestones. These milestones should advance scientific understanding and technical capability, while moving the HPCRM Program towards successful application of these new corrosion-resistant materials in important DOD and DOE applications.

Milestone 1

- Phase Diagrams
- Pourbaix Diagrams
- Time-Temperature-Transformation (TTT) Diagrams

Milestone 2

- HVOF & HDIF of Fe-Cr-Mo-W Coating with Performance of 316L (Formula A)

Milestone 3

- HVOF & HDIF of Fe-Cr-Mo-W Coating with Performance of Alloy 22 (Formula B)

Milestone 4

- HVOF & HDIF of Alternative Coating with Performance of Ti Alloys (Formula C)

Milestone 5

- GC & LC Database for HVOF-HDIF Amorphous Metal Coatings

Milestone 6

- SCC Database for HVOF-HDIF Amorphous Metal Coatings

Milestone 7

- HIC Database for HVOF-HDIF Amorphous Metal Coatings

Milestone 8

- Comprehensive Physical Property Database

Milestone 9

- Prototype Waste Package with HVOF Amorphous Metal Coating
- Prototype Boat Hull/Deck with HVOF Amorphous Metal Coating

Milestone 10

- U.S. Patents for Corrosion Resistant Amorphous Metal and Ceramic Coatings

During FY04, the HPCRM met Milestones 1, 2, 3, and 8, thereby meeting established programmatic objectives.

TEAM & TECHNICAL RESPONSIBILITIES

DARPA DSO and DOE OCWRM management have now established a strong collaboration through a formal memorandum of agreement (MOA) to enable the cost-effective, further development of high-performance, corrosion-resistant coatings. These materials promise to enhance the service life of equipment needed by the Department of Defense, while simultaneously providing a cost-effective alternative for the safe underground storage of the Nation's spent nuclear fuel. Such investments in the future are prudent.

The HPCRM Team involves three of DOE laboratories (LLNL, SNL, ORNL), three DOD laboratories (NSWC, NRL, NRL Key West), industry (NanoSteel, Impreglon, Caterpillar), as well as several universities (Figure 4). Full integration of the industrial team members into this world-class, multi-institutional team promises to enable rapid commercialization and deployment of the new high-performance materials that are under development. Specific responsibilities are summarized below.

- DOD/DARPA/SAM/DTI
  - Provide Guidance for Development of Advanced Materials
- DOE/OCRWM/S&T
  - Provide Guidance for Development of Advanced Materials for Repository
- NSWC/LLNL
  - Identification of DoD & DOE Needs
  - Definition of Environments for Corrosion Testing
  - Application of New Materials & Processes to Ships
- NanoSteel/Impreglon/Caterpillar/UC Davis
  - Development of Fe-Cr-Mo-W Coating with Performance of 316L (Formula A)
  - Development of Fe-Cr-Mo-W Coating with Performance of Alloy 22 (Formula B)
  - Development of Alternative Coating with Performance of Ti Alloys (Formula C)
  - Synthesis of Fully-Dense Pore-Free Amorphous Metals with Melt Spinning
  - HVOF Application of Amorphous Metal Coatings
  - Commercial Demonstration of Coating Systems
- ORNL
  - High-Density IR Fusing
  - Elimination of All Porosity
  - Arc Melting and Drop Casting of Prototypical Amorphous Metals
- SNL/Wisconsin/Case Western Reserve/CALPHAD-MIT
  - Studies of Aging & Phase Stability – Devitrification and Recrystallization
  - Prediction of Thermochemical Equilibria – Phase and Pourbaix Diagram
- LLNL/NSWC/NRL
  - General & Localized Corrosion
  - Environmental Fracture
  - Performance Prediction

MATERIALS DESIGN AND SYNTHESIS

The High Performance Corrosion Resistant Materials (HPCRM) Program has three primary objectives, all directed towards development of advanced amorphous-metal thermal-spray coatings with corrosion resistance superior to: (1) Type 316L stainless steel [UNS # S31603], (2) nickel-based Alloy C-22 [UNS # N06022], and (3) Ti Grade 7 (UNS # R52400). Computational materials science will be used to help guide the design these new materials.

Selection of Thermal Spray Process

A wide variety of thermal spray processes have been developed, and are available through the industrial members of the HPCRM Team (NanoSteel, Impreglon and Cateripillar). These processes include: flame spray, wire-arc; plasma spray; water-stabilized plasma spray; high-velocity oxy-fuel; and the detonation gun. Any of these can be used for the deposition of the formulations discussed here, with varying degrees of residual porosity and crystallinity.

The Flame Spray Process (FSP) uses a combustion flame, and characterized by relatively low gas and particle velocities. Typical metallic coatings produced with this process include Ni-Fe-Al compositions, with typical costs of approximately $10 to $30 per pound. These coatings have bond strengths of about 4,000 pounds per square inch, porosities of approximately 5 percent (5%), and micro-hardness of 85 HRB.

The Wire Arc Process (WAP) uses an electrical discharge instead of a combustion flame, and is more energetic than FSP. Typical metallic coatings produced with this process include 67% FE 28% Cr 5% C compositions, with typical costs of approximately $3 to $20 per pound. These coatings have bond strengths of about 5,800 pounds per square inch, porosities of approximately two percent (2%), and micro-hardness of 55 HRC.

The Plasma Spray Process (PSP) involves the use of and electric arc with inert gas to create a plasma. Flame temperatures as high as 30,000ºC can be achieved. Both metal and ceramic coatings can be produced, with typical costs of approximately $20 to $50 per pound. These coatings have bond strengths of about 8,000 pounds per square inch, porosities of approximately three percent (3%), and micro-hardness of 90 HRB.

The Laser Assisted Plasma Spray Process (LA PSP) was recently developed by Faunhoffer Institute, and involves the direct interaction of a high-intensity laser beam with spray particles and the substrate. This process has been to produce metallic coatings with virtually theoretical density, and with metallurgical bonding. In regard to the distribution of energy released during the process, ninety to ninety-five percent (90-95%) of the energy is transferred from the plasma torch to the spray powder, and used to melt the powder, while five to ten percent (5-10%) of the energy is consumed by the laser, and ultimately used to fuse the spray particles, and to melt the substrate.

The Water Stabilized Plasma Spray Process (WS PSP) has been recently developed by Caterpillar, and provides the capability of spraying at extremely high rates, approaching 200 pounds per hour. This process has already been used for coating large components, such as the Caterpillar Model 3500 Diesel Engine block. This process is shown in Figure 5 (right frame).

The conventional High Velocity Oxy Fuel (HVOF) Process also involves a combustion flame, and is characterized by gas and particle velocities that are three to four times the speed of sound (mach 3 to 4). This process is ideal for depositing metal and cermet coatings, including chromium carbide with a nickel-chromium binder. A typical coating cost is estimated to be approximately $20 to $50 per pound. . These coatings have bond strengths of about 8,600 pounds per square inch, porosities of less than one percent (<1%), and micro-hardness of 68 HRC. This process is also shown in Figure 5 (left frame).

The Detonation Gun Process (DGP) was developed in Russia, and is based upon the discontinuous detonation of an oxygen-fuel mixture. Very high gas and particle velocities are achieved with this novel process, velocities approaching four to five times the speed of sound (mach 4-5). This process is also ideal for depositing metal and cermet coatings, including dense coatings of chromium carbide with nickel-chromium binder. A typical coating cost is estimated to be approximately $20 to $50 per pound. . These coatings have exceptional bond strengths, in excess of 10,000 pounds per square inch, porosities of less than one-half of one percent (<0.5%), and micro-hardness of 68 HRC.

Several processes were rejected on the basis of unacceptable porosity and bond strength. These include: FSP, WAP and PSP. The process selected for the initial production of the coatings was HVOF, based upon the low porosities and high bond strengths that had been achieved in other applications.

Other more advanced processes may provide coatings superior to those possible with HVOF. These processes include HP HVOF, LA PSP, WS PSP, and DGP, and promise the advantages of fully dense coatings, improved bonding to substrates, and high rates of deposition. High-density infrared fusing with high-intensity lamps, a process developed by ORNL, may be used for post-deposition porosity and bonding control, provided that amorphous metals with sufficiently low critical cooling rates (CCRs) can be found.

Based upon the relative costs of the materials proposed for fabrication of SNF and HLW containers (Table 1), which are approximately $24/lb for Ti Grade 7, $8/lb for Alloy C-22, and $3/lb for Type 316L stainless steel, it is believed that Fe-based thermal spray coatings could be used as a cost effective replacement for the two most expensive (titanium and high-performance Ni-based alloys). Based upon current experience, it is believed that ton-quantities of Fe-based amorphous metal powders can be produced for about $20,000 per ton ($10/lb).

Precedents for Thermal Spray

As a member of the HPCRM Team, Caterpillar has now demonstrated the HVOF deposition of macroscopically thick coatings of chromium carbide (85 wt. % carbide with 15% metallic binder) on planar and cylindrical substrates (Figure 6). This large-scale demonstration is on a scale relevant to targeted DOD and DOE applications. Coatings of practical, industrial importance can be produced with thermal spray technology.

Corrosion-resistant, thermal-spray, ceramic coatings were investigated in the 1990s for the long-term storage of spent nuclear fuel. Two thermal-spray processes were compared in these early studies, the HVOF process, and the more conventional plasma spray process. It was found that relatively dense ceramic coatings with little interconnected porosity could be produced with HVOF (only 2% porosity), whereas the plasma spray process produced only porous coatings with substantial interconnected porosity (about 19% porosity). Consequently, the HVOF coatings were determined to be adequate for corrosion protection, whereas the more conventional plasma spray coatings were not, as shown in Figure 7. Similar heuristic principles apply to thermal-spray amorphous metal (metallic glass) coatings.

The results of a six-month immersion test of thermal-spray ceramic coatings in a hot bicarbonate brines confirms the corrosion resistance of the dense HVOF coatings, and the inadequacy of the more primitive plasma spray coatings. In the case of the HVOF coating, 45 mils of Al_2O_3-TiO_2 with a porosity of only 2 percent was deposited onto a carbon steel (1020) substrate, with an intentional 15-mil flaw introduced with a saw blade at the beginning of the test, to investigate the susceptibility of the coating to interfacial corrosion and spallation. This proved not to be an issue with the HVOF coating. A similar 45-mil coating of Al_2O_3, with a porosity of 19 percent, was deposited with the more conventional plasma spray process. In this case, the interconnected porosity led to substantial interfacial corrosion and spallation after the 6-month exposure, showing the inadequacy of plasma spray coatings for corrosion protection (Figure 8).

The thermal-spray coatings were exposed to hot bicarbonate brines for an additional 5-6 years, with the HVOF coating showing no interfacial corrosion or spallation, even with the intential flaw that was introduced with the saw blade. There is clear evidence indicating that such thermal spray coatings can provide adequate corrosion protection, even with substantial surface flaws (Figure 9).

DAR40 Parent Material

The HPCRM Team is investigating a variety of Fe-based amorphous metals for application as corrosion-resistant, thermal-spray coatings. One promising formulation, designated DAR40, was developed by the NanoSteel Company during execution of the DARPA-sponsored project entitled “Devitrified Nanocomposite Steel Coatings.” This early project was part of the larger DARPA-sponsored Structural Amorphous Metals (SAM) Program. The nominal composition of DAR40 is $Fe_{52.3}Mn_2Cr_{19}Mo_{2.5}W_{1.7}B_{16}C_4Si_{2.5}$. This material has exhibited very good glass-forming ability in the range appropriate for thermal spray, while retaining many of the processing characteristics necessary for feedstock production on an industrial scale. This material

was therefore selected as a parent material for the further development of Fe-based amorphous metals with outstanding corrosion resistance, that can be applied with thermal spray processes. Current developmental efforts include systematic studies of the effects of various elemental additions, including nickel, chromium, molybdenum, tungsten, yttrium, titanium, and zirconium, with micro-structural characterization, thermal analysis, and corrosion testing.

Based upon early testing, it is believed that DAR40 coatings have very good bond strength (>11,000 lb/in^2) on a wide variety of substrates including aluminum, stainless steel, and alloy steels, with high resiliency, high toughness, and impact resistance. Experimental Gardner drop impact tests of the DAR40 coatings have shown that the coatings do not fail at least up to 480 inch lbs (maximum available with the test system) which is much higher than what the Navy currently uses as a benchmark (192 inch lbs). The coatings have been shown to be exceptionally hard (>1000 kg/mm^2), and exhibit high wear resistance. Tests conducted by the Naval Surface Warfare Center (NSWC) have revealed that these coatings, in the devitrified condition, have a lower wear rate when subjected to the ASTM G65 (Dry Sand Rubber Wheel Abrasion) Test than other promising materials, such as the "nanoscale alumina-titania" ceramics.

With compositional enhancements of the elemental composition, and further improvements in intrinsic characteristics of the thermal-spray coating (microstructure, density, porosity and bonding), the HPCRM Team anticipates further improvements in damage tolerance, wear resistance, and corrosion resistance of this general class of Fe-based amorphous metals.

HVOF Process for Initial Deposition of Amorphous Metal Coatings

During the initial phase of this project, limited success was achieved with early thermal-spray coatings of DAR35 and DAR40, produced with the high-velocity oxy-fuel (HVOF) process. Unfortunately, these early coatings had unacceptable porosity, bond strength, and corrosion resistance for targeted DOD and DOE applications. These limitations have now been attributed to un-melted and un-consolidated particles, precipitation of undesirable crystalline phases, residual porosity and low density, and inadequate bonding. In response to sponsor recommendations made at the HPCRM Team Meeting in Key West, held in January 2004, the HPCRM Team has spent the past nine months concentrating on the use of synthesis techniques that enable researchers to separate the effects of alloy composition from the effects of coating porosity and other types of defects.

The high-velocity oxy-fuel (HVOF) process used to deposit the early amorphous metal coatings discussed in the following section operates at approximately 100 pounds per square inch, and is well established in industry as the "cutting edge" in thermal spray technology. Existing HVOF systems such as Tafa's JP5000 gun or Sulzer Metco's DJ Hybrid gun are considered to be 3rd generation devices. Recently, 4th generation systems, such as the high-pressure HVOF (HP HVOF) gun, have been developed that operate at 400 pounds per square inch, but have limited availability. Higher particle velocities (1000 m/s) can be achieved with the elevated pressure in the HP HVOF process, which thereby enables to production of coatings with near theoretical density through impact fusion. In impact fusion, a particle is deposited below its melting point but is heated up above its melting point from the high kinetic energy released during impact. The HPCRM Team anticipates that the HP HVOF process will help facilitate the production of

fully dense coatings. This process will be used in FY05 to deposit the amorphous metals with the best thermal stability and corrosion resistance.

Early Attempts with HVOF Coatings

The same thermal spray process used to produce the chromium carbide coating shown in Figure 6 has also been used to apply amorphous metal coatings. As members of the HPCRM Team, Caterpillar produced macroscopically thick sheets of DAR40X3 shown in Figure 10, while Impreglon Company coated stainless steel substrates with DAR35 and DAR40. Subsequent X-ray diffraction (XRD) of these early coatings verified that the coatings were predominantly amorphous, with some residual crystalline structure (Figure 11 and Figure 12).

Microstructure of HVOF Coatings

Five of the early samples with HVOF coatings were shipped from Lawrence Livermore National Laboratory (LLNL) to the University of Wisconsin at Madison (UWM). Three of these samples were coated with DAR35, while one was coated with DAR40, and the last was coated with DAR40X3. Nominal compositions of these formulations are summarized in Table 3. The disks were cut through and the cross-section analyzed with scanning electron microscopy (SEM) and X-ray diffraction (XRD).

DAR35 (PEA 451)

The X-ray diffraction pattern of the sprayed layer is shown in Figure 13. The broad peak centered around 44 degrees is characteristic for an amorphous structure. In addition, diffraction peaks from two other phases were recognized, bcc-(Fe,Cr) and a metasJP-Tableorthorhombic M_2B-phase. This phase seems to compete with a tetragonal Fe_2B at high undercoolings, based on our annealing experiments described previously. Some SEM images are shown in Figure 54. The sprayed coating has a homogeneous thickness; 410-430 μm. Overall, the structure of the coating consists of an amorphous matrix with pockets of crystalline areas (two-phase structure). There is no structural preference, i.e. a higher crystalline volume fraction close to the surface where cooling is slower. It almost seems as if some of the powder was not entirely molten during spray-forming of the sample and that single powders retained their initial crystalline structure. Powder is only partially amorphous; for mesh sizes larger than 20 μm, no glassy phase is retained, as has been observed from pure powder samples. This may explain the periodicity of which the crystalline regions occur throughout the sprayed coating. The amorphous matrix contains some precipitates that were too small for quantitative EDS analysis. The overall composition of the gray, glassy phase shown in Figure 14 is given in Table 4.

The last row of Table 4 indicates the nominal composition accounting for the lack of ability to quantitatively measure the boron content of the sample using this particular EDS system. Some porosity was observed in the sample; however, no quantitative measurements have been made to estimate the volume fraction of voids.

DAR35 (PEA 452)

The overall structure of this sample was virtually identical to PEA451. The X-ray diffraction trace of the as-sprayed coating is shown in Figure 15. A broad peak centered at 44 degrees was observed confirming the presence of an amorphous phase as well as crystalline peaks that could be indexed as bcc-Fe and orthorhombic M_2B.

Representative back-scattered electron images (BSEI) are shown in Figure 16. The coating has a homogeneous thickness approximately 450 μm. The structure was partially amorphous, with pockets of crystalline phases that very much resemble those observed in PEA451. Quantitative analysis with energy dispersive spectroscopy (EDS) is consistent with Table 4, and will not be repeated here.

DAR35 (PEA 504)

Based on the examination of PEA451 and PEA452, this sample was expected to show identical features as to microstructure and phase selection. The XRD trace given in Figure 17 is not surprisingly identical to those of PEA451 and PEA452.

The microstructure of the sprayed coating was identical to that of PEA451 and PEA452 (Figure 14 and 16, respectively) and will not be shown again here.

DAR40 (PEA 479)

The X-ray diffraction trace is shown in Figure 18. The sample is partially amorphous (broad peak centered at about 44 degrees) with some distinct crystalline peaks that are consistent with the presence of bcc-Fe and orthorhombic M_2B, similar to observations made on DAR35 sprayed coatings. The microstructure of the sprayed layer is partially amorphous with pockets of crystalline material, very similar to the microstructure observed in the DAR35 coatings. These pockets mostly spherical, supporting the hypothesis that the powder went through the spray-forming process without completely melting. Again, the spraying process has left a coating with a very uniform thickness of about 330 to 360 μm, somewhat thinner than for the samples described previously. Some representative micrographs are shown in Figure 19 through 21. The porosity of this sample was similar to that of the DAR35 coatings. There are some larger pores on the interface between the sprayed coating and the stainless steel disk (see Figure 19).

DAR40X3

This sample was unfortunately not associated with a PEA number upon reception. Also, only the coating itself was present in the shipment, as if it fell off the stainless steel disk (suggesting very poor bonding to the substrate). The XRD trace is shown in Figure 22.

The diffraction pattern suggests a mostly amorphous material with only a small volume fraction of crystalline material. The crystalline peaks appear to be of the same type as those found in other spray-formed coatings of DAR35 and DAR40. However, when observing the sample in the scanning electron microscope, the coating seemed far less amorphous than the XRD analysis

indicated. Some representative SEM images can be seen in Figure 23. Due to the nature of the sample, we do not have information on which side was facing the substrate.

From the micrographs in Figure 23, the microstructure of the sample resembles those of the other coatings described previously. An important difference is the presence of bright, faceted precipitates; see for example Figure 23d). The composition, as measured with EDS, was approximately 32Fe-35Cr-17Mo-4W-10C-2Mn, suggesting that Mo-carbides have formed at some point during processing. This sample is basically 97% DAR40 and 3% Mo, so it is quit plausible that the addition of extra Mo have caused some unfavorable stability and precipitation of high-melting carbides. Whether these carbides (or possible borides) formed during the spray process or if they were present in the initial powder remain undecided until the initial powder has been examined.

Pore-Free Amorphous Coatings by Careful Control of Powder Size

Early HVOF coatings were found to have too much porosity and residual crystalline structure for targeted DOD and DOE applications. Therefore, a systematic study was undertaken by the HPCRM Team to modify and optimize the HVOF process so that fully dense, pore-free coatings could be produced. This optimization was successful.

A parametric study of the HVOF process was conducted with DAR40, with the mean particle size of the sprayed powder and the substrate temperature systematically varied, and is illustrated in Figure 24. While coatings produced with relatively large particles (≤54 μm) showed un-melted and un-consolidated particles embedded in the coating, with substantial porosity and poor interfacial bonding, coatings produced with smaller particles (20 to 23 μm) are essentially homogeneous, pore-free and well-bonded.

X-ray diffraction (XRD) data for the DAR40 coatings deposited with HVOF during the parametric study represented by Figure 24 are shown in Figure 25. From this data, it is evident that the coatings produced with smaller particles (25 μm) are more amorphous in nature, with fewer residual crystalline phases, than the coatings produced with larger particles (38 to 53 μm).

Bonding

Photographs showing the integrity of the bond formed between a hollow, cylindrical steel substrate and an early Fe-based amorphous-metal coating produced with the HVOF process are shown in Figure 26. The composition of this coating is similar to the DAR-type compositions shown in Table 3. The first frame (a) shows a perspective of the coated hollow cylinder, while the second frame (b) shows a plan view. Optical micrographs of a metallographic cross-section of the coating, with magnifications of 20× and 100×, are shown in the third (c) and fourth (d) frames. The integrity of the interfacial bond formed between this wear-resistant, DAR-type coating and the hollow steel cylinder is good.

Corrosion Resistant Compositions with Theoretical Density

There was some concern regarding the residual porosity in the DAR35, DAR40, and DAR40X3 HVOF coatings produced by the HPRCRM Team. Thus, a decision was made at the 2004 HPCRM Team Meeting held in Key West to produce samples of the amorphous metals having theoretical (full) density and no residual crystalline phases. Melt spinning and arc-melting with drop casting have been used as a methods to synthesize completely amorphous, Fe-based, corrosion-resistant alloys with near theoretical density, thereby enabling the effects of coating morphology on corrosion resistance to be separated from the effects of elemental composition.

A picture of the melt spinning equipment used by NanoSteel to make developmental alloys is located in TNC's Institute of Nanomaterials Research and Development, and is shown in Figure 27. Cooling rates as great as one billion Kelvin per second (10^9 K/s) have been achieved. In contrast, the cooling rate in a typical thermal spray process such as HVOF are on the order of ten thousand Kelvin per second (10^4 K/s). The melt-spun ribbons produced with this equipment are several meters long, several millimeters wide, and approximately 150 microns thick.

The melt spinning involves the ejection of a liquid melt onto a rapidly moving copper wheel with a pressure-controlled gas. The liquid melt solidifies onto the wheel, with subsequent separation from the wheel by thermal contraction and centrifugal force, and collection in a chamber. By changing the tangential velocity of the wheel, as well as other processing parameters, the cooling rate can be controlled over a very broad range. The specific processing parameters for the melt-spinning process can be selected to establish cooling rates that are representative of a given thermal spray process. If a specific cooling rate produces an amorphous, glassy metal during melt spinning, it should also produce a glassy structure during thermal spray. It is therefore possible to use melt spinning to simulate the type of microstructure that can be achievable with thermal spraying, such as the high-velocity oxy-fuel process. Furthermore, an entire series of developmental materials, with different compositions, heat capacities, and thermal conductivity, can be made with the exact same cooling rate, thereby enabling materials scientists and engineers to determine the relative ease of processing.

During FY04, the HPCRM Team produced, characterized, and tested all of the amorphous metal formulations given in Table 3. In principle, all were intended to be compositional modifications of the DAR40 parent material, obeying the following the general formula: $[(DAR40)_{100-x} + Y_x]$ where Y is the added element, and x is the amount of the addition in atomic percent. Additives investigated during FY04 included nickel, chromium, molybdenum, tungsten, yttrium, titanium and zirconium. The nickel and molybdenum additions are known to greatly influence the electrochemical properties of conventional stainless steel alloys. The yttrium, titanium, and zirconium additions, while not normally added to steels are known to form very stable oxides and are expected to increase the stability and passivity of the oxide film in a variety of environments. The HPCRM Team has evaluated these materials, with particular emphasis on glass forming ability, thermal stability, hardness and corrosion resistance, all under conditions of interest. Results are discussed in the subsequent sections of this Annual Report.

The melt-spinning process was used to perform a systematic study of various elemental compositions, each based on the Fe-based DAR40 composition, with 1, 3, 5, and 7 atomic percent additions of specific elements believed to be beneficial to glass formation or corrosion resistance. Elemental additions investigated included nickel, molybdenum, yttrium, titanium, zirconium, and chromium (Table 3).

The densities of the amorphous metals prepared with melt spinning were determined, and all were less dense than nickel-based N06022 (Alloy C-22), and therefore offer a weight advantage over such classical corrosion-resistant alloys (Figure 28).

The first re-crystallization peak for each of melt-spun ribbons was determined with DTA, and was similar to that of the parent material (DAR40). The formula with the yttrium additions showed re-crystallization peaks at higher temperatures than achieved with other formulae, showing that yttrium additions do indeed promote thermal stability and glass formability. This data corroborates results from other DARPA SAM principal investigators at the University of Virginia (Figure 29).

Some formulae exhibited a second re-crystallization process at a higher temperature than the first, with titanium and zirconium based formulations showing these processes at the highest temperatures (Figure 30).

All of the "as-cast" amorphous metal formulae produced by the HPCRM Team exhibited hardness far superior to many of the conventional materials of interest, such as Type 316L stainless steel, and nickel-based N06022 (Alloy C-22). Thus, coatings of these materials would also be expected to be less prone to erosion, wear and gouging than conventional engineering alloys (Figure 31).

Partially de-vitrified samples of the HPCRM materials exhibited dramatic increases in hardness. Thus, carefully controlled heat treatment of these materials can be used to achieve dramatic improvements in resistance to erosion, wear and penetration (Figure 32).

In addition to the melt-spinning process, arc-melted drop-cast ingots of a wide variety of Fe-based amorphous metals were synthesized for corrosion testing by ORNL. These ingots were cast into cylindrical molds, thus forming long rods with a nominal diameter of 2-3 millimeters. By exploring the findings of Poon et al. [2004], another DARPA principal investigator involved in the SAM Program, it has been learned that additions of 2-3 atomic percent yttrium or zirconium can enhance the glass-forming ability (GFA), and substantially lower the required critical cooling rate (CCR). Such formulations are relatively easily cast as large-diameter (several millimeter) rods. The X-ray diffraction (XRD) pattern for drop-cast ingot of CBCTL1651, one version of this material, shows virtually no crystalline structure (Figure 33). Peak broadening of all three HVOF coatings suggest presence of some fine crystalline phases in the amorphous matrix. The exact composition of this material, which has also been produced as melt-spun ribbon, is given in Table 3 (note that the LDAR7 and CBCTL1651 nominal compositions are identical).

PREDICTING MATERIALS PERFORMANCE

A thorough understanding of the corrosion of these thermal-spray coatings must be developed before the materials can be used for the storage of spent nuclear fuel. Such understanding must account for the effects of processing on the metallurgical condition of the material, perturbation of the local service environment by heat (evaporative concentration), radiation, and microbes. The complex relationships that exist between the various processes is illustrated with Figure 34.

An integrated materials degradation model has been developed to predict the long-term performance of materials as a function of time, temperature and local environment [Farmer et al. 1992-2000]. Such a model must account for uniform corrosion, as well as the initiation, propagation and cessation of pitting and crevice corrosion. Thermal stability and environmental cracking are also important considerations. Thorough understanding of general and localized corrosion, as well as stress corrosion cracking, requires sound, scientifically based knowledge of passive film stability (Figure 35).

In regard to Figure 35, fundamental knowledge of the thermochemical equilibrium affecting the long-term performance of the new amorphous metals is needed. The thermochemical code is known as THERMOCALC has been used to calculate the phase and Pourbaix diagrams for these complex multi-component systems, thereby bonding the metallic phases that can exist within the three-dimensional bulk material, and the oxide (and other) phases that can exist at the metal-solution interface.

Detailed differential thermal analysis and wedge casting of these materials has given clear insight into phase transformation kinetics, and the exact nature of the precipitated phases. In regard to devitrification and the precipitation of crystalline phases, insight is summarized in the form of classical time-temperature-transformation (TTT) diagrams.

Corrosion rates are being deduced from changes in weight and dimension during on-going immersion testing, as well as from current density measurements during potentiodynamic and potentiostatic testing.

The initiation of localized corrosion in liquid-phase aqueous environments is quantified with measurements of the threshold (critical or repassivation) potential, relative to the open-circuit corrosion potential.

These experimental measurements serve as the foundation for the integrated materials degradation model shown in Figure 35, and are discussed in detail in the following sections entitled “Phase Stability of Amorphous Metals” and “Corrosion Resistance of Amorphous Metals.” The total system performance assessment (TSPA) required for repository licensing, or for the amendment of an existing license, requires such measurements.

PHASE STABILITY OF AMORPHOUS METALS

Differential thermal analysis (DTA), differential scanning calorimetry (DSC), and the wedge casting technique have been used to study the thermal stability of several developmental amorphous metals listed in Table 3. The results of those studies are summarized here.

Initial Images of Aged Melt-Spun Ribbons and Drop-Cast Ingots

X-ray diffraction (XRD) has been used to show that the matrices of melt-spun ribbons of DAR40, and drop-cast ingots of CBCTL1651 and EBAMD6A5A remain amorphous to 500°C, as shown in Figure 36. However, XRD is not effective for detecting dispersed crystalline phase(s) that account for less than 2 volume % of the material.

Electron microscopy was therefore used to compensate for this shortcoming. From the back-scattered electron images (BSEI) of DAR40, CBCTL1651 and EBAMD5A6A, shown in Figure 37, it is evident that EBAM5A6A is less thermally stable than either DAR40 or CBCTL1651.

Elemental mapping of melt-spun ribbons of DAR40 shows the formation of crystalline phases in after a 1-hour exposure at 800°C. Substantial crystallization occurs after a 1-hour exposure at 1000°C (Figure 38). In contrast, elemental mapping drop cast ingots of CBCTL1651 shows no formation of crystalline phases in arc-melted drop-cast ingots of CBCTL1651 after a 1-hour exposure at 800°C, but the onset of crystallization after a 1-hour exposure at 1000°C. Small yttrium oxide particles remained unaffected in the matrix (Figure 39).

Differential Thermal Analysis & Differential Scanning Calorimetry

Differential thermal analysis (DTA) and differential scanning calorimetry (DSC) have been used to characterize several of the amorphous metals of interest, including DAR35, DAR40 and DAR40X3. Characterization has yielded the melting point (T_m), the liquidus temperature (T_l), the glass transition temperature (T_g), the recrystallization temperature, and the reduced glass transition temperature (T_{rg}), which is in indicator of the ease at which a given material will form a glass. Values of T_{rg} approaching 0.6 are considered favorable.

Thermal analysis was performed with thin ribbon made with the melt-spinning process at the University of Wisconsin Madison. To facilitate rapid quenching of candidate alloys, a single-roller melt-spinner operating in an inert atmosphere is used. Wheel speeds can be selected from 1 to 55 m/s, giving ribbons with thickness between 20 and 100 μm. The samples are induction heated in quartz-crucibles coated with Y_2O_3 to minimize reactions between the molten sample and the crucible. Evacuation pressures are ~ 5×10^{-6} torr. Prior to heating, the furnace chamber is backfilled with argon to about 5 torr below atmospheric pressure. The melt is injected from the crucible onto the spinning Cu-wheel using a jet of argon gas. Typical cooling rates for this type of quenching is of the order 10^5 K/s.

A Perkin-Elmer DTA-7 differential thermal analyzer was used to obtain the melting point (T_m) and liquidus temperature (T_l) of the various alloys. Samples were heated to 1500 °C, held for a

few minutes, and then repeatedly cooled to 850 °C and heated to 1500 °C. The DTA can heat small samples (~100 mg or less) to 1600°C in a titanium-gettered argon atmosphere. Typical heating and cooling rates are between 5 and 40 K/min. This instrument can provide accurate information on phase transformations within the sample, including magnetic transitions, upon heating and cooling of the sample.

A Perkin-Elmer DSC-7 differential scanning calorimeter was used to obtain glass transition temperatures (T_g) and crystallization temperatures (T_x) of the amorphous phase. The DTA can heat small samples (~20 mg or less) to temperatures up to 650°C, in a titanium-gettered argon atmosphere. The 650°C temperature limit is due to the use of an aluminium sample pan. However, the limit can be increased to 800 °C with the use of steel sample pans. Typical heating/cooling rates are between 5 and 40 K/min.

All temperatures are defined as the onset/offset temperature of the reaction in question. That is, the intersection of the baseline tangent and the inflection point tangent for the reaction, as shown in Figure 40, where the onset temperature for glass transition and crystallization are indicated. A similar procedure is used to define melting temperature and liquidus temperature. The solidification temperature (T_s) was recorded during continuous cooling. DTA data is shown in Figures 41-53, and DSC data is shown in Figures 54-56.

A summary of the thermal analysis data for melt-spun ribbons is given in Table 5, which shows all of the acquired information to date on Fe-alloys investigated during the first year of this project. The table lists glass transition temperature T_g, crystallization temperature T_x (of the amorphous phase), onset of melting T_m and liquidus temperature T_l. In addition, a rough measure of the glass forming ability is listed as T_{rg}, the reduced glass transition temperature defined as T_g/T_l where temperatures are given in degrees Kelvin. Good glass forming alloys have high reduced glass transition temperatures of about 0.55-0.60. There are other ways of defining the glass-forming ability (GFA) based on a thermal analysis, however, they all have in common that one method may fit a particular alloy better than a different method. Caution is therefore advised when using thermal analysis as means of estimating GFA.

Identification of Precipitated Phases

The precipitated products of crystallization were identified with X-ray diffraction (XRD) and scanning electron microscopy (SEM) with energy dispersive spectroscopy (EDS). A standard diffractometer was used for XRD and phase identification. Its main features are a standard Bragg-Brentano goniometer, focused beam transmission goniometer, minimum step size 0.001 degrees, reproducibility 0.001 degrees, 2-theta range 0.15 degrees to 140 degrees. Multiple stages to accommodate many specimen types are available. Parallel optics attachment for grazing incidence studies of thin films. Two high temperature furnaces for phase transition studies are available: furnace for sealed capillaries which can go up to 1000 °C and a vacuum furnace that can go up to 2000 °C. Position sensitive detector (PSD) for rapid parallel data collection. Peak refinement and matching software packages use the JCPDS database for peak identification. Also, structure determination software packages are available.

A general-purpose JEOL 6100 scanning electron microscope (SEM) was used for imaging. Operating accelerating voltages between 5 and 30 kV. Resolution:4.0 nm at 30 kV and 8 mm working distance. Light element EDS detector for compositional analysis excluding boron, limited accuracy for samples containing carbon. Back-scattered electron detector allows for good phase contrast on unetched samples. Digital image acquisition and processing. X-ray mapping giving elemental distribution at the sample surface available.

A Phillips CM200 UT intermediate-voltage high-resolution transmission electron microscope (TEM) was also used for imaging The resolution of this instrument is 0.19 nm at 200 kV operating voltage. This instrument had a double tilt sample holder, NORAN high purity Ge EDS detector, and Gatan digital image capturer.

Compositional information was also obtained with the CAMECA SX50 EPMA microprobe. This instrument has five (5) vertical spectrometers, four (4) of which hold two (2) diffracting crystals each and one with four (4) crystals, with detection and quantitative analysis of elements from Be on up the periodic table. Crystals available are LIF, PET, TAP, PC0 (45 A), PC1 (60 A), PC2 (100 A) and PC3 (200 A). This instrument also has: a PGT EDS detector and software (Be window) with detection for Z10; anti-contamination devices (cold finger, gas jet) for light element work; CITZAF online matrix correction with Probe for Windows Enterprise Version. Ability to work at low accelerating voltages for light elements in conductive materials and thin films, and model curved backgrounds (exponential or polynomial) with Probe for Windows. It has the ability to de-convolute first order peak overlaps (e.g. Mo and B) within the matrix correction, using Probe for Windows. Flexible software permits extensive post-processing (e.g., application of alternate stanSAMds and background models). Very few microprobes in the US have similar analyzing capabilities. This instrument is used when accurate boron/carbon quantitative levels need to be determined.

Calculation of Time Temperature Transformation (TTT) Curves

A traditional way of estimating glass forming ability has been to calculate TTT curves, where the position of the nose gives the critical cooling rate to avoid nucleation and growth on cooling. An approach similar to that of Uhlmann [1972] is widely used, where the volume fraction X crystallized in a time t may be expressed (for homogeneous nucleation)

$$X \approx \frac{1}{3}\pi I_v u^3 t^4 \qquad (1)$$

Here I_v is the nucleation frequency per unit volume and u is the growth rate (rate of advance of the crystal-liquid interfaces per unit area of the interfaces). The major difficulty with using equation (1) is that information on the temperature-dependence of the viscosity, which is part of the growth term, is not available. Due to the strong influence of the viscosity at high undercoolings near glass transition, calculated TTT-curves are extremely sensitive to the thermophysical parameters used as well as to Gibbs free energy approximations.

In metallic glasses the glass forming ability is normally limited by heterogeneous nucleation of the undercooled liquid. Taking this into account, the following procedure is used to calculate TTT-curves using DSC isothermal anneal of as-spun ribbons as calibration points.
Based on classical nucleation theory for heterogeneous nucleation the steady-state nucleation rate J can be expressed as [Fecht 1990]

$$J = \Omega \exp\left[\frac{-\Delta G^{*} f(\theta)}{kT}\right] \tag{2}$$

where k is Boltzmann`s constant, $f(\theta)$ is a catalysis factor, $0 \leq f(\theta) \leq 1$ where θ is the contact angle. For a spherical nuclei $f(\theta)=(2-3\cos\theta+\cos^3\theta)/4$. The prefactor term can be expressed as

$$\Omega = \rho_s \nu = \rho_s D_L / a^2 \tag{3}$$

where ρ_s = available site density, ν = attachment frequency, D_L = liquid diffusivity and a = jump distance. The driving force for nucleation of a spherical nucleus, ΔG^{*}, is obtained from classical theory as

$$\Delta G^{*} = (16\pi/3)\left(\sigma^3 / \Delta G_v^2\right) \tag{4}$$

where $16\pi/3$ is a geometrical factor characteristic for the formation of a spherical nucleus, σ is the interfacial energy between liquid and solid and ΔG_v is the free energy difference between the liquid and crystalline phases. Values for ΔG_v have been calculated by Larry Kaufman based on the maximum driving free energy for nucleation from the under-cooled liquid as illustrated in Figure 57.

The onset of crystallization will be defined as when a nucleation occurs within a volume V at a given temperature T after a crystallization time t, i.e.

$$JVt = 1 \tag{5}$$

The significance of the crystallization volume V is that it has to be small enough such that when a crystal nucleates, it will grow and occupy the entire volume V before another nucleation event can take place within the same volume. The volume V will go into a prefactor term as ln $(1/V)$, making the calculations less sensitive to the particular value of V. The diffusion coefficient for nucleation is related to the viscosity through the Stoke-Einstein equation, by assuming that diffusion and viscous flow occur with the same mechanism based on Brownian motion:

$$D = \frac{kT}{3\pi a \eta} \tag{6}$$

where η is the kinematic viscosity. This correlation is widely used to introduce viscosity into the nucleation rate equation, however, it should be noted that there is evidence, mostly collected with molecular glass-formers, that equation (6) does not hold for temperatures around T_g, but

starts to fail around 1.2 to 1.3 T_g, as discussed by Battezati [2004]. In the current work, however, we have used the traditional version of the Stokes-Einstein relation. For glass-forming alloys, a Vogel-Fulcher-Tamann relation can be used to express the viscosity as a function of temperature:

$$\eta = A\exp\left[\frac{B}{T - T_0}\right] \tag{7}$$

where A and B are constants, and T_0 is the temperature at which the excess configurational entropy is zero, the Kauzmann temperature, usually somewhat lower than the measured T_g on heating. T_0 could in theory be measured with infinite slow heating rates. As will be demonstrated later, the parameters A, B and T_0 will be the main fitting parameters when constructing the TTT-diagram.

Inserting equations (2)-(4) and (6)-(7) into (5), we have the following expression linking the onset time for nucleation to the temperature:

$$\ln(t) = \Gamma + \frac{B}{T - T_0} - \ln T + \frac{C}{T\Delta G_v^2} \tag{8}$$

The prefactor $\Gamma=\ln(3\pi a^3 A/\rho_s V k)$ is assumed independent of temperature. The constant C in the driving term is given by $C=(16\pi/3k)\sigma^3 f(\theta)$. Rearranging equation (8) yields

$$\ln(t) - \frac{B}{T - T_0} + \ln T = \Gamma + \frac{C}{T\Delta G_v^2} \tag{9}$$

By plotting the left hand side of equation (9) versus $1/T\Delta G_v^2$, the constants Γ and C can be determined using a linear fit to the data. Onset times as a function of temperature are acquired from isothermal annealing experiments as described in a previous section. In addition, data from a different temperature regime is required to determine the viscosity parameters, since there are many combinations of B an T_0 that would yield a good fit to equation (9), but make little sense in other temperature regions. By wedge casting the alloy in question, the critical cooling rate to avoid crystallization is measured, and this combined with the isothermal onset times is enough to determine the constants of equation (9) through an iterative process. This will be illustrated when discussing TTT-curves for DAR35, DAR40 and DAR40X3.

The outlined procedure uses two principal experimental techniques, isothermal anneal of as-spun ribbons and wedge casting. The experimental temperature range for the annealing experiments is limited to the super-cooled region between T_g and T_x. Accessing other temperature regimes is not trivial, however, we are currently doing experiments on up-quenching of amorphous ribbons by dipping them into molten salt in a temperature range 600-800 °C for various durations with subsequent quenching in ice-water. Subsequent XRD analysis reveals whether the ribbons partially crystallized during the heat treatment. Thus, by varying the holding times in the salt, a portion of the TTT-curve can be mapped out and compared to the calculated curve. This allows us to extend the temperature region in which experiments can be performed to those between T_g

and T_N, the nose of the TTT-curve. It should also be noted that in other temperature ranges there may be a competition between several crystalline phases and it is not possible to say which one will actually nucleate first based on experiments in the low temperature range around T_g. It is recommended that the upper portion of the TTT-curve is evaluated in terms of crystallization products, but there are major experimental difficulties involved due to the speed of which these reactions occur, with rapid nucleation and growth of other phases, a non-existent problem at lower temperatures due to sluggish kinetics. Possible solutions are currently being considered.

TTT Curves for Corrosion Resistant Amorphous Metals

The TTT curves for DAR35, DAR40 and DAR40X3 have been evaluated by using the procedure described in a previous section. Ribbons of these three alloys were heated at 40 K/min to temperatures between T_g and T_x as measured on continuous heating and held there until crystallization was complete. Figures 54-56 show the heat flow vs. time for DAR35, DAR40 and DAR40X3, respectively. The onset time of crystallization is determined with the tangential interception method.

The crystallization reaction of DAR35 ribbons consists of a double peak, evident for lower annealing temperatures, but upon careful analysis of the exothermic peaks we observed that a double peak is observed at all annealing temperatures, although difficult to see for temperatures above 600 °C. For the phases involved, nucleation and growth kinetics decrease with different rates as annealing temperatures are decreased, causing a split of the exothermic crystallization peak. The heat of crystallization is 60-80 J/g, higher values for lower annealing temperatures.

The isothermal behavior of DAR40 is shown in Figure 55. It is not evident that two peaks overlap here, although some indications thereof can be observed for the annealing curve at 570 °C. The crystallization onset temperatures are shorter for DAR40 than for DAR35, even though DAR40 has a higher T_g and T_x (Table 5) and thus a higher stability would be expected if the same crystalline phase was forming. However, as will be discussed in a later section, the primary crystallization products in DAR35 and DAR40 are different. The heat of crystallization is 55-70 J/g, with no clear temperature dependence.

The isothermal crystallization curves for DAR40X3 are shown in Figure 56. Note the difference as compared to DAR35 and DAR40. The peaks of crystallization in DAR40X3 are smaller and wider and in general more difficult to interpret. The onset time for crystallization can in most cases be defined with relative ease, especially for the highest annealing temperatures. For annealing temperatures of 575 and 580 °C, the exothermic peak is stretched out and it is more difficult to define the onset. The heat of crystallization is about 5 J/g, an order of magnitude lower than DAR35 and DAR40, indicating that a completely different crystallization sequence takes place.

Onset times are plotted versus temperature according to equation (9) in Figures 58, 59 and 60 for DAR35, DAR40 and DAR40X3, respectively. The data are fitted with a linear approximation, which gives the slope (constant) C of equation (9) and the interception with the primary axis gives the prefactor Γ. It should be noted that as is common with nucleation kinetics analysis, there is a relative narrow range of temperatures available for measurement. Thus, the kinetic

parameters that are derived from Figures 58-60 have a large uncertainty. In order to overcome this difficulty we are incorporating other kinetics measures such as CCR.

There seems to be some curvature in the data of Figure 58. This may indicate that there is a temperature dependency that is not captured with the model. In particular, this could suggest that the prefactor Γ of equation (8) is not constant, or that the viscosity parameters B or T_0 have a weak temperature dependency. The curvature issue is noted, and we will look closer into it in future calculations. For now, since the deviations are small (within error bands less than 6%), they are neglected

The chemical driving force ΔG_v was calculated for temperatures between T_g and T_L on the assumption that Fe_2B was the first solid phase to precipitate from the amorphous phase. This is indeed the case for alloy DAR35, however, for DAR40, the primary phase is Fe_3B and for DAR40X3 an unidentified phase comes out first during isothermal anneal. More details on the primary phase identification can be found in a later section. However, for the present discussion, the free energies of Fe_2B and Fe_3B will be assumed to be quite similar, based a study done by Palumbo [2003]. Thus, Gibbs free energy data for Fe_2B was used for DAR40 as well.

In order to accurately calculate the TTT-curve for DAR40X3, we need to identify the primary phase. For now, we assume that the driving force for nucleation is similar to those of DAR35 and DAR40 and also for this alloy, the calculations are carried out using data for Fe_2B for the driving free energy.

The viscosity parameters are found through an iterative process, where the final curve has to reproduce both the isothermal points and the critical cooling rate as determined in the wedge-cast experiment, as illustrated in Figure 61 for DAR35. The critical cooling rate of DAR35 has been measured to 425 K/s.

A TTT-diagram for the three alloys discussed in this section is shown in Figure 62. The critical cooling rate of DAR40 and DAR40X3 has not yet been measured, so there will probably be some modifications to these curves when experimental data become available. The TTT-curve for DAR40X3 is known to be incorrect since we have used the driving free energy of bcc-Fe, but this is not the primary crystallization product on annealing. When data for phases such as Fe_2B and Fe_3B become available, these should produce more accurate curves. In Figure 62, the curve for DAR40X3 is obviously incorrect for temperatures above 1100 K as it flattens out well below its melting temperature. Further examination of this issue is in progress.

Kissinger analysis

Kissinger [1957] proposed what has become one of the most common methods for the interpretation of data from the thermal analysis of amorphous metals. Originally, this method was used to study the kinetics of reactions of the "solid → solid + gas" type, but since then it has been applied to a number of reactions that proceeds at a rate varying with temperature, i.e. possesses an activation energy E_a, or in other words the position of the peak of the reaction changes with heating rate if all other experimental conditions are fixed. Due to its simplicity, the

Kissinger analysis is widely used (and sometimes misused) to provide qualitative assessments of the stability of glassy phases. The method can be stated in a single equation:

$$\ln\left(\frac{T_p^2}{R}\right) = \frac{E_a}{R_g T_p} + C \qquad (10)$$

Here, T_p is the peak temperature of the reaction (i.e. crystallization in our case), R is the heating rate and R_g is the gas constant (8.3144 J/mol-K). By plotting the left hand side of equation (10) vs. $1/T_p$, a straight line is obtained, which slope is used to obtain the activation energy of the reaction.

Amorphous, melt-spun ribbons of DAR35, DAR40 and DAR40X3 were heated in the DTA at heating rates 5, 10, 20 and 40 K/min. The peak temperatures for crystallization was recorded, and Kissinger plots (Figure 63) were constructed.

Higher activation energy is interpreted as a more stable glass in terms of avoiding devitrification of the glassy phase. Based on Figure 63, DAR35 and DAR40 have very similar activation energies for crystallization, while DAR40X3 has lower activation energy, thus its amorphous phase is less stable than DAR35 and DAR40. The estimated activation energies are quite reasonable for bulk glass-forming alloys.

Wedge Casting

Evaluation of critical cooling rates (CCRs) for glass formation has been performed on DAR35, LDAR7 (CBCTL1651) and LDAR2X7 alloys using the experimental wedge cast apparatus designed by University of Wisconsin at Madison (UWM) described previously (Figure 64).

The wedge-casting mold is a powerful tool. Using the same furnace and chamber as described above, the sample is induction-melted in an argon-atmosphere and injected into the mold using argon gas. The copper-mold (10 × 10 × 9 cm) with a V-shaped cavity (8 cm high, 4 cm wide with an adjustable opening angle 4-14 °) allows for cooling rates between approximately 10 and 3000 K/s. Thermocouples (type R) are positioned along the vertical center plane of the wedge to monitor temperature in the sample. The thermocouples are connected to a computer using a PCI-DAS-TC input board (Omega Engineering) especially designed for temperature monitoring. A commercially available software system (Daisy-Lab, Omega Eng.) is used to monitor and record the temperatures. The acquisition rate used is 5 Hz, which is chosen based on the tabulated minimum response time for the thermocouple wire (0.2 mm thick, response time approximately 0.3 seconds, according to the manufacturer). Strictly, the minimum response time applies for a butt-welded junction (i.e. junction has the same diameter as the individual wires) but in practice the junction diameter is larger, thus response times somewhat slower than ideal. After casting, samples are cut from the wedge for various micro-structural analysis (SEM, TEM, XRD) and calorimetric analysis (DSC, DTA). The microstructure at any given location within the wedge can be associated with a calculated cooling rate based on a finite element heat transfer analysis of the wedge applying the acquired temperature data for different vertical positions in the wedge.

To obtain cooling rates at various locations within the wedge, the two-dimensional transient heat transfer equation is solved using a finite element approach implemented in commercially available software (FEHT, www.fchart.com). The software allows for a temperature-time-position dependence for all the properties used in the simulation. A two-dimensional (2-D) approximation of the heat flow within the wedge is justified due to the relatively short heat transfer distance to the angled walls compared to the ~ 10 times longer heat diffusion distance to the side walls. Also, typical values for the Biot number are less than 1 (0.2-0.5), which indicates that thermal gradients normal to the primary heat flow direction within the sample are negligible. Thus, a 2-D finite element approach at the middle plane within the wedge (20 mm distance to both front and back walls) seems reasonable. Indeed, when a three-dimensional (3-D) calculation was applied (simulation carried out by Howmet Corporation, which is located in Michigan), the results were virtually identical to the 2-D approach using the same material properties. Material properties of the molten sample are usually not known, so in most cases calculated values for a Fe-10Zr-20B alloy are used, averaged over the temperature range 25-1500 °C. The temperature distribution as a function of time is solved simultaneously for all node positions within the wedge. Using a temperature-dependent heat transfer coefficient (HTC) computed temperature curves can be fitted very well to measured temperature curves, using a trial and error approach. It has been found that the HTC do not significantly depend on position, thus, one set of HTC values that fit well to a particular thermocouple position is as a first approximation taken to be valid for the entire mold-melt interface. However, separate fits are always carried out for each measured curve to ensure that a constant (with respect to position along the interface) HTC is a valid approximation. A linear extrapolation of HTC values can be used if a significant position-dependence is found between two different thermocouple positions.

The wedge-cast design described here allows for quantitative and accurate description of the cooling rate for these Fe-based glass forming alloys, though the technique itself can be used to analyze other casting phenomena as well. Typical cooling rates are between 1 and 2000 K/s, depending on position in the wedge.

Thermocouple wire (type R, Pt-Pt13%Rh) is acquired from Omega Engineering. Wire diameters are normally 0.008 inches, but we have recently (April 2004) started to use 0.005-inch diameter to facilitate faster response times, which is important to monitor the pouring process and the initial cooling properly. In future experiments we will try 0.003-inch diameter wire as well to further improve response times. Attempts to use 0.001-inch wire was not successful due to the inconvenience related to working with such thin wires. The bare thermocouple wires are welded together, making the junction area as small as possible to minimize response time.

In an attempt to improve temperature response times and data acquisition rates, a fiber-optic sensor was added to the wedge-cast experimental setup. Accufiber, now part of Luxtron Corporation, manufactured sensors and analyzers. The sensor is a 2.5 mm-diameter sapphire light-pipe that transmits the emitted light from the melt through a fiber-optic cable to a control unit connected to a PC. The control unit calculates the temperature of the melt based on the wavelength of the incoming light. This system is extremely rapid and also is immune to electromagnetic noise arising from the induction coil. Response times for the control unit is less than a milliseconds, but there is a limitation on the data transfer between the control unit and the computer, limiting the frequency at which temperature data can be written to a file to 50 Hz.

Still, this is a significant improvement as compared to the thermocouples. The fiberoptic sensor allows for more subtle analysis, for example re- coalescence effects upon cooling of the alloy.

Experimental points on the TTT-curve are available through isothermal annealing experiments. By examining a heating trace, the super-cooled liquid region is identified as the temperature range between T_g and T_x. Between these two temperatures, the nucleation rate is sufficiently slow such that analysis is possible using DSC. As-spun ribbons are heated at 40 K/min to a pre-selected temperature and held there until the ribbons are devitrified. This procedure is typically done for 5 degrees interval between T_g and T_x. The experimental data are used in the kinetic analysis.

DAR35

Samples were taken from a sprayed plate (received by UWM in October 2003, and marked DAR35-3). Twenty (20) grams of coarsely crushed material was induction-melted and cast into the wedge-shaped mold. Normally, a sample mass of approximately 50 grams is preferred, but we did not have enough material available at the time. The temperature-time curve, shown in Figure 65, of the quenching alloy was obtained at a distance 20 mm from the tip of the wedge. The wedge-opening angle was seven degrees (7°). The temperature dependence of the heat transfer coefficient (fitting parameter) is shown in Table 6. Note that a comparison of *h* for different wedge-casts can be used qualitative to describe heat transfer properties of the sample alloy, since it is expected that the overall h should not be very different for modest changes in the composition. Thus, when a large difference in the actual value is observed (i.e. is needed to fit the experimental curve), this indicates that the thermal conductivities may be quite different.

The transition from an amorphous to crystalline microstructure may appear different from one wedge to another. In the case of DAR35, the transition from fully glassy structure to fully crystalline structure occurred over a vertical distance of about 3 millimeters. Localized crystallization occurs independent of horizontal position, which suggests heterogeneous nucleation and growth. Homogeneous nucleation and growth is characterized by a C-shaped transition reflecting isotherms in the wedge during cooling, i.e. faster heat removal and cooling rates close to the interface and slower cooling in the middle of the wedge.

The cooling rate at center position (indicated by the star) of Figure 66 was 450 K/s and can be taken as reasonable approximation to the CCR since only limited crystallization is observed at this location. For the remainder of this report, cooling rates are always calculated at positions in the middle of the wedge, i.e. with equal distance to both of mold-melt interfaces. Details from the crystallized regions can be seen in Figure 67, although the small size of the crystals (< 1 μm) makes reliable compositional analysis using EDS virtually impossible. Consequently, we can say very little about the nature of the solid phases appearing in Figures 66 and 67, except they both have a different composition than the matrix based on the contrast in the back-scattered electron images. It may be necessary to make TEM-samples from the wedge in order to acquire detailed information about the solid phases appearing in Figure 67. On a side note, these crystalline structures are very similar to those observed in partially devitrified powder of DAR35. The analysis of powder samples of DAR35 will follow in a later section.

The existence of a glassy phase in the lower portions of the as-cast wedge was confirmed through thermal analysis (DTA). The heating trace, 40 K/min, is shown in Figure 68. The glass transition temperature on heating was not well defined, in fact, by closer examination of the curve prior to the distinct crystallization signal onset at 612°C there are some weak exothermic signals that could be associated with growth or a liquid phase separation. On further heating, exothermic (crystallization) peaks occur at about 680 and 830°C, i.e. complete devitrification of glassy DAR35 takes place over a wide temperature range and the final structure will consist of several phases. The melting temperature is 1082 °C, which compares well with that observed for melt-spun ribbons (see Table 5). The final liquidus temperature was measured as high as 1370 °C, probably due to the formation of high-melting carbides or borides during devitrification of the glassy phase. Most of the melting occurs at temperatures between 1080 and 1180°C.

For cooling rates slower than approximately 400 K/s, the as-cast microstructure is completely crystalline. Figure 69 shows back-scattered electron images for wedge casting sections with calculated cooling rates at about 350 K/s. The two-phase microstructure is similar as that of Figure 67b, although obviously coarser due to the lower cooling rate, which allows more growth of the crystalline phase.

The crystalline phases observed in Figure 69 have not been positively identified yet. The dark phase that appear to be somewhat faceted is likely an M_2B-type phase, either tetragonal or orthorhombic. M_2B is known to be the first phase to form on devitrification of the glassy phase (see TEM-analysis of partially devitrified ribbons). Some segregation of the heavier elements takes place at grain boundaries; see for example the upper left portion of Figure 69.

For even slower cooling rates, the as-cast microstructure starts to resemble that of samples cooled slowly in the DTA, with at least four different solid phases. The dark, faceted M_2B phase in Figure 70 has now grown considerably in size with an average cross-sectional width of about 5 μm as compared to the 500 nm large particles of Figure 69. The composition of the faceted needles as measured with EDS (all numbers are atomic percent) indicated 56%Fe, 36%Cr, 3% Mn, 3%Cr, and small amounts (< 1 %) of Mo and W. Note that no Si was found in this M_2B type phase. Boron cannot be accounted for with this analysis technique. The bcc-phase contains 80% Fe, 5%Cr, 10%Si, 3% C, 2% Mn and small amounts (<1%) of Mo and W. The bulk of molybdenum and tungsten are found in the bright phase, although the typical size of the Mo, W containing phase is too small to obtain reliable quantitative composition data using EDS. The solid phases between the long needles appear to have formed a three-phase eutectic. The microstructure of a sample from the wedge that was re-melted in the DTA is shown in Figure 71 (a and b). The cooling rate was 0.67 K/s. Essentially, the same four phases can be observed for the DTA-melted sample. The width of the M_2B needles has increased to about 50 μm due to slower cooling rates.

X-ray diffraction of a 1.5 mm thick piece from the wedge is shown in Figure 72. Only the bcc-phase has been positively identified so far. A complete phase identification based on XRD may be difficult because of relatively large amounts of element substitution in the respective unit cells causing a shift in the lattice parameters and consequently a shift in the observed peaks compared to the theoretical peaks.

In summary, the critical cooling rate for glass formation was successfully measured using the wedge-casting apparatus. Due to the nature of the transition region between the amorphous and crystalline as-cast microstructure, the CCR is found to be between 420 and 460 K/s. This is well within the capabilities of a spray-forming process to form an amorphous thin coating. Consequently, based on glass formation criteria only, DAR35 is suiJP-Tableas amorphous coating material. The stability of this alloy was discussed in a previous section (Kinetic analysis: Time-temperature-transformation diagrams).

LDAR2X7

This alloy is a modification of DAR40, containing additional Mo according to the formula $DAR40_{93} + Mo_7$. NanoSteel Company supplied these ingots. Standard wedge-casting procedure was applied to yield a cast sample subject to a range of cooling rates.

The measured time-temperatures at z = 10 and 15 mm are shown in Figure 73 along with a calculated curve equivalent to the position of the thermocouple at 10 mm above the tip. The response times of the thermocouples were insufficient to properly reflect the rapid temperature increase in the mold after pouring. The initial solidification which must have taken place based on micro-structural analysis was not captured, i.e. no solidification plateau can be observed for z = 10 mm. The small bump in the t-T curve for z = 15 mm could be related to a recalescence effect as the final liquid solidifies at very high under-coolings. This particular cooling curve behavior has been observed in several wedge cast experiments and is under investigation.

The calculated curve of Figure 73 uses approximations for thermal conductivity, heat capacity and density. Knowing the true values for these properties and their temperature-dependence is not crucial for the assessment of the critical cooling rate. Heat transfer at the melt-mold interface dictates the overall cooling behavior through an apparent temperature dependent heat transfer coefficient, which can be described as a sum of step-functions with values as shown in Table 7. A step-function is used to describe the heat transfer coefficient, as this is the preferred mathematical description by the software in order to minimize computing time, however, other expressions could be used as long as the final result is able to reproduce the measured time-temperature curve such as the one shown in Figure 73.

Scanning electron microscopy images are shown in Figure 74, the tip of the wedge is shown with a mostly amorphous structure, although a few particles can be observed. Some of these are probably carbides/borides with high melting points that were not completely dissolved in the liquid prior to pouring. It also appears that as if Mo-rich crystals formed on have triggered nucleation of a second crystalline phase that appears as dark dendrites.

The transition from a mostly amorphous microstructure to fully crystalline one is well defined in this wedge cast alloy, as seen in Figure 75. The calculated critical cooling rate is 610 K/s at the position indicated with a star symbol in this figure. This is a somewhat higher critical cooling rate compared to DAR35 and LDAR7 (see next section) and implies a more difficult processing in order to obtain a glassy phase compared to other Fe-alloys investigated. Based on observations of the as-cast microstructure, there is evidence that the large amount of Mo in the LDAR2X7

alloy is partially responsible. Not only does it cause difficulties during melting, i.e. longer time/higher temperatures are necessary to dissolve Mo-rich borides/carbides, it also leads to formation of Mo-rich boride/carbide phases during relatively rapid cooling due to increased driving force for nucleation and growth. The Mo-containing particles apparently are potent nucleation sites, as evidenced in Figure 74b.

The shape of the solidification transition region resembles that of the isotherms in the alloy during the quench, as calculated using a finite element heat transfer analysis. Calculated isotherms in the glass-crystal transition region are shown in Figure 76. This is consistent with the notion of a distinct critical cooling rate, as the cooling rate will differ over the cross-section of the wedge with faster cooling closer to the mold surface. The shape of the isotherm is decided by the geometry of the wedge and thermal properties, with the thermal conductivity being the most important. Very high heat transfer rates at the interface will cause the isotherms to take on a sharper C-shape. A low thermal conductivity will have a similar effect on the shape of the isotherms and thus the shape of the transition region. Note how different the amorphous-crystalline transition appears in DAR35 and LDAR2X7 alloys. Examples of the crystalline microstructure of LDAR2X7 are shown in Figures 77-79, and are compared with the DAR35 examples shown in the previously discussed figures.

The effect of more rapid cooling along the edges is visualized in Figure 77c, where the gray featureless region along the mold interface is an as-cast amorphous microstructure. In the middle, where the cooling rates are slower, a fully crystalline structure has developed, consisting of overlapping needles that probably is a result of dendritic growth of the primary phase. As we move up in the wedge, with continuously decreasing cooling rates, the appearance of other phases and coarser structure is the most visible evidence of the importance of kinetically controlled structure.

Verification of a glassy structure in the wedge-cast LDAR2X7 has not yet been obtained using other techniques such as thermal analysis or X-ray diffraction. A sample from the tip of the wedge was crushed and sieved into a powder sample (diameter < 100μm). However, the resulting XRD trace did not show any significant occurrence of a glassy phase. Instead, a complex peak pattern is evident in Figure 80, where several of the peaks remain unidentified suggest that most of the powder sample was crystalline. Now, since crystalline peaks will always dominate the XRD diffraction pattern, we cannot say whether the observations of the microstructure are inconsistent with the XRD analysis. It is possible that even a substantial amount of glassy phase as observed in Figure 75 will, with respect to intensity, not be able to produce amorphous peaks that can compete with those characterizing the at least two crystalline phases that seem to be present more or less throughout the entire wedge cast sample.

LDAR7 (CBCTL1651)

This alloy was received in as-sprayed powder form from the Naval Surface Warfare Center (NSWC) for a total of about 500 grams. The labeled composition was $Fe_{48}Mo_{14}Cr_{14}Y_2C_{15}B_6$. Prior to wedge-casting, some of the powder (30 grams) was encapsulated in a quartz crucible under vacuum, sintered using a regular torch as heat source, cooled and then induction melted to form a single ingot. This ingot was subsequently crushed coarsely to proper size as the final preparation before wedge-casting the alloy. Wedge casting was performed using the standard procedure, as well as using a fiber-optic sensor to monitor temperature decay in the wedge.

The cooling curves as measured with two thermocouples at 10 and 15 mm height are shown in Figure 81 together with calculated cooling curves fit to the experimental data. As will be shown later, the thermocouple at 10 mm was very close to the transition region between the amorphous and crystalline sections of the as-cast wedge. Thus, the critical cooling rate is calculated based on heat transfer properties that fitted the 10-mm curve. However, when the same heat transfer parameters are used to fit the cooling curve at 15 mm, there is a small discrepancy, some of which is related to the fact that the wedge does not fill up instantaneously, but locations higher up in the wedge start to cool later than those further down. In the calculations, the entire wedge is filled up at t_0, the onset time of cooling. Taking this into account, the calculated curve for z=15 mm should be shifted to the right (approximately 0.5 seconds). There are still some discrepancies, although their origin is difficult to assess. There is, as a result, a slightly higher error margin in the calculated cooling rates. Table 8 lists the values for *h* that were used to fit the calculated cooling curve to the measured cooling curve of Figure 81.

In addition to thermocouple measurements, we also used the fiber-optic sensor system, which has a much faster response time to rapid temperature changes. Thus, the idea is to be able to properly monitor the initial cooling process better. The fiberoptic sensor was located at z=23 mm, and it produced a cooling curve that is shown in Figure 82.

The as-cast microstructure in the lower parts of the wedge was completely amorphous, which indicates a very good glass forming ability of the alloy. The transition between glassy and crystalline microstructure did not occur before the casting thickness exceeded 3.5 mm. Indeed, due to insufficient initial sample mass, a fully crystalline structure could not be found in the as-cast wedge. Thus, it is necessary to repeat the experiment with a larger sample, probably of the order 50 grams. The existence of an amorphous phase was verified both by thermal analysis and X-ray diffraction analysis. Figure 83 shows the DTA heating/cooling trace for a sample taken from a 2-mm thick cross-section of the wedge, and Figure 84 is an XRD trace from a region of similar thickness.

The differential thermal analysis (DTA) heating trace shown in Figure 83, combined with scanning electron images, shows that the as-cast sample was fully amorphous up to a casting thickness of about 3.5 millimeters. The measured T_g on heating was 580 °C, T_x = 633 °C with subsequent crystallization onsets at 654, 687, 740 and 974 °C, i.e. the devitrification of this alloy goes through several stages and possible solid state transformations. The onset of melting was measured to 1116 °C, followed by a double endothermic peak on further heating before the true

liquidus temperature at 1286 °C marked the end of the melting range. On cooling, substantial under-cooling occurred until solidification onset at about 1137 °C. These thermal data are very similar to those measured on the as-received amorphous powder that was used to make the wedge-cast, indicating that the composition has been preserved during the sample preparation.

The microstructure of the LDAR7 (CBCTL1651) wedge was overall amorphous, reflecting the excellent glass forming ability of this alloy. Figure 85 shows a typical back-scattered electron image (BSEI) from the lower part of the wedge that was fully amorphous. It is important to note that back-scattered electron images alone is not sufficient to declare that an amorphous structure has been cast, as the resolution of the microscope is limited to approximately 50 nanometers, i.e. small particles may not be easily observed. In addition, crystal phases with the same composition as the matrix would not show up either, as the contrast is based on average atomic number for the phase being analyzed. However, with the XRD and DTA data for this sample described earlier, there is no ambiguity of the nature of the as-cast microstructure.

Moving up in the wedge, the casting thickness increases and the cooling rates decreases. At a thickness of about 2.6 mm, the first crystalline precipitates are found (Figure 86). Crystallization has occurred in C-shaped bands similar to the isotherms during quenching. But the transition region is not very symmetric; in fact, there is a large region relatively close to the edge that clearly crystallized, while the center region, which was subjected to lower cooling rates, remained amorphous. This suggest either a more complex heat flow pattern in the wedge than accounted for in the calculations were liquid flow is neglected. Also, heterogeneous nucleation may play an important role as to determining the final microstructure. Remember that the wedge-cast DAR35 also showed irregular transition between glassy and crystalline regions of the wedge.

Identification of the crystalline phases was attempted using XRD (Figure 87). A thin slice from the casting section with thickness 4 mm was crushed and sieved into a powder sample (diameter less than 100 μm). The results indicate presence of both several crystalline phases as well as a glassy phase. Some of the peaks can be attributed to $M_{23}(B,C)_6$, M_7C_3 and bcc-(Fe,Cr), as well as unknown Mo-rich carbides. At this stage, further analysis is required to pinpoint the exact phase selection in the wedge cast sample.

It was mentioned that in the case of Figure 86, the transition between crystalline and amorphous areas did not seem to follow isothermal contour curves, and among other reasons heterogeneous nucleation and growth could be the culprit. Further evidence was found when cross-sections higher up in the wedge were examined. Amorphous structure was contained even as cooling rates approached 80 K/s (Figure 88).

There is an apparent inconsistency here, as Figure 86 indicated that crystallization of the wedge was about to occur, yet as we move higher up in the wedge, the microstructure returns to being glassy again until cooling rates approaches 80 K/s. A possible explanation is, as mentioned earlier, related to heterogeneous nucleation on impurities in the melt. This is consistent with the observations of the as-cast microstructure of the entire wedge.

Devitrification of Melt Spun Ribbons – DAR35, DAR40 and DAR40X3

As-spun ribbons were annealed at different temperatures between their respective T_g and T_x as measured on continuous heating. These curves were previously shown in Figure 54, 55, and 56. Based on these results, ribbons from the three respective alloys were annealed at a suitable temperature until crystallization just had begun, as observed as a deviation of the heat flow trace from the baseline. The ribbons were then quickly cooled to avoid extended growth and possible formation of other phases, see Figure 89 for a summary of annealing times and temperature. Samples were investigated by X-ray diffraction and transmission electron microscopy. The TEM samples were prepared by mechanically polishing the annealed ribbons to approximately 50 μm and ion-milled in a Fischione 1010 Ion mill.

DAR35

XRD traces for as-spun ribbons and ribbons annealed for 45 minutes at 590 °C, are shown in Figure 90 and 91, respectively. Obviously, the as-spun ribbons were completely amorphous as evidenced by the two broad peaks centered at 44° and 80°. The annealed ribbons showed up with some weak crystalline peaks in addition to those caused by the existence of an amorphous phase, indicating that partial devitrification took place during annealing of the ribbons. The peaks were somewhat consistent with a tetragonal Fe_2B structure, although some shifts were observed. In any circumstance, among candidate phases the Fe_2B structure fit the experimental data best.

TEM bright field (Figure 92) shows needle-shaped precipitates in an amorphous matrix. By applying standard TEM analyzing techniques, it was found that Fe_2B is the most likely candidate for the primary devitrification product.

Except for the needle-like precipitates, no other crystals were observed in this sample. Although not 100% conclusive, the claim that Fe_2B is the first phase to precipitate is supported by circumstantial evidence through observations of wedge-cast samples, where Fe_2B needle-like precipitates have been confirmed by X-ray diffraction, although in a different Fe-B-Cr alloy. These needles were virtually identical to those observed in DAR35 wedge cast (Figures 69 and 70). Finally, it should be noted that a number of possible candidate phases normally occurring in Fe-B-C-Cr systems were ruled out due to incompatibility with the CBED pattern, in particular bcc-Fe, fcc-Fe, $M_{23}B_6$ and M_7B_3 type phases.

DAR40

XRD traces for as-spun ribbons and ribbons annealed at 585 °C for 30 minutes are shown in Figure 93 and 94, respectively. The XRD analysis is relatively conclusive as to the nature of the precipitating phase, and this phase is Fe_3B, a metastable phase that has been reported earlier to be a possible crystallization product at low-temperature annealing. TEM pictures are shown in Figure 95.

Summary of Thermal Properties of Melt Spun ribbons

Table 5 shows all of the thermal properties acquired to date on Fe-alloys investigated during the first year of this project. This table lists the glass transition temperature T_g, crystallization temperature T_x (of the amorphous phase), onset of melting T_m and liquidus temperature T_l. In addition, a rough measure of the glass forming ability is listed as T_{rg}, the reduced glass transition temperature defined as T_g/T_l where temperatures are given in degrees Kelvin. Good glass forming alloys have high reduced glass transition temperatures of about 0.55-0.60. There are other ways of defining GFA based on a thermal analysis. They all have in common that one method may fit a particular alloy better than a different method, so caution is advised when using thermal analysis as means of estimating GFA. At the same time, the majority of investigators use the T_{rg} scale as a means of indicating relative ease of glass formation.

Some of these alloys have been evaluated several times with some data discrepancy that may be caused by minor compositional changes and different thermal histories. The three first entries in Table 3 have a temperature range listed in the column for T_g, which reflects the different thermal analysis results that have been acquired. For example, for DAR35 we have measured glass properties of as-sprayed bulk samples, bulk wedge cast samples, as-spun ribbons and powder samples, so it does not come as a surprise that measured values for T_g are recorded as this parameter depends among other factors on the cooling rate of the as-quenched amorphous phase. The temperatures are all defined by their tangential intersection onset outlined earlier.

Prediction of Multicomponent Phase Diagrams

In addition to the kinetic modeling discussed in the previous section, the THERMOCALC code has been used to predicted phase (phase fraction vs. temperature) diagrams for DAR40X3, one showing all precipitated crystalline phases, and another with the precipitated phases (bcc, χ, μ, ρ, P, M_2B) suppressed.

Overview of Amorphous Metal Phase Stability

The glass-forming ability (GFA) and glass stability of several amorphous Fe-based alloys has been investigated. Candidate alloys were made amorphous by melt spinning, high velocity spray forming or gravity chill casting. Thermal properties such as the glass transition temperature, crystallization temperature, melting temperature and liquidus temperature were measured using thermal analysis (DTA and DSC). Microstructure characterization of amorphous and devitrified samples was done using electron microscopy (SEM and TEM) and X-ray diffraction (XRD).

The GFA of an alloy is defined by its critical cooling rate (CCR). Very good glass-forming alloys have CCR less than 1 K/s, whereas Fe-based alloys have CCR between ~100 and 1000 K/s. Although investigators in the past have attempted to calculate the CCR based on a kinetics analysis, such analysis produces results that are very sensitive to the choice of parameters and thus rather inaccurate. In order to accurately quantify the CCR, an experimental design based on gravity chill casting into a wedge-shaped mold equipped with thermocouples has been developed. Finite element transient heat transfer analysis of the liquid alloy quenching in the wedge allows calculation of temperature vs. time for any position in the wedge. By examining the microstructure of the as-cast sample, one can assign a critical cooling rate to that alloy without any information on the thermal properties of the particular alloy, which is a great advantage compared to a kinetics analysis where a large number of parameters needs to be estimated. The critical cooling rate for glass formation was measured for LDAR7, DAR35 and LDAR2X7 and found to be 80, 425 and 610 K/s, respectively. Note that LDAR7 has a lower CCR than any Fe-based alloy reported in the literature.

The stability of the amorphous phase was investigated for DAR35, DAR40 and DAR40X3 using a novel approach based on a heterogeneous nucleation model coupled with isothermal annealing of amorphous ribbons. The annealing experiments yield onset times for crystallization as a function of annealing temperature, as well as information on what solid phase is the first to precipitate with means of TEM and XRD of the annealed ribbons. Identification of the primary precipitating solid allows for calculation of the driving free energy for nucleation, and by using the procedure outlined in this report, the TTT-diagram can be calculated.

CORROSION RESISTANCE OF AMORPHOUS METALS

Relevant Environments

The tri-lateral diagram shown in Figure 96 can be used to classify natural waters as calcium chloride, sulfate-chloride, or bicarbonate brines. In principle, any natural water falling in the calcium chloride region (upper area of diagram, bounded by dashed red line) will evolve to concentrated calcium chloride brine during evaporative concentration, which will cause the precipitation of other salts. Examples include 5M $CaCl_2$ at 105°C. Similarly, any natural water falling within the sulfate-chloride region (left side of diagram, bounded by the dashed red and blue lines) will evolve to concentrated sulfate-chloride brine during evaporative concentration. Examples are sodium chloride solution, seawater, and simulated saturated water (SSW). Any natural water falling within the bicarbonate region (right side of diagram, bounded by the dashed blue line) will evolve to concentrated bicarbonate brine during evaporative concentration. Examples are simulated acidic water (SAW), simulated concentrated water (SCW) and basic saturated water (BSW).

Prediction Pourbaix Diagrams

The predicted Pourbaix diagram for CBCTL1651 in pure water at near-ambient temperature is shown in Figure 97. In addition to promoting glass formation, yttrium promotes passive film stability under alkaline conditions through the formation of yttrium oxide.

The predicted Pourbaix diagrams for DAR40X3 and CBCTL1651 in synthetic seawater (40 grams of NaCl in 1 liter of water) at near-ambient temperature is shown in Figure 98. Both DAR40X3 and CBCTL1651 have high concentrations of molybdenum and chromium, like nickel-based alloys such as UNS N06022. The DAR40X3 also includes substantial amounts of tungsten. Chromium, molybdenum and tungsten all form oxides that are insoluble at very low pH. These alloying elements can therefore stabilize the passive film under the acidic conditions found in pits and crevices. Acidification is due to the hydrolysis of polyvalent metal cations dissolved during localized corrosion. The CBCTL1651 formulation has 2 percent (2 atomic %) yttrium, which lowers the critical cooling rate, and promotes glass formation. The yttrium contributes to passive film formation under alkaline conditions.

The predicted Pourbaix diagrams for CBCTL1651 and LDAR8 (CBCTL1651 with tungsten) in synthetic seawater at near-ambient temperature (30°C) are shown in Figure 99. In the later case, the presence of tungsten leads to the formation of $FeWO_4$ and $WO_2(OH)_2$, while the presence of molybdenum leads to the formation of MoO_2 and MO_3. Chromium and iron oxides (Cr_2O_3 and Fe_2O_3) also contribute to passive film stability. Under alkaline conditions, stable Y_2O_3 and NaO_4W surface phases are predicted. Such predicted Pourbaix diagrams, and the capability developed to make such predictions, is a clear and concrete evidence that Milestone 1 has been met.

The predicted Pourbaix diagrams for CBCTL1651 in concentrated calcium chloride brines at 30 and 90°C are shown in Figure 100. Under acidic-to-neutral conditions, MoO_2, MO_3, $CaO\text{-}MO_3$, Cr_2O_3 and Fe_2O_3 contribute to passive film stability. Under alkaline conditions, stable Y_2O_3 and $Ca(OH)_2$ surface phases are also predicted.

The predicted Pourbaix diagrams for LDAR8, CBCTL1651 with tungsten at a concentration of 3 atomic percent, in concentrated calcium chloride brines at 105 and 118°C are shown in Figure 101. The presence of tungsten leads to the formation of $FeWO_4$ and $WO_2(OH)_2$, while the presence of molybdenum leads to the formation of MoO_2, MO_3 and $CaO\text{-}MO_3$. Chromium and iron oxides (Cr_2O_3 and Fe_2O_3) also contribute to passive film stability. Under alkaline conditions, stable Y_2O_3 and $Ca(OH)_2$ surface phases are predicted.

The predicted Pourbaix diagrams for DAR40X3 and CBCTL1651 in standard bicarbonate brines used for testing (SCW and BSW), at near-ambient temperature (30°C), are shown in Figure 102. As previously discussed, CBCTL1651 has high concentrations of molybdenum and chromium, like nickel-based alloys such as UNS N06022. This alloy also has yttrium at a concentration of 2 atomic percent, which lowers the critical cooling rate and promotes glass formation. Since the pH of SCW is near neutral (pH~7-8), the passive film near the open-circuit corrosion potential would include Fe_2O_3, Cr_2O_3 and MoO_2. Since the pH of BSW is alkaline (pH~12-14), the passive film near the open-circuit corrosion potential would include Fe_2O_3, Fe_3O_4, Cr_2O_3, $CrFeO_4$ and Y_2O_3.

Cyclic Polarization

Cyclic polarization (CP) is used as a means of measuring the critical potential of the corrosion-resistant outer layer of waste package ($E_{critical}$), relative to the open-circuit corrosion potential (E_{corr}). Spontaneous breakdown of the passive film and localized corrosion require that the open-circuit corrosion potential exceed the critical potential:

$$E_{corr} \geq E_{critical}$$

In the published scientific literature, different bases exist for determining the critical potential from electrochemical measurements. For example, Scully et al. (1999) define the critical potential for crevice corrosion of Alloy 22 as the point where the current density increases to 1 to 10 $\mu A/cm^2$ (10^{-6} to 10^{-5} A/cm^2) during the forward (anodic) scan. Gruss et al. (1998) define the repassivation potential as the point where the current density drops to 0.1 to 1 $\mu A/cm^2$ (10^{-6} to 10^{-7} A/cm^2), and use the repassivation potential as a conservative estimate of the critical value.

Cyclic polarization measurements have been based on a procedure similar to ASTM G 5, with slight modification [American Society for Testing and Materials]. For example, ASTM G 5 calls for an electrolyte of 1N H_2SO_4, whereas natural seawater, synthetic bicarbonate brines (SDW, SCW, SAW and BSW), synthetic sulfate-chloride brines (SSW), 4M NaCl solutions, and 5M $CaCl_2$ solutions with various levels of nitrate were used in this study. The compositions of the synthetic brines are given in the literature [Farmer et al. 2000], and are known as simulated dilute water (SDW), simulated concentrated water (SCW), simulated acidic water (SAW), basic saturated water (BSW), and simulated saturated water (SSW). Furthermore, ASTM G 5 calls for

the use of de-aerated solutions, whereas aerated and de-aerated solutions were used here. After a 24-hour hold period, during which the open circuit corrosion potential is determined, the potential is scanned in the positive (anodic) direction from a level slightly more negative than the corrosion potential (cathodic limit), to a reversal potential (E_{rev}) near that required for oxygen evolution (anodic level). During the positive scan, anodic oxidation peaks may be observed (centered at E_{peak}) that have been correlated with the oxidation of molybdenum at the alloy surface (passive film), as well as current excursions that are usually associated with catastrophic breakdown of the passive film. During the negative (cathodic) scan, a hysteresis loop will be observed in cases where passivity has been lost. As the scan continues, the current density may eventually decrease to a level equivalent to that experienced during the positive scan, and indicative of reformation of the passive film. The potential at which this occurs is known as the repassivation potential (E_{rp}).

The temperature-controlled, borosilicate glass (Pyrex), electrochemical cell is shown in Figure 103. This cell has three electrodes, a working electrode (test specimen), the reference electrode, and the counter electrode. A standard silver silver-chloride electrode, filled with near-saturation potassium chloride solution, was used as the reference, and communicated with the test solution via a Luggin probe placed in close proximity to the working electrode, thereby minimizing Ohmic losses. Numerical corrections for the reference electrode junction potential have been estimated, and have been found to be insignificant (Farmer et al. 2000). The electrochemical cell is equipped with a water-cooled junction to maintain reference electrode at ambient temperature, hereby maintaining integrity of the potential measurement, and a water-cooled condenser to prevent the loss of volatile species from the electrolyte.

Critical Potential Concept

The corrosion-resistance of Fe-based amorphous metals has been improved by systematic addition of alloying elements such as chromium, molybdenum, and tungsten, all of which are known to enhance passive film stability. Such elemental additions account for the observed difference in the corrosion resistance of Type 316L stainless steel, and nickel-based C-22 (alloy N06022). The resistance to localized corrosion is quantified through measurement of the open-circuit corrosion potential ($E_{corrosion}$ or E_{corr}), the breakdown potential ($E_{breakdown}$ or E_{crit}), and the repassivation potential (E_{rp}). The greater the difference between the open-circuit corrosion potential and the repassivation potential (ΔE), the more resistant a material is to modes of localized corrosion such a pitting and crevice corrosion (Figure 104).

A premise of this research is that the corrosion-resistance of Fe-based amorphous metals can be improved by systematic addition of alloying elements such as chromium, molybdenum, and tungsten, all of which are known to enhance passive film stability. Such elemental additions account for the observed difference in the corrosion resistance of Type 316L stainless steel, and nickel-based C-22 (alloy N06022).

Any improvement in the resistance to localized corrosion can then be quantified through measurement of the open-circuit corrosion potential ($E_{corrosion}$ or E_{corr}), the breakdown potential ($E_{breakdown}$ or E_{crit}), and the repassivation potential (E_{rp}). The greater the difference between the open-circuit corrosion potential and the repassivation potential (ΔE), the more resistant a material is to modes of localized corrosion such a pitting and crevice corrosion.

Hypothetical cyclic polarization curves for Type 316L stainless steel, nickel-based Alloy C-22 (N06022), and titanium are shown in Figure 104. The differences in corrosion resistance between Type 316L stainless steel and Alloy C-22 illustrate the beneficial effects of molybdenum additions on the corrosion resistance, while the performance of titanium is due to the formation of a titanium oxide (TiO_2) passive film.

Competing methodologies exist for the interpretation of experimental data in terms of the critical potential (E_{crit}). Method A strives to identify the potential where the passive film disappears during the forward (anodic) potential scan. The loss of passivity is indicated by a sudden, dramatic increase in the measured current density. The current density corresponding to a complete loss of passivity is assumed to be approximately 20 or 200 $\mu A/cm^2$. The breakdown potential may be the best estimate of the true critical potential, since it corresponds to the onset of passive film destabilization. Methods B and C strive to identify the potential where the passive film reappears during the negative (cathodic) potential scan. Repassivation is indicated by a sudden, precipitous decrease in the measured current density, to levels indicative of an intact passive film. Method C relies on no arbitrary threshold, and is therefore preferred by the HPCRM Team.

Method A – Initial Breakdown of Passive Film
Critical Potential (E_{crit}) = Breakdown Potential (E20 or E200)
Based Threshold Current Density of 20 or 200 $\mu A/cm^2$

Method B – Repassivation of Surface
Critical Potential (E_{crit}) = Repassivation Potential (ER1 or ER2)
Based Threshold Current Density of 1 or 2 $\mu A/cm^2$

Method C – Repassivation of Surface
Critical Potential (E_{crit}) = Repassivation Potential (ERP)
Intersection of Forward Scan with Hysteresis Loop (Cross-Over Point)

Figure 105 shows an actual cyclic polarization curve for Alloy C-22 in 5M $CaCl_2$ at 105°C, with three methodologies illustrated for determining the threshold potential for the initiation of localized corrosion in performance assessment models. Method A is based upon the critical potential at which the passive film breaks down (current excursion, 2 or 20 $\mu A/cm^2$). Method B is based upon the repassivation potential, which in turn is based upon an arbitrary threshold (1 or 2 $\mu A/cm^2$). Method C is based upon the repassivation potential, determined from the intersection of the hysteresis loop with the forward scan.

Calcium Chloride Brines

Cyclic polarization testing of reference materials and Fe-based amorphous metals were conducted in hot, concentrated, calcium chloride solution. Unless otherwise stated, conducted in 5M $CaCl_2$ at 105°C. A compilation of the measured values of the open circuit corrosion potential (E_{corr}), the potential coinciding with the anodic oxidation peak (E_{peak}), the repassivation potential (E_{rp}), and the penetration rate based upon the maximum passive current density (dx/dt) is given in Table 9.

Cyclic polarization curves for wrought nickel-based Alloy C-22 (N06022) and iron-based CBCTL1651 amorphous metal ingot, both, are shown in Figure 106. The data for Alloy C-22 show a catastrophic breakdown of the passive film at 100 mV, which causes a very large hysteresis loop. During the reverse scan, repassivation occurs at a relatively low potential (–150 to –200 mV vs. Ag/AgCl). These data indicate that Alloy C-22 has relatively poor resistance to localized corrosion in the test environment. In sharp contrast to Alloy C-22, the CBCTL1651 ingot showed no breakdown of the passive film, even at potentials approaching that required for oxygen evolution. It is therefore concluded that the corrosion resistance of the amorphous metal is superior to that of Alloy C-22 in hot concentrated calcium chloride solution.

This cyclic polarization curve for a melt-spun ribbon of LDAR8 in 5M CaCl2 at 105°C is shown in Figure 107. The LDAR8 formulation uses CBCTL1651 (Y-containing, high-Mo Fe-based amorphous metal) as the parent material, with the addition of tungsten at 3 atomic percent. The repassivation potential for LDAR8 in this aggressive environment (300-400 mV vs. Ag/AgCl) is substantially higher than that for Alloy C-22 (-100 mV vs. Ag/AgCl).

A cyclic polarization curve for the Fe-based P-containing amorphous metal is shown in Figure 108. During the positive scant, an elevation in the current density is observed at approximately 100-200 mV vs. Ag/AgCl. Despite the elevated current density, this alloy exhibited excellent corrosion resistance.

The cyclic polarization curve for a melt-spun ribbon of LDAR6 in 5M CaCl2 at 105°C is shown in Figure 109. The LDAR6 formulation has the same nominal elemental composition as the P-containing Fe-based amorphous metal formulation discussed in the literature by Pang et al. [2002]. The repassivation potential for LDAR6 in this aggressive environment (400 mV vs. Ag/AgCl) is substantially higher than that for Alloy C-22 (-100 mV vs. Ag/AgCl).

Cyclic polarization curves for wrought Alloy C-22 (N06022) in 5M $CaCl_2$ in 105°C, and in seawater at 90°C, are compared in Figure 110. The test in seawater shows only a very small hysteresis loop, and a relatively high repassivation potential, indicative of good resistance to localized attack. The test in calcium chloride shows a very large hysteresis loop, and a relatively low repassivation potential of between –150 to –200 mV vs. Ag/AgCl. These data indicate that Alloy C-22 has relatively poor resistance to localized corrosion in concentrated calcium chloride brines at elevated temperature.

Seawater

Cyclic polarization testing of reference materials and Fe-based amorphous metals were conducted in Half Moon Bay seawater at various temperatures, ranging from 30 to 90°C, as well as in Key West seawater at ambient temperature. A compilation of the measured values of the open circuit corrosion potential (E_{corr}), the potential coinciding with the anodic oxidation peak (E_{peak}), the repassivation potential (E_{rp}), and the penetration rate based upon the maximum passive current density (dx/dt) is given in Table 10.

The cyclic polarization curve for wrought nickel-based Alloy C-22 (N06022) at 30°C is shown in Figure 111. This curve has a small hysteresis loop, and a repassivation potential close to the potential required for oxygen evolution. As anticipated, the wrought Alloy C-22 sample performed well in ambient temperature seawater.

The cyclic polarization curve for wrought nickel-based Alloy C-22 (N06022) at 90°C is shown in Figure 112. This curve has a very small hysteresis loop, and a repassivation potential close to the potential required for oxygen evolution. As anticipated, the wrought Alloy C-22 sample performed well in heated seawater.

Figure 113 shows the cyclic polarization curve for a nickel-based Alloy C-22 (N06022) coating deposited on a Type 316L stainless steel substrate with HVOF. The repassivation potentials of HVOF DAR40 and DAR40X3 are very high, whereas HVOF Alloy C-22 (reference material) has relatively poor performance, with a repassivation potential of only –100 mV vs. Ag/AgCl. It is therefore concluded that the amorphous-metals under development can be used to produce corrosion-resistant thermal-spray coatings, but that limitations in the phase stability of Alloy C-22 prevents the deposition of corrosion-resistant thermal spray coatings.

Figure 114 shows the cyclic polarization curve for FBAM114 ingot at 30°C. This curve has a large hysteresis loop, and a repassivation potential below the open circuit corrosion potential. This particular amorphous metal exhibited poor corrosion resistance in ambient temperature seawater.

Figure 115 shows the cyclic polarization curve for CBCTL1651 at 30°C. This curve has a very small hysteresis loop, and a repassivation potential close to the potential required for oxygen evolution. It is therefore concluded that this Y-containing Fe-based amorphous metal performs very well in ambient temperature seawater. Furthermore, this material appears be less electrochemically active than wrought and thermal-spray Alloy C-22.

Macro photographs and scanning electron micrographs (SEMs) of CBCTL1651 ingots are shown in Figure 116. No corrosive attack of this Fe-based amorphous metal was observed during cyclic polarization in seawater at 30°C (top). However, the onset of pitting is observed during cyclic polarization in heated seawater at 90°C (middle). No corrosive attack was observed in 5M CaCl2 at 105°C (bottom). In regard to the pitting observed in the heated seawater at 90°C, it is important to note that polarization to an extremely anodic potential, near oxygen evolution, was required for initiation.

A comparison of the cyclic polarization curves for a CBCTL1651 amorphous metal ingot, a sample of wrought nickel-based Alloy C-22, and a sample of thermal spray (HVOF) C-22 in ambient temperature Half Moon Bay seawater is shown in Figure 117. The CBCTL1651 amorphous metal has better corrosion resistance than both wrought and HVOF Alloy C-22. From the degraded performance of HVOF Alloy C-22, it is concluded that corrosion-resistant.

The cyclic polarization curves for melt-spun ribbons and thermal-spray coatings of DAR40 are compared to that of wrought Type 316L stainless steel in Figure 118, all obtained with Half Moon Bay seawater at ambient temperature. In both cases, the performance of the DAR40 amorphous metal is better than that of the wrought stainless steel. Furthermore, the fully-dense ribbon of DAR40 is superior to the HVOF coating, which has residual porosity and crystalline structure.

The comparison shown in Figure 119 is similar to that shown in Figure 118, with the exception of the temperature. The data shown here are for Half Moon Bay seawater at 90°C. The fully dense ribbon of DAR40 maintains reasonable passivity as the temperature increases, whereas the performance of this early HVOF coating of DAR40 diminishes, and approaches that of Type 316L stainless steel.

In contrast to the amorphous metals that are under development, Type 316L stainless steel shows relatively poor resistance to localized corrosion in seawater, even at ambient temperature (Figure 120).

The corrosion resistance, quantified with cyclic polarization, is temperature dependent, as illustrated by Figure 121. The polarization curves for early DAR40 HVOF coatings at 30, 60 and 90°C show outstanding resistance to localized attack at 30 and 60°C, but substantially reduced corrosion resistance at 90°C.

Cyclic polarization measurements of early HVOF coatings of DAR35 and DAR40 showed greater resistance to localized corrosion in ambient temperature seawater than Type 316L stainless steel in wrought condition (Figure 122). The passive film on Type 316L stainless steel experienced catastrophic breakdown at approximately 600 mV relative to a standard Ag/AgCl reference electrode, whereas no breakdown was experienced with DAR35 and DAR40 until the potential was pushed to levels where oxygen evolution occurs.

A comparison of the cyclic polarization curves for early HVOF coatings of DAR40 and DAR40X3 HVOF in seawater at ambient temperature is shown in Figure 123. Both coatings have relatively repassivation potentials (~900 mV vs. Ag/AgCl). The differences in apparent current density are attributed to differences in surface roughness. The data compared in Figure 124 is similar to that compared in Figure 123, with the exception of the test temperature, which was 60°C. The data compared in Figure 125 is also similar to that compared in Figure 123, with the exception of the test temperature, which was 90°C.

Cyclic polarization curves for DAR27, DAR40, and Fe-Zr-Y melt-spun ribbons are shown in Figure 126. In the case of DAR27 and DAR40 ribbons, no breakdown of the passive film is observed. However, in the case of the Fe-Zr-Y material, a large excursion in the anodic current density was observed at 500 mV during the forward scan, with the corresponding hysteresis loop evident.

LDAR4X3 is a variant of DAR40 with a titanium addition of 3 atomic percent. A comparison of the cyclic polarization curve for LDAR4X3 melt-spun ribbon to that of wrought nickel-based Alloy C-22 in Key West seawater at 30°C is shown in Figure 127. LDAR4X3 has lower passive current density than Alloy C-22.

Cyclic polarization data for melt-spun ribbon of LDAR2X7 is compared to that of wrought nickel-based Alloy C-22 in Key West seawater at 30°C is shown in Figure 128. Increases in the molybdenum concentration, from 1 to 5 atomic % (not shown) causes a corresponding increase in the amplitude of the anodic oxidation peak, whereas the increase to 7 atomic % causes an overall drop in the passive current density, and associated corrosion rate.

Macro photographs of melt-spun ribbons of LDAR2X1 (only 1 atomic percent molybdenum), after cyclic polarization in seawater from Key West at 30°C, are shown in Figure 129. There may be some evidence of corrosion, but at high anodic potential, close to that required for oxygen evolution.

Macro photographs of melt-spun ribbons of LDAR2X3 (3 atomic percent molybdenum), after cyclic polarization in seawater from Key West at 30°C, are shown in Figure 30. There is no apparent evidence of corrosion, even after polarization at potentials close to that required for oxygen evolution. It is therefore concluded that a minimum molybdenum concentration of 3 atomic percent is needed in the parent Fe-based amorphous metal to prevent localized corrosion in ambient temperature seawater.

Macro photographs of melt-spun ribbons of LDAR2X7 (7 atomic percent molybdenum) after cyclic polarization in seawater from Key West at 30°C, are shown in Figure 131. There is no apparent evidence of corrosion, even after polarization at potentials close to that required for oxygen evolution. The parent Fe-based amorphous metal with an addition of molybdenum at 7 atomic percent performs very well.

Bicarbonate Solutions

Results from cyclic polarization of reference materials and Fe-based amorphous metals in test environments other than calcium chloride solution and seawater are compiled in Table 11. Test solutions include: 4M NaCl, simulated concentrated water (SCW), and basic saturated water (BSW). Both SCW and BSW are classified as bicarbonate-type brines. Reference materials were Type 316L stainless steel and nickel-based Alloy C-22, both in wrought condition. All of the amorphous metal samples found in this compilation are early HVOF coatings of DAR35, DAR40, and DAR40X3. These data were reported at the HPCRM Team Meeting in Key West, held in January 2004. These results were used as the basis of recommending the pursuit of

theoretically dense, pore-free materials for testing, so that the effects of alloy composition could be separated from the effects of coating morphology.

The cyclic polarization curve for wrought Alloy C-22 in a standard bicarbonate solution at 90°C is shown in Figure 132. This bicarbonate brine is known as SCW (simulated concentrated water) and used for evaluating alloy performance for repository applications. A small hysteresis loop is observed, indicating breakdown of the passive film. After scan reversal, repassivatioin occurs at 600 mV, a level much higher than the open-circuit corrosion potential. The large anodic oxidation peak between 200 and 300 mV is attributed to the oxidation of molybdenum in the passive film.

Figure 133 shows the cyclic polarization curves (positive scans) for early DAR35 and DAR40 HVOF coatings, as well as for Type 316L stainless steel. The tests were conducted in a bicarbonate-brine test solution (SCW) at 30°C. All three materials he amorphous metals have comparable performance (based upon threshold potential) in such benign solutions. The DAR35 and DAR40 HVOF coatings show higher current densities than the fully dense Type 316L stainless steel due to the greater surface roughness of these early coatings. The data compared in Figure 134 is similar to that compared in Figure 133, with the exception of the test temperature, which was higher in this case.

The cyclic polarization curves for early DAR40X3 HVOF coatings in SCW (concentrated bicarbonate brine) at 30, 60 and 90°C are shown in Figure 135, 136, and 137, respectively. Each curve has an anodic peak, typical of Mo-containing nickel-based alloys (see Figure 132). At the lowest temperature (30°C), the anodic peak is observed between 400 and 700 mV, with no loss of passivity at reversal potentials as high as 1100 mV vs. Ag/AgCl. At the intermediate temperature (60°C), the anodic peak is observed between 300 and 600 mV, with no loss of passivity at reversal potentials as high as 1000 mV vs. Ag/AgCl. At the highest temperature (90°C), the anodic peak is observed between 200 and 500 mV, with no loss of passivity at reversal potentials as high as 900 mV vs. Ag/AgCl.

The cyclic polarization curves for early DAR40X3 HVOF coatings in BSW (saturated bicarbonate brine) at 30, 60 and 90°C are shown in Figure 138, 139, and 140, respectively. The curve for 30°C shows two anodic peaks (100 and 200 mV vs. Ag/AgCl) and no loss of passivity with reversal potentials as high as 650 mV vs. Ag/AgCl. At least one of these anodic oxidation peaks may also be associated with the oxidation of Mo in the passive film. The curve for 60°C shows two anodic peaks (50 and 100 mV vs. Ag/AgCl). A hysteresis loop is observed, however, a simultaneous loss of passivity has not yet been confirmed. At least one of these anodic oxidation peaks may also be associated with the oxidation of Mo in the passive film. The curve for 90°C shows no distinct anodic peak, but does exhibit a hysteresis loop. A loss of passivity associated with this hysteresis loop has not yet been confirmed.

Summary of Cyclic Polarization Data

The ranking of various alloy samples, based upon their measured resistance to localized corrosion ($\Delta E=E_{corr}-E_{rp}$) in 5M $CaCl_2$ at 105°C, is shown in Figures 141a (line chart) and 141b (bar chart). Most of the amorphous-samples performed very well in this aggressive environment. In contrast, wrought nickel-based Alloy C-22 (N06022) performed relatively poorly, as did the P-containing, Fe-based metallic glass, and the LDAR1X7 with high nickel content (7 atomic percent).

Nitrate anion is known to serve as an inhibitor to localized attack of nickel-based Alloy C-22 in concentrated calcium chloride solutions. A parametric study was performed to determine the effects of nitrate on the susceptibility of LDAR2X7 (7 atomic percent molybdenum) to localized corrosion in concentrated calcium chloride at 120°C, and is illustrated with Figure 142. In contrast to the inhibitory effect observed with nickel-based austenitic alloys such as C-22, nitrate additions cause a slight decrease in the difference between the repassivation and open-circuit corrosion potentials.

As shown in Figure 143, a parametric study was performed to determine the effects of nitrate on the susceptibility of LDAR2X5 (5 atomic percent molybdenum) to localized corrosion in concentrated calcium chloride at 120°C. In contrast to the inhibitory effect observed with nickel-based austenitic alloys such as C-22, nitrate additions cause a significant decrease in the difference between the repassivation potential and open-circuit corrosion potential, larger than the decrease observed with LDAR2X7 (7 atomic percent molybdenum).

In general, increases in temperature lower the resistance of an alloy to localized corrosion, with a commensurate decrease in the separation of the open-circuit corrosion potential and the repassivation potential. A parametric study was performed to determine the effects of temperature on the susceptibility of MSR samples of LDAR2X5 (5 atomic percent molybdenum), LDAR2X7 (7 atomic percent molybdenum), and CBCTL1651 (yttrium addition) to localized attack in concentrated calcium chloride, and is illustrated by Figure 144. All three materials have comparable performance at 105°C. However, LDAR2X5 and LDAR2X7 have slightly greater resistance to localized attack at 120°C than CBCTL1651.

Figure 145 shows a ranking of various alloy samples, based upon their measured resistance to localized corrosion ($\Delta E=E_{corr}-E_{rp}$) in Half Moon Bay seawater at ambient temperature (30°C). Most of the amorphous-samples performed very well, with the arc-melted drop-cast ingot and melt-spun ribbon of CBCTL1651 (also designated as LDAR7) showing the best performance. DAR40X3 coatings deposited with the HVOF process also performed well. A melt-spun ribbon of DAR40 had relatively poor performance, and was the exception. Nickel-based alloy C-22 coatings (N06022) deposited with HVOF performed poorly, as did samples of wrought Type 316L stainless steel, ingots of CBAM83, and HDIF-HVOF samples of DAR40. In this case, the devitrification caused by high-density infrared fusing was detrimental to corrosion resistance.

Figure 146 shows a ranking of various alloy samples, based upon their measured resistance to localized corrosion ($\Delta E=E_{corr}-E_{rp}$) in Half Moon Bay seawater at 90°C. Most of the amorphous-samples performed very well, with the arc-melted drop-cast ingot of CBCTL1651 (also designated as LDAR7) showing the best performance. DAR40X3 coatings deposited with the HVOF process also performed well. Nickel-based alloy C-22 coatings (N06022) deposited with HVOF performed more poorly, as did samples of wrought Type 316L stainless steel, ingots of FBAM117, and HVOF DAR35 and DAR40 produced early in the program and reported at the 2004 HPCRM Team Meeting in Key West. HVOF DAR35 and DAR40 have sufficient molybdenum to perform well in seawater at ambient temperature; however, these formulations require modification for good performance at higher temperature.

As discussed in regard cyclic polarization testing in concentrated calcium chloride solutions at various temperature levels, increases in temperature lower the resistance of an alloy to localized corrosion, with a commensurate decrease in the separation of the open-circuit corrosion potential and the repassivation potential. A similar parametric study was performed to determine the effects of temperature on the susceptibility of numerous alloys to localized attack in seawater at 30, 60 and 90°C, and is illustrated with Figure 147. The materials tested include: wrought Type 316L stainless steel; early HVOF nickel-based Alloy C-22 (N06022); early HVOF DAR35; early HVOFDAR40; MSR DAR40; MSR LDAR2X5 (5 atomic percent molybdenum); MSR CBCTL1651 (yttrium addition); and MSR P-containing Fe-based amorphous metal developed by Inoue. Of the tested materials, only two amorphous metal formulations, LDAR2X5 and CBCTL1651, maintained consistently high resistance to localized corrosion (quantified as E_{rp}-E_{corr}) over the entire range of temperature (30 to 90°C), though the P-containing formulation developed by Inoue was close in performance. The HVOF coatings of DAR35 and DAR40 exhibited good resistance to localized attack at 30 and 60°C, but became susceptible to attack at 90°C (E_{rp}-E_{corr} approaching zero). The performance of the wrought Type 316L stainless steel and the HVOF coating of Alloy C-22 was relatively poor over the entire range of potential. In conclusion, corrosion resistant thermal-spray coatings can be produced with powders of Fe-based amorphous metal, but not with powders of nickel-based Alloy C-22 (N06022).

The repassivation potential, taken alone, is a measure of passive film stability against a true thermodynamic reference, and is not affected by spurious changes in the open-circuit corrosion potential that may be due to instantaneous changes in the concentration of oxidants in the electrolyte, including species such as hydrogen peroxide that can be formed by gamma radiolysis. Thus, there is merit in ranking the materials on the basis of the repassivation potential alone.

A ranking of materials based upon their repassivation potentials in 5M $CaCl_2$ at 105°C is shown in Figure 148. From this ranking, it is evident that all of the new high-Mo Fe-based amorphous metals under development by the HPCRM Team perform very well in, as does the P-containing Fe-based material developed by Inoue. However, several samples of wrought, nickel-based Alloy C-22 (N06022) perform poorly, with very little resistance to localized corrosion in such environments. This finding is roughly consistent with the ranking based upon (E_{rp}-E_{corr}). These data were collected at Lawrence Livermore National Laboratory, and are corroborated by independent measurements at the Naval Research Laboratory in Key West, Florida, which are discussed subsequently.

A ranking of materials based upon their repassivation potentials in seawater is shown in Figure 149. In this ranking, all of the new high-Mo Fe-based amorphous metals under development by the HPCRM Team perform very well in Half Moon Bay seawater at 90°C, as does the P-containing Fe-based material developed by Inoue. However, several samples of wrought Type 316L stainless steel, wrought and HVOF nickel-based Alloy C-22 (N06022), and HVOF DAR35 and DAR40 perform poorly, with very little resistance to localized corrosion in such environments. It is evident that corrosion-resistant thermal-spray coatings can be produced with Fe-based amorphous metals, but not with Ni-based Alloy C-22. These data were collected at Lawrence Livermore National Laboratory, and are corroborated by independent measurements at the Naval Research Laboratory in Key West, Florida.

As shown in Figure 150, the Naval Research Laboratory (NRL) at Key West used cyclic polarization to determine the pitting potentials for the materials of interest, and then ranked the alloys based upon the measurements. In this ranking, all of the dense high-Mo Fe-based amorphous metals under development by the HPCRM Team perform very well in Key West seawater. However, many of the early HVOF coatings discussed at the 2004 HPRCRM Team Meeting in Key West, including Type 316L stainless steel, nickel-based Alloy C-22 (N06022), DAR35, and DAR40 perform poorly, with very little resistance to localized corrosion in such environments. It is evident that corrosion-resistant thermal-spray coatings can be produced with Fe-based amorphous metals, but not with Ni-based Alloy C-22. These data were collected at NRL in Key West, and are corroborated by independent measurements at Lawrence Livermore National Laboratory (LLNL).

As shown in Figure 151, the Naval Research Laboratory (NRL) at Key West also measured the anodic current density during potentiostatic polarization of 0 and 300 mV vs. Ag/AgCl, and used these measurements as indicators of the instantaneous corrosion rates. The current density measurements were also used as the basis of ranking the dense high-Mo Fe-based amorphous metals under development by the HPCRM Team, and produced by melt spinning. All exhibit low current densities in Key West seawater, and perform very well. However, many of the early HVOF coatings discussed at the 2004 HPRCRM Team Meeting in Key West, including Type 316L stainless steel, nickel-based Alloy C-22 (N06022), DAR35, and DAR40 perform poorly, with relatively high current densities.

Salt Fog Tests

The salt fog test was used to compare various wrought ant thermal-spray alloys, melt-spun ribbons, arc-melted drop-cast ingots, and thermal-spray coatings for their susceptibility to corrosion by salt sprays, like those that might be encountered aboard naval ships (this test is also known as the “salt spray” test). Two separate salt fog tests were conducted in the cabinet shown in Figure 152. The most recent tests have focused on refined, state-of-the-art iron-based amorphous-metal formulations, in the form of drop-cast ingots and melt-spun ribbons, which have near theoretical density and virtually no porosity. In contrast, the first tests focused on early thermal-spray coatings, which had residual porosity and crystalline structure, and lower resistance to corrosion.

Both salt fog tests were conducted according to ASTM B117 "Standard Test Method of Salt Spray (Fog) Testing". A General Motors test cycle, GM9540P, was used in both tests. The performance of the test developmental amorphous metal samples was evaluated by qualitative comparison to baseline or reference samples. Four types of reference samples were included to establish baseline performance. These references include: Type 316L stainless steel, nickel-based Alloy C-22 (N06022), Ti Grade 7, and the 50:50 nickel-chromium binary.

During the initial phase of the project, coatings of Type 316L stainless steel, nickel-based Alloy C-22, DAR40, DAR40X3 were deposited on stainless steel substrates (Type 316L) with the high-velocity oxy-fuel (HVOF) process. These "early thermal-spray coatings" were made for the corrosion tests reported here by Impreglon Company in the fall of 2003, and discussed at the HPCRM Team Meeting in Key West, held in January 2004. There was no significant rusting of the reference samples, or thermal-spray coatings of Alloy C-22. The "white spots" or "surface discolorations" on the wrought and spray-formed reference samples are due to water spots and salt deposits. Some rust spots were observed on the early thermal spray coatings of DAR40, DAR40X3 and Type 316L stainless steel after 13 cycles, so the test was terminated. The rusting of these early coatings is attributed to non-optimal elemental composition, residual porosity, and partial devitrification during the thermal-spray process.

The post-test condition of early thermal-spray coatings and reference samples after 13 cycles in the salt fog test is shown in the macro photographs shown in Figures 153 through 160. Rust is seen on the early DAR40 coatings in Figures 154b and 154d, on the early DAR40X3 coatings in Figures 155b and 155d, and on the early 316L coatings in Figures 156b and 156d. The rust stains on the early DAR40 and DAR40X3 coatings, visible in Figures 154b, 154d, 155b and 155d, are believed to be due to attack of alpha-ferrite in the partially devitrified coatings. The cause of the corrosion in the 316L thermal-spray coatings is unclear at the present time, but is under further investigation. The coated specimens are being subjected to additional metallurgical examination during the preparation of this report. Figure 161 shows some of these early thermal-spray coatings, while still in the chamber used for the salt fog test.

During the past nine months, advanced formulations of Fe-based corrosion-resistant amorphous-metals have been developed. These materials have lower critical cooling rates, and are therefore more easily deposited in a glassy state, and have optimized elemental compositions that exhibit much more stable passive film stability. To avoid the experimental difficulties encountered with the early thermal-spray coatings, these new materials were made into fully dense, pore-free samples with melt spinning. The compositions of these new "LDAR-series" formulations are summarized in Table 3. These new formulations, in the form of melt-spun ribbons and ingots, were tested in the salt fog chamber for 24 cycles. Melt-spun ribbons of Alloy C-22 and Type 316L stainless steel were used as reference samples. In stark contrast to the early thermal spray coatings of DAR40 and DAR40X3, none of these new "LDAR-series" ribbon samples exhibited any signs of corrosive attack. Macro photographs of the tested pre-test and post-test ribbons are shown in Figures 162 and 163, respectively.

Results of the salt fog testing of arc-melted drop-cast ingots of FBAM37 are shown in Figure 164. Note that the formula for FBAM37 is $Fe_{61}Y_2Zr_8Co_5Mo_7Cr_2B_{15}$. These samples showed no rusting along the barrel section (cylindrical wall). However, there was some indication of rusting on the top cross-section of the ingot, where the composition of the ingot is known to be non-representative of the bulk alloy. This non-homogeneity in alloy composition is at the trailing tip of the drop cast ingot, and is comprised of residue from the arc-melting process. Future testing of ingots should use freshly fractured surfaces, which would be representative of the bulk alloy.

SUMMARY AND CONCLUSIONS

The Defense Advanced Projects Agency (DARPA) Defense Science Office (DSO) and the Department of Energy (DOE) Office of Civilian and Radioactive Waste Management (OCRWM) has co-funding a multi-institutional program to develop high-performance corrosion-resistant materials (HPCRMs) for naval applications and the long-term storage of spent nuclear fuel. These high-Mo Fe-based amorphous metals have no grain boundaries, and therefore have more corrosion resistance in than the more expensive nickel-based Alloy C-22. While the passive film on nickel-based C-22 undergoes catastrophic breakdown in 5-molar calcium chloride at 105°C at low potential, the passive film on the new Fe-based amorphous metal remains stable at a potential above that required for oxygen evolution.

These novel materials can be produced as either bulk alloys or coatings. For example, melt spinning, arc melting with drop casting, and spray forming can be used to render these materials as fully dense pore-free bulk alloys. Coatings can be produced with advanced thermal spray processes, or by physical vapor deposition processes such as magnetron sputtering or electron-beam evaporation.

The materials can also be rendered as bulk alloys. For example, the HPCRM Team has now used induction melting with spray forming to produce large-scale crack free plates with macroscopic thickness. HVOF can also be used to form square-foot, half-inch thick plates of amorphous metal. Near theoretical density is achieved through precise control of powder size with atomization and classification.

Early HVOF coatings of DAR35, DAR40, DAR40X3 had non-optimal elemental compositions, and were produced with non-optimal thermal spray parameters (powder size, gun pressure, and particle velocity), and exhibited light rusting after 13 cycles in the classic salt fog test. However, additional work with optimized elemental compositions of these Fe-based amorphous metals, and samples in the form of fully dense pore-free materials, have shown no corrosion after 24 cycles in this aggressive test. The most promising formulations at the present time are believed to be LDAR2X5 and CBCTL1651.

Electrochemical tests at both the Naval Research Laboratory and Lawrence Livermore National Laboratory have proven that corrosion performance superior to wrought and thermal-spray coatings of nickel-based Alloy C-22 can be achieved with the new iron-based amorphous metals. For example, the passive film on wrought Alloy C-22 undergoes catastrophic breakdown at 100-200 mV vs. Ag/AgCl in 5M $CaCl_2$ at 105°C, whereas CBCTL1651 maintains stable passivity, even as the potential is increased to levels approaching that required for oxygen evolution. These materials are far superior to thermal-spray coatings of Alloy C-22 in seawater. While it has not been possible to render Alloy C-22 as a corrosion resistant, thermal spray coating, such possibilities do exist with the amorphous metal formulations.

The current Fe-based amorphous metals include specific elements known to impart corrosion and oxidation resistance, such as Cr, Mo, W. Additions of Y and Zr improve glass formability, while forming protective oxide scales at high temperature. In the future, the addition of titanium may also lead improved passive film stability at higher temperatures.

NanoSteel Company and Oak Ridge National Laboratory have now produced atomized powders of these new optimized formulations, LDAR2X5 and CBCTL1651, in nominal one-ton quantities. Preliminary trials with conventional thermal spray (HVOF) indicate that both formulations can be used to produce dense coatings.

Optimization of the thermal spray process at the University of California at Davis, and at Sandia National Laboratory, through careful selection of powder size and process temperature, has now yielded coatings of DAR40 (non-optimized elemental coating) that are virtually pore-free, and for all practical purposes, fully dense. These new coating architectures have also been shown, through detailed examination with XRD and SEM, to be amorphous. During the fall of FY05, the new LDAR2X5 and CBCTL1651 will be rendered as fully dense, pore-free, amorphous metal coatings for corrosion testing, using the optimized thermal spray process at Davis.

In addition to having enhanced corrosion resistance, these new Fe-based amorphous metals have substantially improved thermal characteristics, which will improve processing ability, and performance in targeted applications, as shown by the University of Wisconsin at Madison. While there was some sample-to-sample variability, results were generally consistent For example, LDAR2X5 has a glass transition temperature of ~579°C, a recrystallization temperature of ~628°C, a melting point of ~1133°C, and a reduced glass transition temperature of ~0.57 (with a value of 0.6 being ideal). LDAR2X7, an alloy in the same family as LDAR2X5, has a glass transition temperature of ~573°C, a recrystallization temperature of ~630°C, a melting point of ~1137°C, and a reduced glass transition temperature of 0.57. Similarly, CBCTL1651 has a glass transition temperature of ~584°C, a recrystallization temperature of ~653°C, a melting point of ~1121°C, and a reduced glass transition temperature of ~0.55. The critical cooling rates for LDAR2X7 and CBCTL1651, have been determined to be ~ 610 and ≤ 80 K per second, respectively. Clearly, the yttrium additions in CBCTL1651 enhance glass-forming ability, as reported by other participants in the DARPA SAM program.

Based upon the relative costs of the materials proposed for fabrication of SNF and HLW containers (Table 1), which are approximately $24/lb for Ti Grade 7, $8/lb for Alloy C-22, and $3/lb for Type 316L stainless steel, it is believed that Fe-based thermal spray coatings could be used as a cost effective replacement for the two most expensive (titanium and high-performance Ni-based alloys). Based upon current experience, it is believed that ton-quantities of Fe-based amorphous metal powders can be produced for roughly $20,000 per ton (on the order of $10/lb).

ACKNOWLEDGEMENTS

Work was sponsored by the Defense Advanced Projects Agency Defense Science (DARPA) Office (DSO), and the United States Department of Energy (DOE) Office of Civilian and Radioactive Waste Management (OCRWM). This work was done under the auspices of the U.S. DOE by Lawrence Livermore National Laboratory (LLNL) under Contract No. W-7405-Eng-48.

The HPCRM Team expresses their gratitude to sponsors for financial support, and supportive colleagues for making this work possible. A special thanks to Dr. Leo Christodoulou for sharing his insight and knowledge in field of materials science, and for his innovative solutions to many of the technical problems that have been addressed. Professor Joe Payer is also gratefully acknowledged, and has helped the HPCRM Team reach the level of scientific and technical success that is now enjoyed.

Sponsors

Tony Tether, Director, DARPA
Steven Wax, Director, DARPA DSO
Leo Christodoulou, Program Manager, DARPA DSO
Heather Hiegele, Administrative Assistant, DARPA DSO
Dory Holder, Resource Manager, DARPA DSO

Margaret Chu, Director, DOE OCRWM
John Wengele, Director, Office of Science & Technology, DOE OCRWM
Jeff Walker, Technology Manager, Office of Science & Technology, DOE OCRWM
Thomas Kiess, Program Manager, Office of Science & Technology, DOE OCRWM
Joe Payer, Professor, Case Western Reserve; Corrosion Thrust Leader, DOE OCRWM
Bob Budnitz, Special Advisor to Director, DOE OCRWM
John Arthur, Deputy Director, Yucca Mountain Project, Nevada, DOE OCRWM
Dick Spence, Manager, Yucca Mountain Project, Nevada, DOE OCRWM

Others

Adrian (Chip) Smith, Program Manager, Directed Technology, DARPA
Milt Finger, Director's Office, LLNL
C. K. Chou, Associate Director (Retired), Energy & Environment, LLNL
Cindy Atkins-Duffn, Deputy Associate Director, Energy & Environment, LLNL
Tomas de la Rubia, Associate Director, Energy & Environment, LLNL
Jeff Kass, Deputy Associate Director, Chemistry & Materials, LLNL
David McCallen, Program Leader, Repository Science, LLNL
Martha Kohler, Program Leader (Former), Repository Science, LLNL
Lesa Christman, Administrative Assistant, Energy & Environment, LLNL
Cynthia Jensen, Resource Manager, Energy & Environment, LLNL
Bob Brown, Program Development Manager, Geo-Centers Corporation, NRL

REFERENCES

United States Government Accounting Office, Defense Management, Opportunities to Reduce Corrosion Costs and Increase Readiness, Report to Congress, GAO-03-753, July (2003).

United States Department of Defense, Long-Term Strategy to Reduce Corrosion and the Effects of Corrosion on the Military Equipment and Infrastructure of the Department of Defense, Report to Congress, December (2003).

L. F. Aprigliano, L. K. Kohler, NSWCCD FY04 Report, Part 1, September (2004).

L. Battezzati, Mat.Sci.Eng.A, 375-377, 60-65 (2004).

D. Chidambaram, C. R. Clayton, M. R. Dorfman, Surface and Coatings Technology 176, 307-317 (2004).

Y. Y. Chuang and Y. A. Chang, Z. Metallkunde, 77, 460-466 (1986).

J. C. Farmer et al., Nuclear Engineering Design, Vol. 129, pp. 57-88 (1991).

J. C. Farmer et al., Proc. 2000 ASME Pressure Vessel and Piping Conference, Seattle, Washington, July 23-27, 2000, Transportation, Storage, and Disposal of Radioactive Materials, PVP Vol. 408, pp. 53-70 (2000).

J. C. Farmer et al., Proc. 2000 ASME Pressure Vessel and Piping Conference, Seattle, Washington, July 23-27, 2000, Transportation, Storage, and Disposal of Radioactive Materials, PVP Vol. 408, pp. 71-81 (2000).

Fecht, J.Appl.Phys., 68, 4494-4502 (1990).

F. Guo, S. J. Poon, Applied Physics Letters, 83 (13) 2575-2577.

J. A. Juarez-Islas, D. H. Warrington and H. Jones, Journal of Materials Science, 24, 2076-2084 (1989).

W. T. Kim, K. Clay, C. Small, B. Cantor, Journal of Non-Crystalline Soids, 127 (1991) 273-286 (1991).

K. Kishitake, H. Era, F. Otsubo, Journal of Thermal Spray Technology, 5 (2) 145-153 (1996).

H. E. Kissinger, Analytical Chemistry, 29, 1702-1706 (1957).

L. K. Kohler, L. F. Aprigliano NSWCCD-61-TR-2002/07, September (2002).

R. M. Latanison, Workshop on Amorphous Metals and Semiconductors, EPRI, May 12-18 (1985).

M. L. Lau, E. J. Lavernia, Thermal Spray Processing of Nanocrystalline Materials, Chapt. 2, Thermal Spray and Atomization, Wiley and Sons, 51-72 (2002).

Z. P. Lu, C. T. Liu, W. D. Porter, Applied Physics Letters, 83 (13) 2581-2583 (2003).

A. F. Norman and P. Tsakiropoulos, International Journal of Rapid Solidification, 6, (3-4), 185-213 (1991).

P. Nash, Phase diagrams of binary nickel alloys, 75-84 (1991).

M. Palumbo, Intermetallics, 11, 1293-1299 (2003).

S. J. Pang, T. Zhang, K. Asami, A. Inoue, Acta Materialia 50, 489-497 (2002).

S. Pang, T. Zhang, K. Asami, A. Inoue, Materials Transactions, 43 (8) 2137-2142 (2002).

N. H. Pryds and X. Huang, Metallurgical and Materials Transactions A, 31A, 3155-3166 (2000).

N. H. Pryds, M. Eldrup, M. Ohnuma, A. S. Pedersen, J. Hattel and S. Linderoth, Materials Transactions, JIM, 41 (11), 1435-1442 (2000).

M. Telford, Materials Today, 36-43, March (2004).

D. R. Uhlmann, J.Non-Crys.Sol, 7, 337-348 (1972).

TABLES

Table 1 – Baseline Costs Associated with Spent Nuclear Fuel (SNF) Containers

Evaluation Item	Units	Container (21 PWR Type)	Pallet	Drip Shield
Baseline Materials	None	C22 & 316NG	C22 & 316NG	Ti Gr 7
Unit Weight	kg	26,035	2,108	4,203
Unit Weight	tons	28.67	2.32	4.63
Cost C22	$/lb	$7.97	$7.97	$7.97
Fraction C22	None	0.29	0.78	0.00
Cost 316 NG	$/lb	$2.62	$2.62	$2.62
Fraction 316NG	None	0.71	0.23	0.00
Cost TiGr7	$/lb	$24.00	$24.00	$24.00
Fraction TiGr7	None	0.00	0.00	1.00
Unit Total Cost	$/Unit	$390,000	$56,200	$313,000
Unit Material Cost	$/Unit	$237,903	$31,417	$222,185
Unit Fabrication Cost	$/Unit	$152,097	$24,783	$90,815

Table 2 – Overall Costs for Two Bounding Cases

SNF Container & Pallet Pairs (21 PWR Type)			Drip Shield		System
Pairs	Container Cost	Pallet Cost	Units	Drip Shield Cost	Total Cost
14,749	$5,759,910,000	$830,017,800	13,297	$4,161,961,000	$10,751,888,800
11,000	$4,290,000,000	$618,200,000	9,910	$3,101,830,000	$8,010,030,000

Table 3 – The melt-spinning process was used to perform a systematic study of various elemental compositions, each based on the Fe-based DAR40 composition, with 1, 3, 5, and 7 atomic percent additions of specific elements believed to be beneficial to glass formation or corrosion resistance. Elemental additions investigated included nickel, molybdenum, yttrium, titanium, zirconium, and chromium.

Original Data	Formula	Fe	Cr	Mn	Mo	W	B	C	Si	Y	Zr	Ti	Ni	P	Other
DAR27	$(Fe_{0.8}Cr_{0.2})_{73}Mo_2W_2B_{16}C_4Si_1Mn_2$	58.4	14.6	2.0	2.0	2.0	16.0	4.0	1.0						
DAR35	$Fe_{54.5}Mn_2Cr_{15}Mo_2W_{1.5}B_{16}C_4Si_5$	54.2	15.0	2.0	2.0	1.5	16.0	4.0	5.0						0.3
DAR40	$Fe_{52.3}Mn_2Cr_{19}Mo_{2.5}W_{1.7}B_{16}C_4Si_{2.5}$	52.3	19.0	2.0	2.5	1.7	16.0	4.0	2.5						
DAR40X3	$Fe_{50.7}Mn_{1.9}Cr_{18.4}Mo_{5.4}W_{1.6}B_{15.5}C_{3.9}Si_{2.4}$	50.7	18.4	1.9	5.4	1.6	15.5	3.9	2.4						0.2
LDAR1	$(DAR40)_{100-x} + Ni_x$														
LDAR1X1	$(DAR40)_{99} + Ni_1$	51.8	18.8	2.0	2.5	1.7	15.8	4.0	2.5				1.0		
LDAR1X3	$(DAR40)_{97} + Ni_3$	50.7	18.4	1.9	2.4	1.6	15.5	3.9	2.4				3.0		
LDAR1X5	$(DAR40)_{95} + Ni_5$	49.7	18.1	1.9	2.4	1.6	15.2	3.8	2.4				5.0		
LDAR1X7	$(DAR40)_{93} + Ni_7$	48.6	17.7	1.9	2.3	1.6	14.9	3.7	2.3				7.0		
LDAR2X1	$(DAR40)_{99} + Mo_1$	51.8	18.8	2.0	3.5	1.7	15.8	4.0	2.5						
LDAR2X3	$(DAR40)_{97} + Mo_3$	50.7	18.4	1.9	5.4	1.6	15.5	3.9	2.4						
LDAR2X5	$(DAR40)_{95} + Mo_5$	49.7	18.1	1.9	7.4	1.6	15.2	3.8	2.4						
LDAR2X7	$(DAR40)_{93} + Mo_7$	48.6	17.7	1.9	9.3	1.6	14.9	3.7	2.3						
LDAR3X1	$(DAR40)_{99} + Y_1$	51.8	18.8	2.0	2.5	1.7	15.8	4.0	2.5	1.0					
LDAR3X3	$(DAR40)_{97} + Y_3$	50.7	18.4	1.9	2.4	1.6	15.5	3.9	2.4	3.0					
LDAR3X5	$(DAR40)_{95} + Y_5$	49.7	18.1	1.9	2.4	1.6	15.2	3.8	2.4	5.0					
LDAR3X7	$(DAR40)_{93} + Y_7$	48.6	17.7	1.9	2.3	1.6	14.9	3.7	2.3	7.0					
LDAR4X1	$(DAR40)_{99} + Ti_1$	51.8	18.8	2.0	2.5	1.7	15.8	4.0	2.5			1.0			
LDAR4X3	$(DAR40)_{97} + Ti_3$	50.7	18.4	1.9	2.4	1.6	15.5	3.9	2.4			3.0			
LDAR4X5	$(DAR40)_{95} + Ti_5$	49.7	18.1	1.9	2.4	1.6	15.2	3.8	2.4			5.0			
LDAR4X7	$(DAR40)_{93} + Ti_7$	48.6	17.7	1.9	2.3	1.6	14.9	3.7	2.3			7.0			
LDAR5X1	$(DAR40)_{99} + Zr_1$	51.8	18.8	2.0	2.5	1.7	15.8	4.0	2.5		1.0				
LDAR5X3	$(DAR40)_{97} + Zr_3$	50.7	18.4	1.9	2.4	1.6	15.5	3.9	2.4		3.0				
LDAR5X5	$(DAR40)_{95} + Zr_5$	49.7	18.1	1.9	2.4	1.6	15.2	3.8	2.4		5.0				
LDAR5X7	$(DAR40)_{93} + Zr_7$	48.6	17.7	1.9	2.3	1.6	14.9	3.7	2.3		7.0				
LDAR6	$Fe_{43}Cr_{16}Mo_{16}B_5C_{10}P_{10}$	43.0	16.0		16.0		5.0	10.0						10.0	
LDAR7	CBCTL1651 = $Fe_{48}Mo_{14}Cr_{15}Y_2C_{15}B_6$	48.0	15.0		14.0		6.0	15.0		2.0					
LDAR8	$(CBCTL161)_{97} + W_3$	46.6	14.6		13.6	3.0	5.8	14.6		1.9					
LDAR9	$(DAR40)_{90} + Mo_7 + Y_3$	47.1	17.1	1.8	9.3	1.5	14.4	3.6	2.3	3.0					
LDAR10	$Fe_{57.3}Cr_{21.4}Mo_{2.6}W_{1.8}B_{16.9}$	57.3	21.4		2.6	1.8	16.9								

Table 4 – Composition of observed phases in PEA451 as detected by quantitative EDS-analysis. All numbers are atomic percent, with an accuracy of +/- 0.5 %.

Phase	Fe	Cr	Mo	C	W	Si	Mn
Amorphous	58	14	3	11	1	11	2
Dark	58.0	24	3	8	1	4	3
Bright	53	12	4	17	1	10	3
Overall (entire Figure 51)	59	19	3	7	1	9	3
Nominal composition (neglecting boron)	64.9	17.9	2.4	4.8	1.8	6.0	2.4

Table 5 – Summary of thermal analysis (DTA or DSC) on Fe-based glass forming alloys suitable for spray deposition.

Alloy	T_g (°C)	T_x (°C)	T_m (°C)	T_L (°C)	T_{rg} (°C)
DAR35	545-565	613	1074	1350	0.51
DAR40	568-574	623	1110	1338	0.53
DAR40X3	561-567	630	1130	1260	0.55
LDAR1X1	not clear	612	1121	min. 1270	N.A.
LDAR1X3	560	589	1119	min. 1300	0.53
LDAR1X5	540	572	1115	min. 1300	0.52
LDAR1X7	510	545	1112	min. 1300	0.50
LDAR2X1	575	620	1124	1190-1210	0.57
LDAR2X3	578	626	1131	1190-1210	0.57
LDAR2X5	579	628	1133	1190-1210	0.57
LDAR2X7	573	630	1137	1190-1210	0.57
LDAR3X1	560	614	1108	min. 1320	0.52
LDAR3X3	573	659	1138	min. 1380	0.51
LDAR3X5	590	677	1143	min. 1400	0.52
LDAR3X7	not clear	697	1164	min. 1420	
LDAR4X1	573	621	1135	min. 1300	0.54
LDAR4X3	568	623	1146	min. 1320	0.53
LDAR4X5	580	623	1194	1290	0.55
LDAR4X7	558	616	1198	1255	0.54
LDAR5X1	570	622	1134	min. 1360	0.52
LDAR5X3	575	641	1147	min. 1410	0.50
LDAR5X5	596	659	1193	min. 1420	0.51
LDAR6	580	623 [2)]	995	1238-1250	0.56
LDAR7	584	653 [2)]	1121	1290	0.55
LDAR8	565	637 [2)]	1137	1350-1370	0.52
LDAR9	572	677 [2)]	1146	1223	0.56
LDAR10	535	568 [1)]	1210	1350-1370	0.50
LDAR11	535	572 [1)]	1202	1365-1395	0.49

Table 6 – Temperature-dependent heat transfer coefficients used in modeling heat transfer during wedge-cast of DAR35.

Temperature (°C)	Heat transfer coefficient (W/m^2K)
1200	900
900	900
900	700
800	700
800	650
700	650
700	600
50	600

Table 7 – Temperature-dependent heat transfer coefficients used in modeling heat transfer during wedge-cast of LDAR2X7.

Temperature (°C)	Heat transfer coefficient (W/m^2K)
1500	800
800	800
800	700
600	700
600	500
500	500
500	450
400	450
400	400
50	400

Table 8 – Temperature-dependent heat transfer coefficients used in modeling heat transfer during wedge-cast of LDAR7 (CBCTL1651).

Temperature (°C)	Heat transfer coefficient (W/m^2K)
1500	1700
1200	1700
1200	1200
800	1200
800	900
600	900
600	600
500	600
500	500
400	500
400	400
50	400

Table 9 – A compilation of various amorphous-metal samples, and the measured values of the open circuit corrosion potential (E_{corr}), the potential coinciding with the anodic oxidation peak (E_{peak}), the repassivation potential (E_{rp}), and the penetration rate based upon the maximum passive current density (dx/dt), in concentrated calcium chloride solutions at elevated temperature.

Various Alloys at 105 Degrees Centigrade - No Nitrate				
Material	E_{corr}	E_{rp}	E_{rp}-E_{corr}	dx/dt
	mV (Ag/AgCl)	mV (Ag/AgCl)	mV	cm/yr
LDAR1X7	-396	-321	75	7.31E-04
LDAR6 (Inoue)	125	407	282	2.31E-03
Alloy C-22	-482	-110	372	1.06E-02
LDAR2X3	-327	363	690	2.31E-03
LDAR8	-327	363	690	2.91E-03
LDAR2X7	-109	671	780	7.31E-03
LDAR2X5	-301	546	847	1.84E-03
LDAR2X7	-178	677	855	4.61E-03
LDAR2X3	-151	713	864	4.61E-03
LDAR7 (CBCTL1651)	-164	705	869	2.91E-01
LDAR10 (LMDAR4022)	-300	610	910	7.31E-03
LDAR11 (LMDAR1922)	-323	622	945	2.31E-03
LDAR3X1	-281	666	947	4.61E-03
LDAR5X1	-352	601	953	9.21E-04
LDAR2X5	-408	548	956	1.84E-04
LDAR1X3	-409	579	988	1.46E-03
LDAR3X3	-339	692	1031	2.31E-03

Table 9 – Continuation showing a compilation of various amorphous-metal samples, and the measured values of the open circuit corrosion potential (E_{corr}), the potential coinciding with the anodic oxidation peak (E_{peak}), the repassivation potential (E_{rp}), and the penetration rate based upon the maximum passive current density (dx/dt), in concentrated calcium chloride solutions at elevated temperature, with the effects of nitrate-chloride ratio at 120 ℃ shown.

LDAR2X5 at 120 Degrees Centigrade				
[NO3]/[Cl]	E_{corr}	E_{rp}	E_{rp}-E_{corr}	dx/dt
equiv/equiv	mV (Ag/AgCl)	mV (Ag/AgCl)	mV	cm/yr
0.00	-196	509	705	2.91E-03
0.05	-266	677	943	5.81E-04
0.10	-33	537	570	1.16E-02
0.10	-33	539	572	1.16E-02
0.20	231	397	166	9.21E-03
0.20	231	389	158	9.21E-03
LDAR2X7 at 120 Degrees Centigrade				
[NO3]/[Cl]	E_{corr}	E_{rp}	E_{rp}-E_{corr}	dx/dt
equiv/equiv	mV (Ag/AgCl)	mV (Ag/AgCl)	mV	cm/yr
0.00	-267	519	786	2.91E-03
0.10	-241	555	796	1.46E-03
0.10	-241	549	790	
0.20	31	568	537	1.84E-02
0.20	31	568	537	1.84E-02
CBCTL1651 at 120 Degrees Centigrade				
[NO3]/[Cl]	E_{corr}	E_{rp}	E_{rp}-E_{corr}	dx/dt
equiv/equiv	mV (Ag/AgCl)	mV (Ag/AgCl)	mV	cm/yr
0.05	72	412	340	1.16E-03

Table 10 – A compilation of various amorphous-metal samples, and the measured values of the open circuit corrosion potential (E_{corr}), the potential coinciding with the anodic oxidation peak (E_{peak}), and the repassivation potential (E_{rp}) in Half Moon Bay seawater at various temperatures, ranging from 30 to 90 ℃

Seawater at 30 Degrees Centigrade						
Material	Process	Composition	E_{corr}	E_{rp}	E_{rp}-E_{corr}	dx/dt
			(Ag/AgCl)	(Ag/AgCl)	mV	cm/yr
DAR40	HDIF	$Fe_{52.3}Mn_2Cr_{19}Mo_{2.5}W_{1.7}B_{16}C_4Si_{2.5}$	-668	-645	23	
CBAM83	Arc-Melt Drop-Cast Ingot	Fe-Based	-165	-92	73	4.61E-03
DAR40	MSR	$Fe_{52.3}Mn_2Cr_{19}Mo_{2.5}W_{1.7}B_{16}C_4Si_{2.5}$	-275	-126	149	1.84E-01
316L	Wrought	Fe-Cr-Mo	-227	-227	190	3.67E-03
C22	HVOF	Fe-Cr-Mo	-392	-127	265	1.84E-01
LDAR2X5	MSR	$(DAR40)_{95} + Mo_5$	-19	894	913	9.21E-04
DAR40	HVOF	$Fe_{52.3}Mn_2Cr_{19}Mo_{2.5}W_{1.7}B_{16}C_4Si_{2.5}$	-94	830	924	9.21E-02
DAR35	HVOF	$Fe_{54.5}Mn_2Cr_{15}Mo_2W_{1.5}B_{16}C_4Si_5$	-248	720	968	1.16E-02
LDAR6 (Inoue)	MSR	$Fe_{43}Cr_{16}Mo_{16}B_5C_{10}P_{10}$	-160	884	1044	4.61E-04
LDAR10 (LMDAR4022)	MSR	$Fe_{57.3}Cr_{21.4}Mo_{2.6}W_{1.8}B_{16.9}$	-233	858	1091	2.31E-03
LDAR1X7	MSR	$(DAR40)_{93} + Ni_7$	-353	815	1168	1.84E-03
LDAR5X1	MSR	$(DAR40)_{99} + Zr_1$	-275	930	1205	1.84E-03
DAR40X3	HVOF	$Fe_{50.7}Mn_{1.9}Cr_{18.4}Mo_{5.4}W_{1.6}B_{15.5}C_{3.9}Si_{2.4}$	-370	878	1248	4.61E-01
CBCTL1651	Arc-Melt Drop-Cast Ingot	$Fe_{48}Mo_{14}Cr_{15}Y_2C_{15}B_6$	-376	881	1257	4.61E-02
LDAR1X3	MSR	$(DAR40)_{97} + Ni_3$	-310	972	1282	1.16E-03
LDAR7 (CBCTL1651)	MSR	$Fe_{48}Mo_{14}Cr_{15}Y_2C_{15}B_6$	-384	908	1292	9.21E-04
Seawater at 60 Degrees Centigrade						
Material	Process	Composition	E_{corr}	E_{rp}	E_{rp}-E_{corr}	dx/dt
			(Ag/AgCl)	(Ag/AgCl)	mV	cm/yr
316L	Wrought	Fe-Cr-Mo	-241	-241	122	7.31E-03
C22	HVOF	Fe-Cr-Mo	-415	-222	193	7.31E-01
DAR40	HVOF	$Fe_{52.3}Mn_2Cr_{19}Mo_{2.5}W_{1.7}B_{16}C_4Si_{2.5}$	-362	750	1112	2.31E-01
DAR35	HVOF	$Fe_{54.5}Mn_2Cr_{15}Mo_2W_{1.5}B_{16}C_4Si_5$	-360	752	1112	7.31E-02
DAR40	MSR	$Fe_{52.3}Mn_2Cr_{19}Mo_{2.5}W_{1.7}B_{16}C_4Si_{2.5}$	-274	822	1096	1.84E-03
Seawater at 90 Degrees Centigrade						
Material	Process	Composition	E_{corr}	E_{rp}	E_{rp}-E_{corr}	dx/dt
			(Ag/AgCl)	(Ag/AgCl)	mV	cm/yr
DAR35	HVOF	$Fe_{54.5}Mn_2Cr_{15}Mo_2W_{1.5}B_{16}C_4Si_5$	-505	-409	96	
316L	Wrought	Fe-Cr-Mo	-210	none	130	1.84E-02
DAR40	HVOF	$Fe_{52.3}Mn_2Cr_{19}Mo_{2.5}W_{1.7}B_{16}C_4Si_{2.5}$	-504	-346	158	7.31E-02
FBAM117	Arc-Melt Drop-Cast Ingot	Fe-Based	336	591	255	9.21E-03
C22	HVOF	Fe-Cr-Mo	-576	-277	299	1.46E+00
LDAR6 (Inoue)	MSR	$Fe_{43}Cr_{16}Mo_{16}B_5C_{10}P_{10}$	-97	560	657	2.31E-03
DAR40	MSR	$Fe_{52.3}Mn_2Cr_{19}Mo_{2.5}W_{1.7}B_{16}C_4Si_{2.5}$	-115	716	831	2.91E-03
LDAR7 (CBCTL1651)	MSR	$Fe_{48}Mo_{14}Cr_{15}Y_2C_{15}B_6$	-313	543	856	3.67E-03
LDAR2X7	MSR	$(DAR40)_{93} + Mo_7$	-182	680	862	1.84E-03
LDAR8	MSR	(CBCTL1651)97 + W3	-355	553	908	4.61E-03
LDAR2X3	MSR	$(DAR40)_{97} + Mo_3$	-241	693	934	2.91E-03
LDAR4X7	MSR	$(DAR40)_{93} + Ti_7$	-21	1000	1021	4.61E-03
LDAR5X1	MSR	$(DAR40)_{99} + Zr_1$	-198	823	1021	3.67E-03
LDAR2X7	MSR	$(DAR40)_{93} + Mo_7$	-234	805	1039	3.67E-03
LDAR11 (LMDAR1922)	MSR	DAR40 Variant	-287	771	1058	3.67E-03
LDAR10 (LMDAR4022)	MSR	$Fe_{57.3}Cr_{21.4}Mo_{2.6}W_{1.8}B_{16.9}$	-296	807	1103	5.81E-03
LDAR4X5	MSR	$(DAR40)_{95} + Ti_5$	-224	910	1134	3.67E-03
LDAR2X5	MSR	$(DAR40)_{95} + Mo_5$	-203	949	1152	2.31E-03
LDAR3X3	MSR	$(DAR40)_{97} + Y_3$	-371	789	1160	1.84E-03
CBCTL1651	Arc-Melt Drop-Cast Ingot	$Fe_{48}Mo_{14}Cr_{15}Y_2C_{15}B_6$	-270	944	1214	2.31E-01

Table 11. A compilation of the results from early cyclic polarization of Type 316L stainless steel, Alloy C-22, HVOF DAR35, HVOF DAR40, and HVOF DAR40X3 in standard 4M NaCl, SCW and BSW test solutions. Note that both SCW and BSW are bicarbonate-type brines. These data were reported at the HPCRM Team Meeting in Key West, held in January 2004. These results were used as the basis of recommending the pursuit of theoretically dense, pore-free materials for testing, so that the effects of alloy composition could be separated from the effects of coating morphology.

Material	Form	Solution	Temp	Ecorr	Ecrit	Ereverse	Erp	E20	E200	ER2	ER1
			C	mV/AgCl	mV/AgCl	mV/AgCl	mV/AgCl	mV/AgCl	mV/AgCl	mV/AgCl	mV/AgCl
316L	Wrought	4M NaCl	30	-142	121	144	none	136	136	none	none
316L	Wrought	4M NaCl	60	-239	54	68	none	61	70	none	none
316L	Wrought	4M NaCl	90	-102	-24	-10	none	-12	-12	none	none
DAR35	HVOF	4M NaCl	30	-350	293	440	-284	308	308	-277	-277
DAR35	HVOF	4M NaCl	60	-405	925	977	none	-380	-184	none	none
DAR35	HVOF	4M NaCl	90	-354	none	-151	none	-273	-218	none	none
DAR40	HVOF	4M NaCl	30	-356	28	62	none	-271	19	none	none
DAR40	HVOF	4M NaCl	60	-412	874	982	891	-381	-139	-367	-367
DAR40	HVOF	4M NaCl	90	-591	-234	-176	-426	-442	-223	-440	none
DAR40X3	HVOF	BSW	30	-136	475	640	none	35	83	-58	-72
DAR40X3	HVOF	BSW	60	-294	468	555	261	-137	19	none	none
DAR40X3	HVOF	BSW	90	-353	448	489	298	-78	451	-88	-102
DAR35	HVOF	SAW	30	-252	918	1079	773	-75	603	-147	-161
DAR35	HVOF	SAW	60	-208	800	999	802	-119	394	-146	-143
DAR35	HVOF	SAW	90	-393	883	991	892	-348	716	-166	-172
DAR40	HVOF	SAW	30	-258	814	1055	none	-133	470	-98	-104
DAR40	HVOF	SAW	60	-285	739	988	766	-73	809	-110	-121
DAR40X3	HVOF	SAW	30	-155	845	1025	833	40	651	none	none
DAR40X3	HVOF	SAW	60	-214	732	976	809	2	789	none	none
DAR40X3	HVOF	SAW	90	-354	895	1054	813	-141	917	none	none
316L	Wrought	SCW	30	-20	886	1075	848	928	962	832	719
316L	Wrought	SCW	60	-113	785	904	750	800	836	205	78
316L	Wrought	SCW	90	-76	651	985	552	670	698	528	505
C22	HVOF	SCW	30	-265	828	979	none	-174	385	-82	-94
C22	HVOF	SCW	60	-242	707	774	691	-145	268	-12	-25
C22	HVOF	SCW	90	-605	648	702	616	-505	163	-133	-143
DAR35	HVOF	SCW	30	-149	932	1031	911	-30	428	-48	-53
DAR35	HVOF	SCW	60	-354	791	899	789	-247	295	-52	-59
DAR35	HVOF	SCW	90	-685	600	820	705	157	684	213	175
DAR40	HVOF	SCW	30	-92	943	1075	918	156	925	-58	-64
DAR40	HVOF	SCW	60	-189	833	939	813	-63	691	-118	-138
DAR40	HVOF	SCW	90	-460	678	809	683	-123	682	-323	-6
DAR40X3	HVOF	SCW	30	-98	967	1110	none	332	513	306	294
DAR40X3	HVOF	SCW	60	-18	891	1006	899	224	377	none	none
DAR40X3	HVOF	SCW	90	-95	786	887	721	57	246	none	none
DAR40	MSR	SCW	30	-110	973	1204	none	401	1008	none	none

FIGURES

Figure 1 – Corrosion-resistant amorphous-metal coatings applied with thermal spray processes could have several applications of importance to the Navy.

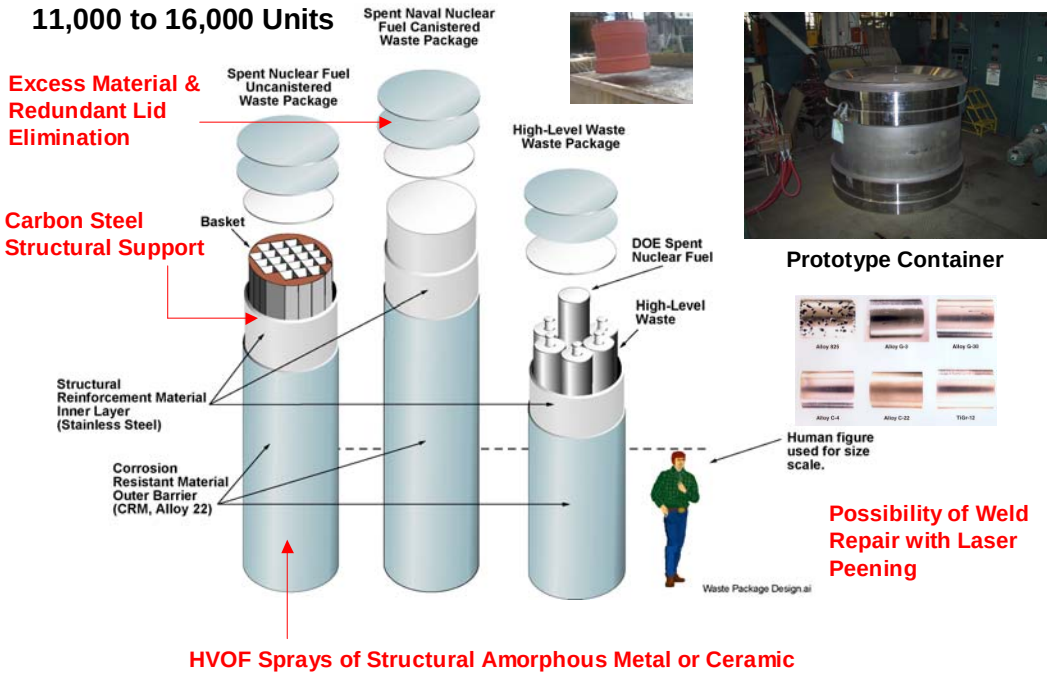

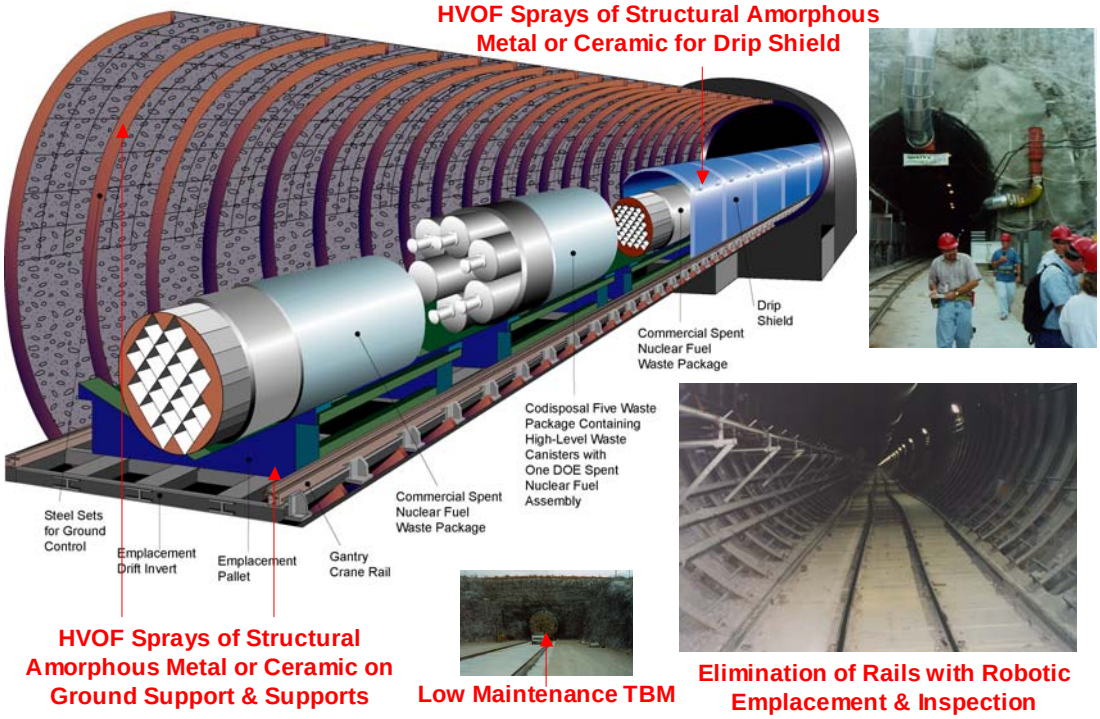

Figure 2 – Advanced corrosion-resistant materials are also needed for the long term storage of the nation's spent nuclear fuel.

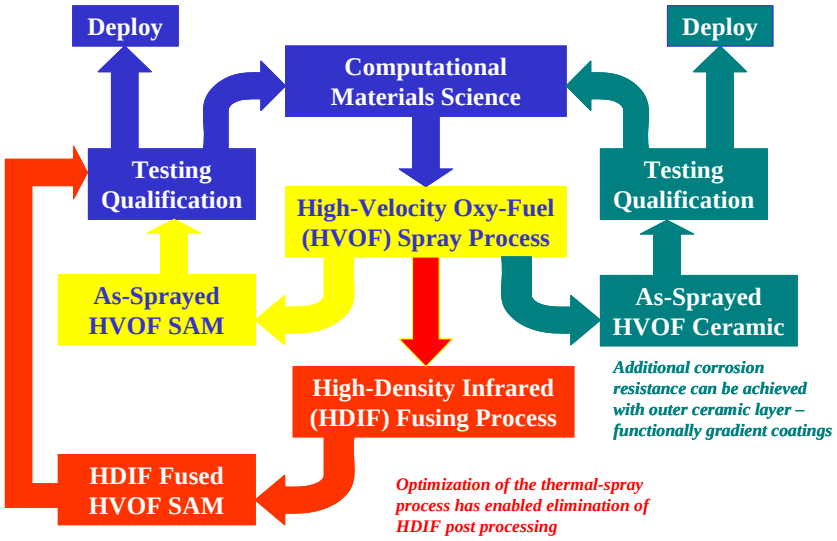

Figure 3 – The High-Performance Corrosion-Resistant Materials (HPCRM) Program is co-funded by DARPA DSO and DOE OCRWM, and utilizes both theoretical and experimental materials science to develop corrosion-resistant amorphous-metal coatings suiJCF-Table for the desired applications.

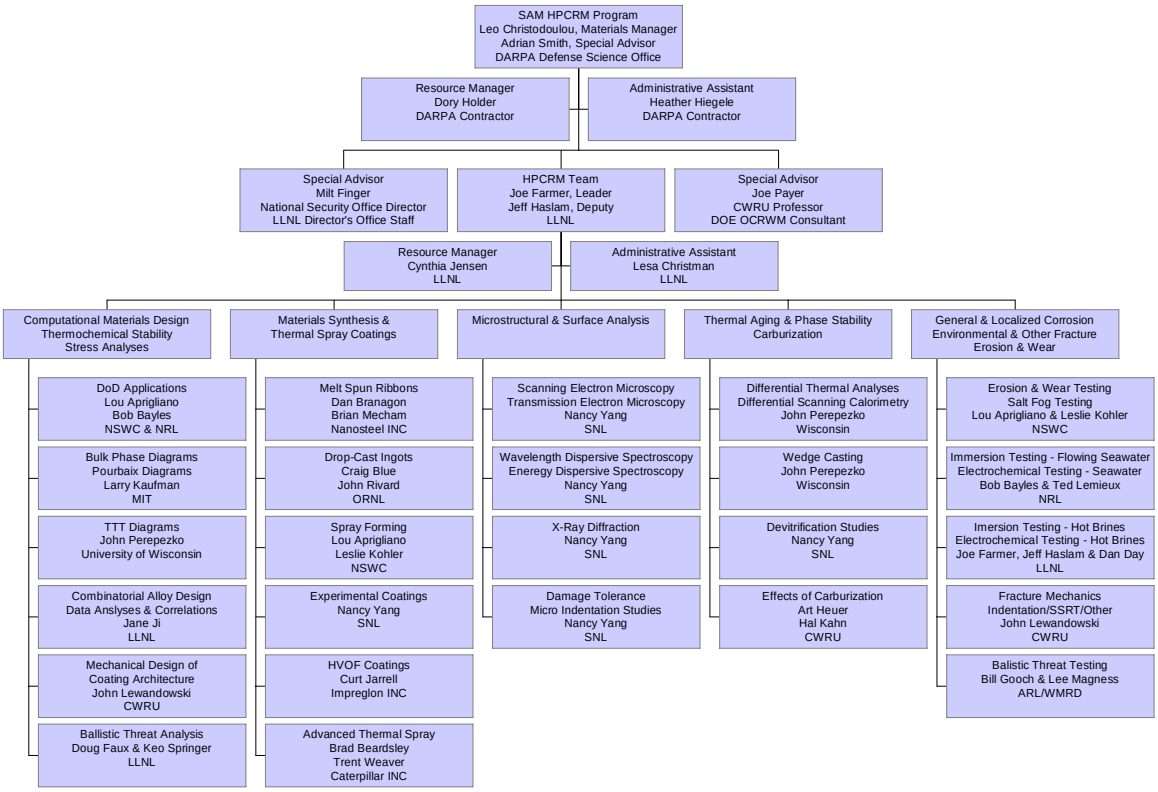

Figure 4 – The HPCRM Team is multi-institutional and involved three of DOE laboratories (LLNL, SNL, and ORNL), three DOD laboratories (NSWC Carderock, NRL Washington, and NRL Key West), industry (NanoSteel and Caterpillar), as well as several universities.

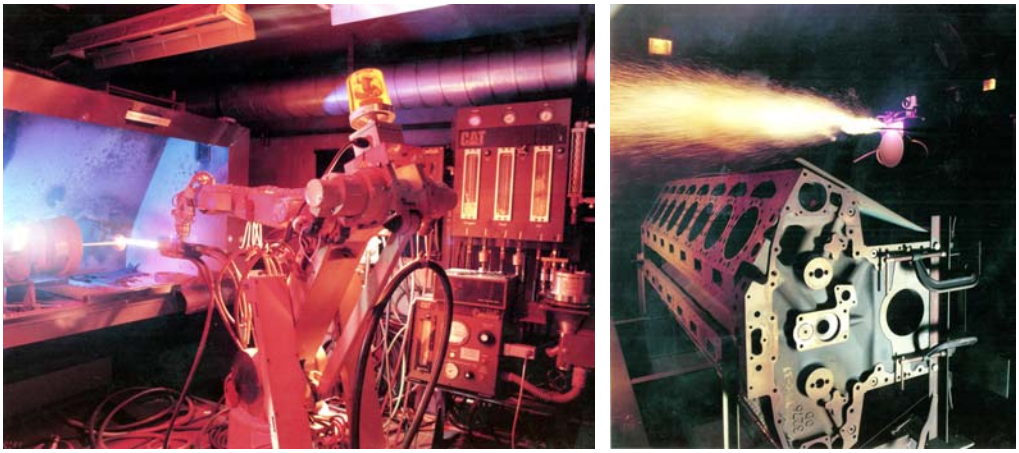

Figure 5 – Advanced thermal spray processes are available at Caterpillar for the application of atomized powders produced by NanoSteel Company, as well as other contractors to the Team. A precision three-dimensional translation of a spray gun with advanced manufacturing robotics is shown (left), with a photograph of the water-stabilized plasma-spray, capable of increasing deposition rates by an order of magnitude, to a rate of about 200 pounds per hour (right).

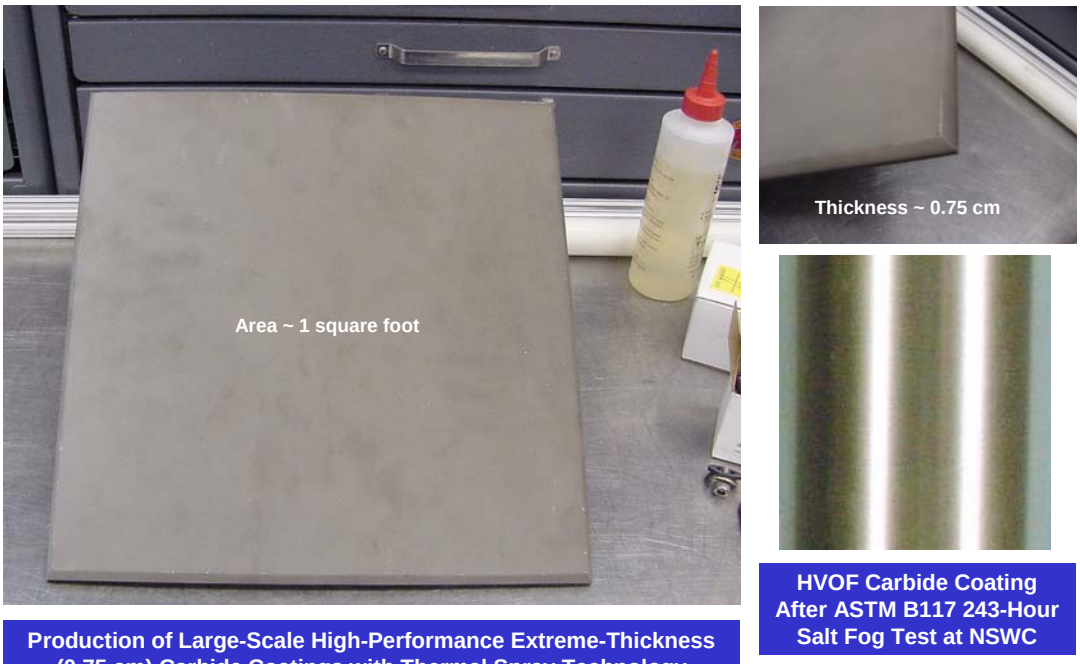

Figure 6 – As a member of the HPCRM Team, Caterpillar has demonstrated the deposition of macroscopically thick coatins of chromium carbide (85 wt. % with 15% metallic binder) on planar and cylindrical substrates.

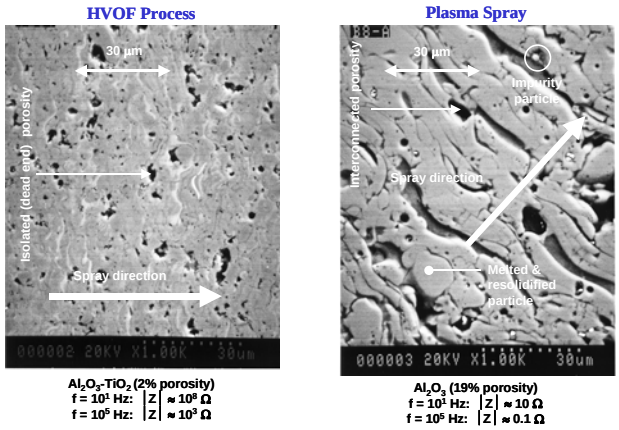

Figure 7 – Thermal-spray coatings have already been investigated for applications to the long-term storage of spent nuclear fuel, thus, a precedent exists. Two thermal-spray processes were compared in these early studies, the high-velocity oxy-fuel (HVOF) process, and the more conventional plasma spray process. It was found that relatively dense coatings with little interconnected porosity could be produced with HVOF (only 2% porosity), whereas the plasma spray process produced only porous coatings with substantial interconnected porosity (about 19% porosity). Consequently, HVOF coatings are adequate for corrosion protection, whereas the more conventional plasma spray coatings are not. Similar heuristic principles apply to thermal-spray amorphous metal (metallic glass) coatings.

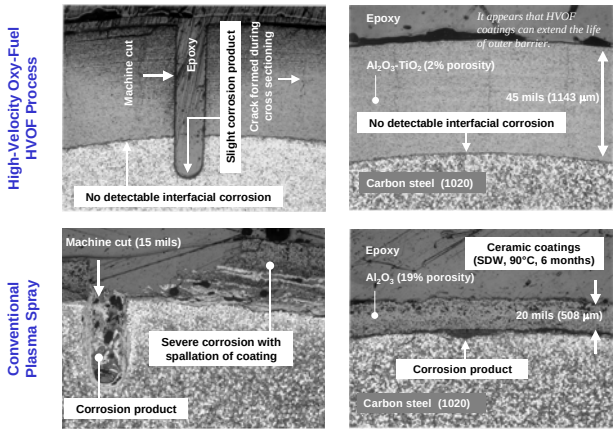

Figure 8 – The results of a six-month immersion test of thermal-spray ceramic coatings in a hot bicarbonate brines confirms the corrosion resistance of the dense HVOF coatings, and the inadequacy of the more primitive plasma spray coatings. In the case of the HVOF coating, 45 mils of Al_2O_3-TiO_2 with a porosity of only 2 percent was deposited onto a carbon steel (1020) substrate, with an intentional 15-mil flaw introduced with a saw blade at the beginning of the test, to investigate the susceptibility of the coating to interfacial corrosion and spallation. This proved not to be an issue with the HVOF coating. A similar 45-mil coating of Al_2O_3, with a porosity of 19 percent, was deposited with the more conventional plasma spray process. In this case, the interconnected porosity lead to substantial interfacial corrosion and spallation after the 6-month exposure, showing the inadequacy of plasma spray coatings for corrosion protection.

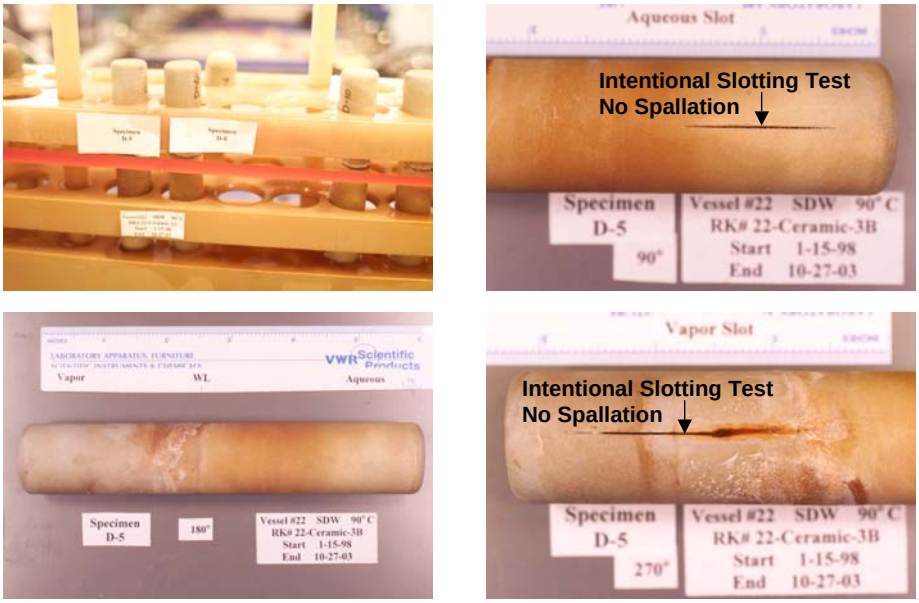

Figure 9 – The thermal-spray coatings were exposed to hot bicarbonate brines for an additional 5-6 years, with the HVOF coating showing no interfacial corrosion or spallation, even with the intential flaw that was introduced with the saw blade. There is clear evidence indicating that such HVOF coatings can provide adequate corrosion protection, even with substantial surface flaws.

Figure 10 – The thermal spray process used to produce the chromium carbide coating has also been used to apply amorphous metal coatings. Caterpillar has also produced macroscopically thick sheets of amorphous metals, such as DAR40X3.

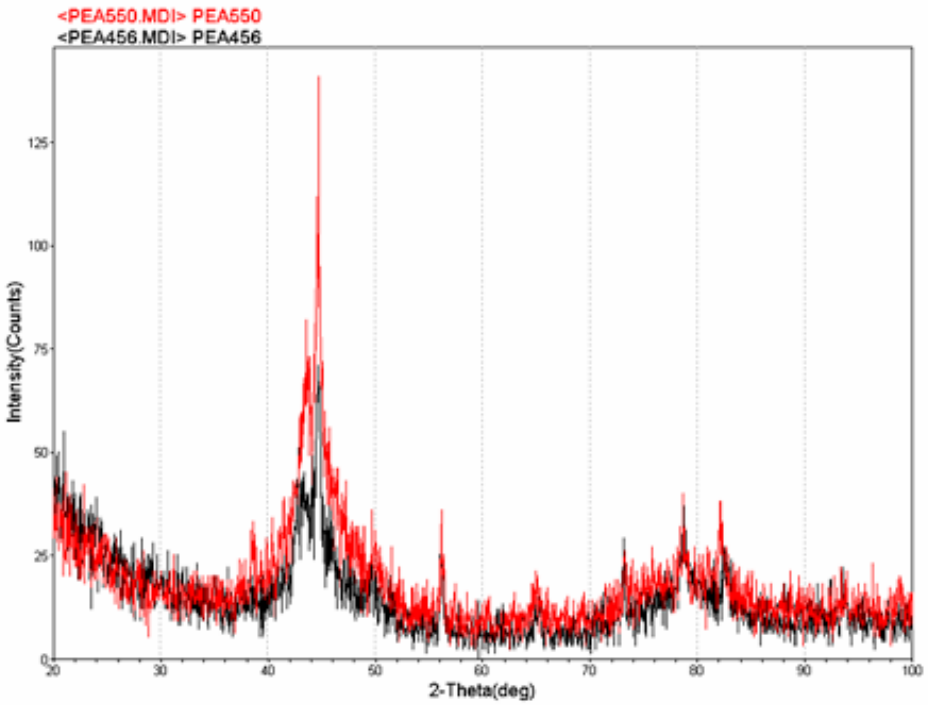

Figure 11 – X-ray diffraction (XRD) patterns for thermal-spray coatings of DAR35 (red) and DAR40 (black), both produced with the high-velocity oxy-fuel (HVOF) process. While there is some residual crystalline structure, these coatings are predominantly amorphous.

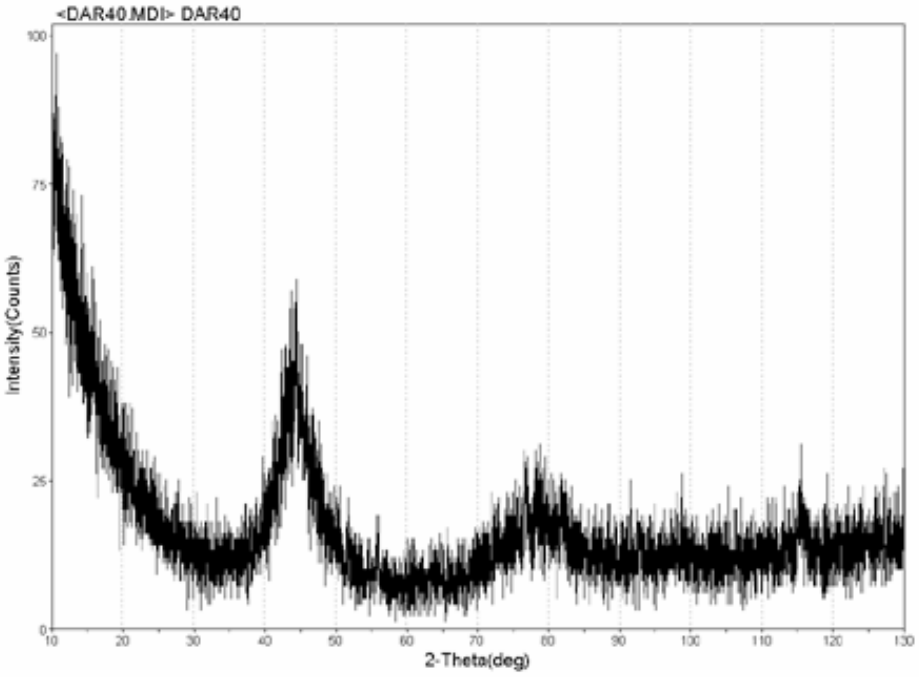

Figure 12 – X-ray diffraction (XRD) pattern for thermal-spray coating of DAR40 produced with the HVOF process. The lack of crystalline structure is also evident in this case, with only a few very broad peaks evident.

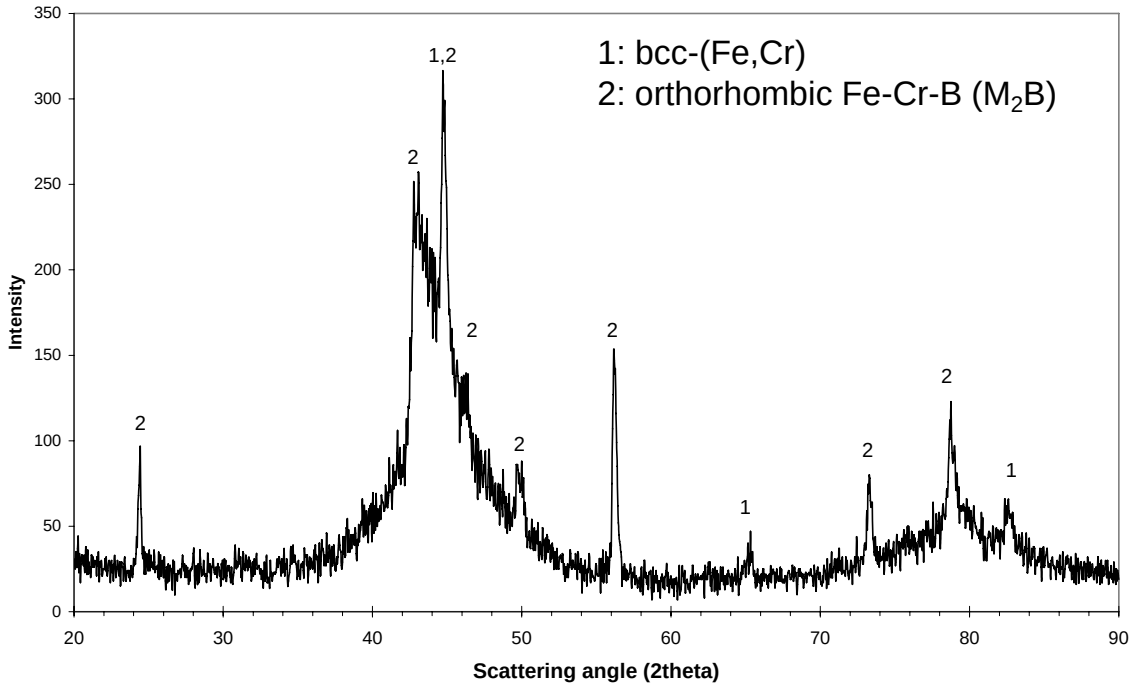

Figure 13 – X-ray diffraction (XRD) pattern for partially amorphous spray-formed coating on a stainless steel disk (PEA 451).

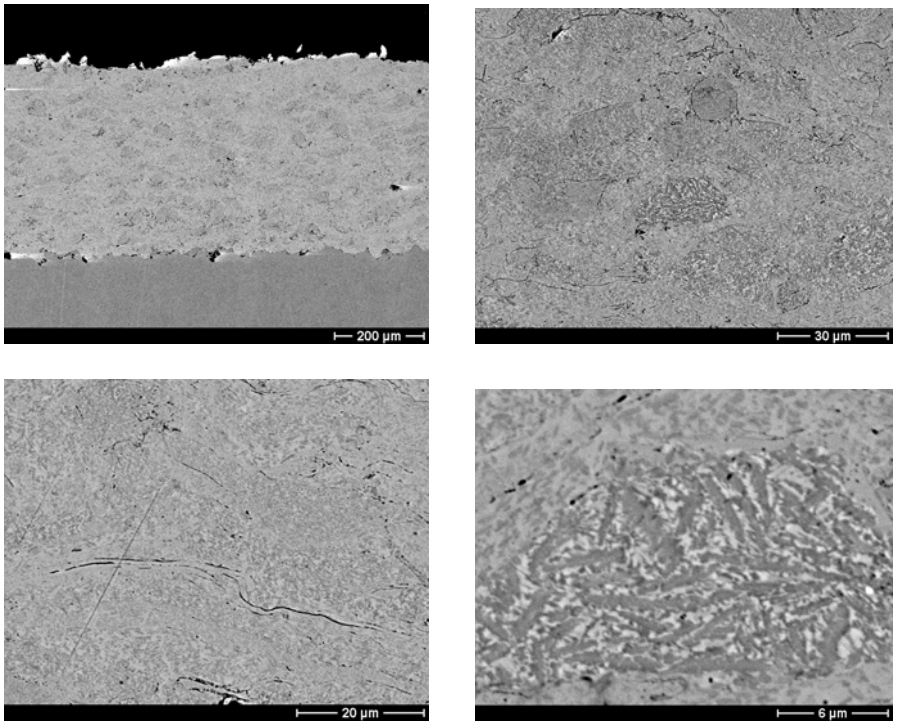

Figure 14 – Back-scattered electron images (BSEI) of PEA451. As JP-Table8 indicates, the phases present in the sample differ very little in composition, thus, little contrast in back-scattered electron mode.

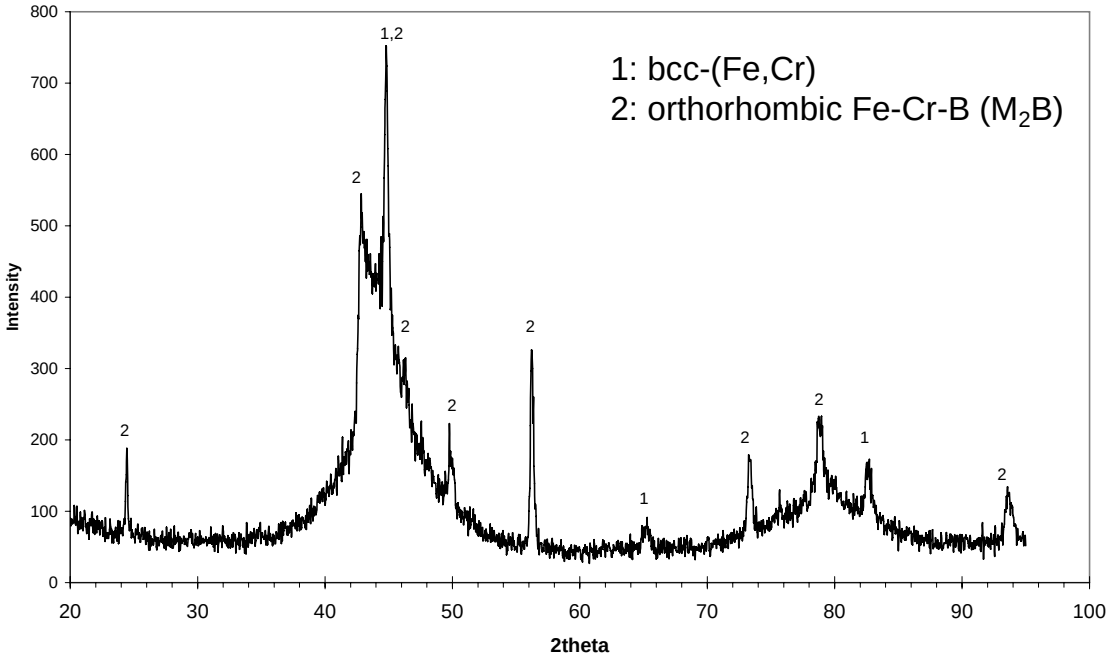

Figure 15 – X-ray diffraction (XRD) trace from PEA 452, virtually identical to that of PEA 451.

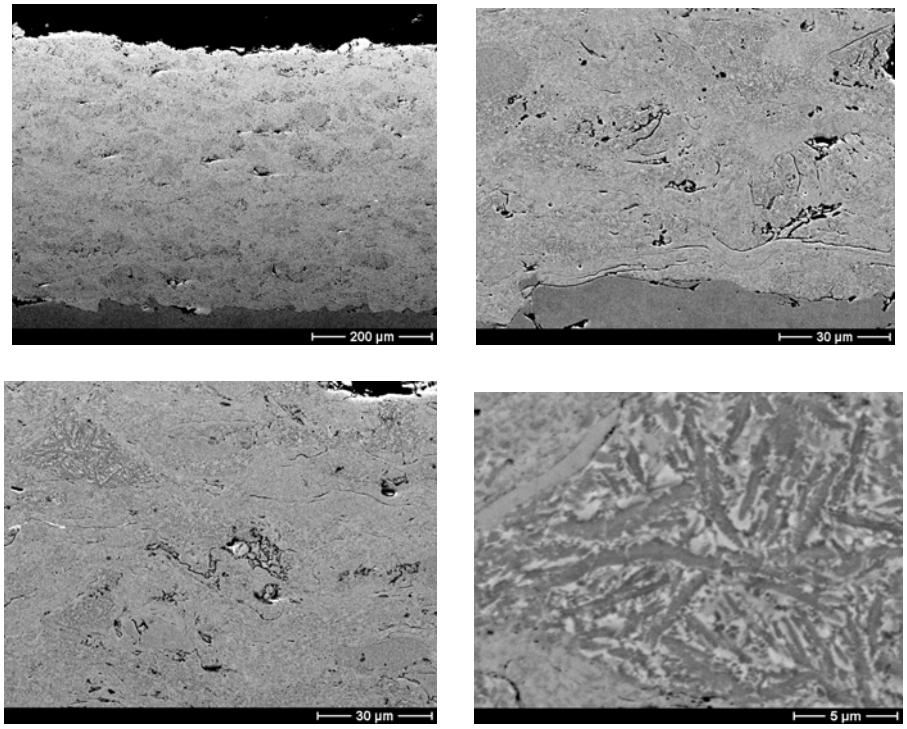

Figure 16 – Back-scattered electron images (BSEI) of PEA 452, showing representative micrographs from the partially amorphous coating.

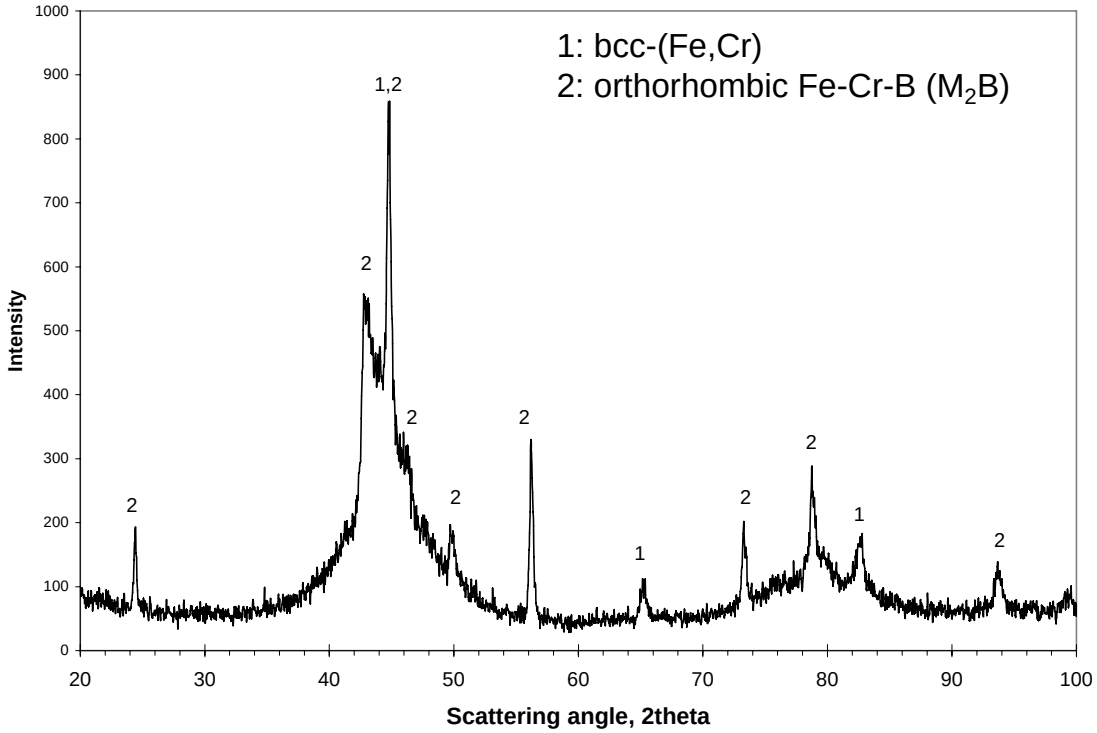

Figure 17 – X-ray diffraction (XRD) trace of partially amorphous coating (PEA 504).

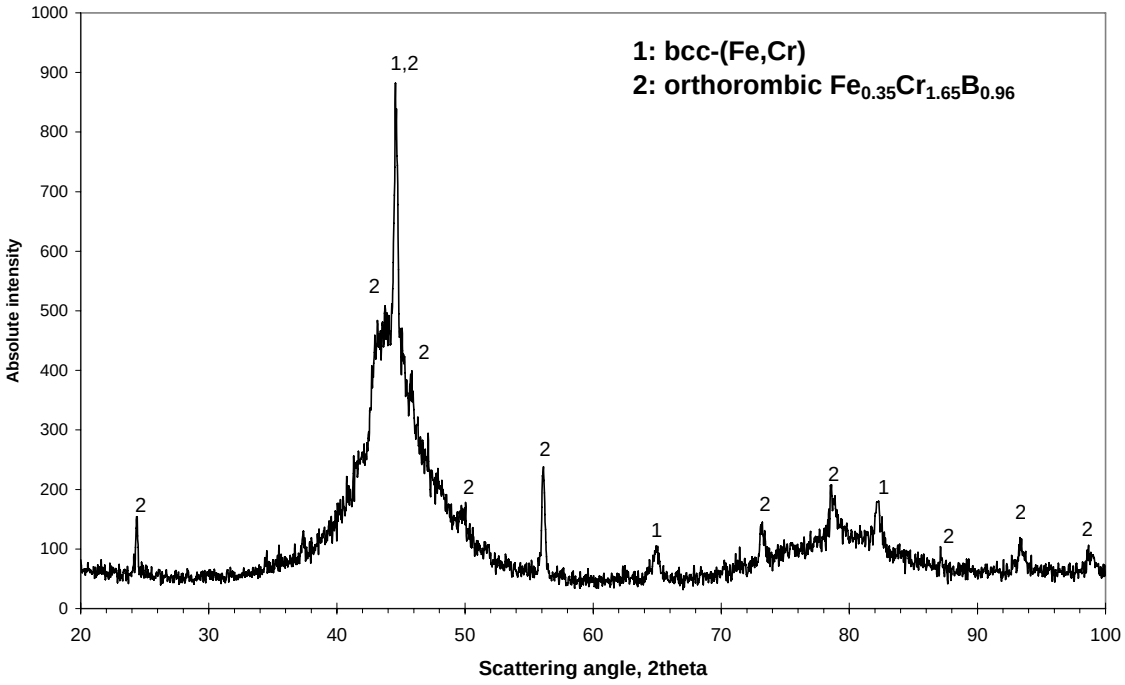

Figure 18 – X-ray diffraction (XRD) trace of the sprayed coating DAR40 (PEA 479). Peaks identical to those observed for sprayed DAR35 coatings.

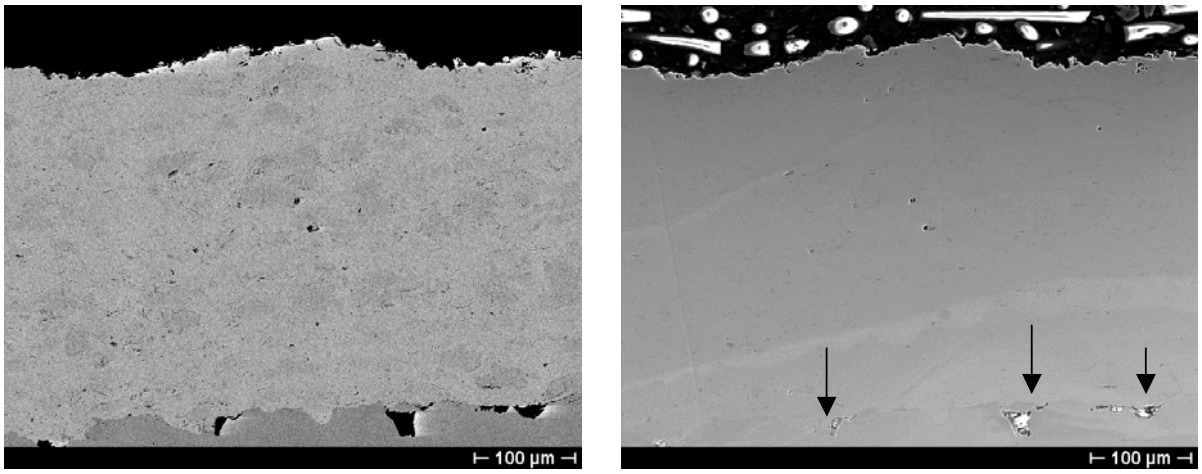

Figure 19 – Sprayed coating of DAR40 showing the same region but with in different scanning modes; BSEI (back-scattered electron image) to the left and SEI (secondary electron image) to the right. Arrows indicate large pores at the coating/disk interface.

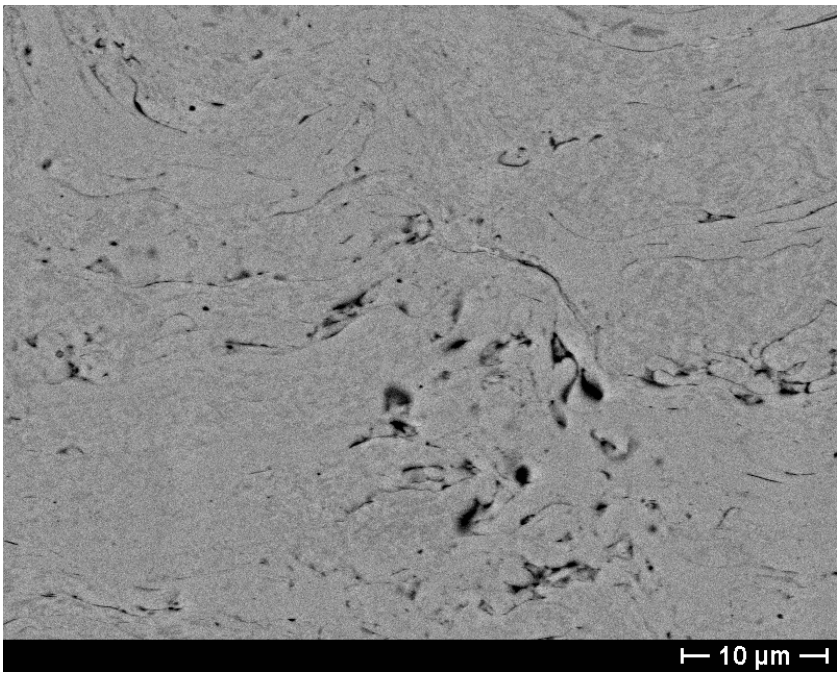

Figure 20 – A mostly amorphous region of DAR40 spray-formed coating. Some nano-crystalline precipitates (dark gray) can be observed as well as pores (black) and the amorphous matrix (gray).

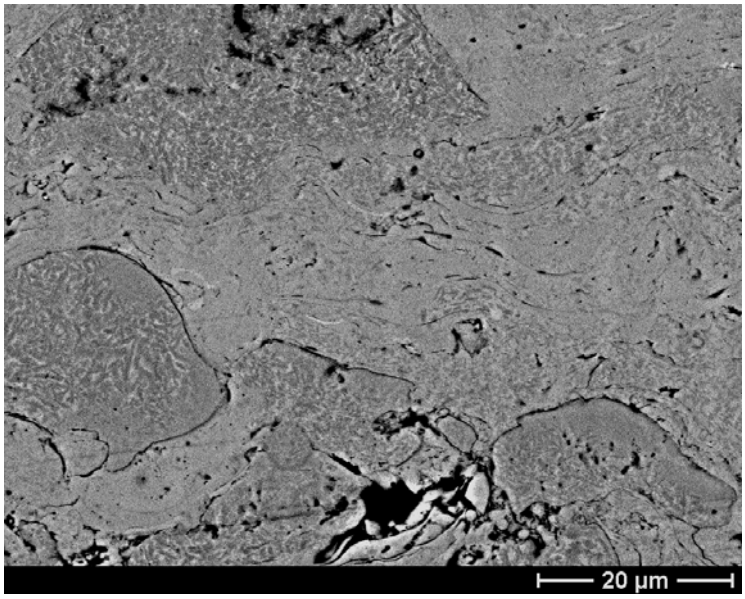

Figure 21 – Back scatter electron (BSE) image of PEA 479, showing pockets of crystalline regions embedded in an amorphous/nanocrystalline matrix.

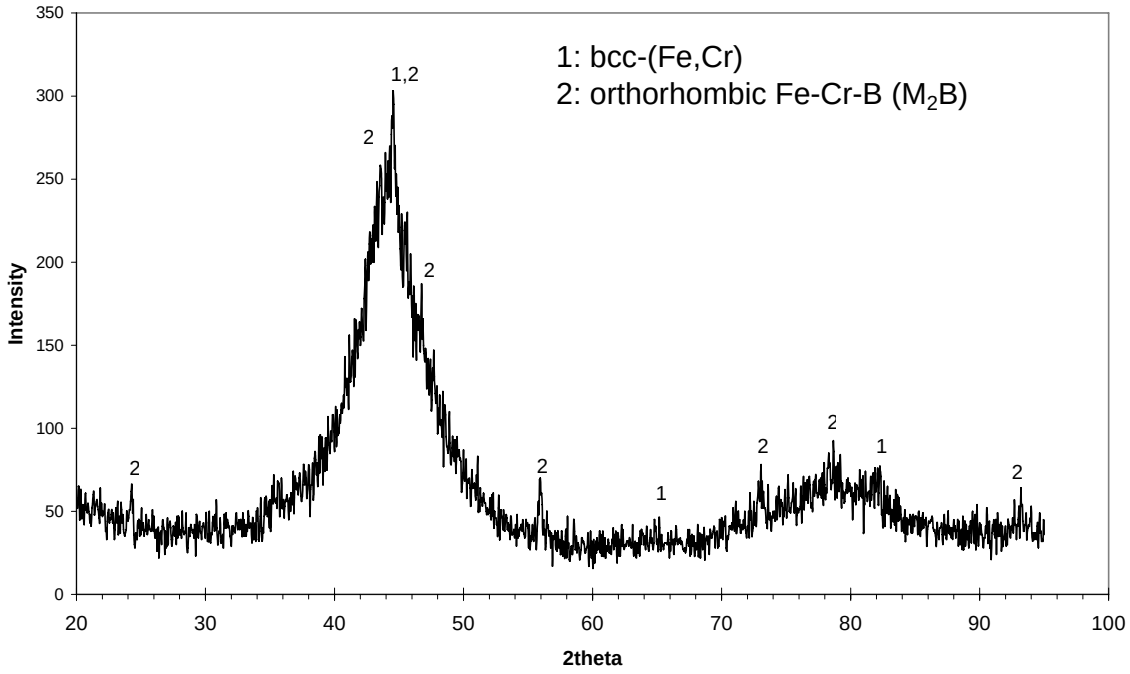

Figure 22 – X-ray diffraction (XRD) trace from DAR40X3 sprayed coating.

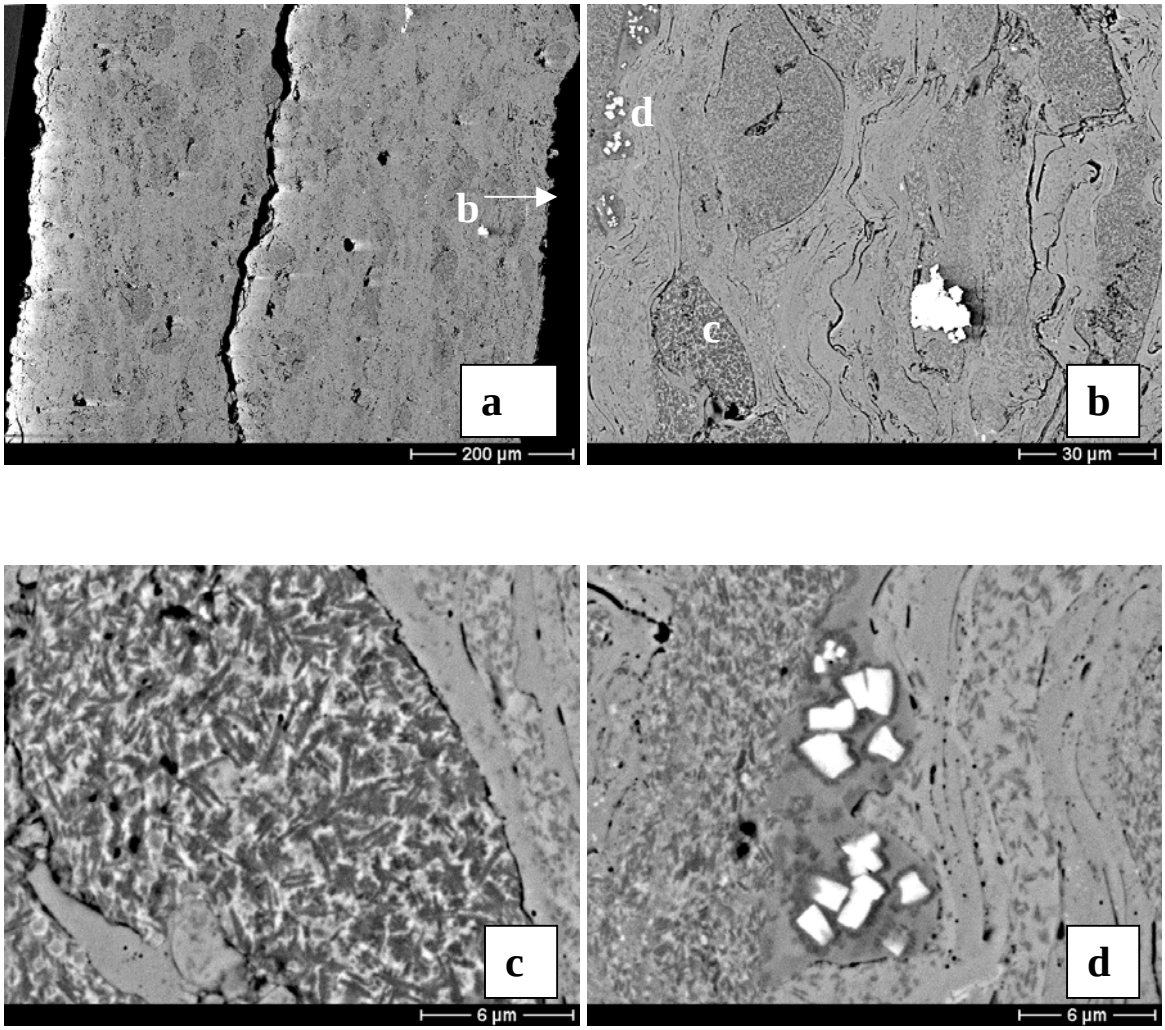

Figure 23 – Back-scattered electron images (BSEI) from the sprayed DAR40X3 coating. Regions marked b, c and d are shown separately.

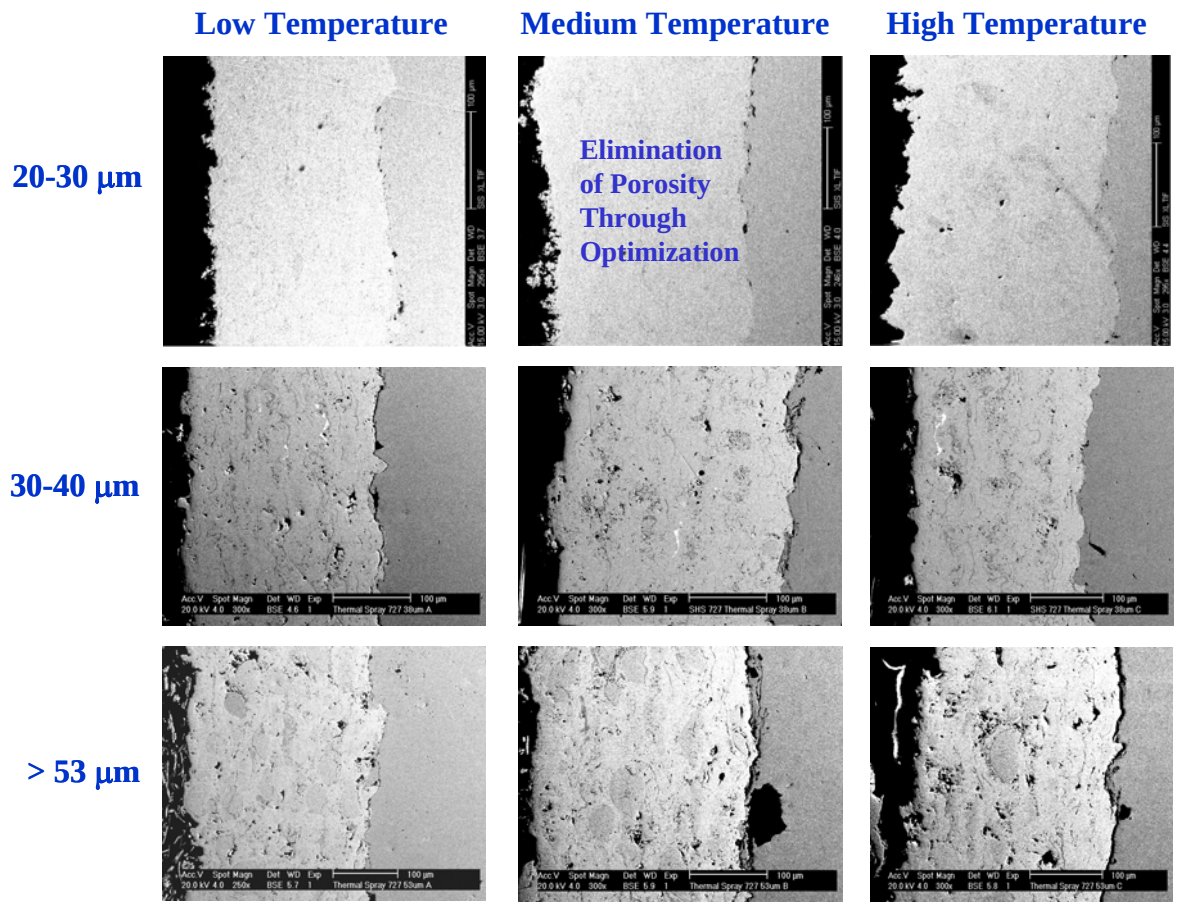

Figure 24 – A parametric study of the HVOF process was conducted with DAR40, with the mean particle size of the sprayed powder and the substrate temperature systematically varied. While coatings produced with relatively large particles (> 54 μm) showed un-melted and un-consolidated particles embedded in the coating, with substantial porosity and poor interfacial bonding, coatings produced with smaller particles (20 to 23 μm) are essentially homogeneous, pore-free and well-bonded.

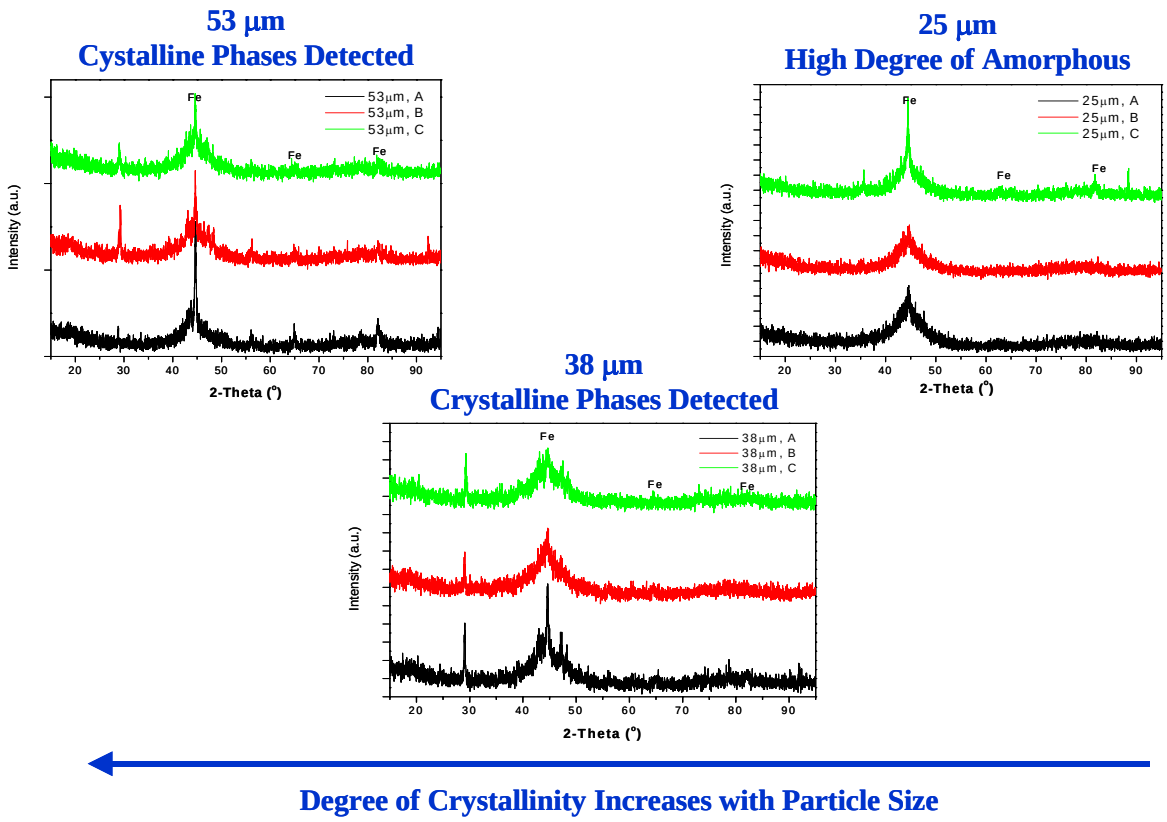

Figure 25 – X-ray diffraction DAR40 deposited with HVOF during the parametric study shown in Figure 24 show that the coatings produced with smaller particles (25 µm) are more glassy, with fewer residual crystalline phases, than the coatings produced with larger particles (38 to 53 µm).

(a) Perspective view of hollow cylinder (shaft) with wear-resistant DAR-type HVOF coating having high-integrity interfacial bond on outer diameter.

(b) Plan view of hollow cylinder (shaft) with wear-resistant DAR-type HVOF coating with high integrity interfacial bond.

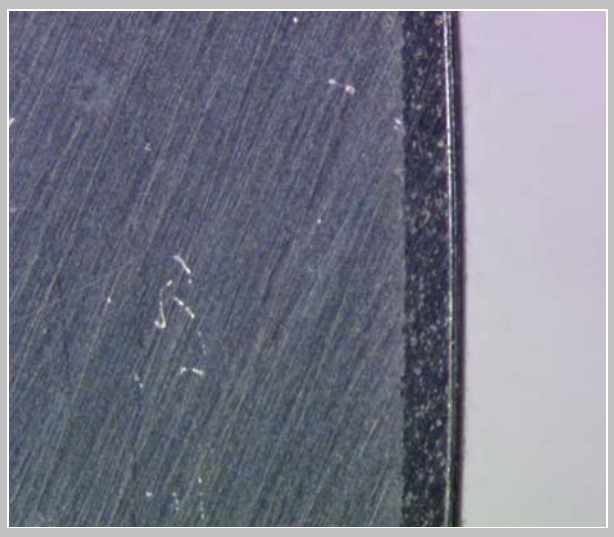

(c) Metallographic cross-section of wear-resistant DAR-type HVOF coating on hollow cylinder (shaft), at a magnification of 20×, showing bond of coating to the substrate.

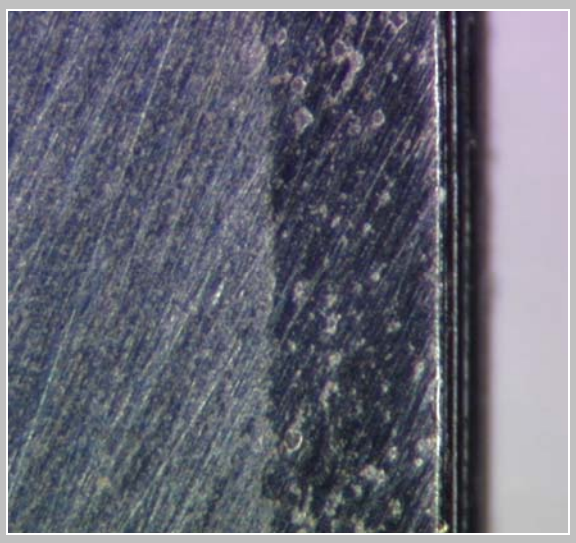

(d) Metallographic cross-section of wear-resistant DAR-type HVOF coating on hollow cylinder (shaft), at a magnification of 100×, showing bond of coating to the substrate.

Figure 26 – Photographs showing integrity of bond between steel substrate and HVOF DAR-type coating.

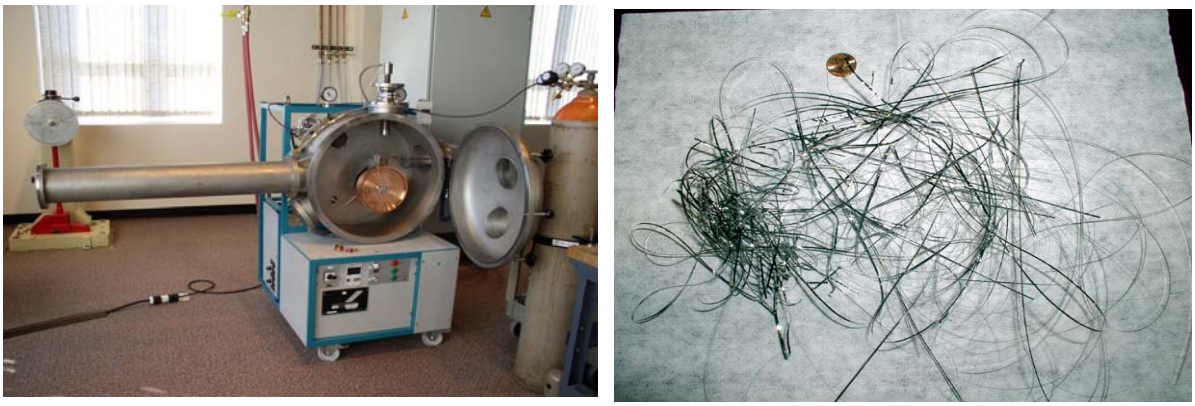

Figure 27 – There was some concern regarding the residual porosity in the DAR35, DAR40, and DAR40X3 HVOF coatings produced by the HPRCRM Team. Thus, a decision was made at the 2004 HPCRM Team Meeting held in Key West to produce samples of the amorphous metals having theoretical density and no residual crystallinity. Melt spinning was used to make such materials for testing and characterization, realizing that the performance of these materials would represent the limits of what can be achieved with a given elemental composition (formula).

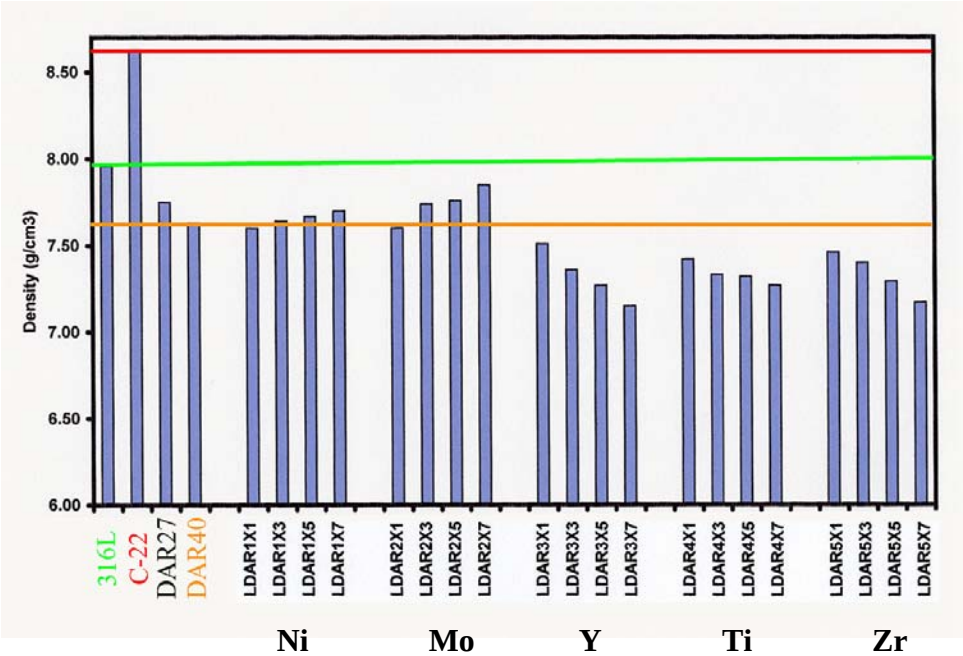

Figure 28 – The densities of the amorphous metals prepared with melt spinning were determined, and all were less dense than nickel-based N06022 (Alloy C-22), and therefore offer a weight advantage over such classical corrosion-resistant alloys.

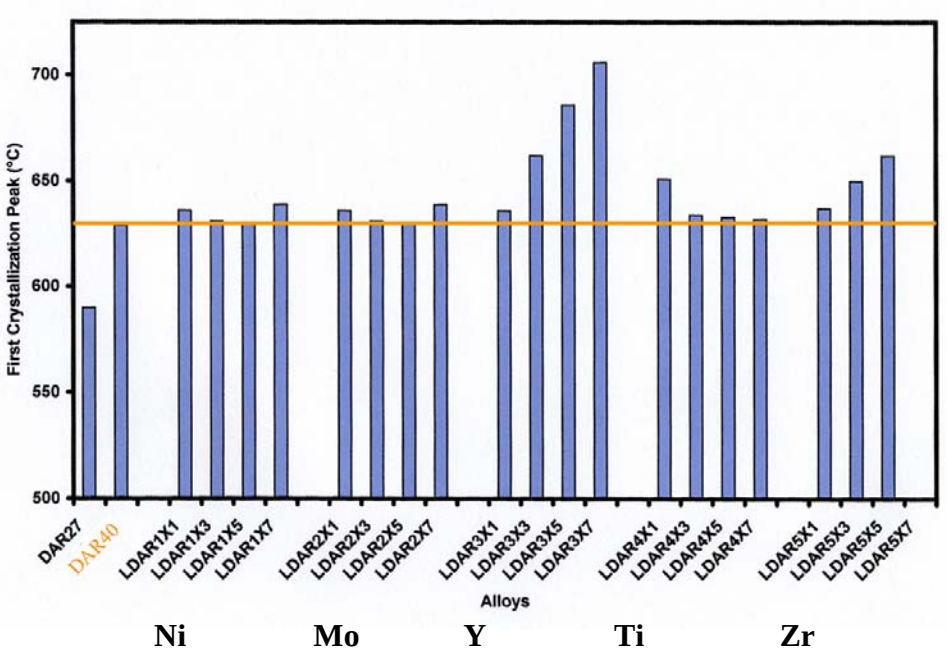

Figure 29 – The first recrystallization peak was determined for each of melt-spun ribbons with DTA, and were similar to that of the parent material (DAR40). The formula with the yttrium additions showed re-crystallization peaks at higher temperatures than achieved with other formulae, showing that yttrium additions do indeed promote thermal stability and glass formability. This data corroborates results from other DARPA SAM principal investigators at the University of Virginia.

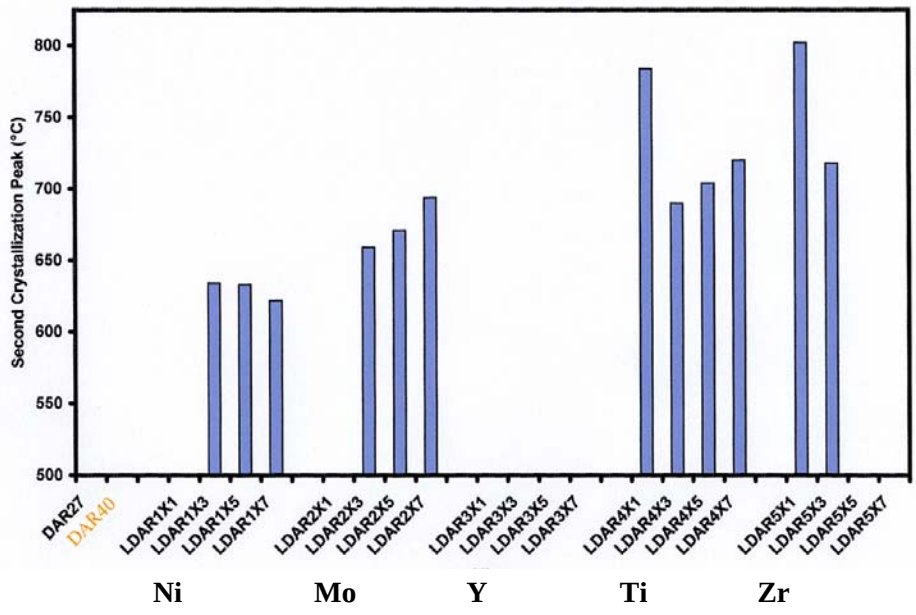

Figure 30 – Some formulae exhibited a second re-crystallization process at a higher temperature than the first, with titanium and zirconium based formulations showing these processes at the highest temperatures.

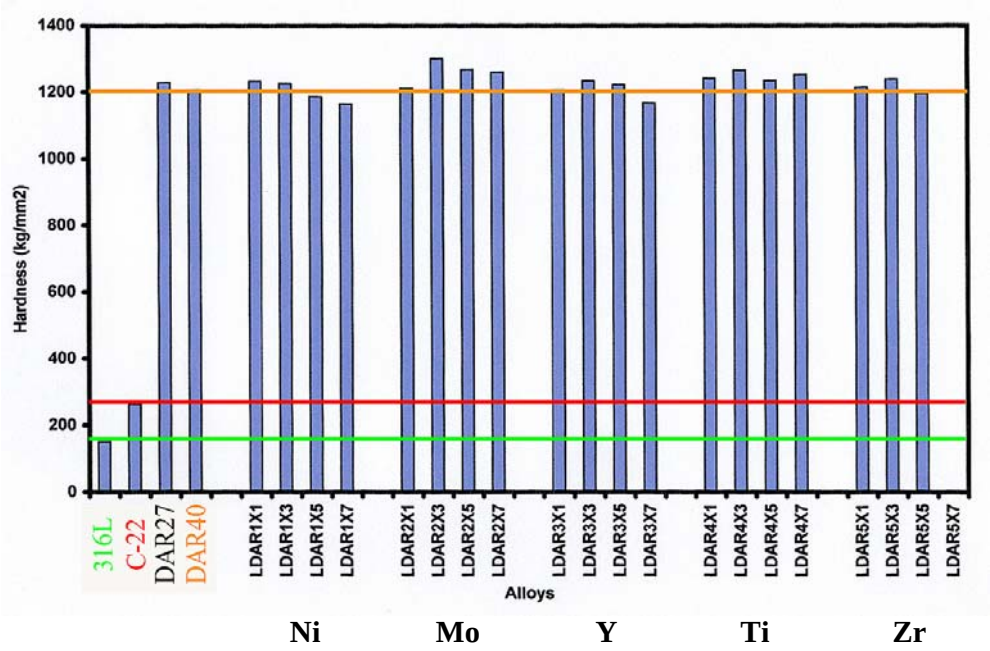

Figure 31 – All of the "as-cast" amorphous metal formulae produced by the HPCRM Team exhibited hardness far superior to many of the conventional materials of interest, such as Type 316L stainless steel, and nickel-based Alloy C-22 (N06022). Thus, coatings of these materials would also be expected to be less prone to erosion, wear and gouging than conventional engineering alloys.

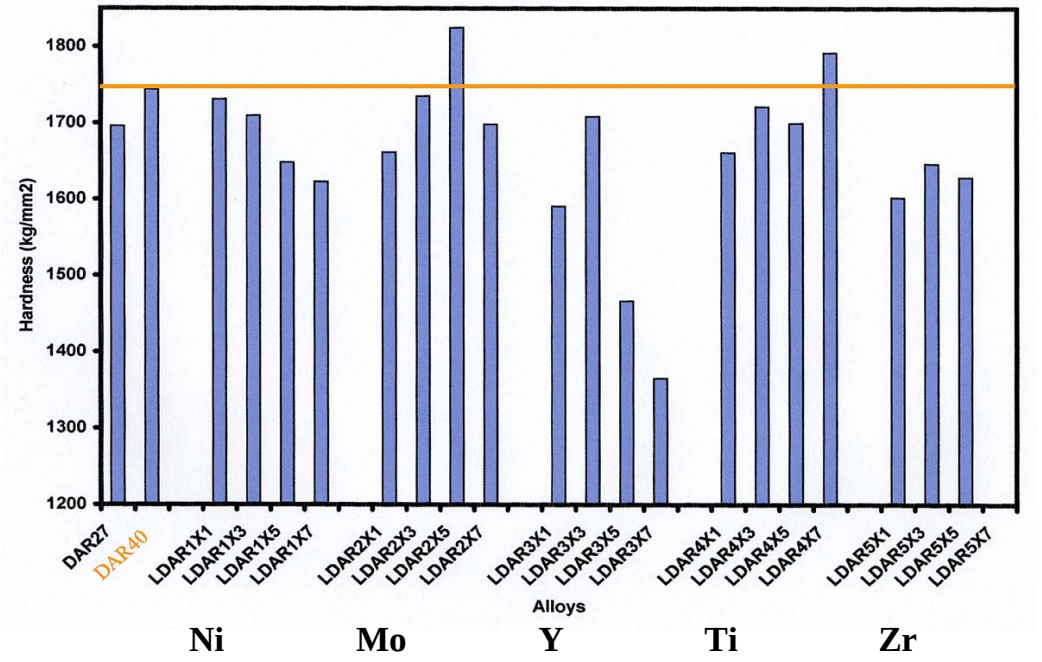

Figure 32 – Partially de-vitrified samples of the HPCRM materials exhibited dramatic increases in hardness. Thus, carefully controlled heat treatment of these materials can be used to achieve dramatic improvements in resistance to erosion, wear and penetration.

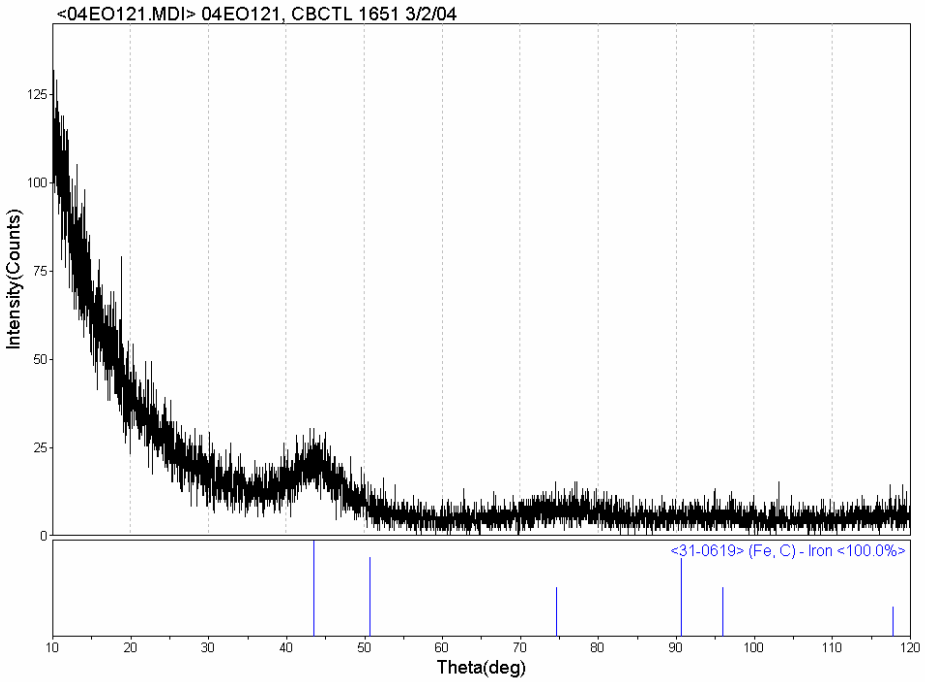

Figure 33 – X-ray diffraction pattern for drop-cast ingot of CBCTL1651, that shows virtually no crystalline structure. Peak broadening of all three HVOF coatings suggest presence of some fine crystalline phase(s) in the amorphous matrix.

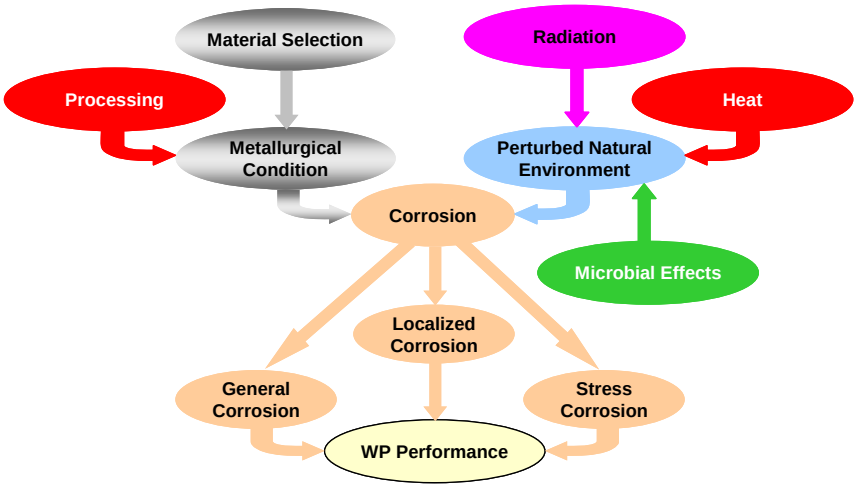

Figure 34 – A thorough understanding of the corrosion of these thermal-spray coatings must be developed before the materials can be used for the storage of spent nuclear fuel. Such understanding must account for the effects of processing on the metallurgical condition of the material, perturbation of the local service environment by heat (evaporative concentration), radiation, and microbes.

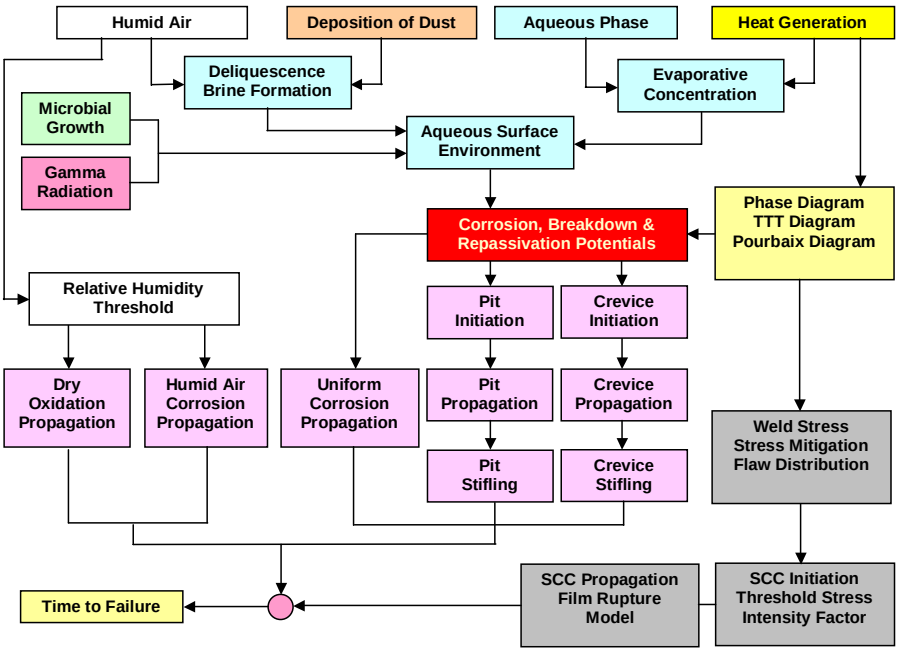

Figure 35 – An integrated predicted model must be developed to predict the long-term performance of materials as a function of time, temperature and local environment. Such a model must account for uniform corrosion, as well as the initiation, propagation and cessation of pitting and crevice corrosion. Thermal stability and environmental cracking are also important considerations. Thorough understanding of general and localized corrosion, as well as stress corrosion cracking, requires sound, scientifically based knowledge of passive film stability. Pourbaix diagrams, predicted with thermodynamic codes such as THERMOCALC, serve as a foundation stone in the stability of passive films.

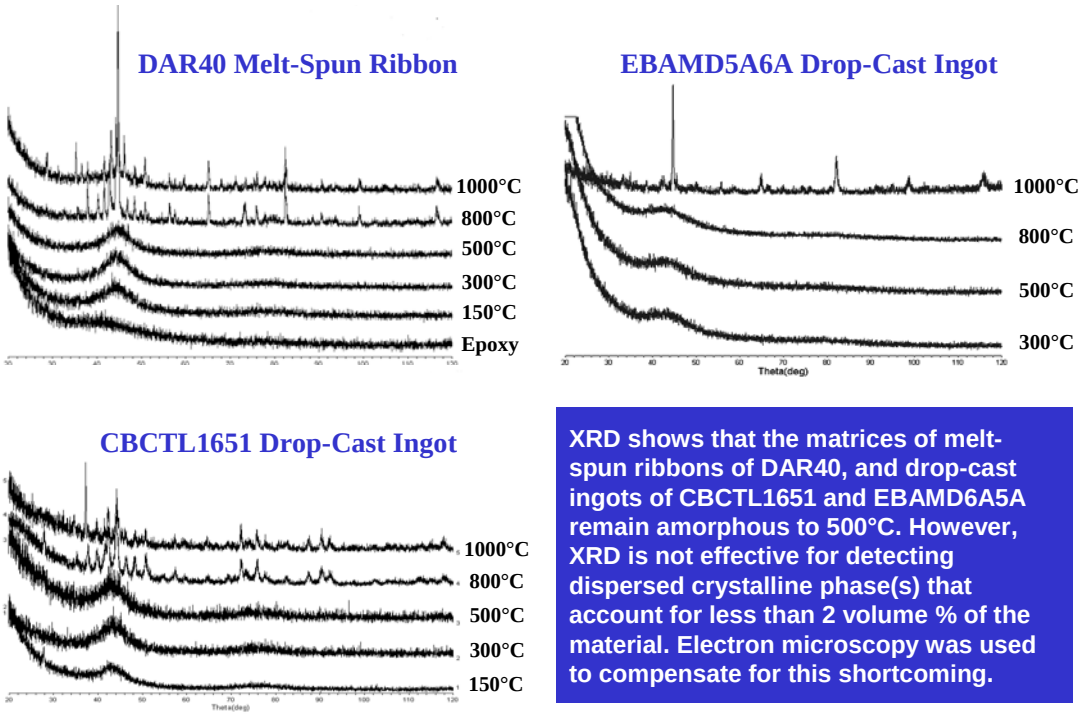

Figure 36 – X-ray diffraction (XRD) shows that the matrices of melt-spun ribbons of DAR40, and drop-cast ingots of CBCTL1651 and EBAMD6A5A remain amorphous to 500°C. However, XRD is not effective for detecting dispersed crystalline phase(s) that account for less than 2 volume % of the material. Electron microscopy was used to compensate for this shortcoming.

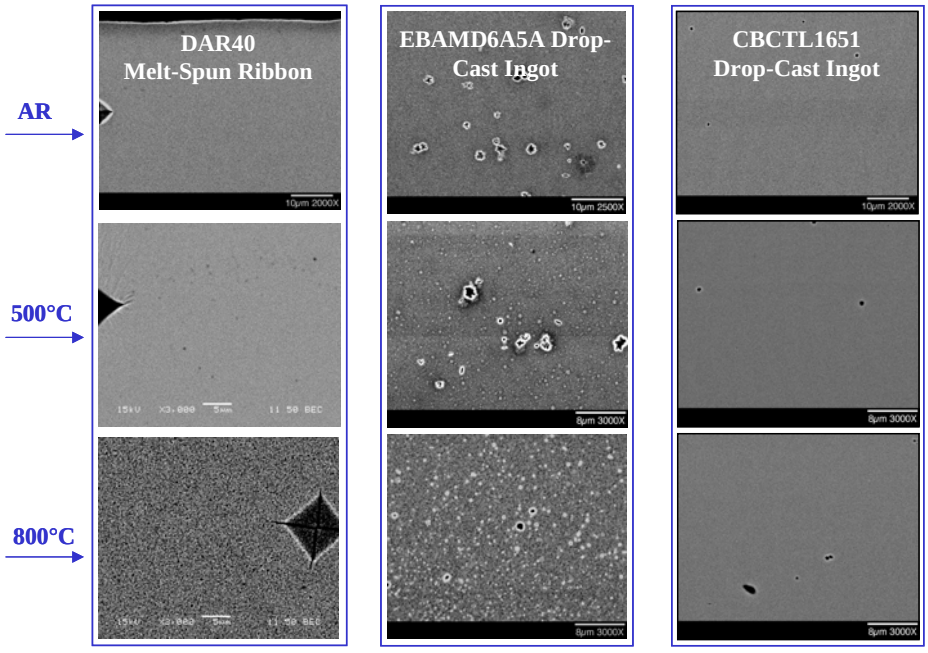

Figure 37 – Back-scattered electron (BEI) images of DAR40, CBCTL1651 and EBAMD5A6A show that the EBAM5A6A is less thermally sJCF-Table than either DAR40 or CBCTL1651.

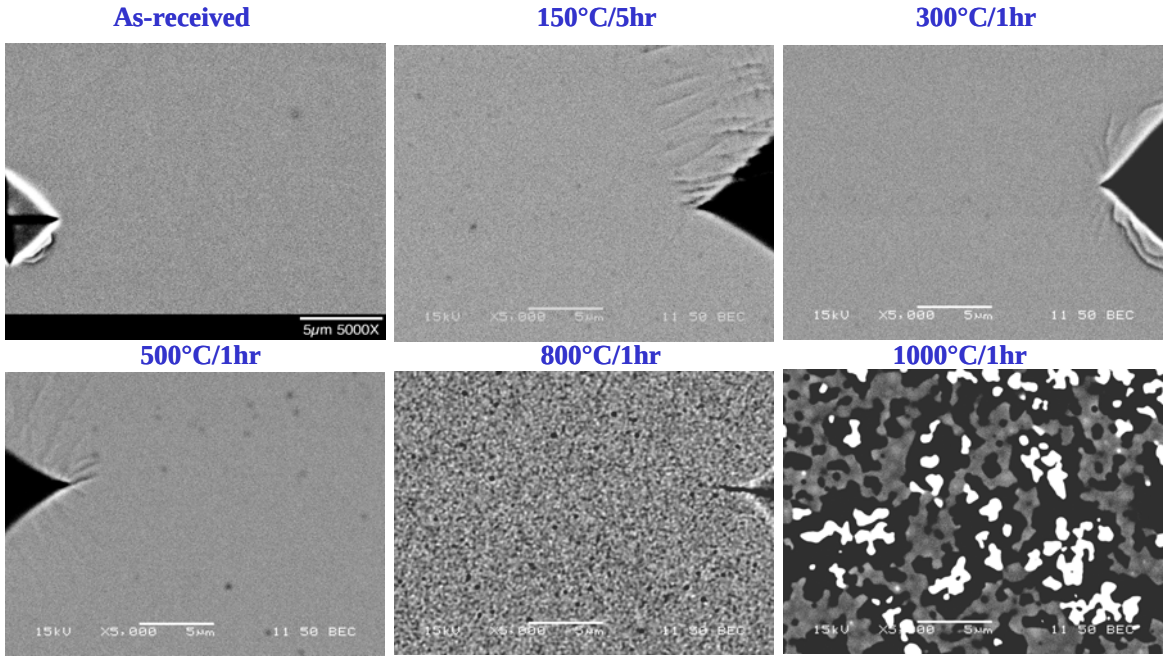

Figure 38 – Elemental mapping shows the formation of crystalline phases in melt-spun ribbons of DAR40 after a 1-hour exposure at 800 ℃. Substantial crystallization occurs after a 1-hour exposure at 1000 ℃.

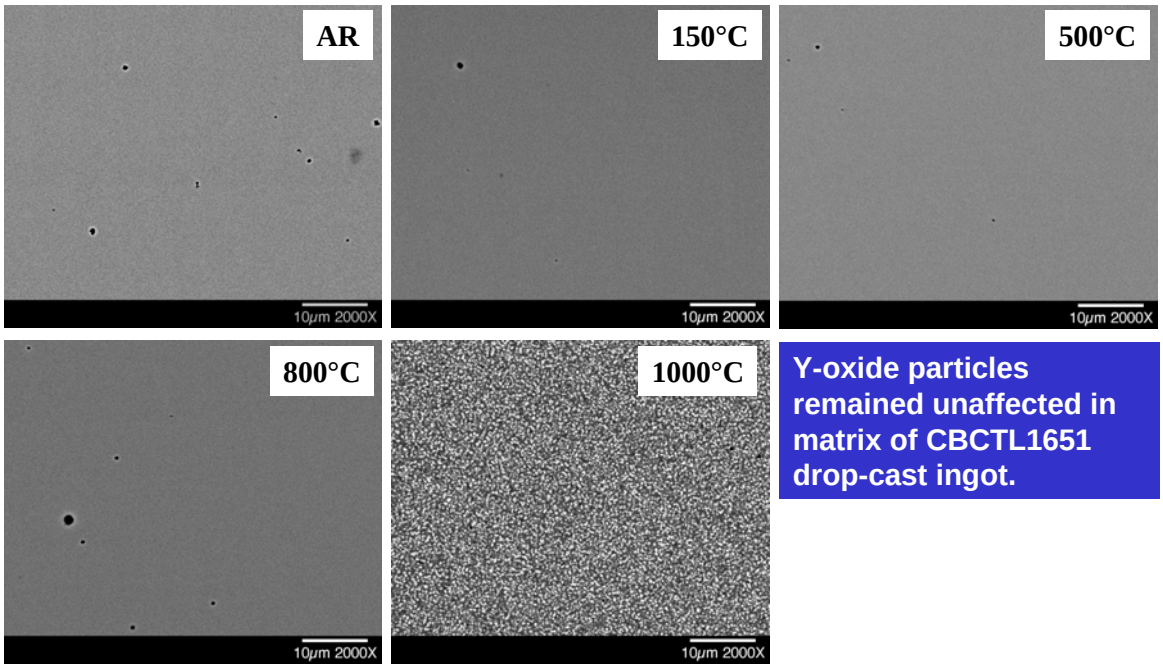

Figure 39 – Elemental mapping shows no formation of crystalline phases in arc-melted drop-cast ingots of CBCTL1651 after a 1-hour exposure at 800 ℃, but the onset of crystallization after a 1-hour exposure at 1000 ℃. Small yttrium oxide particles remained unaffected in the matrix.

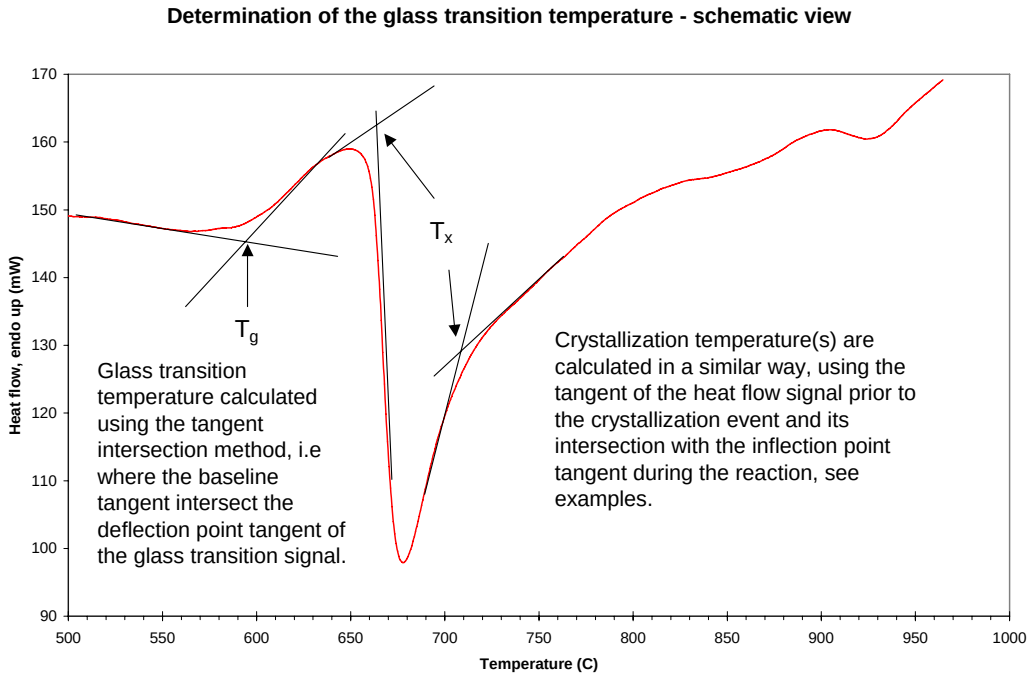

Figure 40 – Illustration of how onset temperatures are defined in thermal analysis (DTA, DSC). In the above case, the crystallization occurs in several steps, where each crystallization reaction can be identified with its onset temperature.

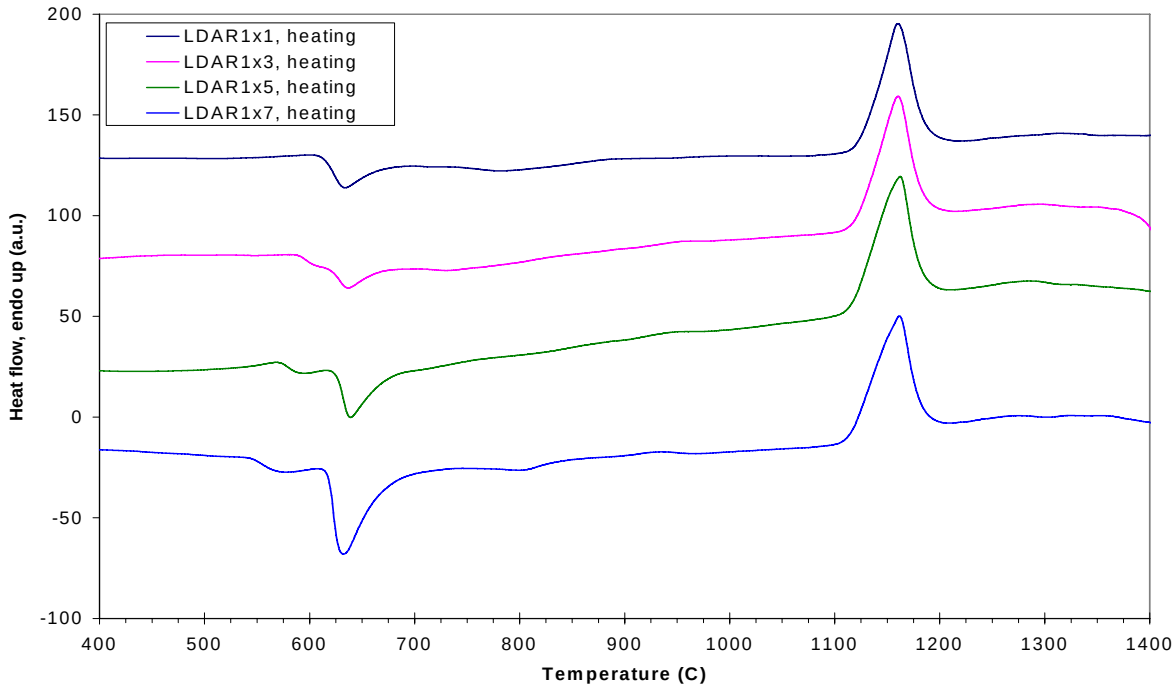

Figure 41 – Continuous heating of as-spun ribbons of LDAR1XY-alloys.

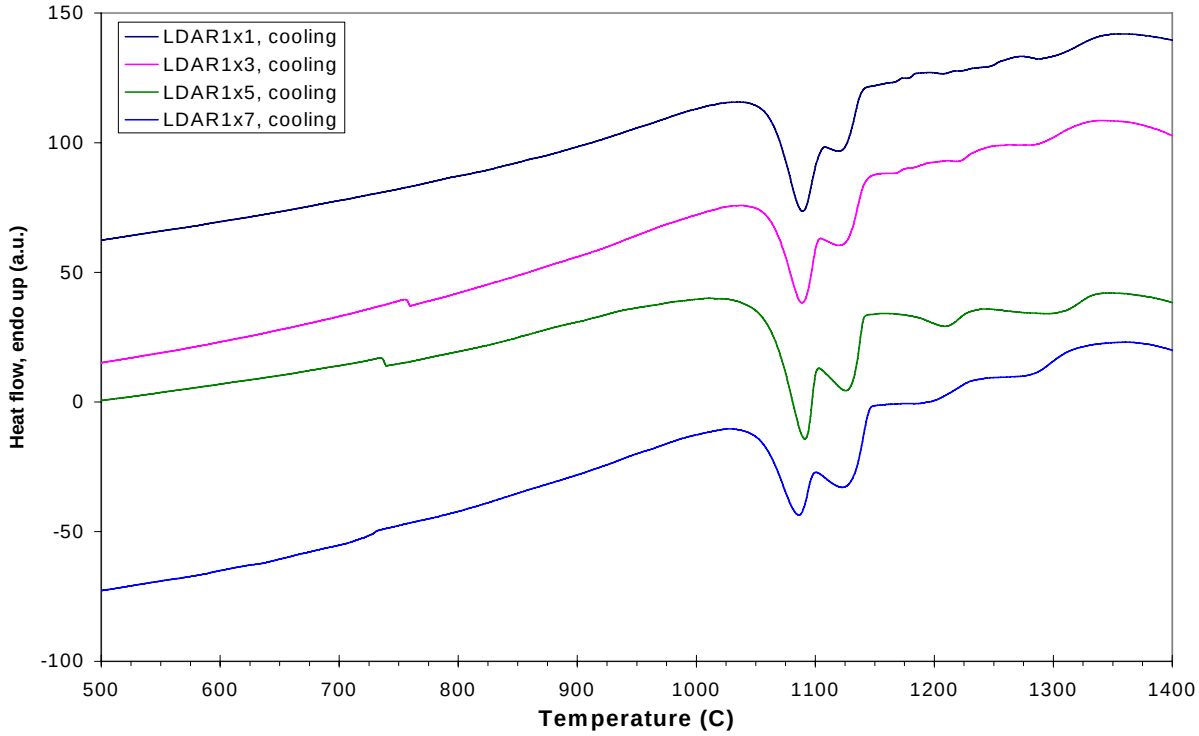

Figure 42 – Continuous cooling of LDAR1XY-alloys.

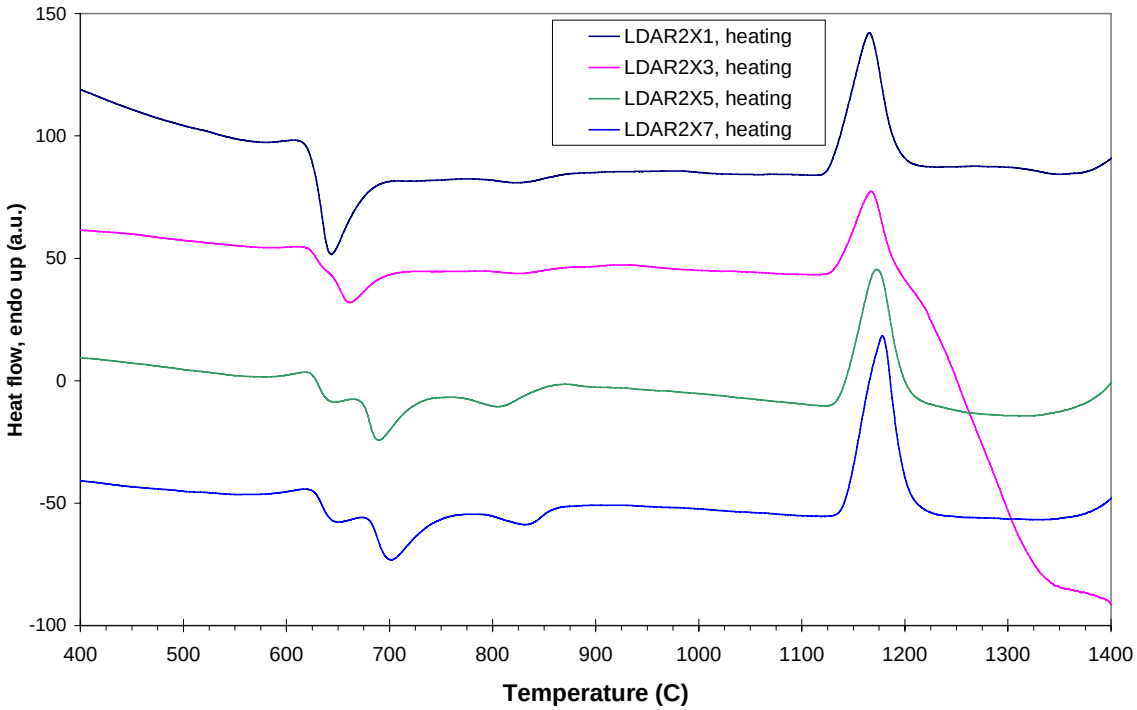

Figure 43 – Continuous heating of as-spun ribbons of LDAR2XY-alloys.

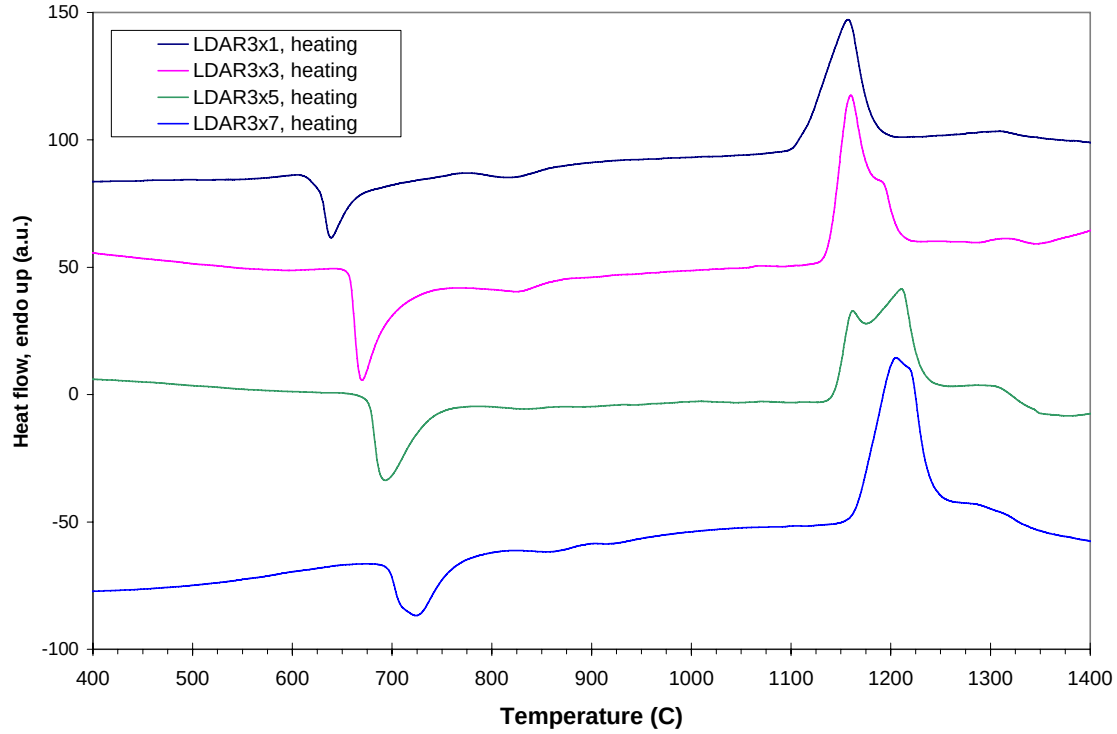

Figure 44 – Continuous heating of as-spun ribbons of LDAR3XY-alloys.

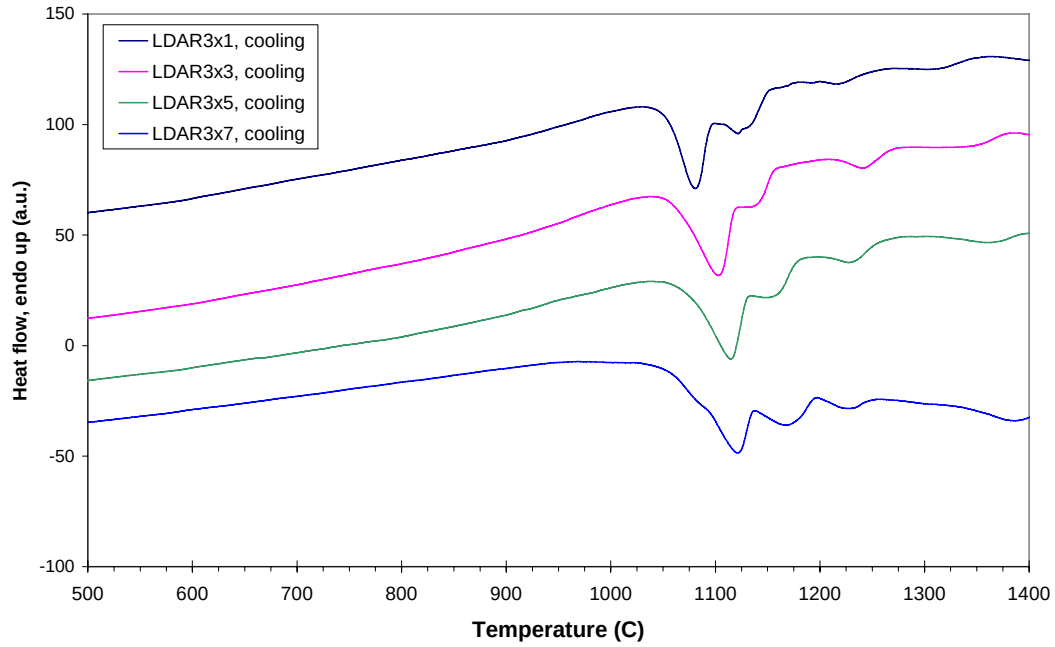

Figure 45 – Continuous cooling of LDAR3XY-alloys.

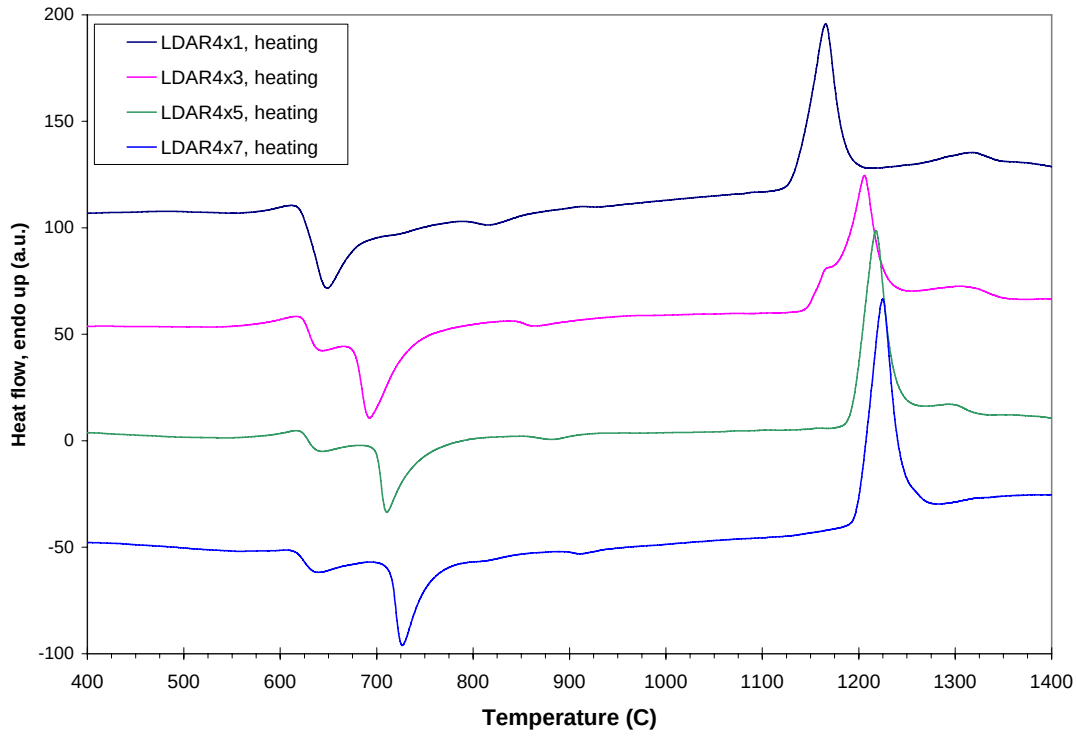

Figure 46 – Continuous heating of as-spun ribbons of LDAR4XY-alloys.

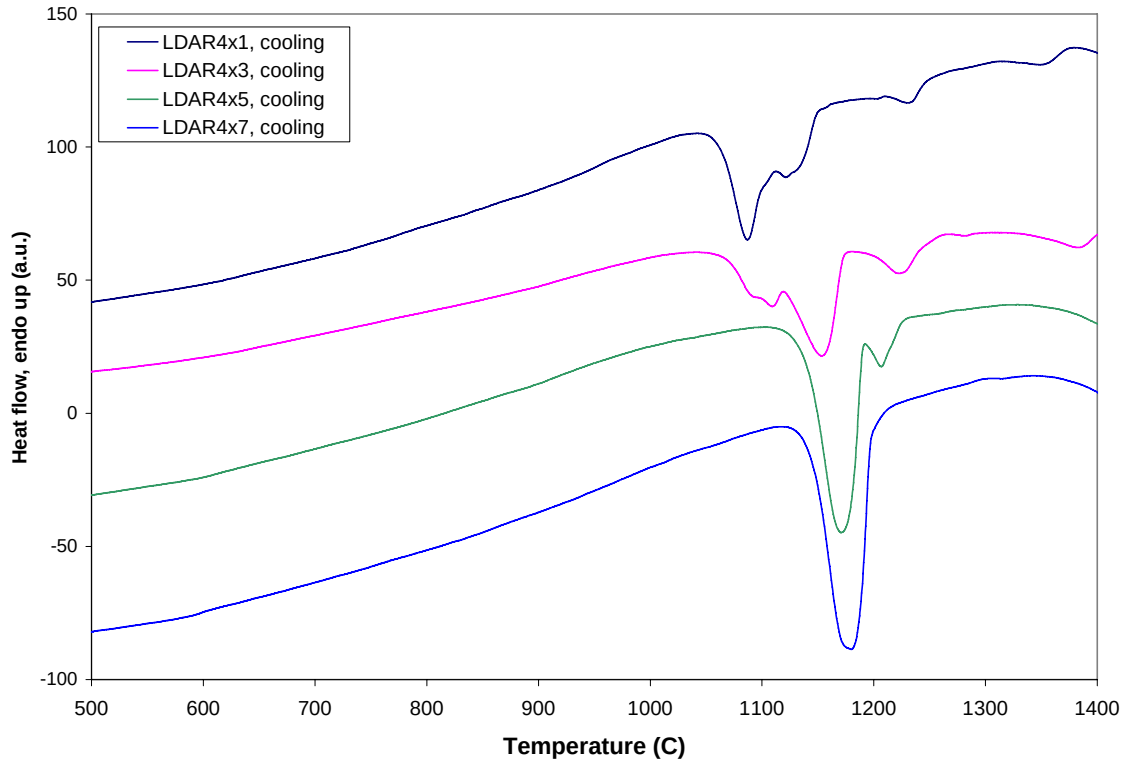

Figure 47 – Continuous cooling of LDAR4XY-alloys.

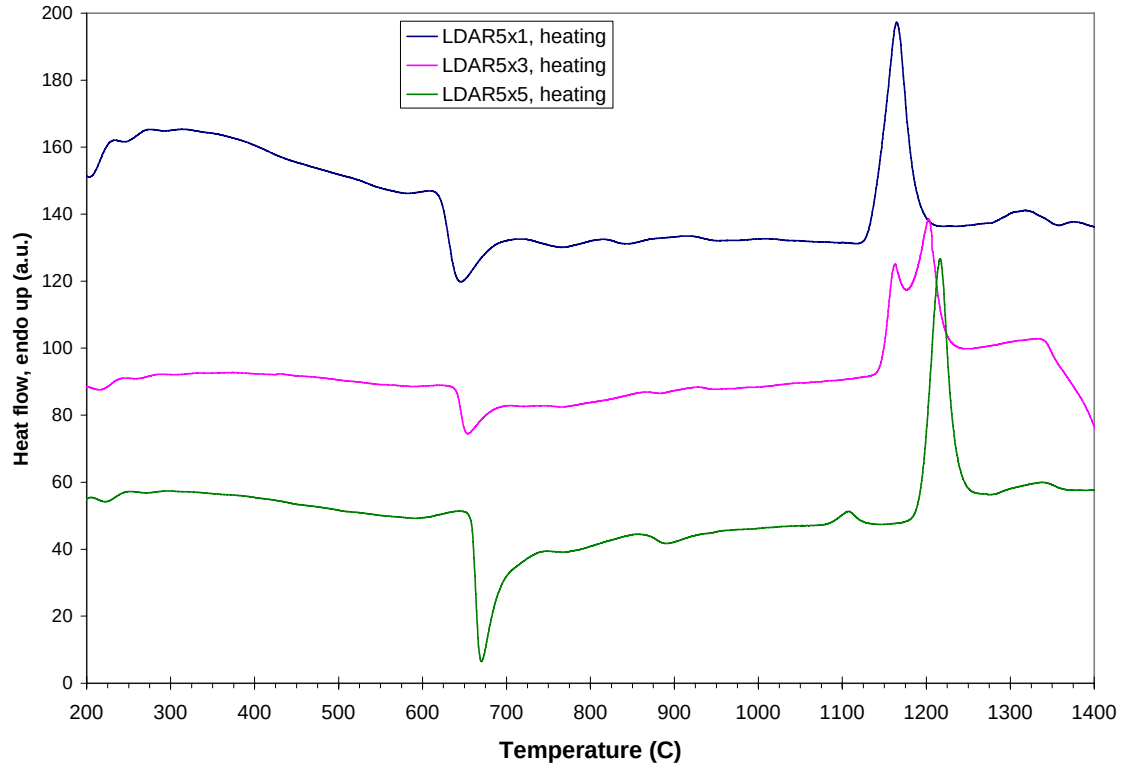

Figure 48 – Continuous heating of as-spun ribbons of LDAR5XY-alloys.

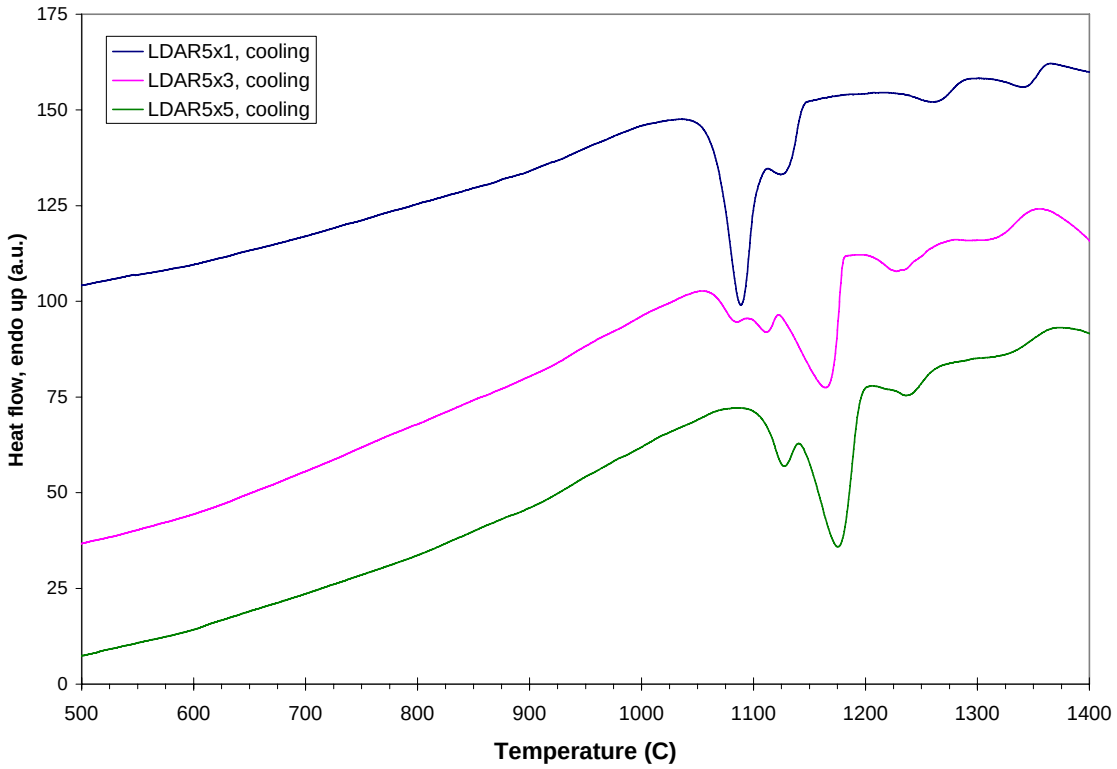

Figure 49 – Continuous cooling of LDAR5XY-alloys.

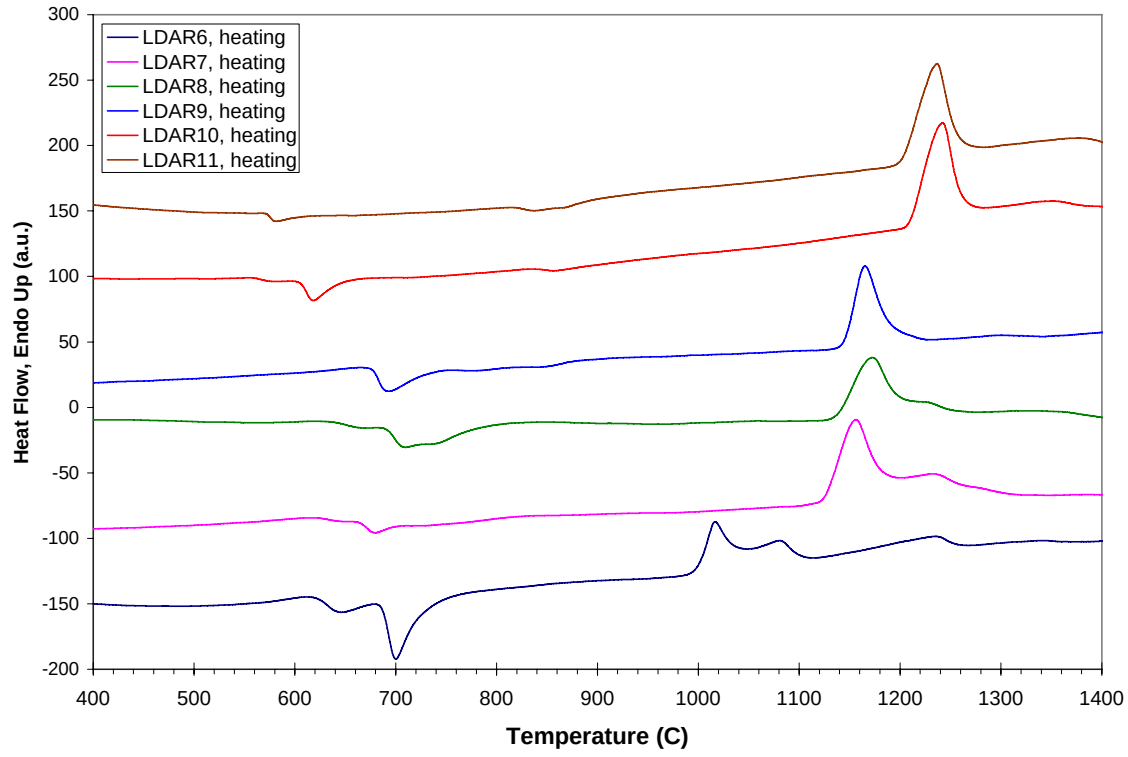

Figure 50 – Continuous heating of as-spun ribbons of LDAR6 through 11 alloys.

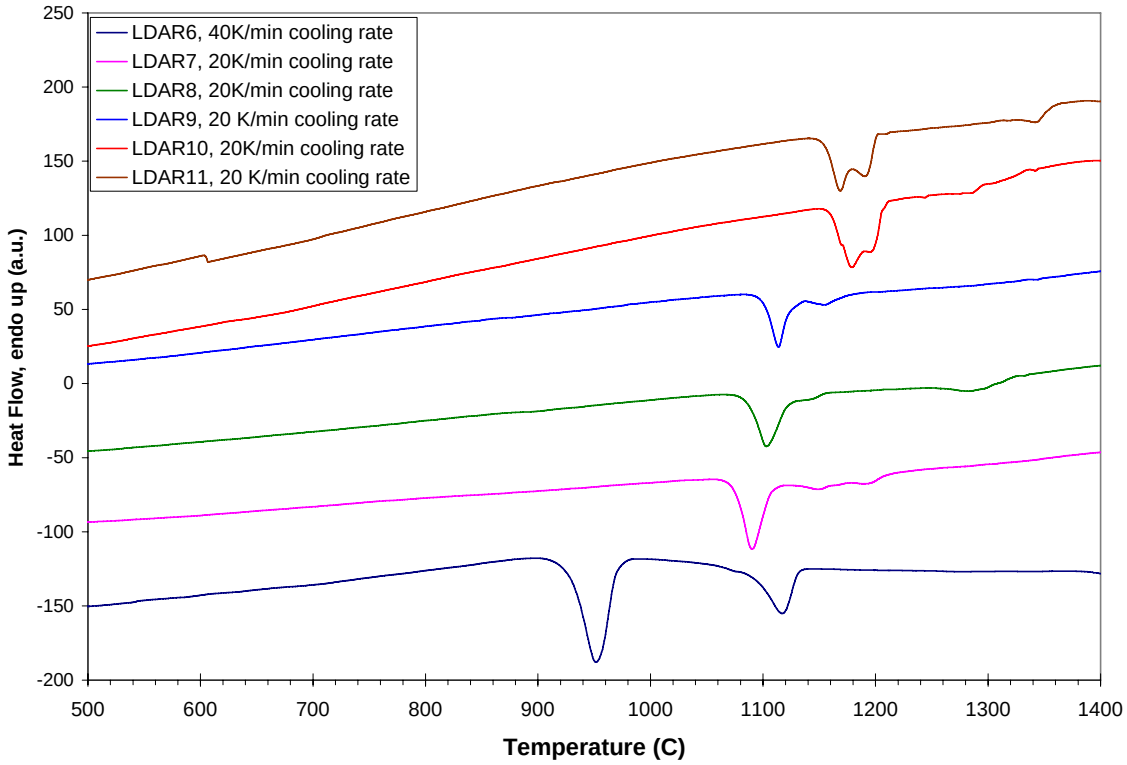

Figure 51 – Continuous cooling curves for LDAR6 through LDAR1 alloys corresponding to heating traces shown in Figure 50.

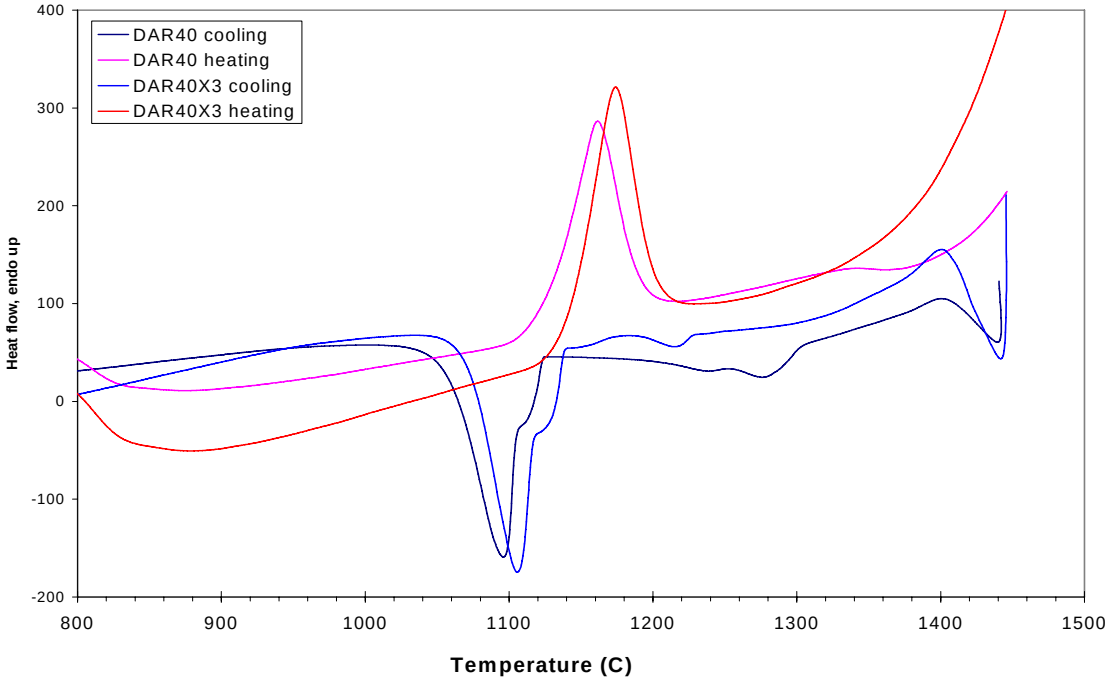

Figure 52 – Differential thermal analysis (DTA) heating/cooling curves for bulk samples of DAR40 and DAR40X3. If the Figure is not printed in colors, the DAR40X3 curve is the one with the highest endothermic peak on heating and the lowest exothermic peak on cooling.

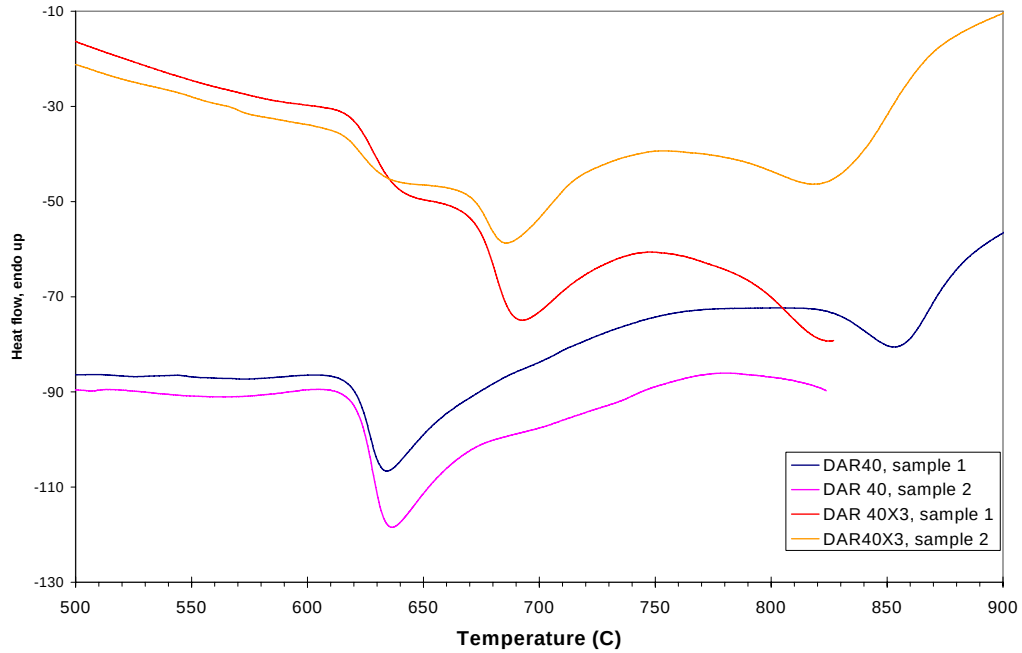

Figure 53 – Differential thermal analysis (DTA) heating trace for alloys DAR40 and DAR40X3 being heated through glass transition and crystallization of the amorphous phase (melt-spun ribbons). Two samples of each alloy were heated to check consistency of ribbons. If the Figure is not printed in color, the two lower curves are DAR40 (DAR40), while the two upper curves are DAR40X3 (DAR40X3).

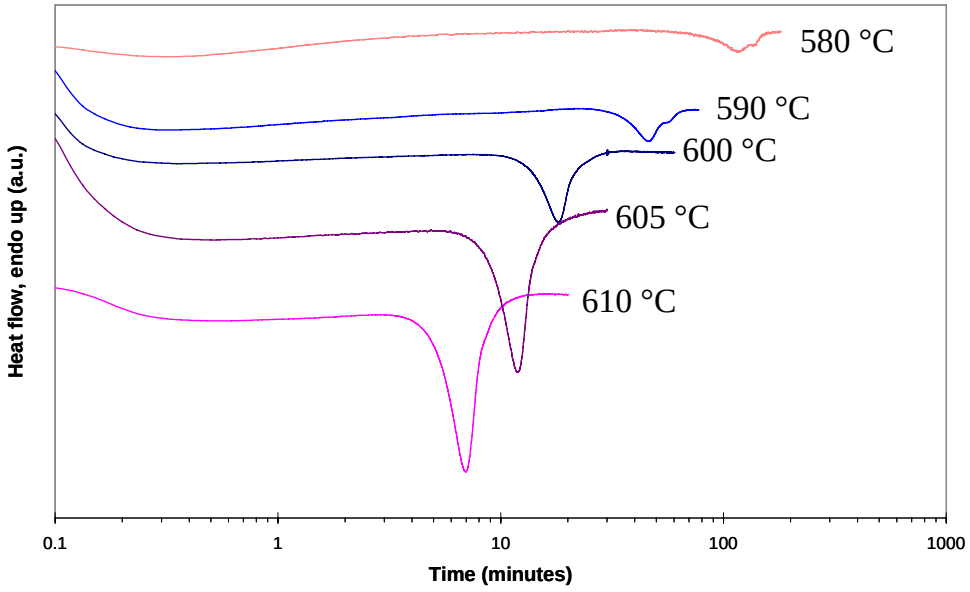

Figure 54 – Differential scanning calorimetry (DSC) isothermal anneal of as-spun ribbons of DAR35. Due to use of a log-scale, the exothermic peaks appear to be smaller for lower annealing temperatures, but the integral of the curve is the same for all of the peaks.

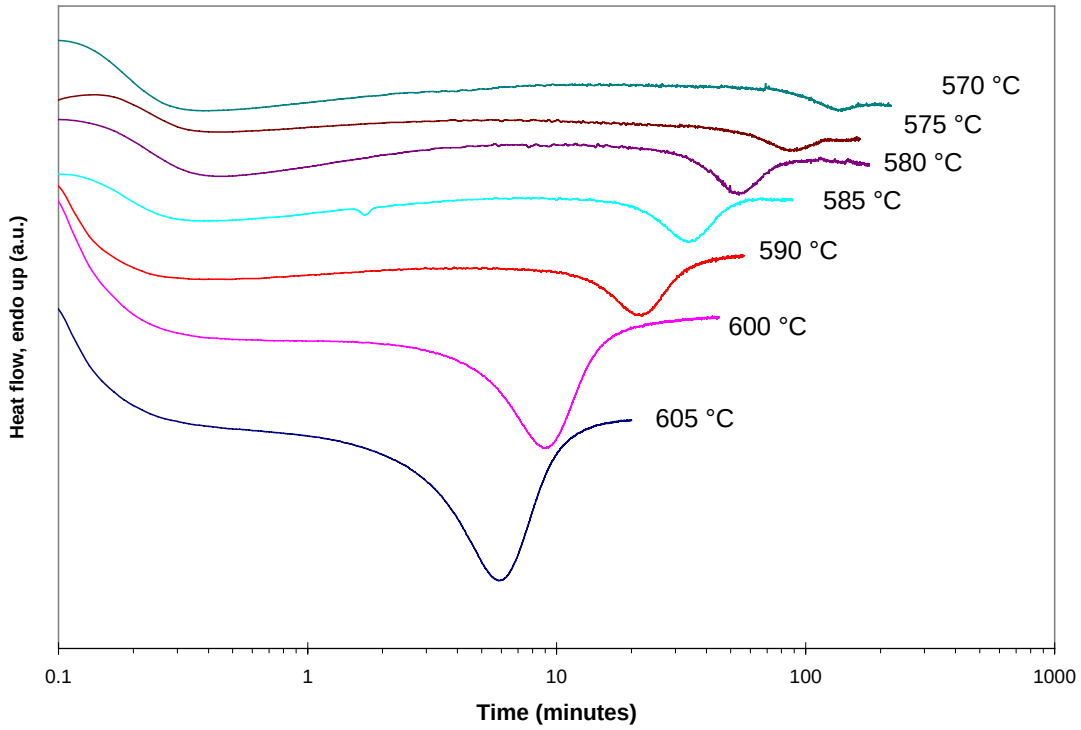

Figure 55 – DSC isothermal anneal of as-spun ribbons of DAR40.

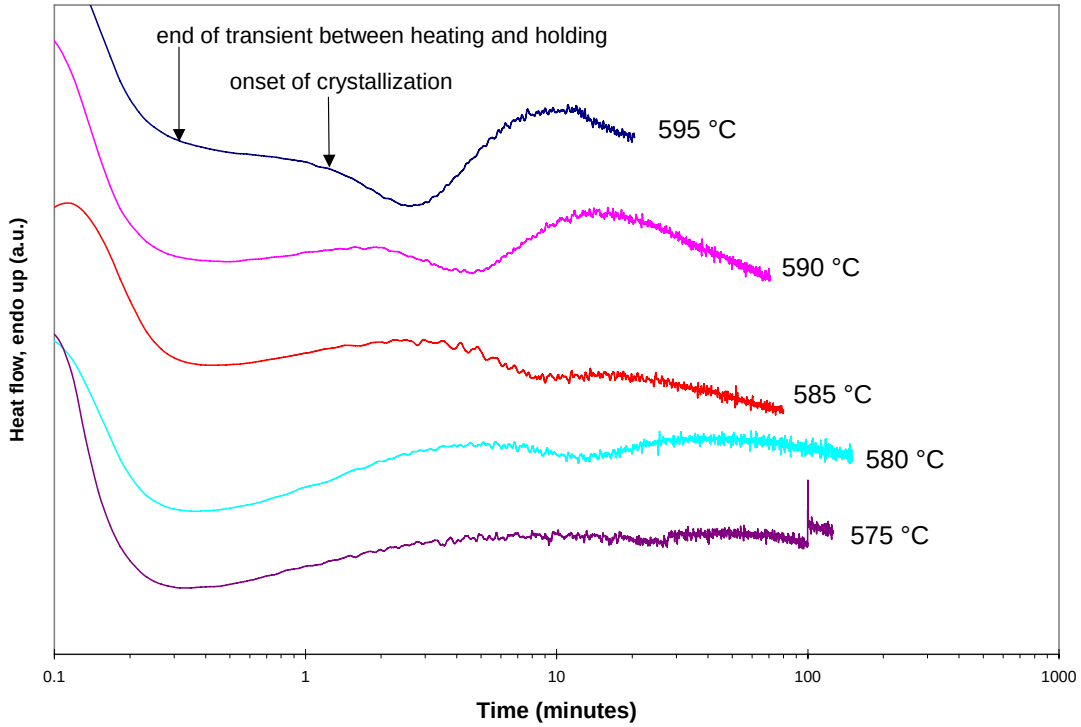

Figure 56 – Heat flow trace during isothermal holding of as-spun ribbons of DAR40X3.

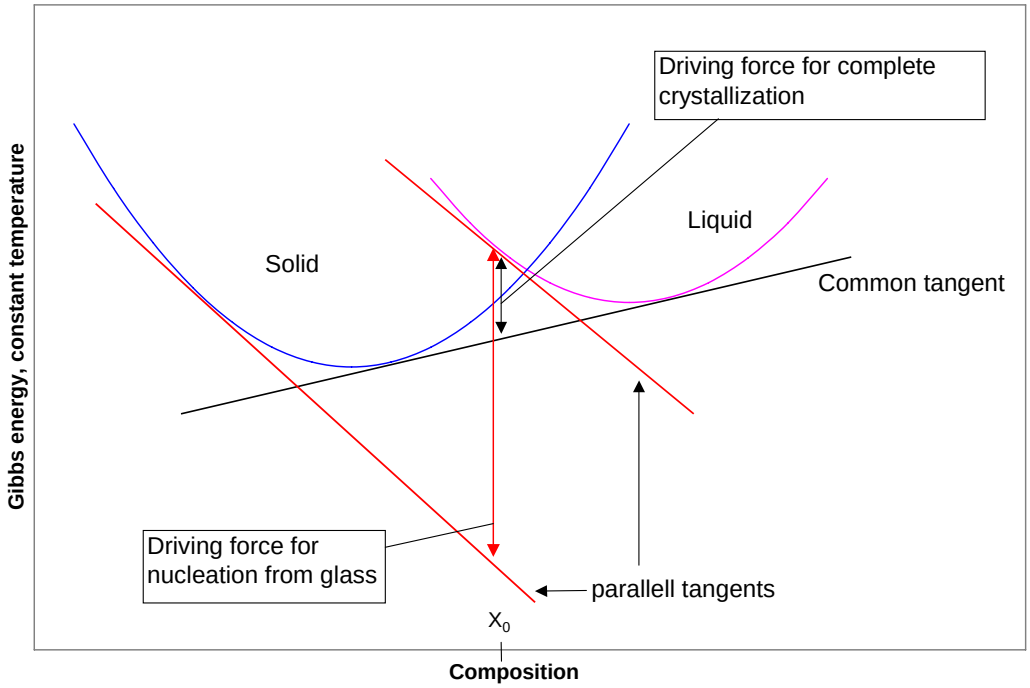

Figure 57 – Schematic view of the Gibbs free energy difference between the amorphous phase and the primary crystalline phase.

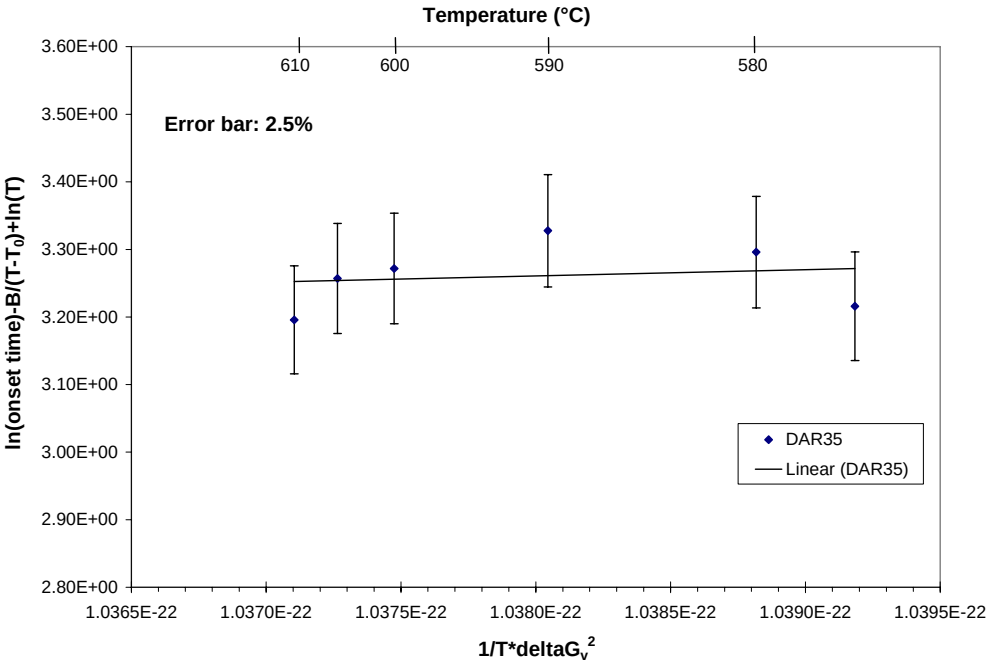

Figure 58 – Plot of equation (9) for DAR35, annealed ribbons.

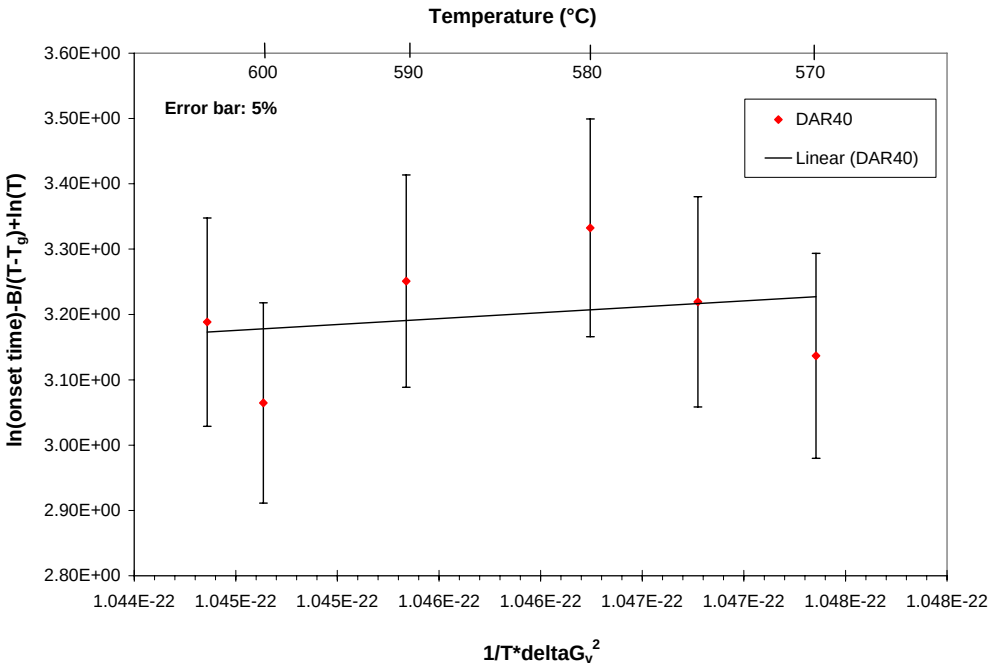

Figure 59 – Plot of equation (9) for DAR40, annealed ribbons.

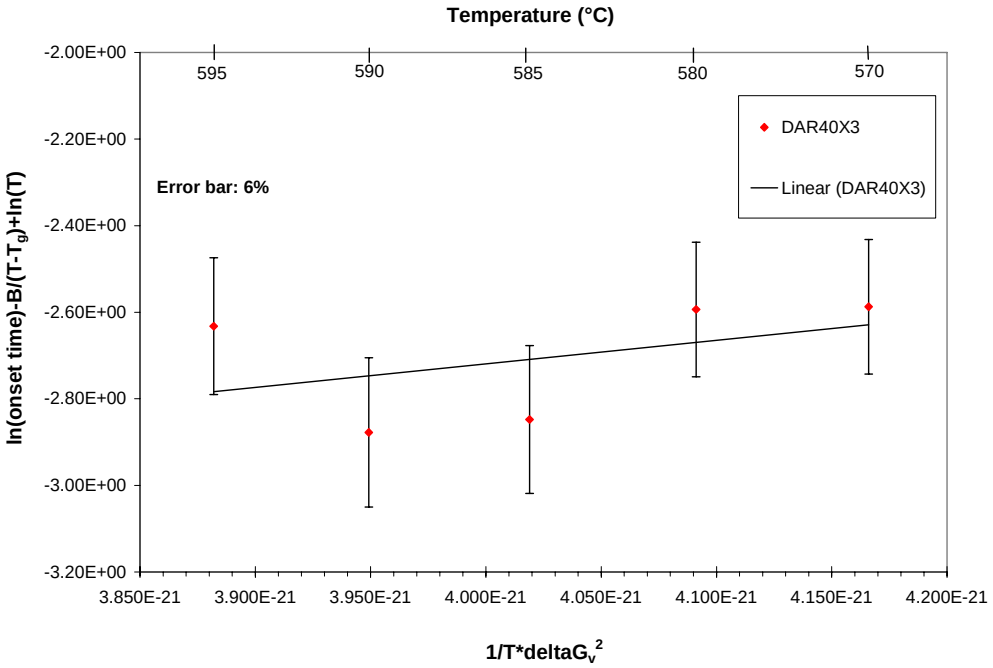

Figure 60 – Plot of equation (9) for DAR40X3, annealed ribbons.

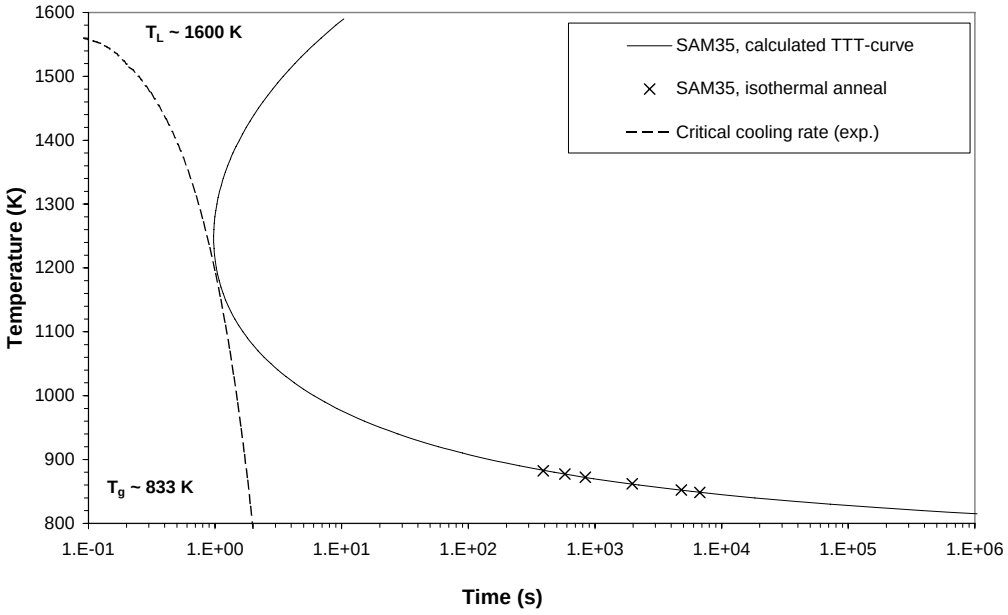

Figure 61 – Calculated Time-Temperature-Transformation (TTT) curve for DAR35 (SAM) fitted to measured critical cooling rate and crystallization onset times as measured with isothermal annealing experiments.

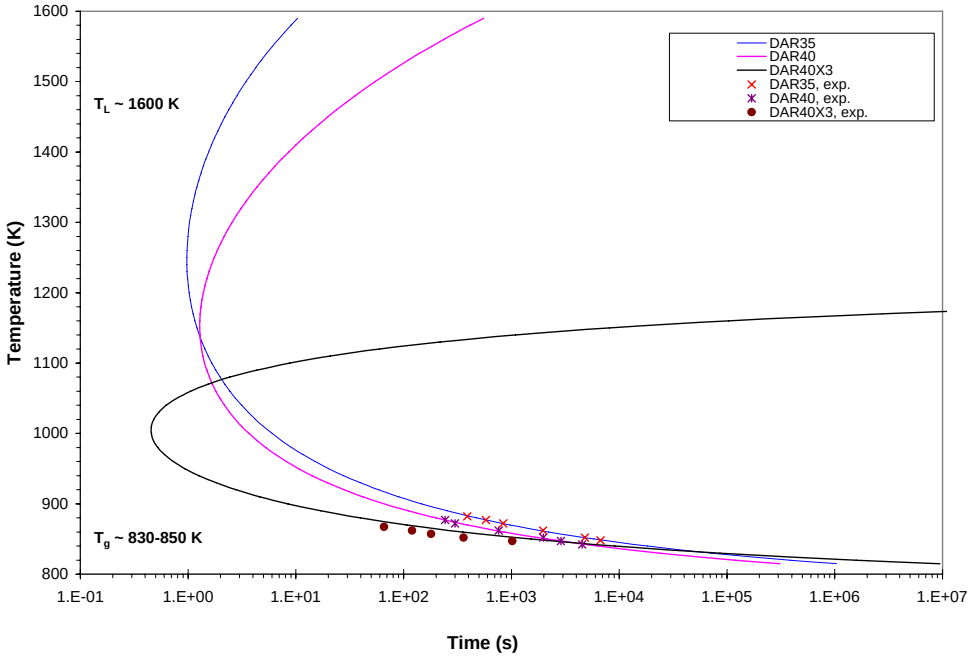

Figure 62 – Calculated Time-Temperature-Transformation (TTT) curves for DAR35, DAR40 and DAR40X3 including experimentally obtained onset times for nucleation.

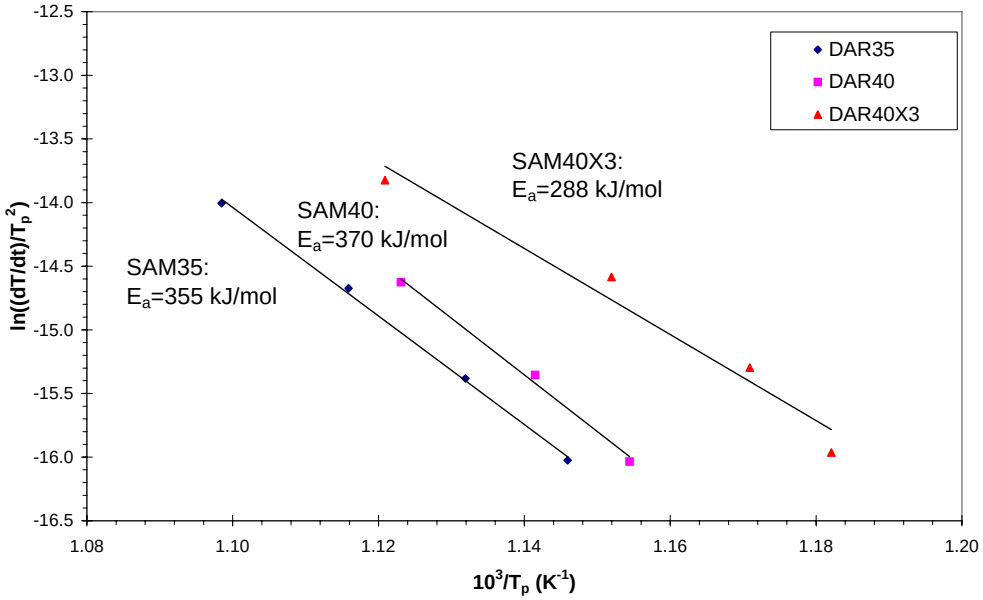

Figure 63 – Kissinger plot for the activation energy for crystallization (peak temperatures) for alloys DAR35, DAR40 and DAR40X3 (SAM35, SAM40, and SAM40X3).

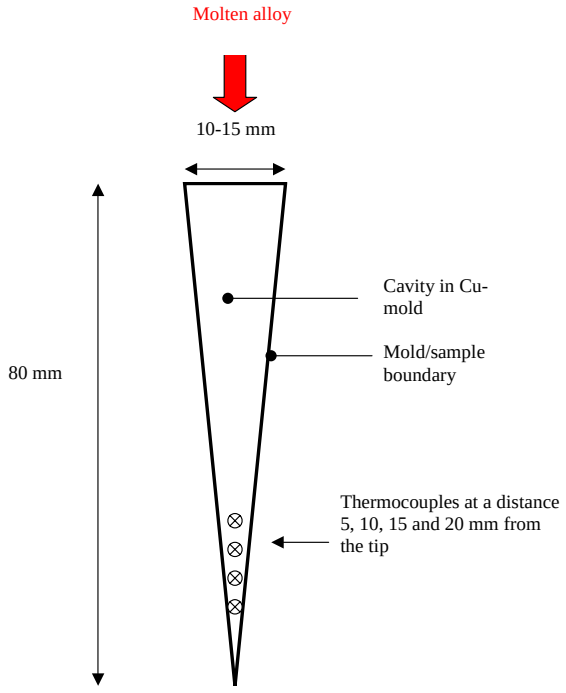

Figure 64 – Schematic view of the wedge-shaped cavity in the casting mold indicating the location of the thermocouples normally used. If glass-forming ability of material is very good, a thermocouple can also be applied at a vertical distance of 40 mm from the tip using the existent setup. The Accufiber sensor (not shown) is directed to observe the melt 27 mm from the tip.

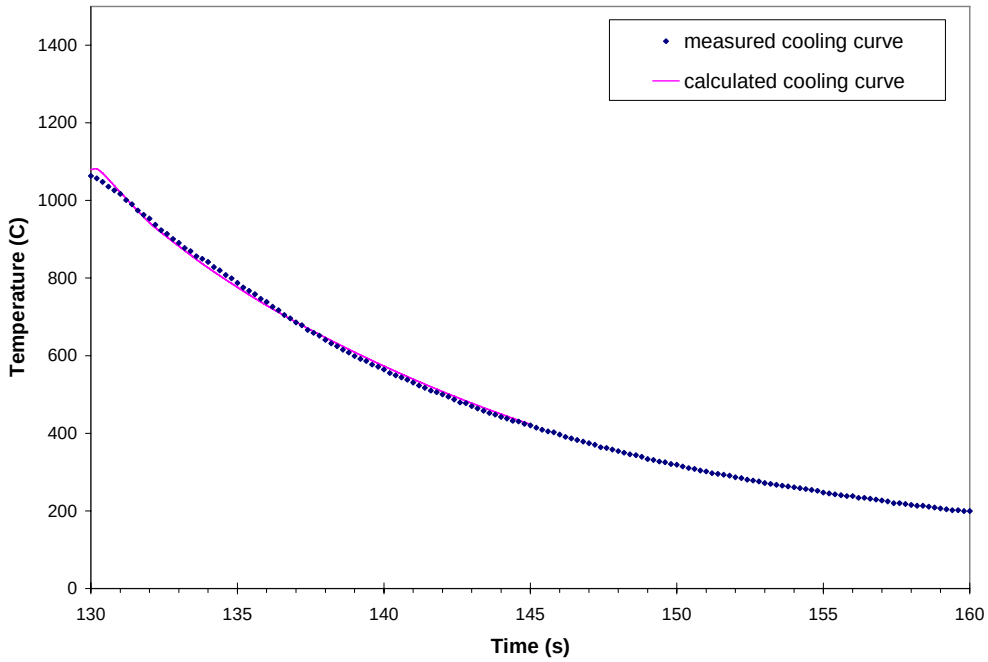

Figure 65 – Measured and calculated cooling curves for DAR35 cast into the wedge shaped mold for a position 20 mm from the tip of the wedge along the center symmetry line.

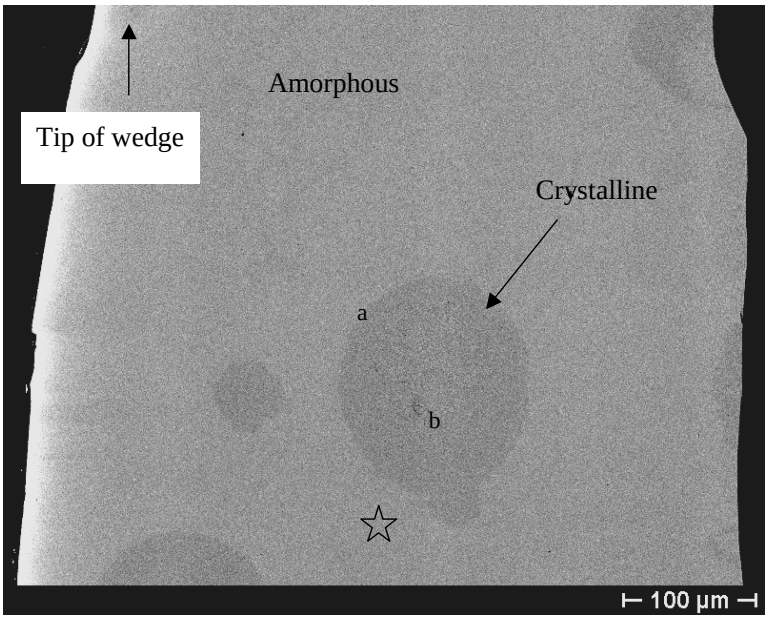

Figure 66 – Back-scattered electron image (BSEI) of wedge cast DAR35. Higher magnifications of regions a and b are shown in Figure 67.

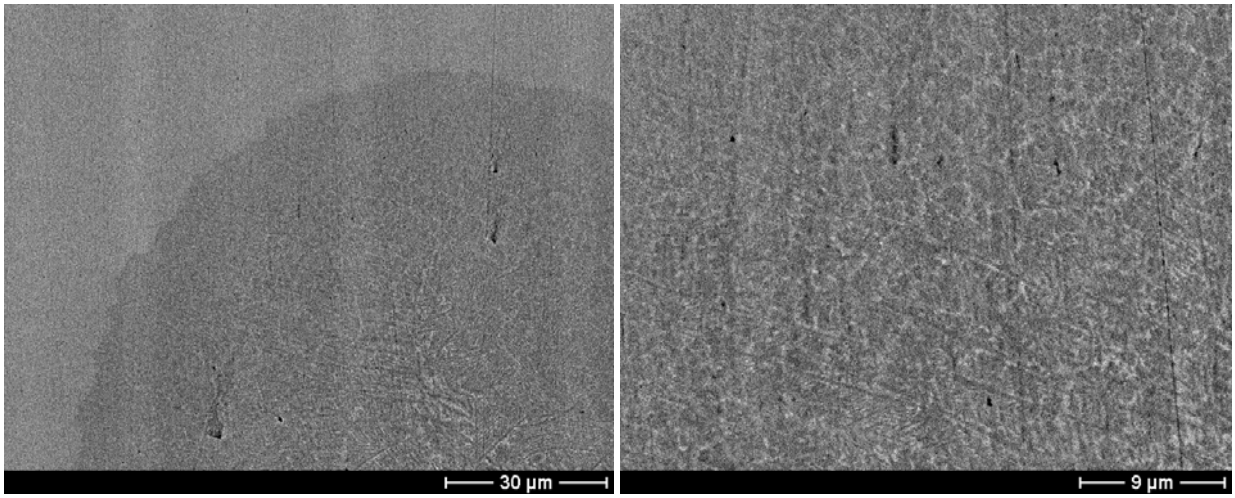

Figure 67 – Magnified regions a and b of Figure 66 shown left and right, respectively. The left image pictures the boundary between the glassy matrix and spherical crystalline area, and the right image shows details from the center of the crystallized area

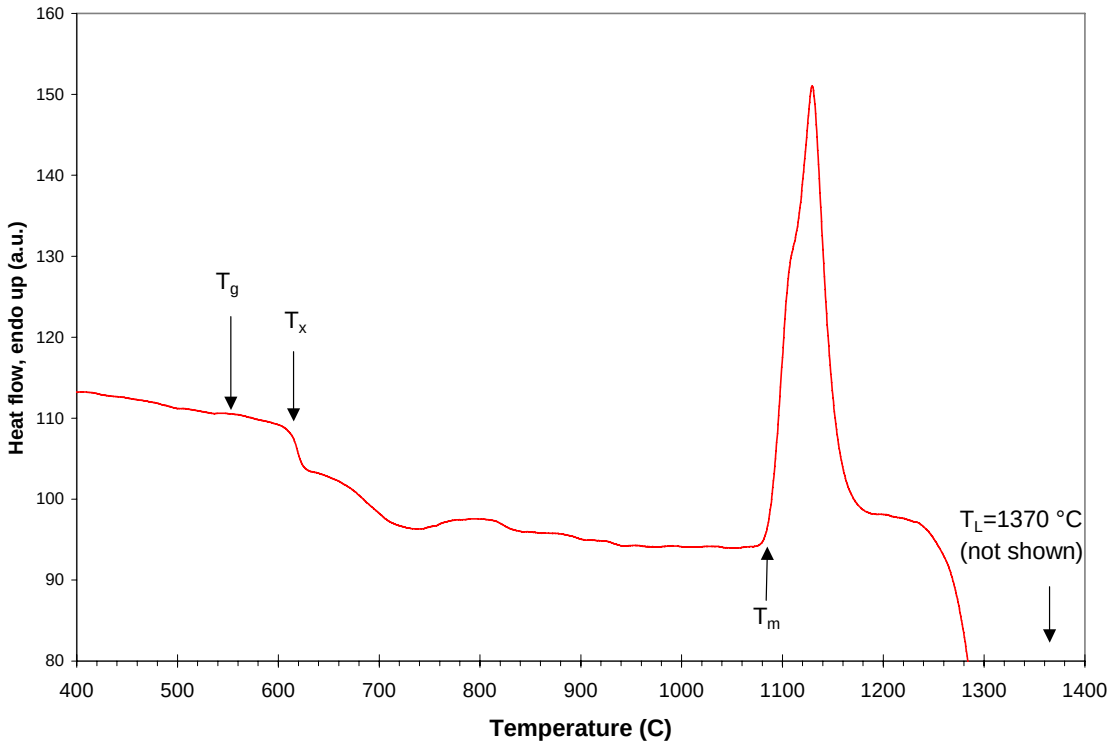

Figure 68 – Differential thermal analysis (DTA) heating trace of the tip of the wedge. Glass transition and recrystallization on heating confirms the presence of an amorphous phase.

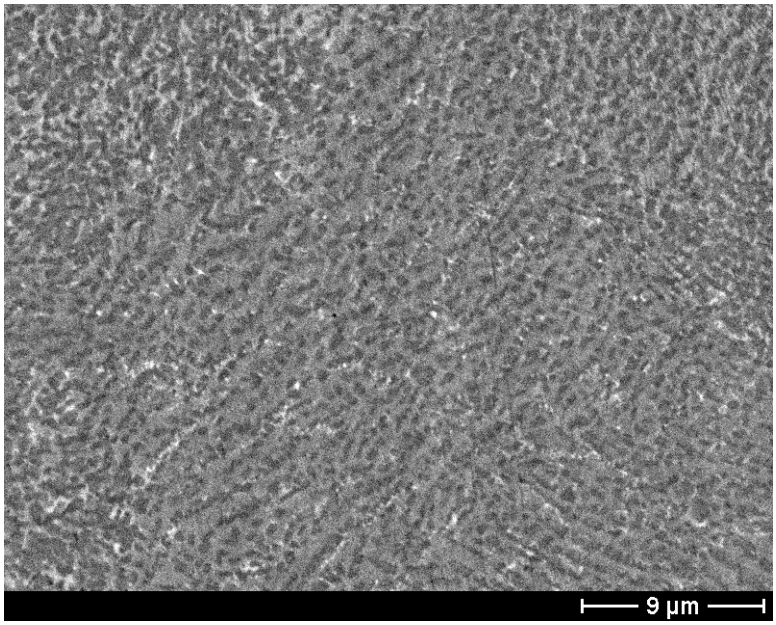

Figure 69 – Wedge cast sample, DAR35, cooling rate approximately 350 K/s.

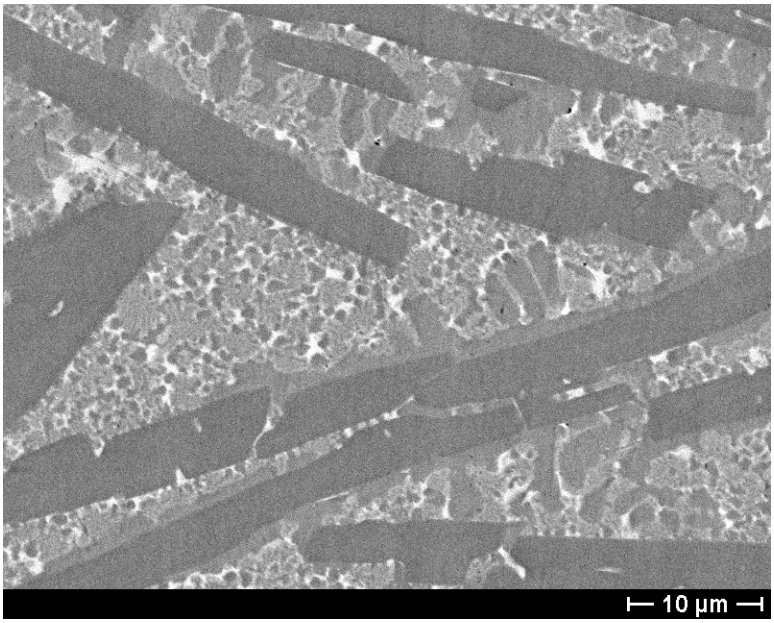

Figure 70 – Wedge cast DAR35, cooling rate approximately 40 K/s.

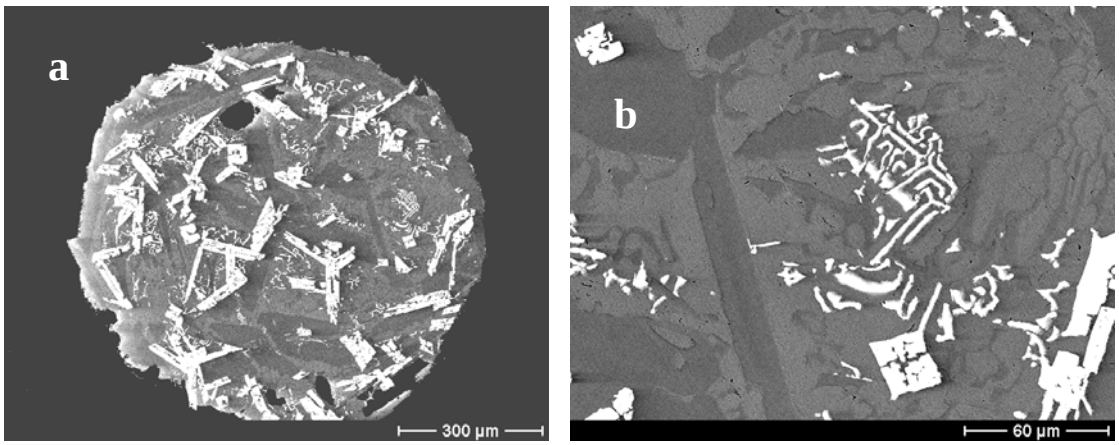

Figure 71 – Microstructure of a DTA-melted sample, heating/cooling rate 40 K/min.

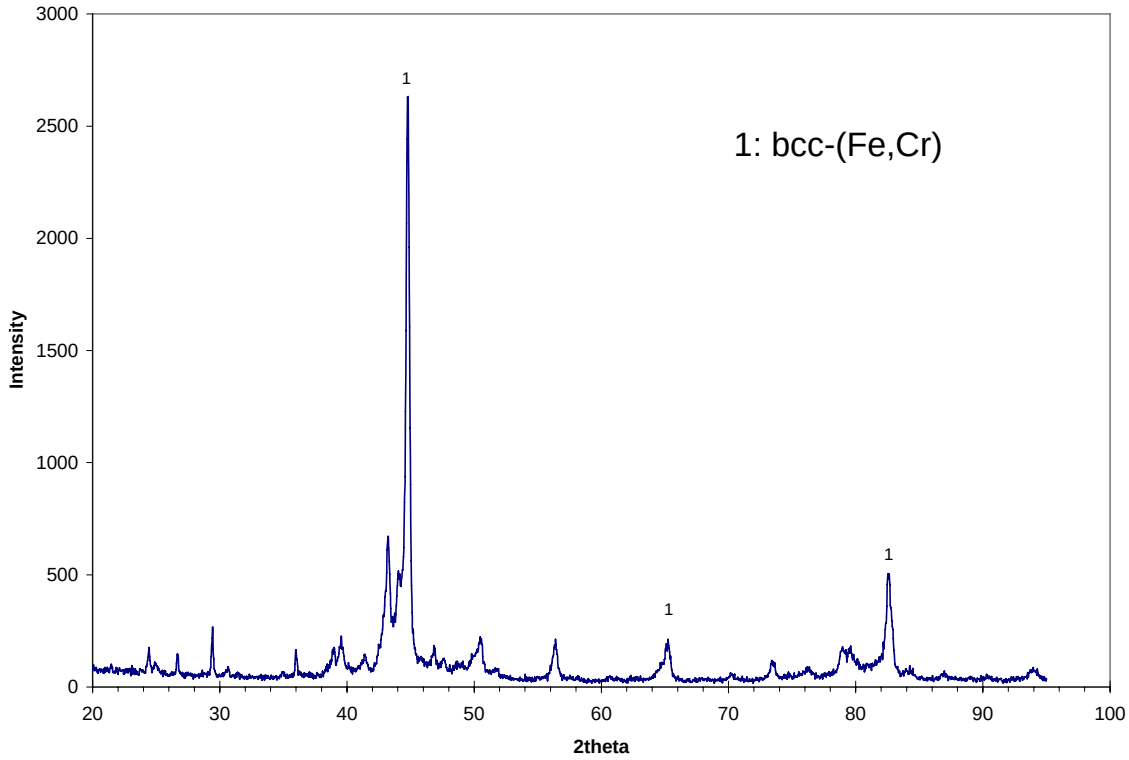

Figure 72 – X-ray diffraction (XRD) of a 1.5 mm thick piece from the wedge cast DAR35 sample.

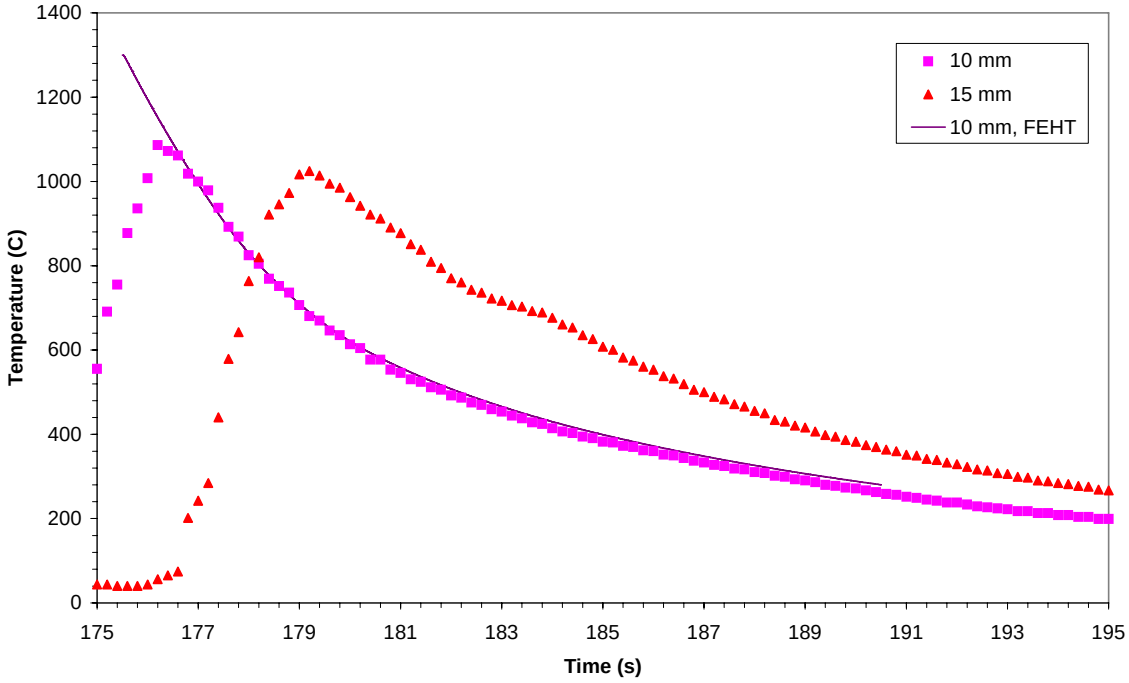

Figure 73 – Time-temperature curves (measured and calculated) for the LDAR2X7 wedge cast. The fitted curve yields a heat transfer coefficient that is assumed constant for all mold-melt interfaces.

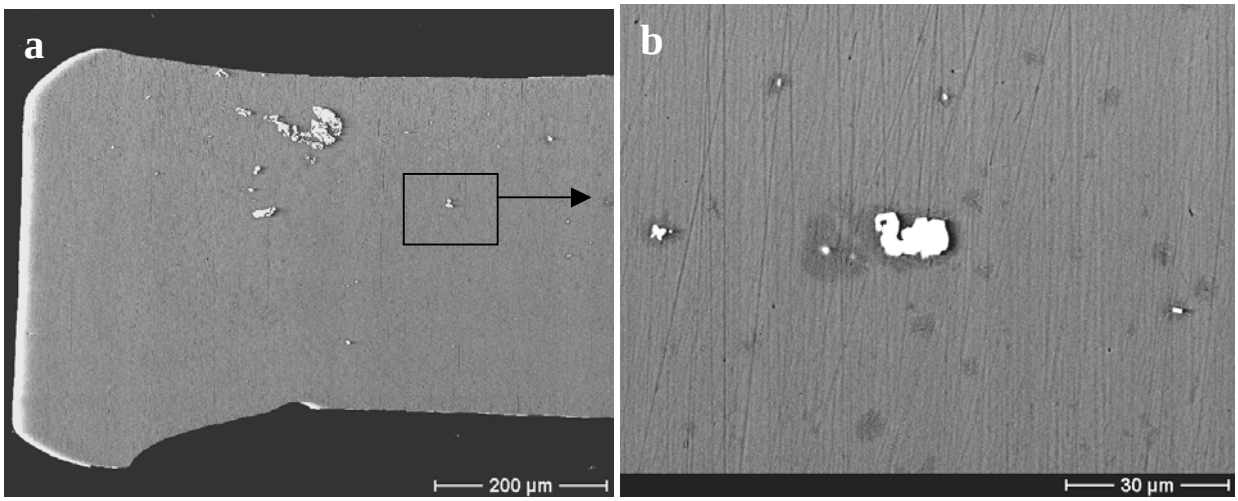

Figure 74 – Back-scattered electron image (BSEI) of LDAR2X7 wedge cast, (a) tip of wedge and (b) magnified portion of Figure 74a showing a few crystals embedded in an amorphous matrix. The cooling rate was approximately 680 K/s for the tip region. The peculiar shape of the wedge-tip arises from sample preparation. A part of the tip broke off, and the sample was not sufficiently polished to show the proper V-shaped geometry.

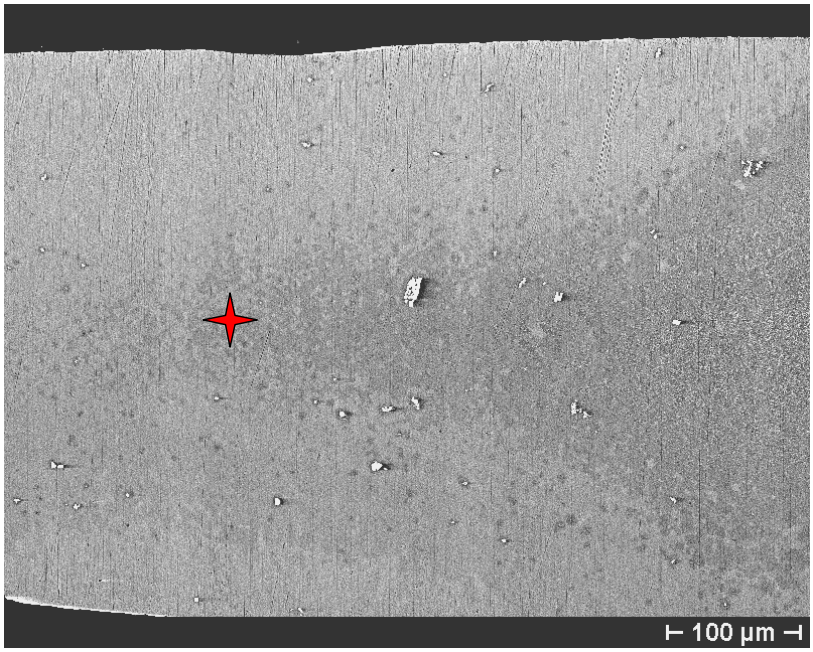

Figure 75 – Back-scattered electron image (BSEI) of the transition between amorphous and crystalline microstructure in alloy LDAR2X7 cast in the wedge-shaped mold.

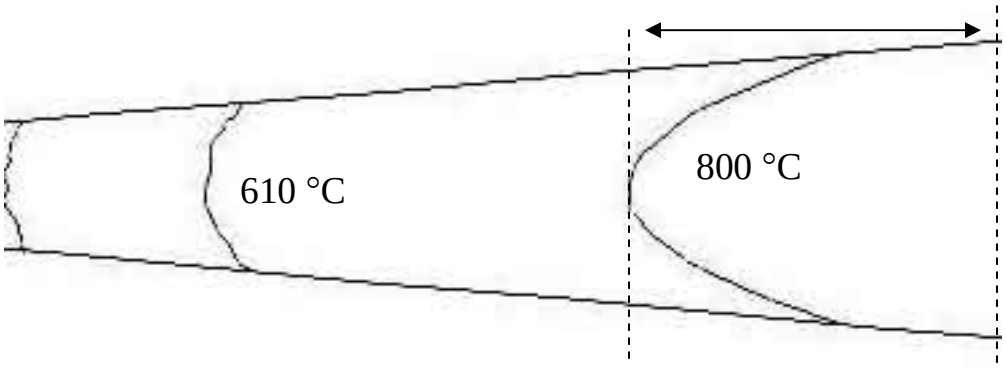

Figure 76 – Isotherms in LDAR2X7 after 1 second cooling for the same area (indicated by the vertical lines) in the wedge as the one shown in Figure 75.

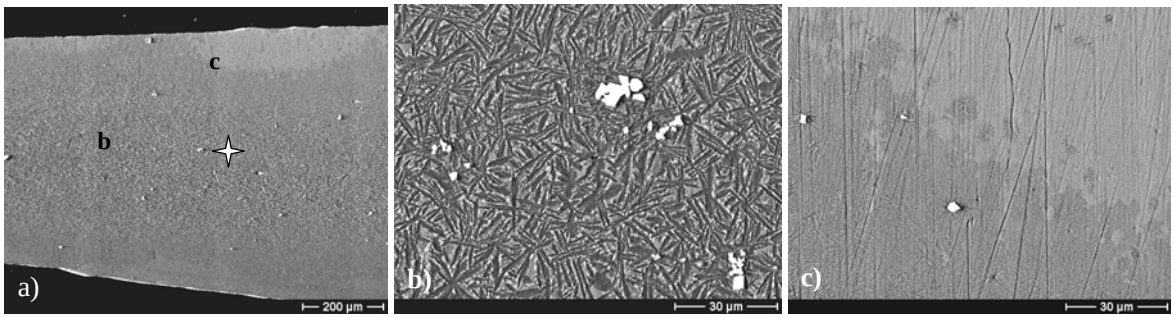

Figure 77 – (a-c) Back-scattered electron images (BSEIs) of LDAR2X7, where a) shows the entire cross-section of the wedge and the coarsening of the microstructure as cooling rates are decreasing, b) and c) are magnified BSE images of the regions indicated in a). The calculated cooling rate is 340 K/s at the indicated position (white start symbol) in Figure 77a.

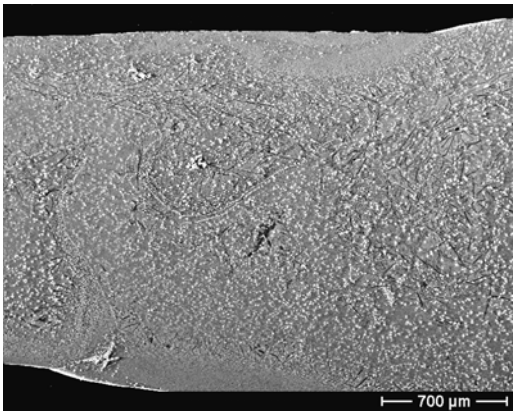

Figure 78 – Back-scattered electron image (BSEI) of wedge-cast LDAR2X7, cooling rate approximately 115 K/s. Some representative areas away from the edges are magnified and shown in Figure 79 (a-c).

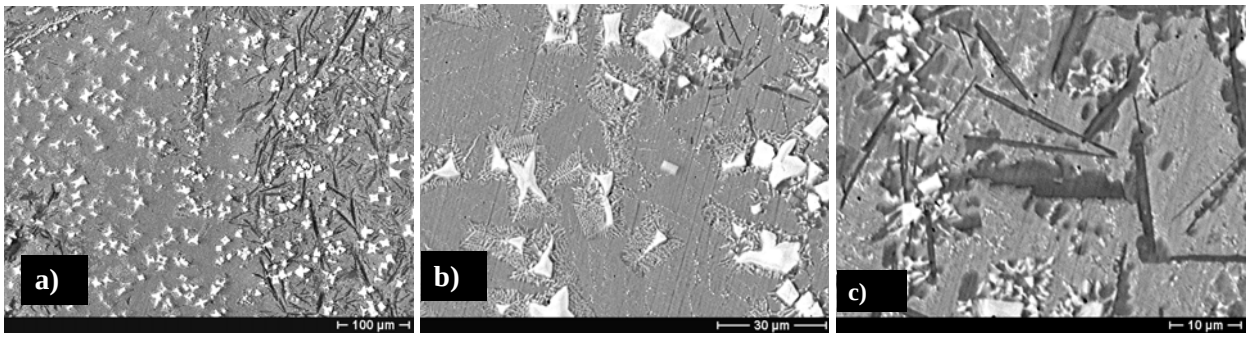

Figure 79 – (a,b,c) Back-scattered electron images (BSEIs) of LDAR2X7, magnified areas of image shown above in Figure 78.

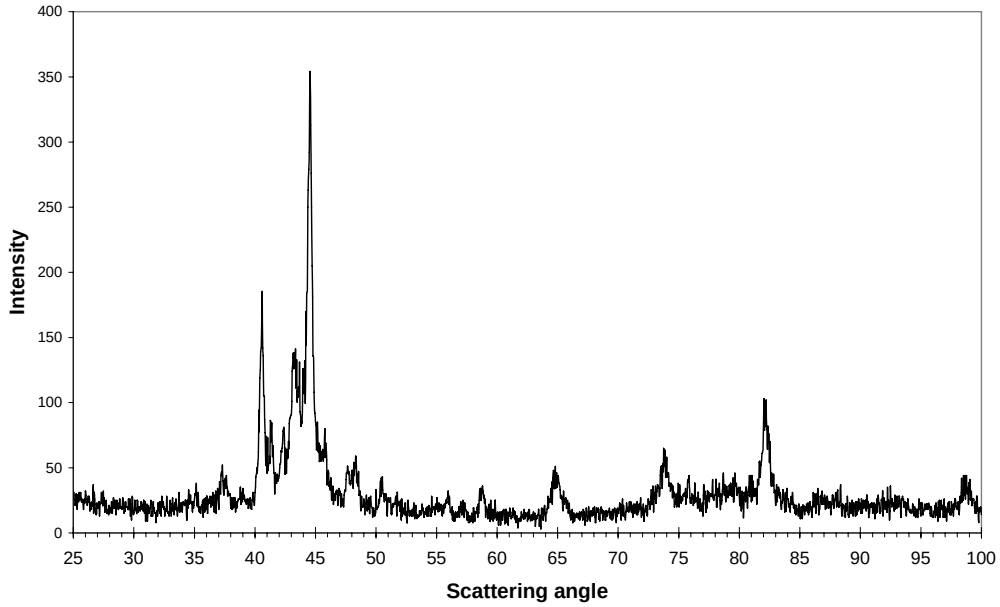

Figure 80 – X-ray diffraction (XRD) trace of a powder sample from wedge cast LDAR2X7. The tip of the wedge was crushed and sieved. The bcc-Fe phase dominates, but other unknown crystalline phases are also present. Identification of these phases is ongoing.

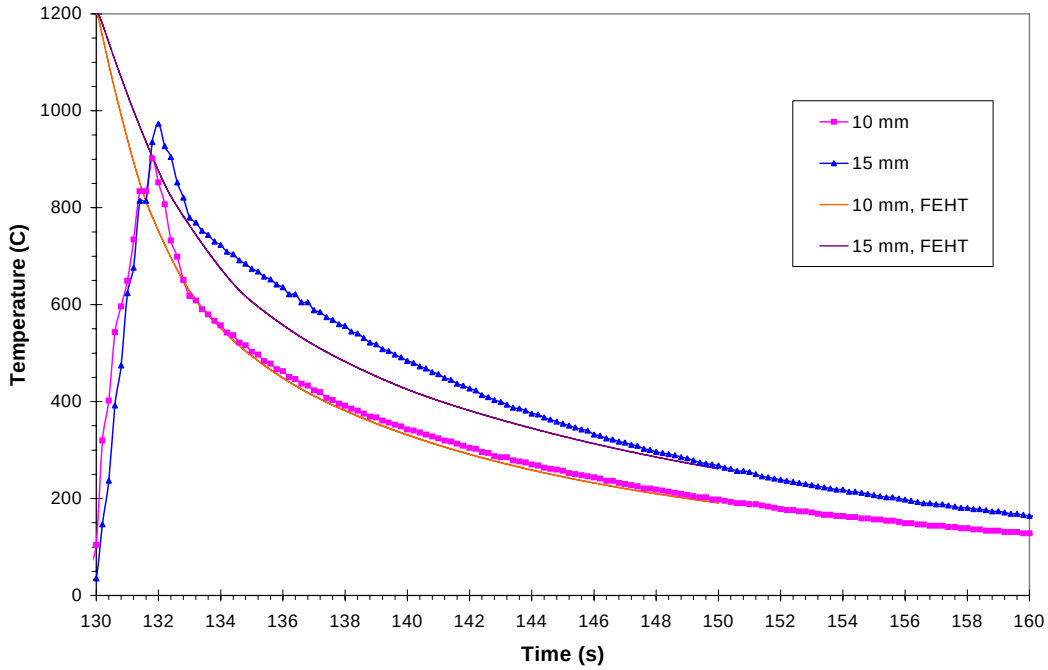

Figure 81 – Measured and calculated cooling curves during casting of LDAR7 into the wedge-shaped mold. Insufficient response times following pouring cause flawed data between 130 and 132 seconds. The time scale is absolute and refers to the time elapsed since heating of the sample was initiated.

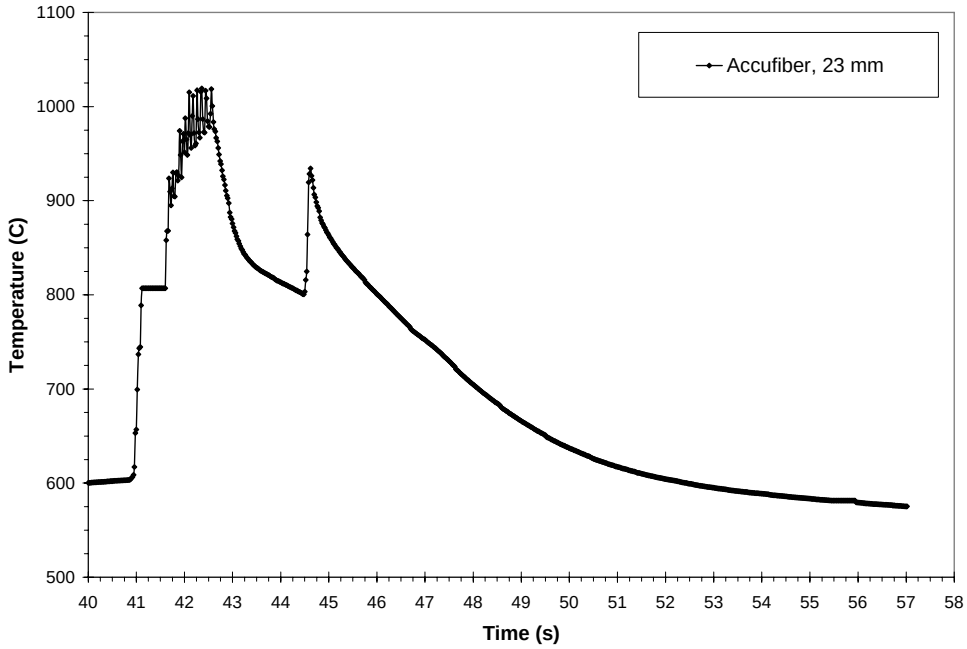

Figure 82 – Cooling curve as measured with the fiberoptic sensor. The sudden jump at t ~ 45 seconds is likely due to the late arrival of molten material from the crucible. The temperature data were acquired at a rate of 50 Hz.

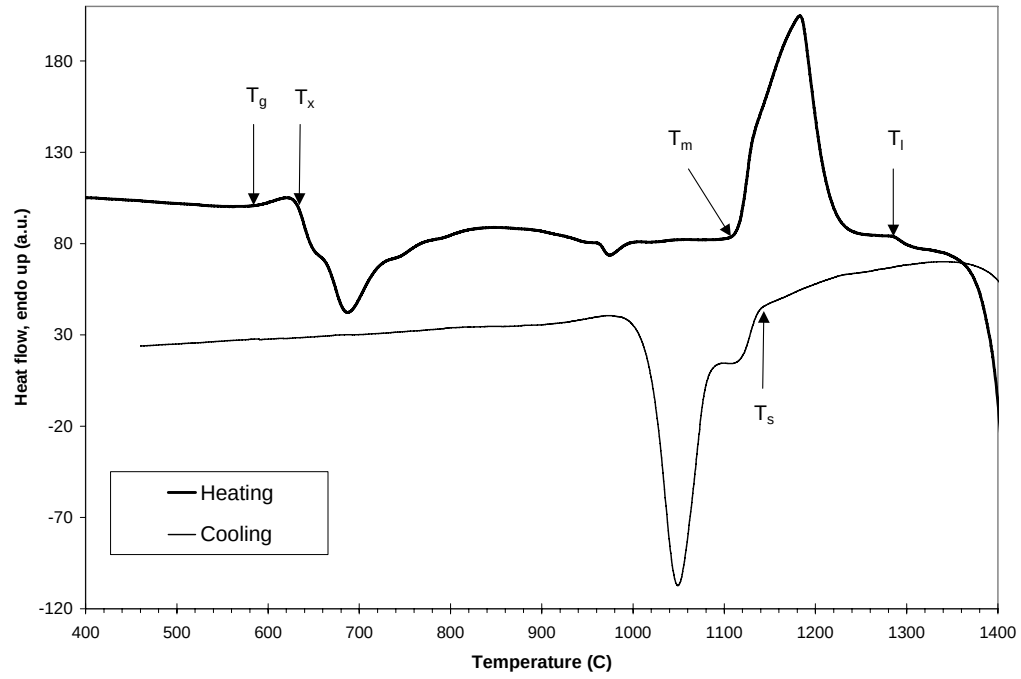

Figure 83 – Differential thermal analysis (DTA) heating/cooling curves for LDAR7 wedge cast amorphous sample.

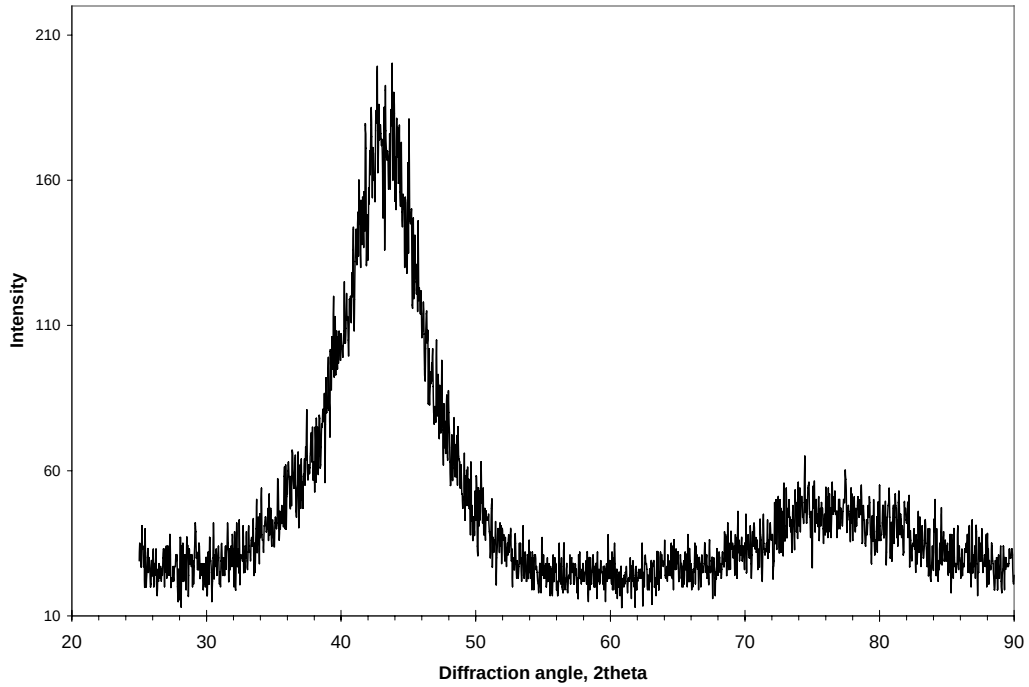

Figure 84 – X-ray diffraction (XRD) pattern from a powder sample of the wedge-cast LDAR7 alloy. The wedge casting thickness was about 1.5 mm where the sample was collected.

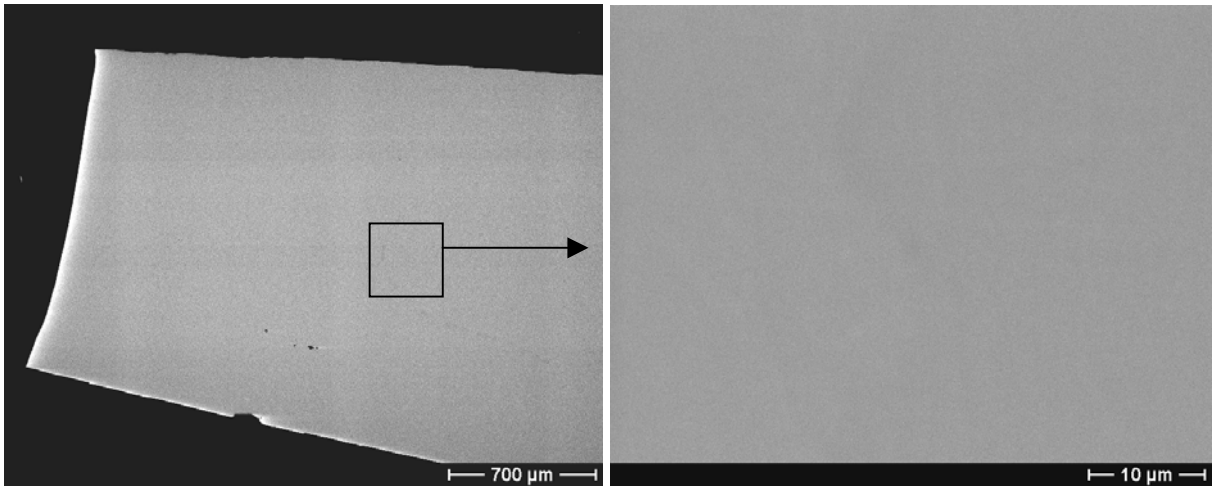

Figure 85 – Back-scattered electron image (BSEI) of wedge-cast LDAR7 showing a 2 mm thick cross-section that is completely amorphous. The calculated cooling rate at this location was about 175 K/s.

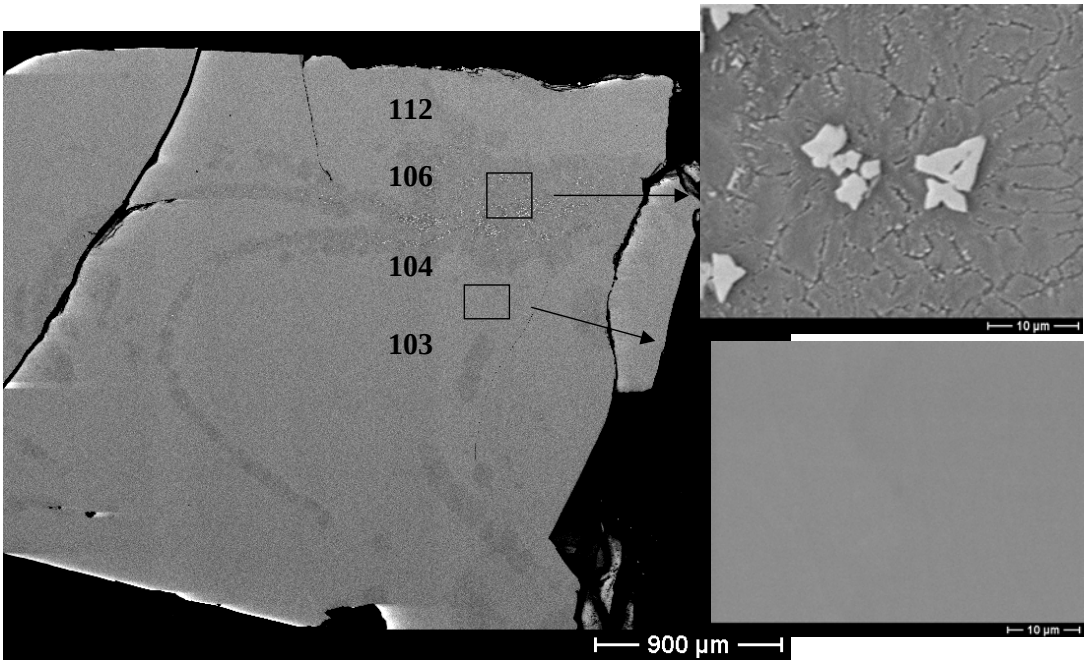

Figure 86 – Back-scattered electron image (BSEI) of wedge cast LDAR7, showing some crystalline phases embedded in an amorphous matrix. The cooling rates (in K/s) are indicated to reflect how much slower the center of the wedge is cooled compared to the edges.

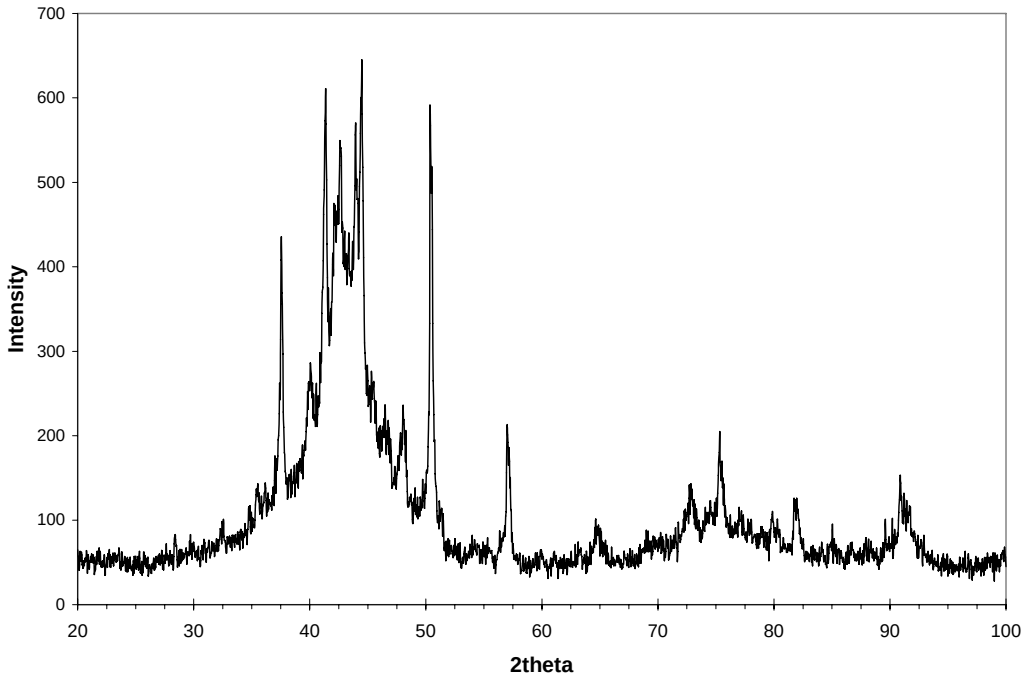

Figure 87 – X-ray diffraction (XRD) pattern from a 4 mm thick wedge cast section of LDAR7. Both crystalline peaks and two broad amorphous peaks can be observed.

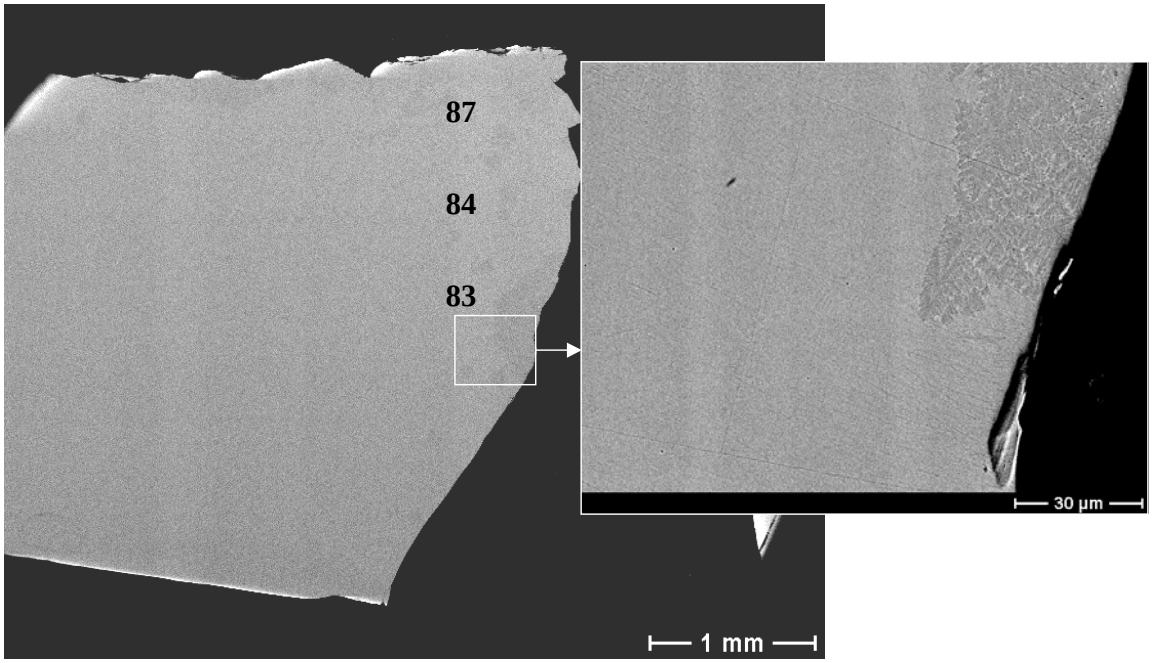

Figure 88 – Back-scattered electron image (BSEI) of wedge-cast LDAR7, casting thickness approximately 3.5 millimeters.

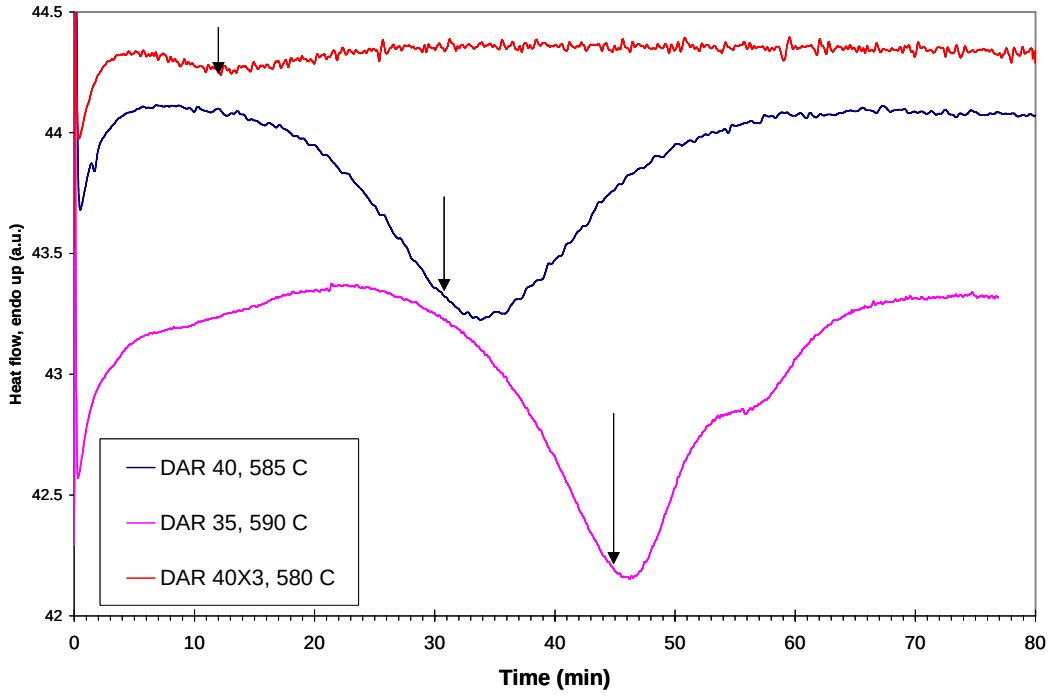

Figure 89 – Differential scanning calorimetry (DSC) isothermal annealing curves for three selected DAR-alloys. The arrows indicate the time at which the annealing was terminated and the ribbons quenched. Evidently, holding times were selected such that a considerable fraction of crystals would develop from the glassy phase, without precipitating other phases.

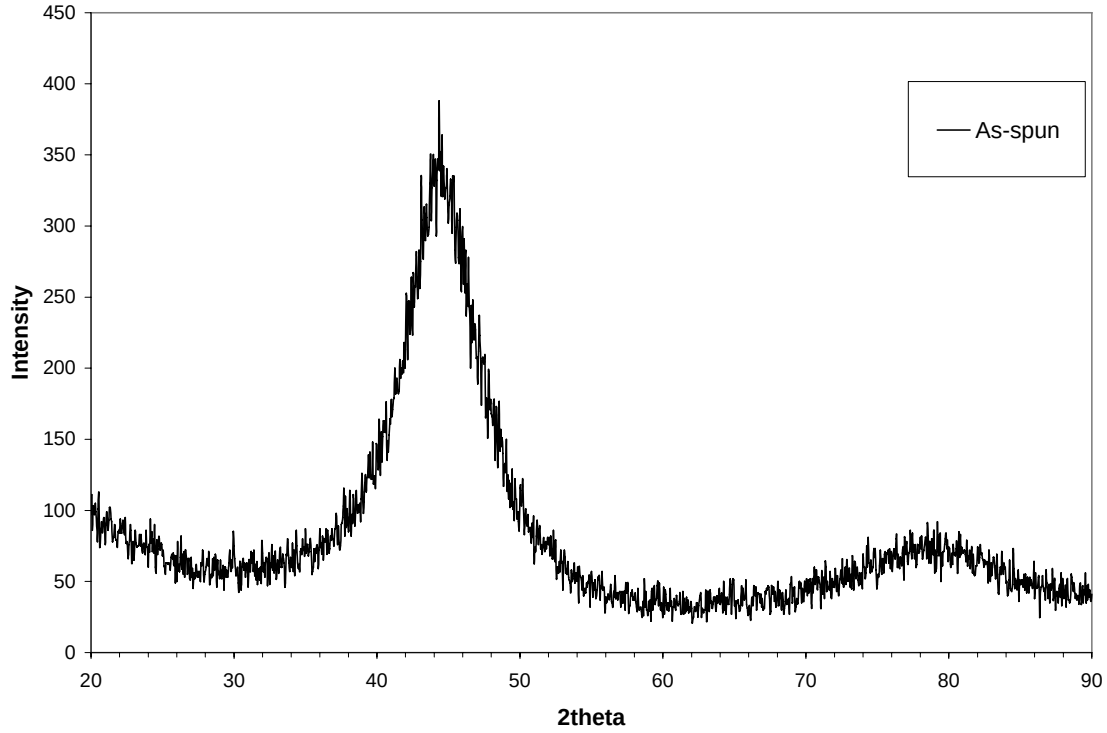

Figure 90 – X-ray diffraction (XRD) peak pattern of as-spun ribbons of DAR35.

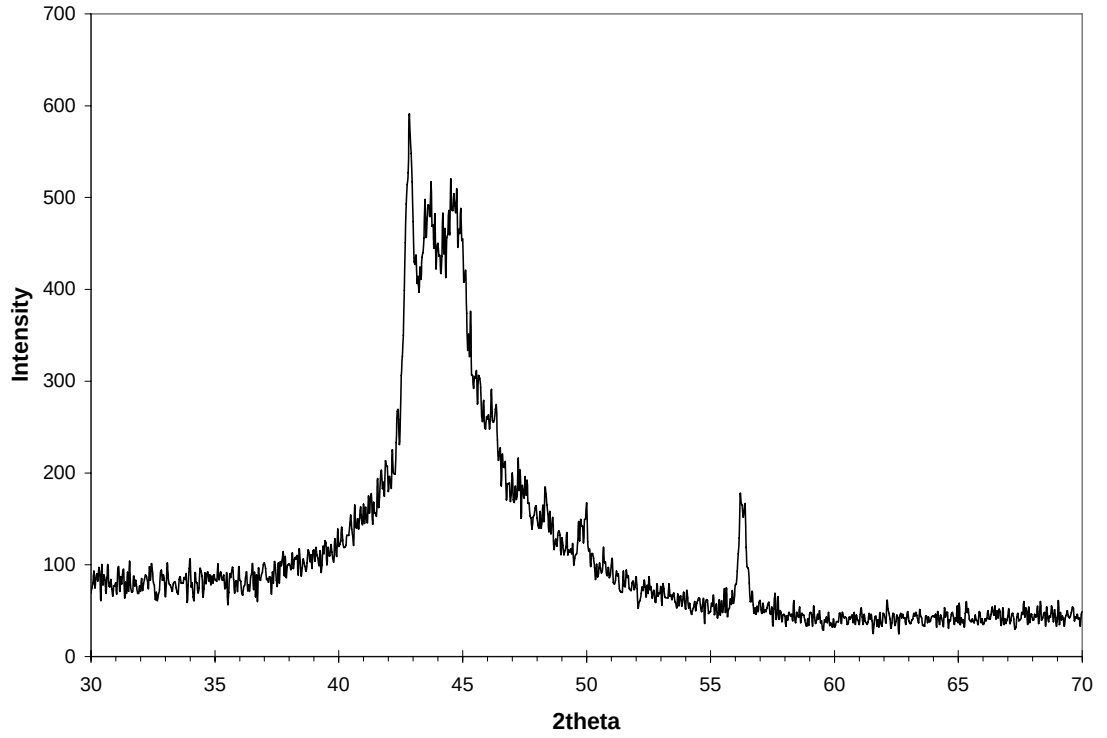

Figure 91 – X-ray diffraction (XRD) peak pattern of devitrified ribbons (45 min at 590℃) of DAR35.

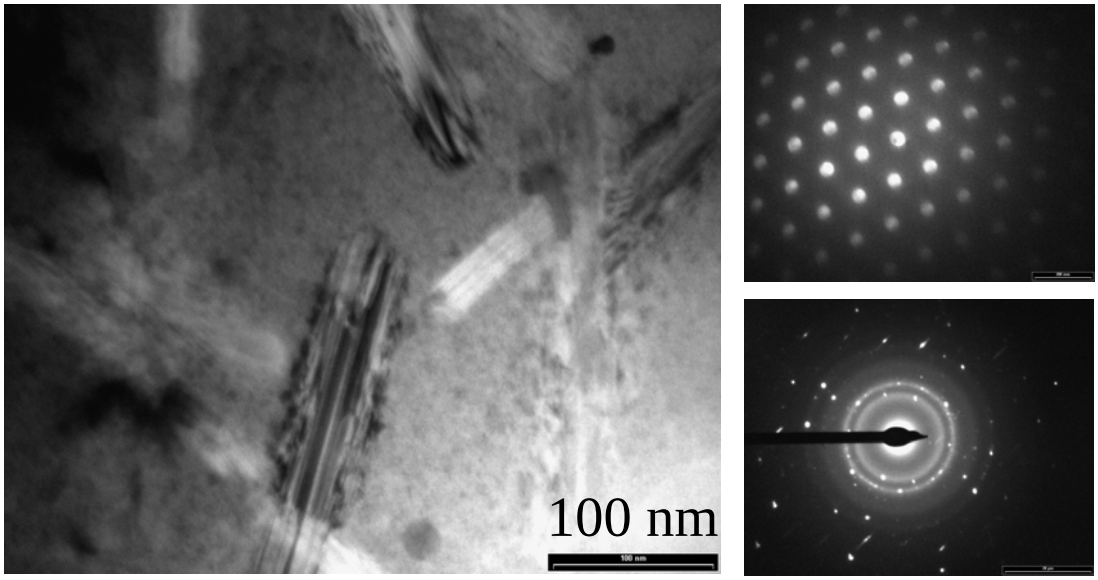

Figure 92 – Transmission electron microscopy (TEM) analysis of partially devitrified DAR35 ribbons. Left: Bright field (BF) image showing needle-like precipitates in a possible glassy matrix. Upper right: Convergent beam electron diffraction (CBED) from a single needle. Lower right: Selected area electron diffraction (SAED) showing crystal reflexes as well as the ring pattern characteristic for amorphous structures.

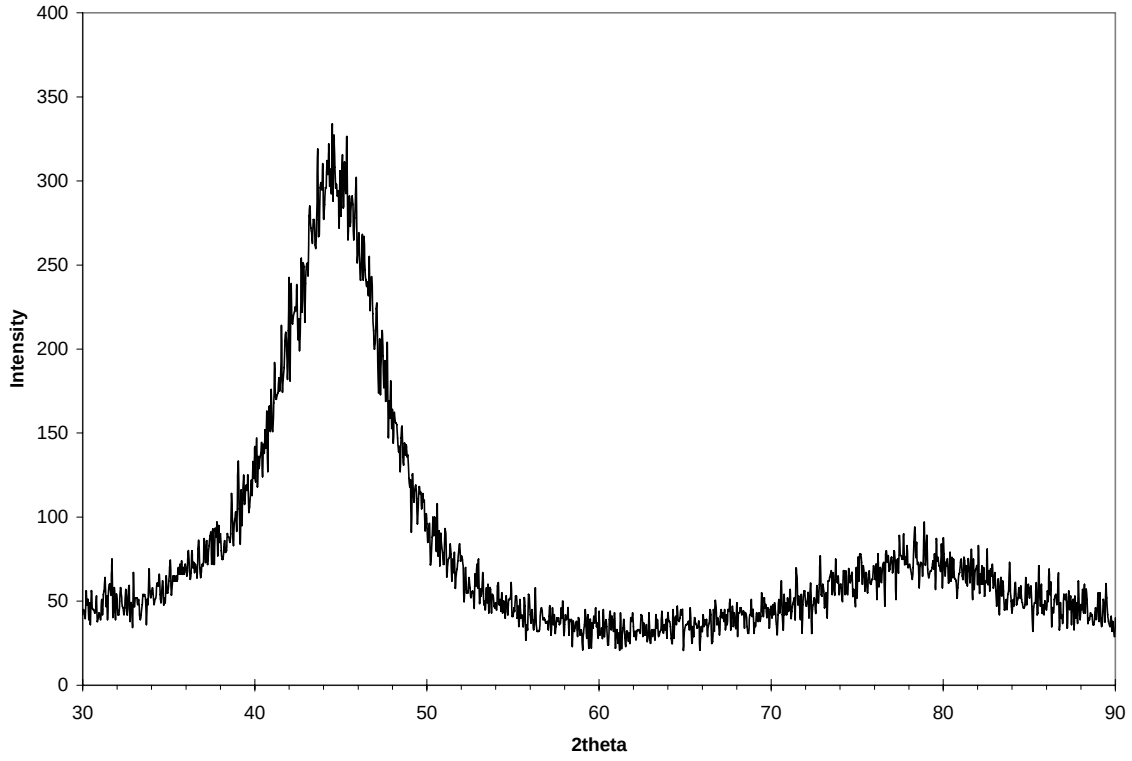

Figure 93 – X-ray diffraction (XRD) trace of as-spun ribbons of DAR40 confirming the presence of a glassy phase only.

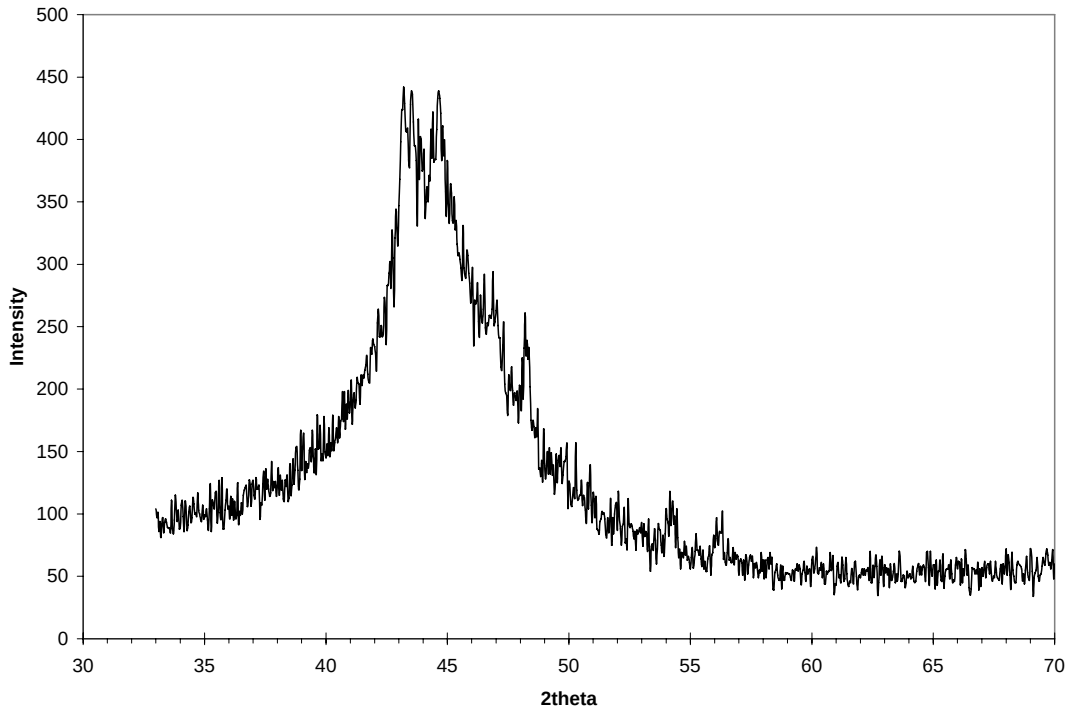

Figure 94 – X-ray diffraction (XRD) trace of partially devitrified ribbons, peaks consistent with a Fe_3B primary precipitating phase.

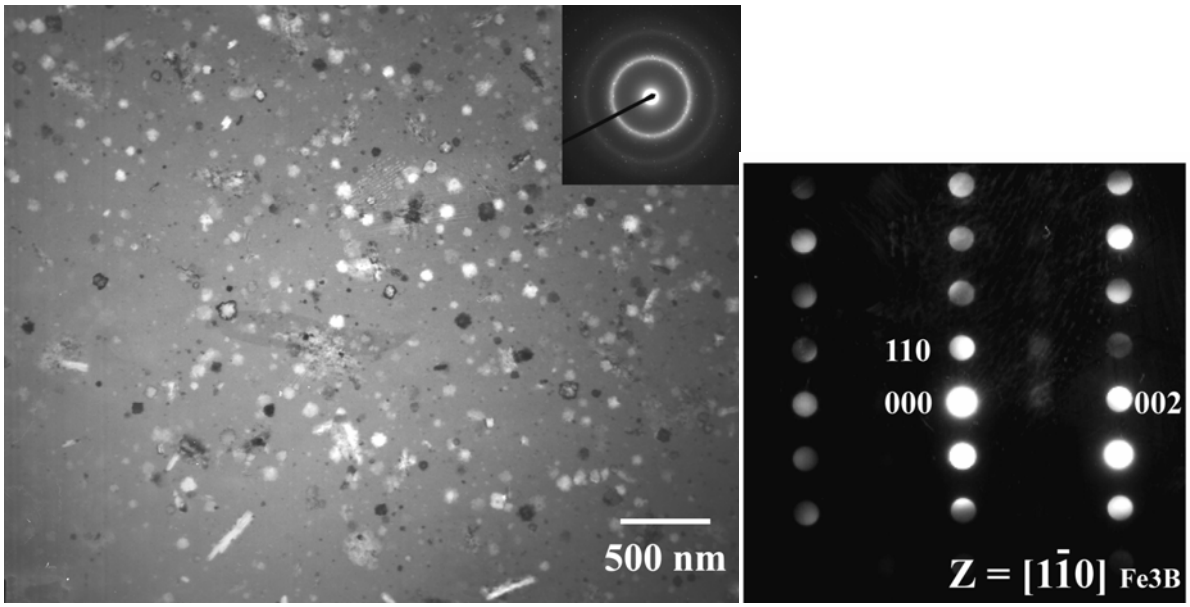

Figure 95 – Transmission electron micrographs (TEMs) from partially devitrified DAR40 ribbons. Left: BF showing an amorphous matrix with spherical precipitates and a few rod-like precipitates. Center, up: convergent beam electron diffraction (CBED) image from the matrix, confirming the amorphous structure through the characteristic ring pattern. Right: CBED image from a spherical particle, consistent with a Fe_3B structure.

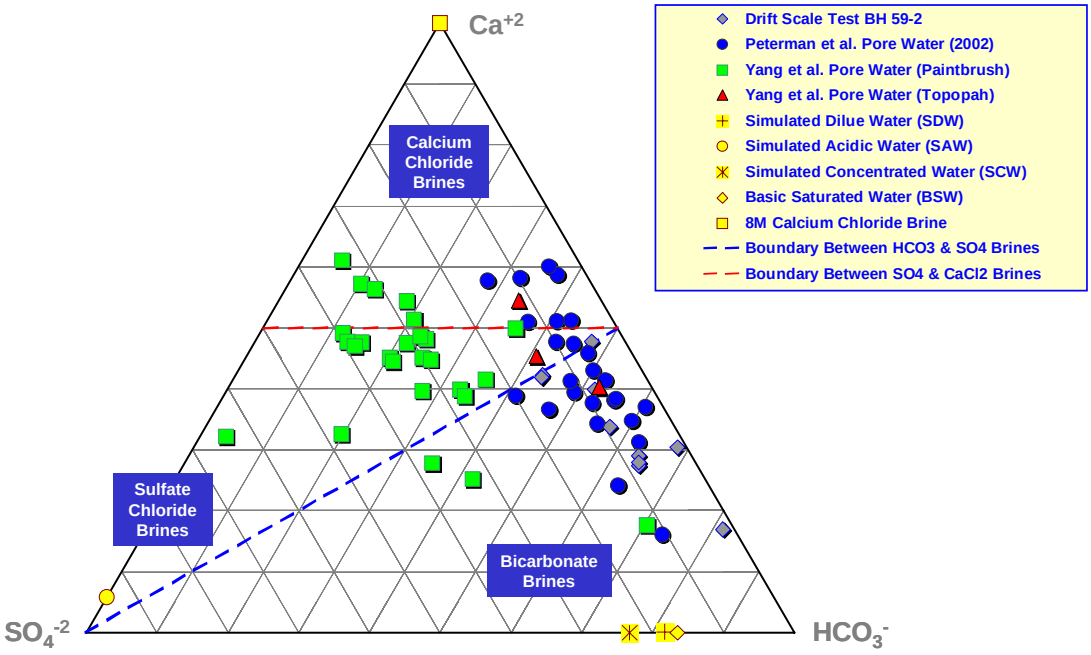

Figure 96 – This tri-lateral diagram can be used to classify natural waters as calcium chloride, sulfate-chloride, or bicarbonate brines. In principle, any natural water falling in the calcium chloride region (upper area of diagram, bounded by dashed red line) will evolve to concentrated calcium chloride brine during evaporative concentration, which will cause the precipitation of other salts. Examples include 5M $CaCl_2$ at 105°C. Similarly, any natural water falling within the sulfate-chloride region (left side of diagram, bounded by the dashed red and blue lines) will evolve to concentrated sulfate-chloride brine during evaporative concentration. Examples are sodium chloride solution, seawater, and simulated saturated water (SSW). Any natural water falling within the bicarbonate region (right side of diagram, bounded by the dashed blue line) will evolve to concentrated bicarbonate brine during evaporative concentration. Examples are simulated acidic water (SAW), simulated concentrated water (SCW) and basic saturated water (BSW).

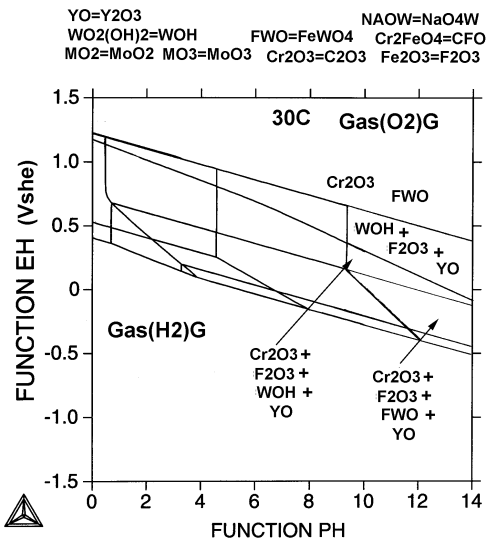

Figure 97 – Predicted Pourbaix diagrams for CBCTL1651 amorphous metal formulations in pure water at near-ambient temperature. In addition to promoting glass formation, yttrium promotes passive film stability under alkaline conditions through the formation of yttrium oxide.

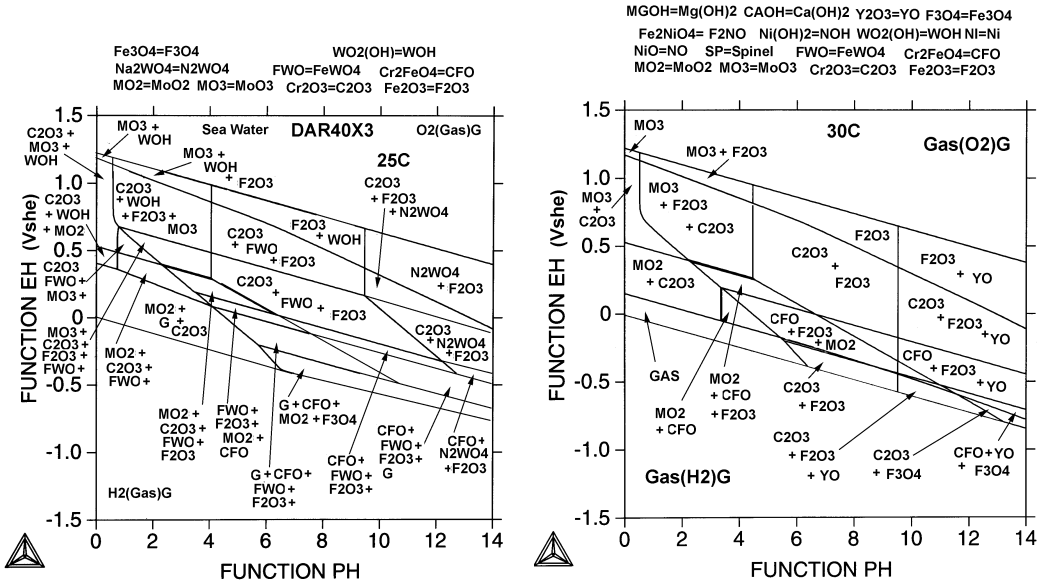

Figure 98 – Predicted Pourbaix diagrams for DAR40X3 and CBCTL1651 amorphous metal formulations in synthetic seawater (40 grams of NaCl in 1 liter of water) at near-ambient temperature. Both DAR40X3 and CBCTL1651 have high concentrations of molybdenum and chromium, like nickel-based alloys such as UNS N06022. The DAR40X3 also includes substantial amounts of tungsten. Chromium, molybdenum and tungsten all form oxides that are insoluble at very low pH. These alloying elements can therefore stabilize the passive film under the acidic conditions found in pits and crevices. Acidification is due to the hydrolysis of polyvalent metal cations dissolved during localized corrosion. The CBCTL1651 formulation has 2 percent (2 atomic %) yttrium, which lowers the critical cooling rate, and promotes glass formation. The yttrium contributes to passive film formation under alkaline conditions.

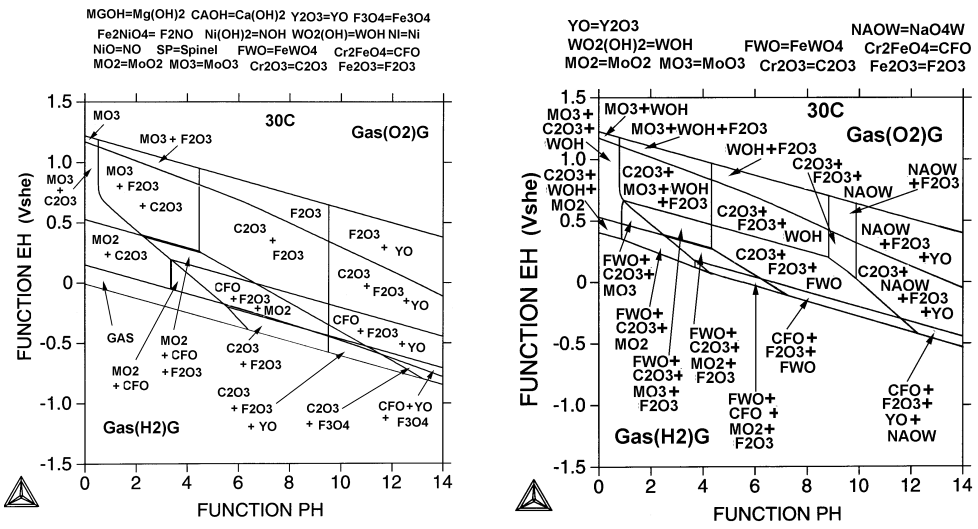

Figure 99 – Predicted Pourbaix diagrams for CBCTL1651 and CBCTL1651+W amorphous metal formulations in synthetic seawater at near-ambient temperature (30°C). In the later case, the presence of tungsten leads to the formation of $FeWO_4$ and $WO_2(OH)_2$, while the presence of molybdenum leads to the formation of MoO_2 and MO_3. Chromium and iron oxides (Cr_2O_3 and Fe_2O_3) also contribute to passive film stability. Under alkaline conditions, sJCF-Table Y_2O_3 and NaO_4W surface phases are predicted. Such predicted Pourbaix diagrams, and the capability developed to make such predictions, is clear evidence that Milestone 1 has been met.

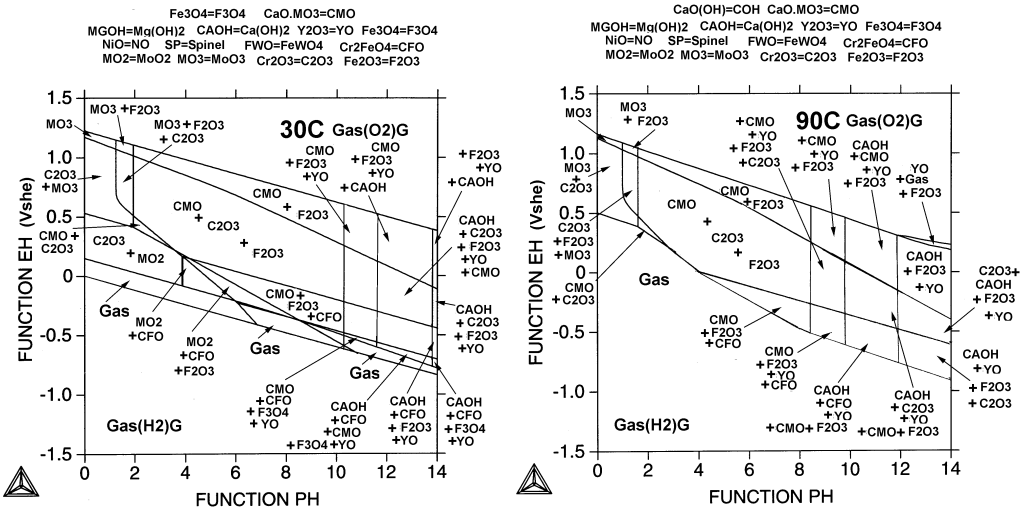

Figure 100 – Predicted Pourbaix diagrams for CBCTL1651 amorphous metal formulations in concentrated calcium chloride brines at 30 and 90°C. Under acidic-to-neutral conditions, MoO_2, MO_3, $CaO\text{-}MO_3$, Cr_2O_3 and Fe_2O_3 contribute to passive film stability. Under alkaline conditions, sJCF-Table Y_2O_3 and $Ca(OH)_2$ surface phases are also predicted.

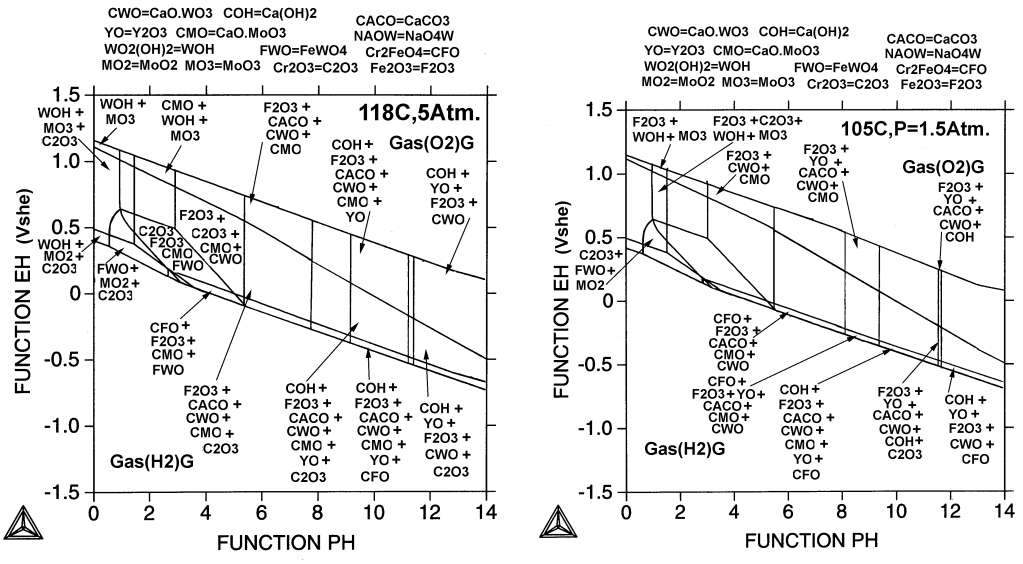

Figure 101 – Predicted Pourbaix diagrams for CBCTL1651 + W amorphous metal formulations in concentrated calcium chloride brines at 105 and 118°C. The presence of tungsten leads to the formation of $FeWO_4$ and $WO_2(OH)_2$, while the presence of molybdenum leads to the formation of MoO_2, MO_3 and $CaO\text{-}MO_3$. Chromium and iron oxides (Cr_2O_3 and Fe_2O_3) also contribute to passive film stability. Under alkaline conditions, sJCF-Table Y_2O_3 and $Ca(OH)_2$ surface phases are predicted.

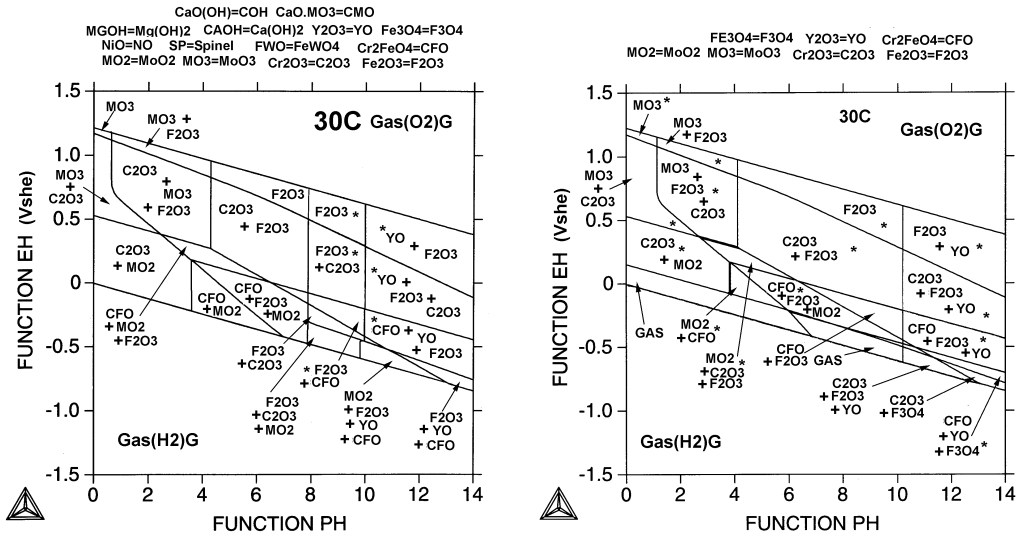

Figure 102 – Predicted Pourbaix diagrams for DAR40X3 and CBCTL1651 amorphous metal formulations in two standard bicarbonate test brines (SCW and BSW) at near-ambient temperature (30°C). As previously discussed, CBCTL1651 has high concentrations of molybdenum and chromium, like nickel-based alloys such as UNS N06022. This alloy also has 2 percent (2 atomic %) yttrium, which lowers the critical cooling rate, and promotes glass formation. Since the pH of SCW is near neutral (pH~7-8), the passive film near the open-circuit corrosion potential would include Fe_2O_3, Cr_2O_3 and MoO_2. Since the pH of BSW is alkaline (pH~12-14), the passive film near the open-circuit corrosion potential would include Fe_2O_3, Fe_3O_4, Cr_2O_3, $CrFeO_4$ and Y_2O_3.

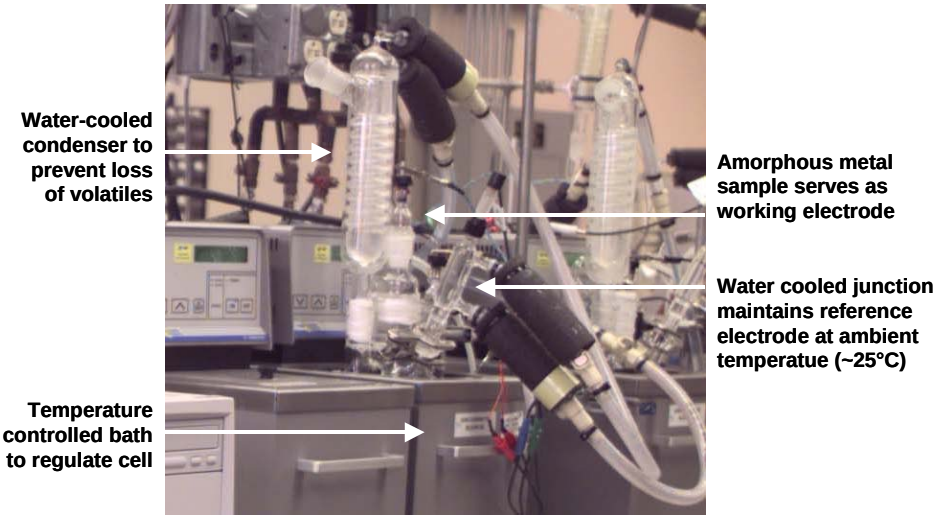

Figure 103 – The corrosion-resistance of Fe-based amorphous metals has been improved by systematic addition of alloying elements such as chromium, molybdenum, and tungsten, all of

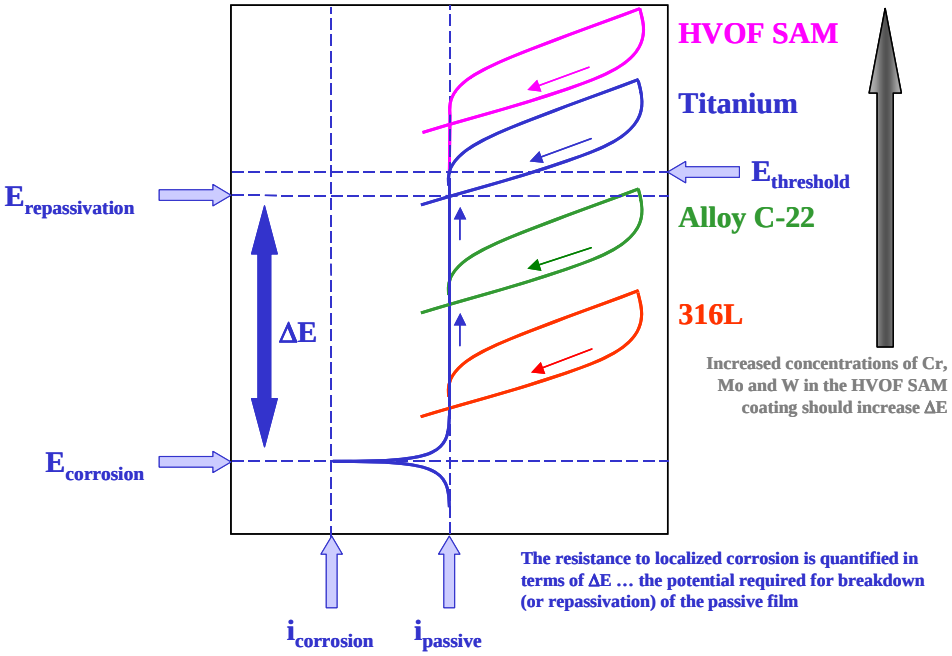

Figure 104 – The corrosion-resistance of Fe-based amorphous metals has been improved by systematic addition of alloying elements such as chromium, molybdenum, and tungsten, all of which are known to enhance passive film stability. Such elemental additions account for the observed difference in the corrosion resistance of Type 316L stainless steel, and nickel-based C-22 (alloy N06022). The resistance to localized corrosion is quantified through measurement of the open-circuit corrosion potential ($E_{corrosion}$ or E_{corr}), the breakdown potential ($E_{breakdown}$ or E_{crit}), and the repassivation potential (E_{rp}). The greater the difference between the open-circuit corrosion potential and the repassivation potential (ΔE), the more resistant a material is to modes of localized corrosion such a pitting and crevice corrosion.

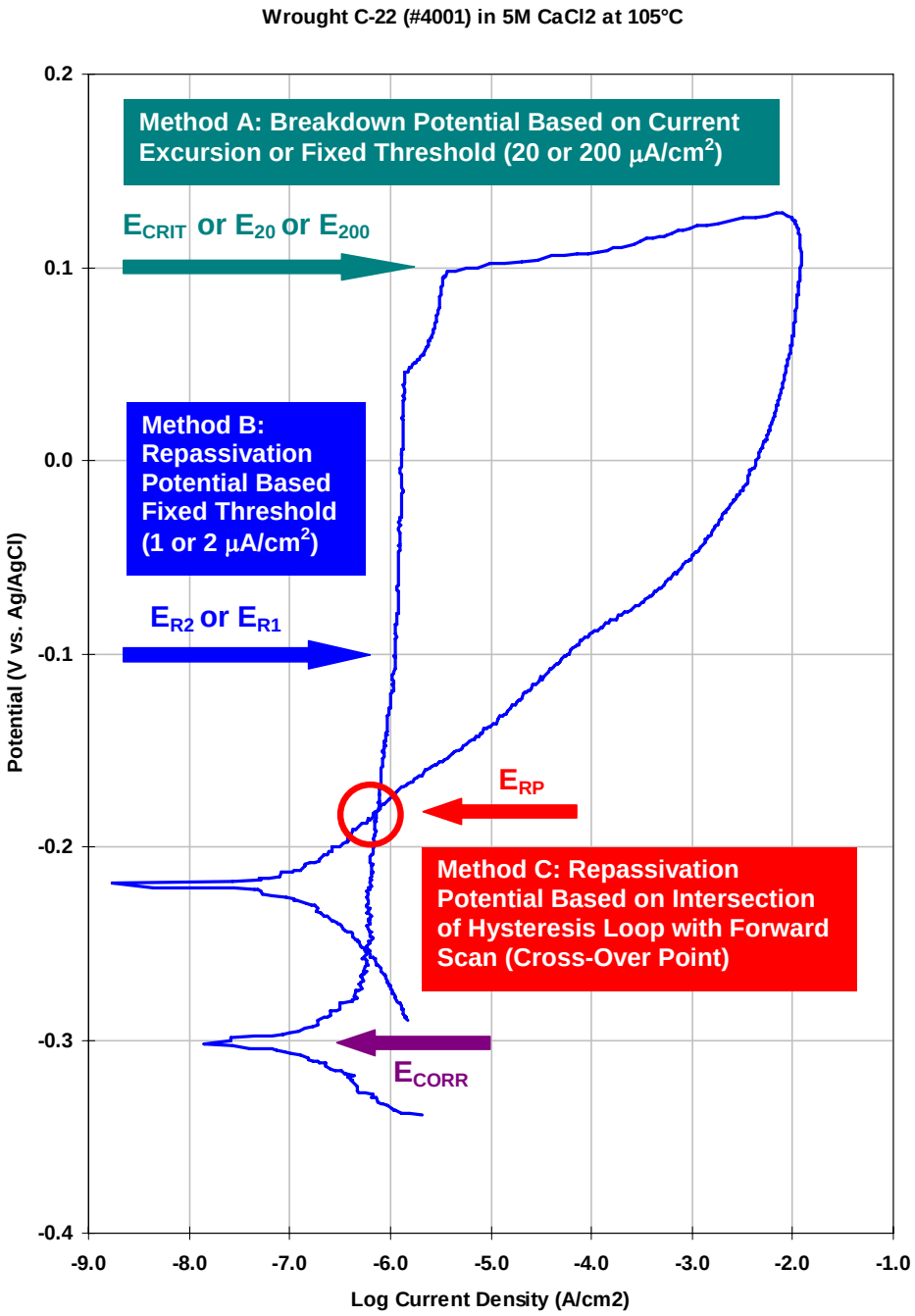

Figure 105 – This is an actual cyclic polarization curve for Alloy C-22 in 5M $CaCl_2$ at 105°C, showing three methodologies for determining the threshold potential for the initiation of localized corrosion in performance assessment models. Method A is based upon the critical potential at which the passive film breaks down (current excursion, 2 or 20 $\mu A/cm^2$). Method B is based upon the repassivation potential, which in turn is based upon an arbitrary threshold (1 or 2 $\mu A/cm^2$). Method C is based upon the repassivation potential, determined from the intersection of the hysteresis loop with the forward scan.

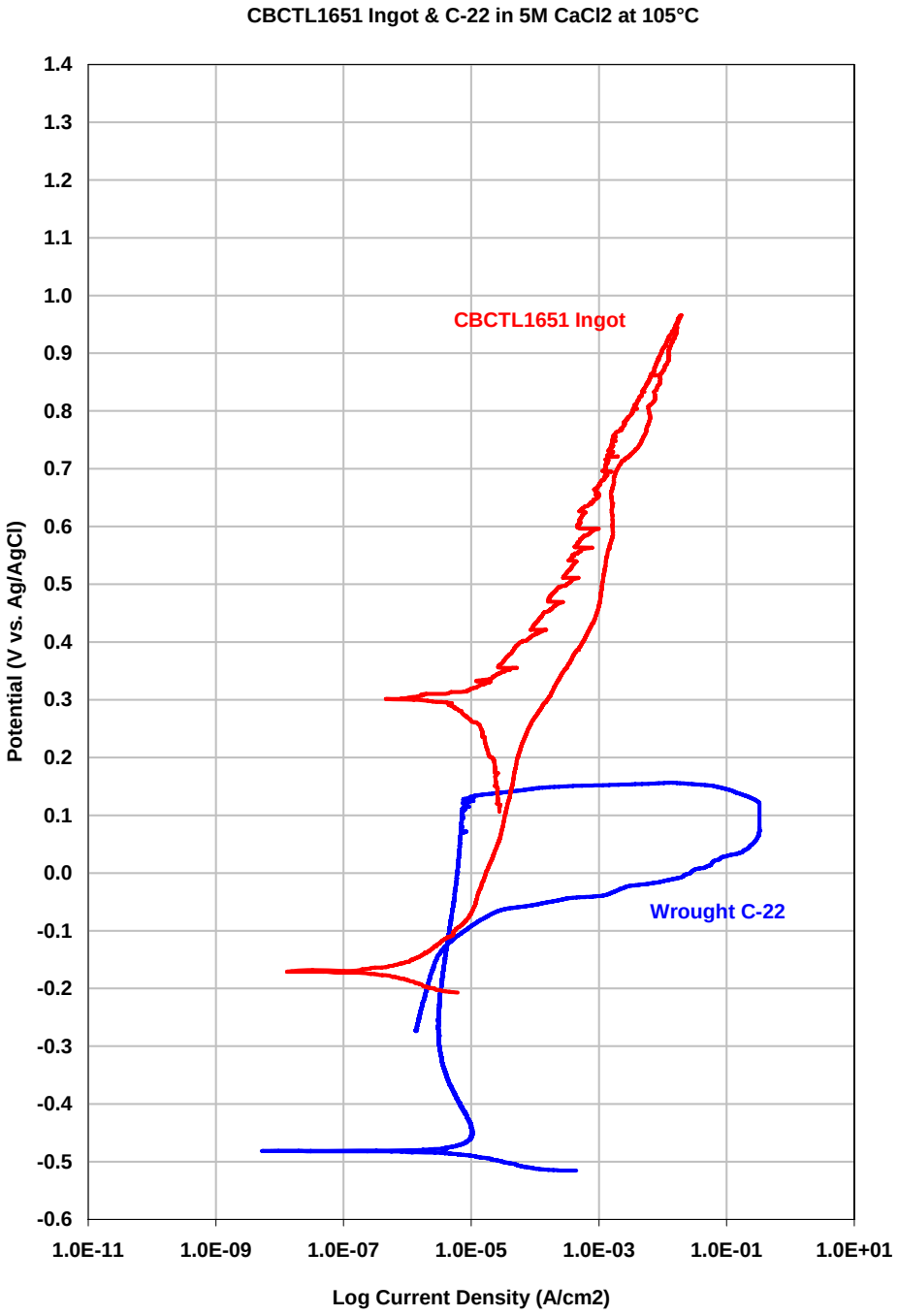

Figure 106 – Cyclic polarization of wrought nickel based Alloy C-22 (N06022) and iron-based amorphous metal (CBCTL1651) ingot in 5M $CaCl_2$ at 105°C. Alloy C-22 shows catastrophic breakdown of the passive film at 100 mV vs. Ag/AgCl, which causes a very large hysteresis loop. During the reverse scan, repassivation occurs at a relatively low potential (–150 to –200 mV). While there was catastrophic breakdown of the Alloy C-22 at very low potential (100 to 200 mV vs. Ag/AgCl), no breakdown of the passive film on CBCTL1651 ingot was observed, even at potentials approaching that required for oxygen evolution.

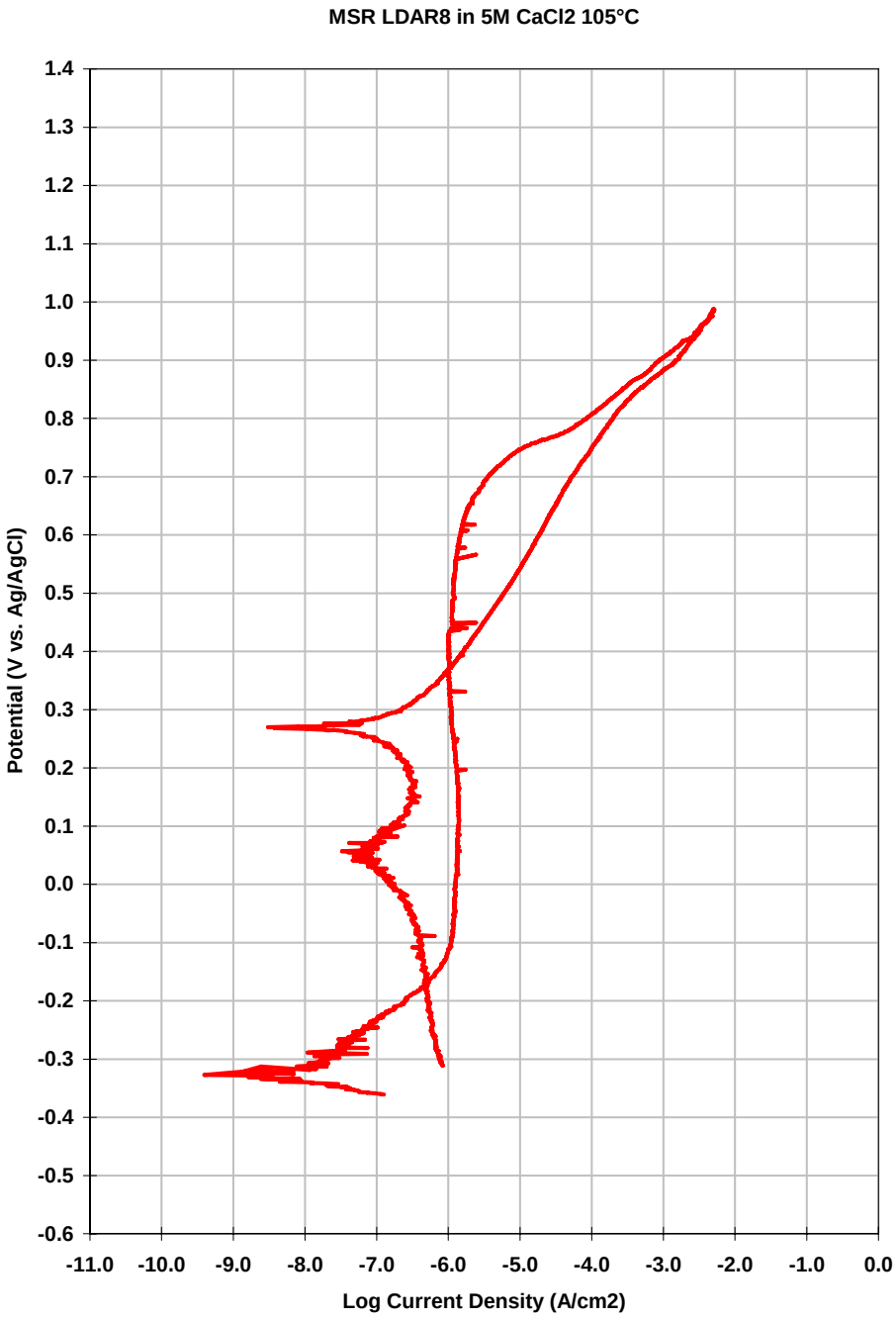

Figure 107 – This cyclic polarization curve is for a melt-spun ribbon of LDAR8 in 5M CaCl2 at 105℃. The LDAR8 formulation uses CBCTL1651 (Y-containing, high-Mo Fe-based amorphous metal) as the parent material, with the addition of tungsten at 3 atomic percent. The repassivation potential for LDAR8 in this aggressive environment (300-400 mV vs. Ag/AgCl) is substantially higher than that for Alloy C-22 (-100 mV vs. Ag/AgCl).

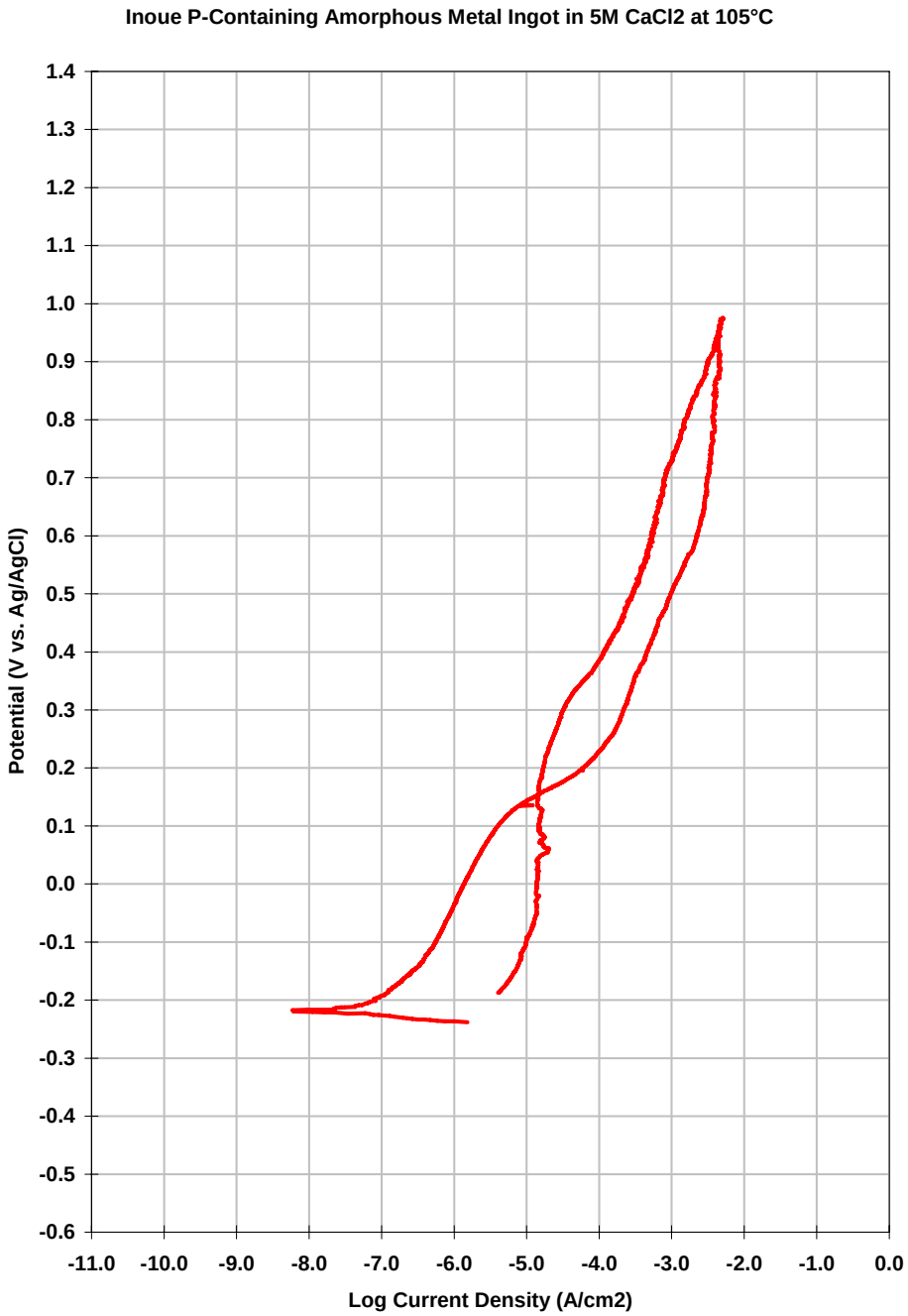

Figure 108 – Cyclic polarization of an Fe-based, P-containing amorphous metal ingot in 5M $CaCl_2$ in 105°C, showing an elevation in the current density at 100 to 200 mV vs. Ag/AgCl. Despite the elevated current density, this alloy exhibited excellent corrosion resistance. This arc-melted, drop-cast ingot has same nominal elemental composition as the P-containing Fe-based amorphous metal formulation discussed in the literature by Pang et al. [2002].

Figure 109 – This cyclic polarization curve is for a melt-spun ribbon of LDAR6 in 5M CaCl2 at 105°C. The LDAR6 formulation has the same nominal elemental composition as the P-containing Fe-based amorphous metal formulation discussed in the literature by Pang et al. [2002]. The repassivation potential for LDAR6 in this aggressive environment (400 mV vs. Ag/AgCl) is substantially higher than that for Alloy C-22 (-100 mV vs. Ag/AgCl).

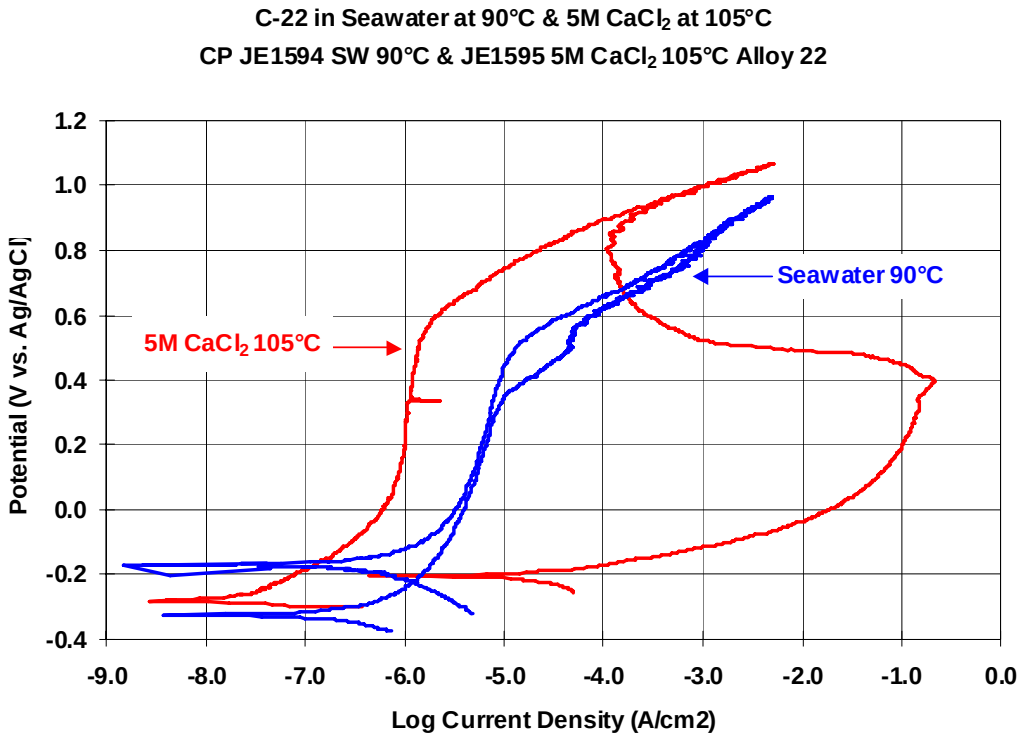

Figure 110 – Cyclic polarization of wrought Alloy C-22 (N06022) in seawater at 90°C and in 5M $CaCl_2$ in 105°C. The test in seawater shows only a very small hysteresis loop, and a relatively high repassivation potential, indicative of good resistance to localized attack. The test in calcium chloride shows a very large hysteresis loop, and a relatively low repassivation potential of between –150 to –200 mV vs. Ag/AgCl. These data indicate that Alloy C-22 has relatively poor resistance to localized corrosion in concentrated calcium chloride brines at elevated temperature.

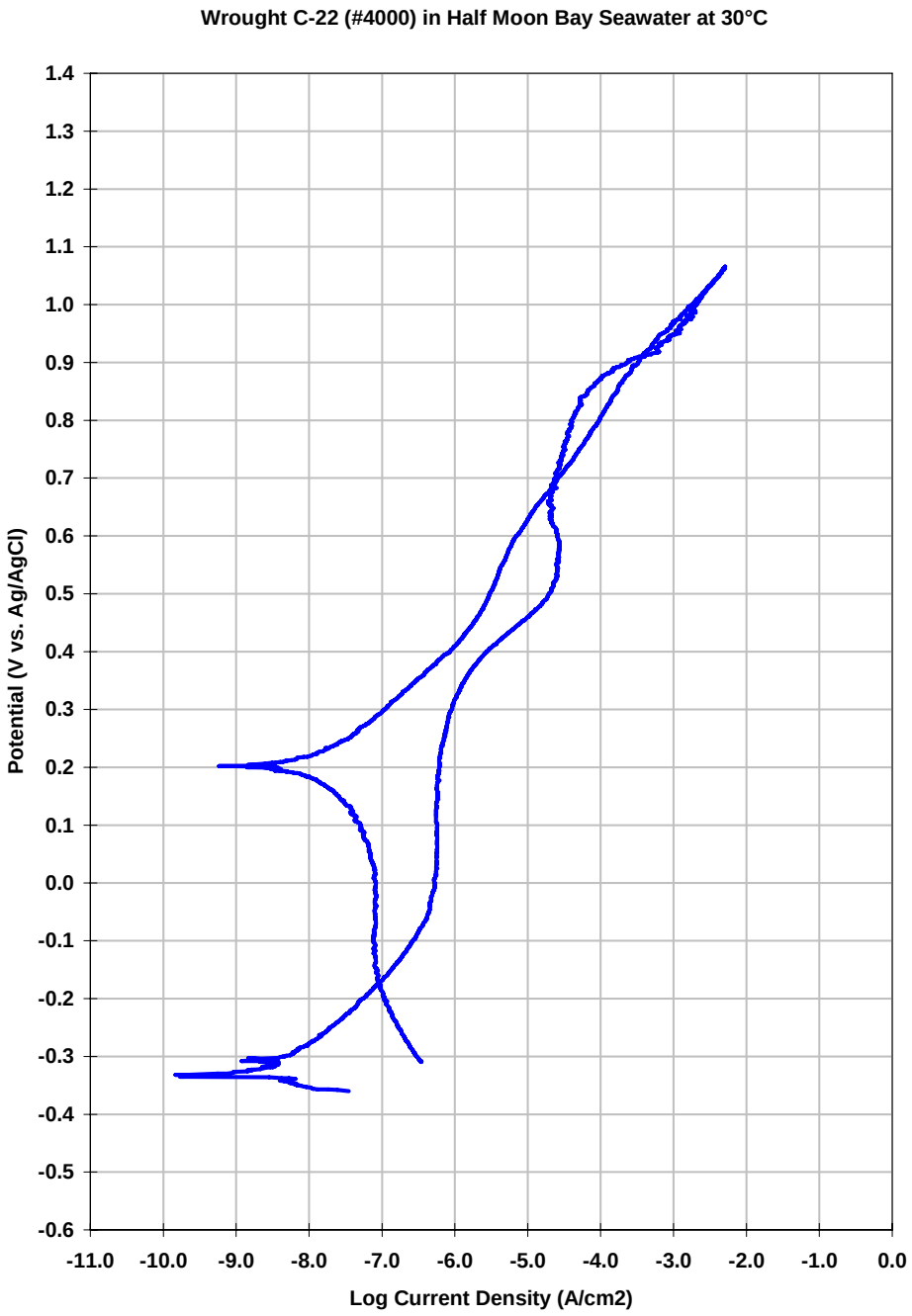

Figure 111 – Cyclic polarization of wrought, nickel based N06022 (Alloy C-22) in Half Moon Bay seawater at 30 ℃ shows a very small hysteresis loop, and a repassivation potential close to the potential required for oxygen evolution. As anticipated, the wrought Alloy C-22 sample performed well in ambient temperature seawater.

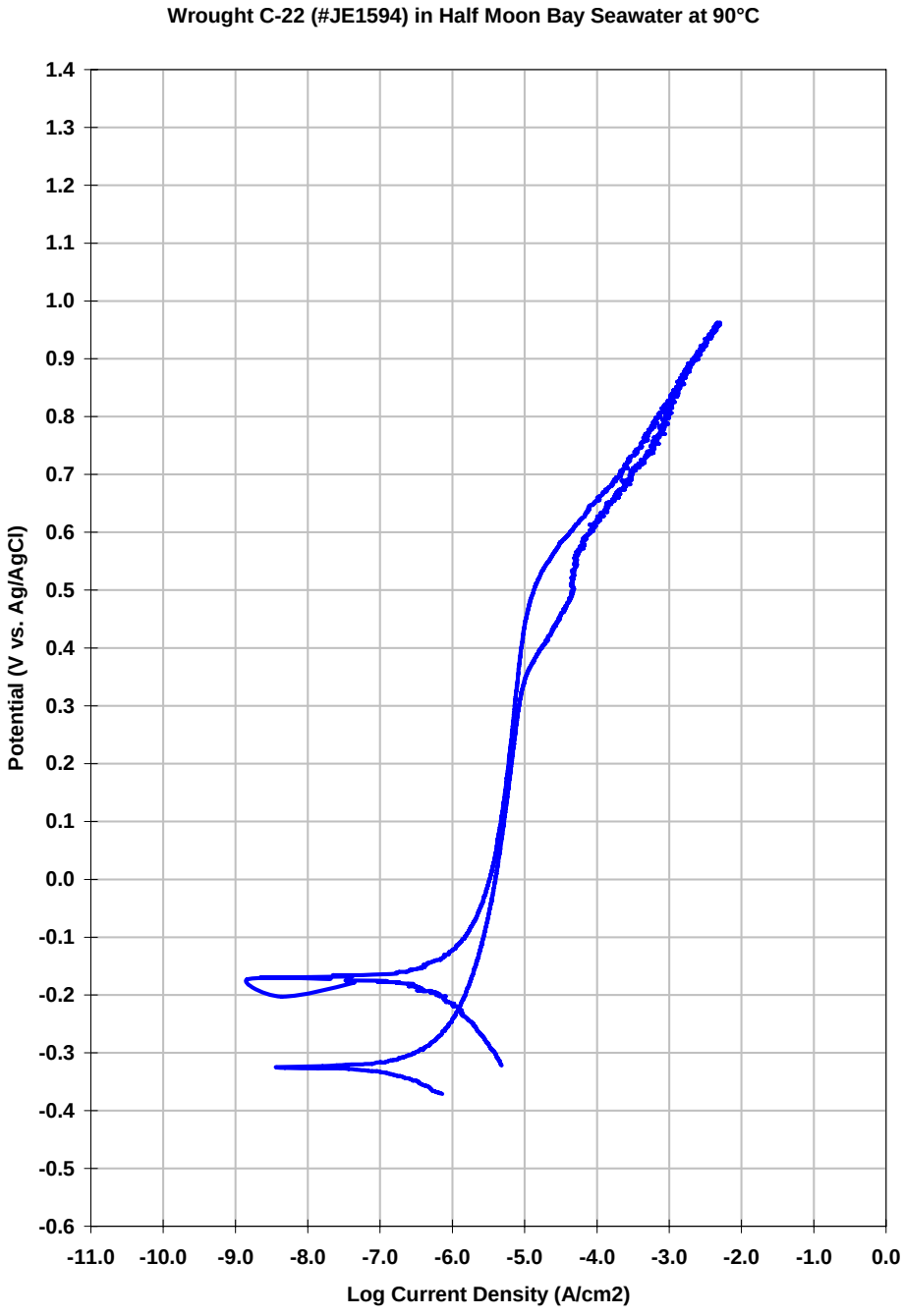

Figure 112 – Cyclic polarization of wrought, nickel based N06022 (Alloy C-22) in Half Moon Bay seawater at 90℃ also shows a very small hysteresis loop, and a repassivation potential close to the potential required for oxygen evolution. As anticipated, the wrought Alloy C-22 sample performed well in heated seawater.

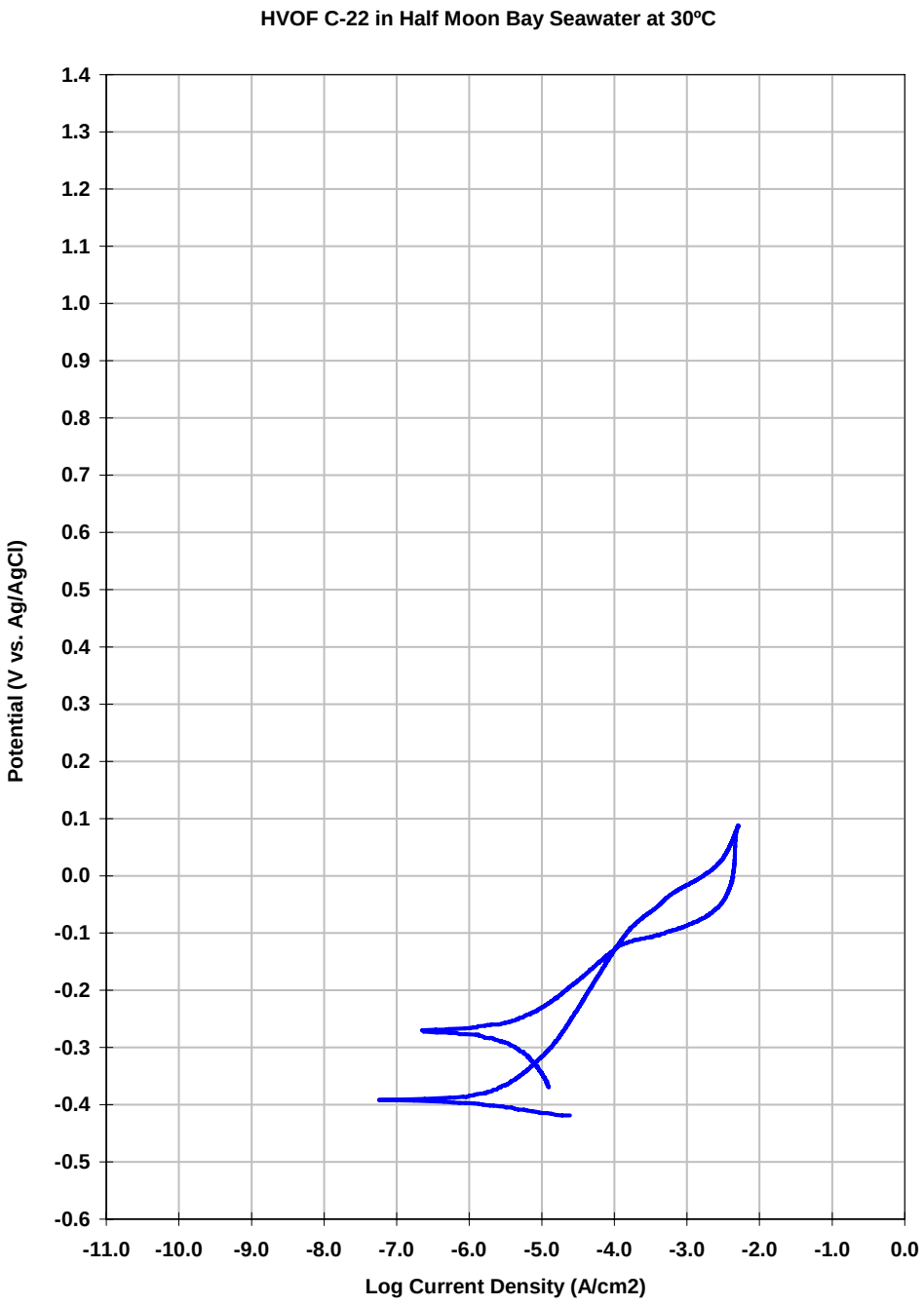

Figure 113 – Cyclic polarization of nickel based Alloy C-22 (N06022) coating deposited with HVOF. The repassivation potentials of HVOF DAR40 and DAR40X3 are very high, whereas HVOF Alloy C-22 (reference material) has relatively poor performance, with a repassivation potential of only –100 mV vs. Ag/AgCl. It is therefore concluded that the amorphous-metals under development can be used to produce corrosion-resistant thermal-spray coatings, but that limitations in the phase stability of Alloy C-22 prevents the deposition of corrosion-resistant thermal spray coatings.

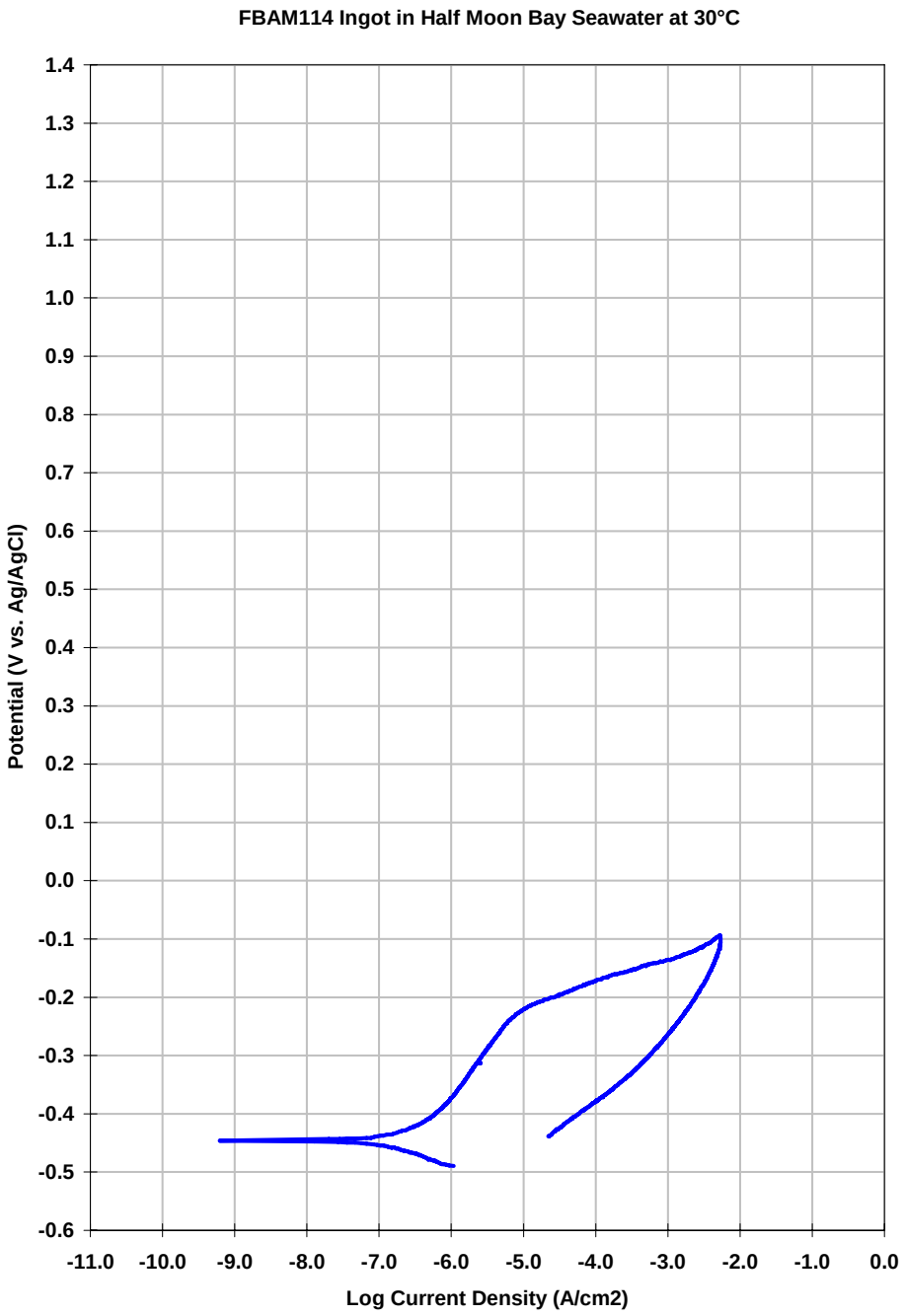

Figure 114 – Cyclic polarization of amorphous-metal, FBAM114, arc-melted, drop-cast in Half Moon Bay seawater at 30℃ also shows a large hysteresis loop, and a repassivation potential below the the open circuit corrosion potential. This particular amorphous metal exhibited poor corrosion resistance in ambient temperature seawater.

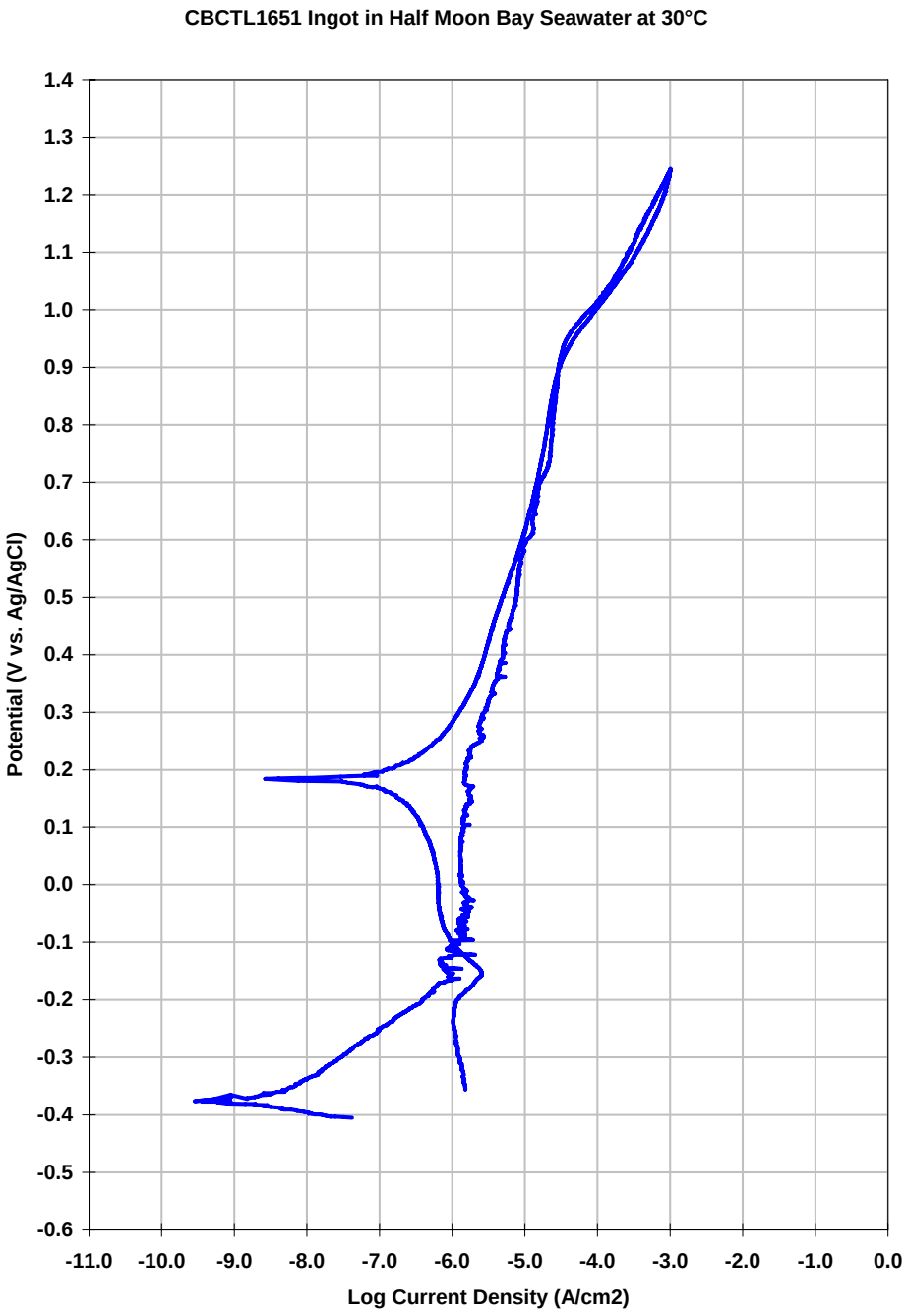

.

Figure 115 – Cyclic polarization of CBCTL1651, amorphous-metal, arc-melted, drop-cast ingot in Half Moon Bay seawater at 30℃ shows a very small hysteresis loop, and a repassivation potential close to the potential required for oxygen evolution. This new high-Mo, Fe-based, Y-containing amorphous metal performed well in ambient temperature seawater, superior to wrought and HVOF Alloy C-22.

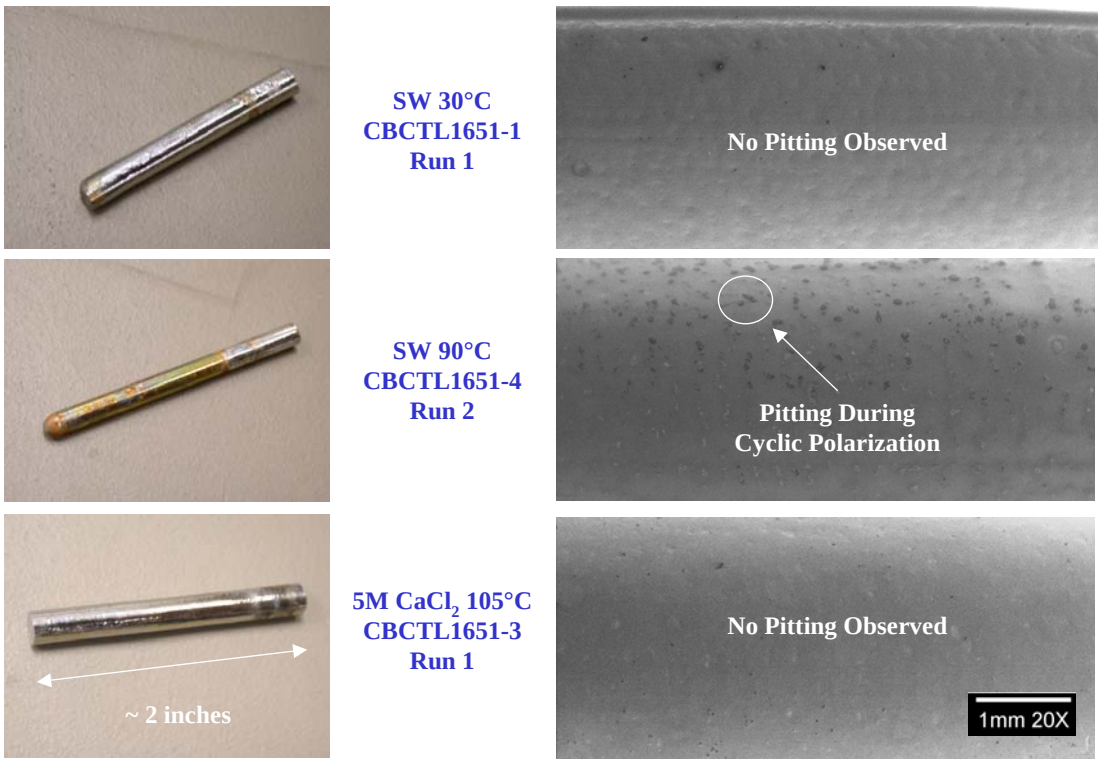

Figure 116 – Macro photographs and scanning electron micrographs of arc-melted drop-cast ingots after cyclic polarization to the oxygen evolution potential show no noticeable corrosive attack in seawater at 30℃ (top), the onset of pitting in seawater at 90℃ (middle), and no noticeable corrosive attack in 5M CaCl2 at 105℃ (bottom). In regard to the pitting observed in seawater at 90C, it is important to note that polarization to an extremely anodic potential, near oxygen evolution, was required for initiation.

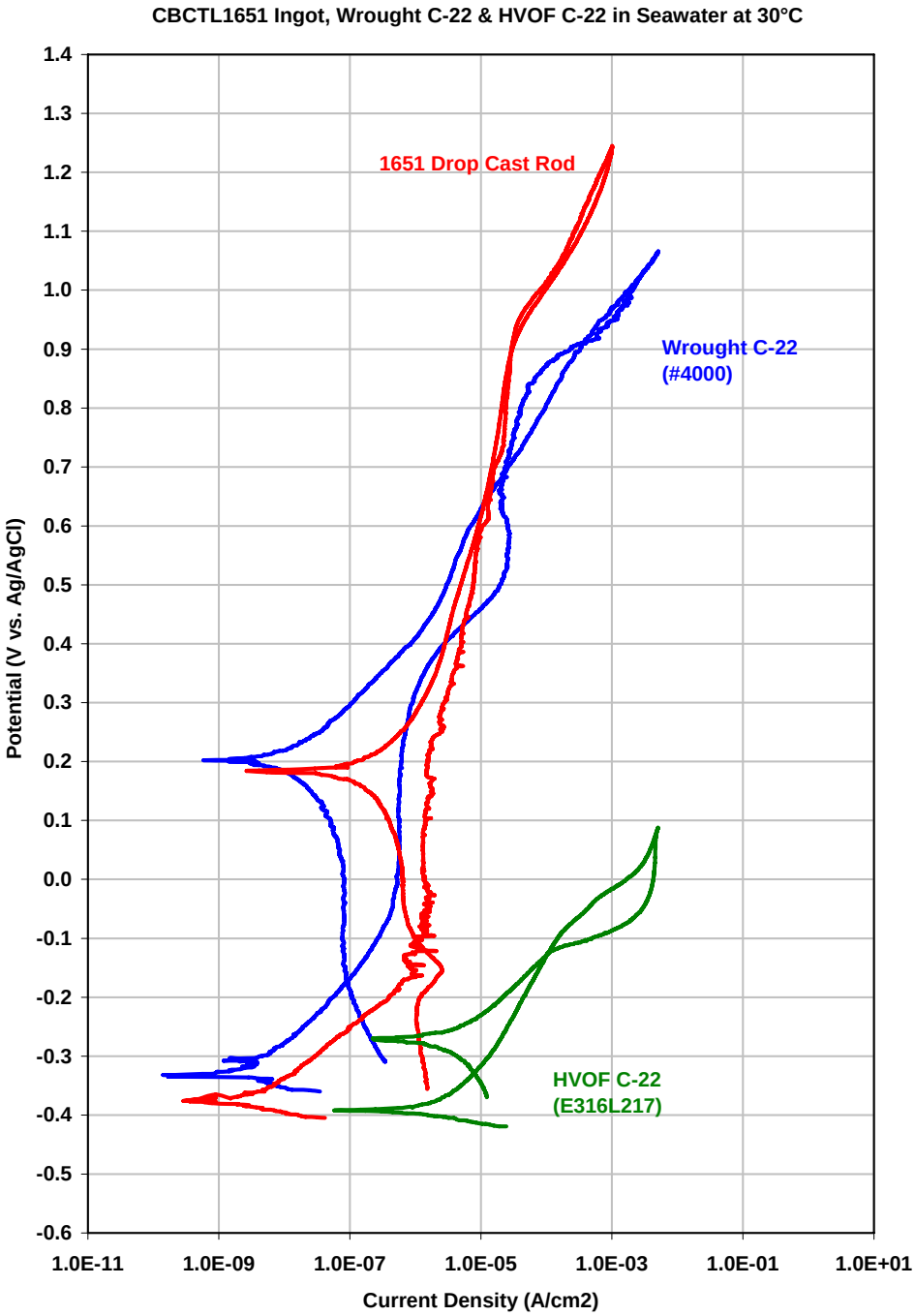

Figure 117 – A comparison of the cyclic polarization curves for a CBCTL1651 amorphous metal ingot, a sample of wrought nickel-based Alloy C-22, and a sample of thermal spray (HVOF) C-22 in ambient temperature Half Moon Bay seawater is shown. The CBCTL1651 amorphous metal has better corrosion resistance than both wrought and HVOF Alloy C-22. From the degraded performance of HVOF Alloy C-22, it is concluded that corrosion-resistant.

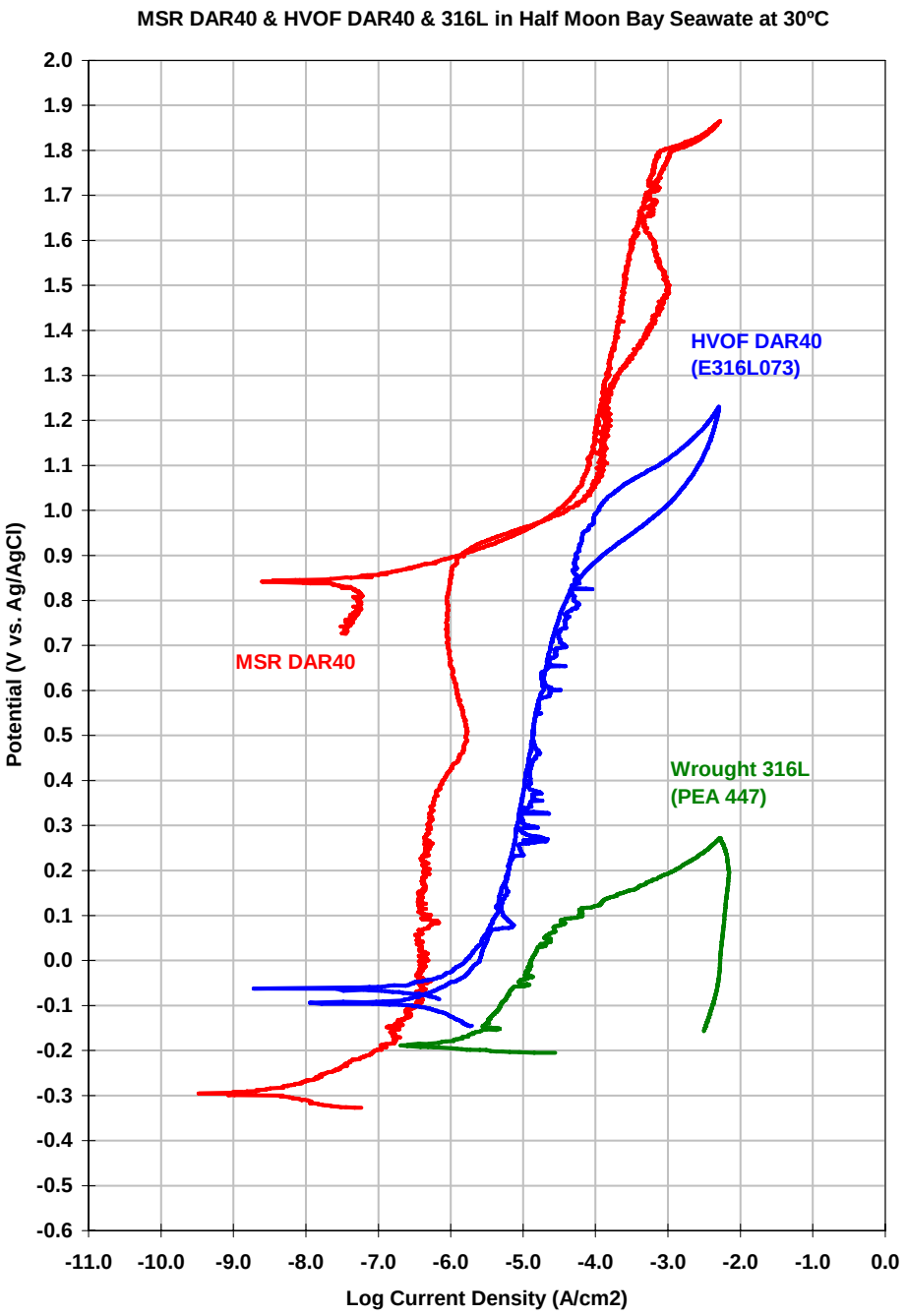

Figure 118 – The cyclic polarization curves for melt-spun ribbons and thermal-spray coatings of DAR40 are compared to that of wrought Type 316L stainless steel, all obtained with Half Moon Bay seawater at ambient temperature. In both cases, the performance of the DAR40 amorphous metal is better than that of the wrought stainless steel. Furthermore, the fully-dense ribbon of DAR40 is superior to the HVOF coating, which has residual porosity and crystalline structure.

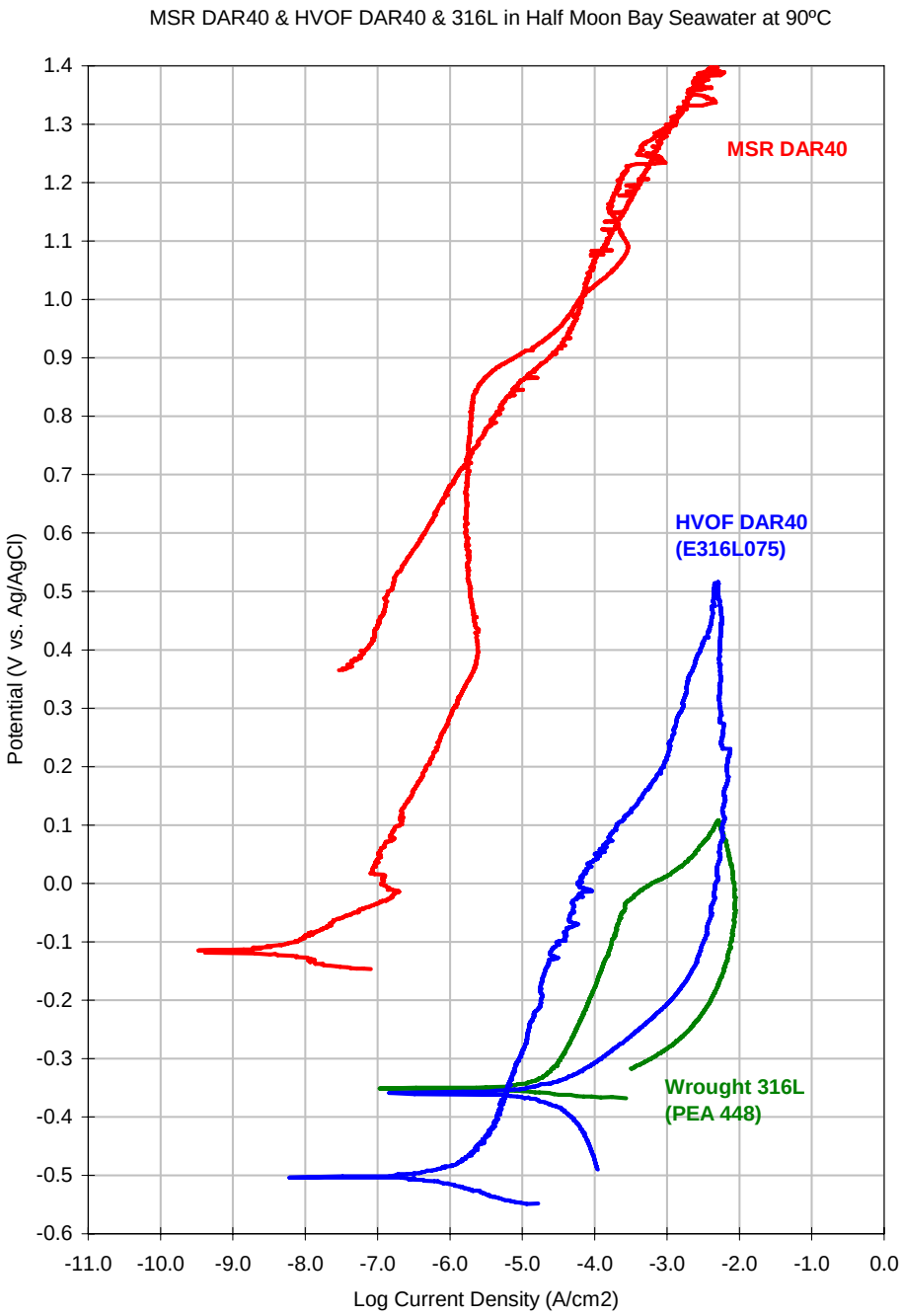

Figure 119 – The comparison shown here is similar to that shown in Figure 118, with the exception of the temperature. The data shown here are for Half Moon Bay seawater at 90°C. The fully dense ribbon of DAR40 maintains reasonable passivity as the temperature increases, whereas the performance of this early HVOF coating of DAR40 diminishes, and approaches that of Type 316L stainless steel.

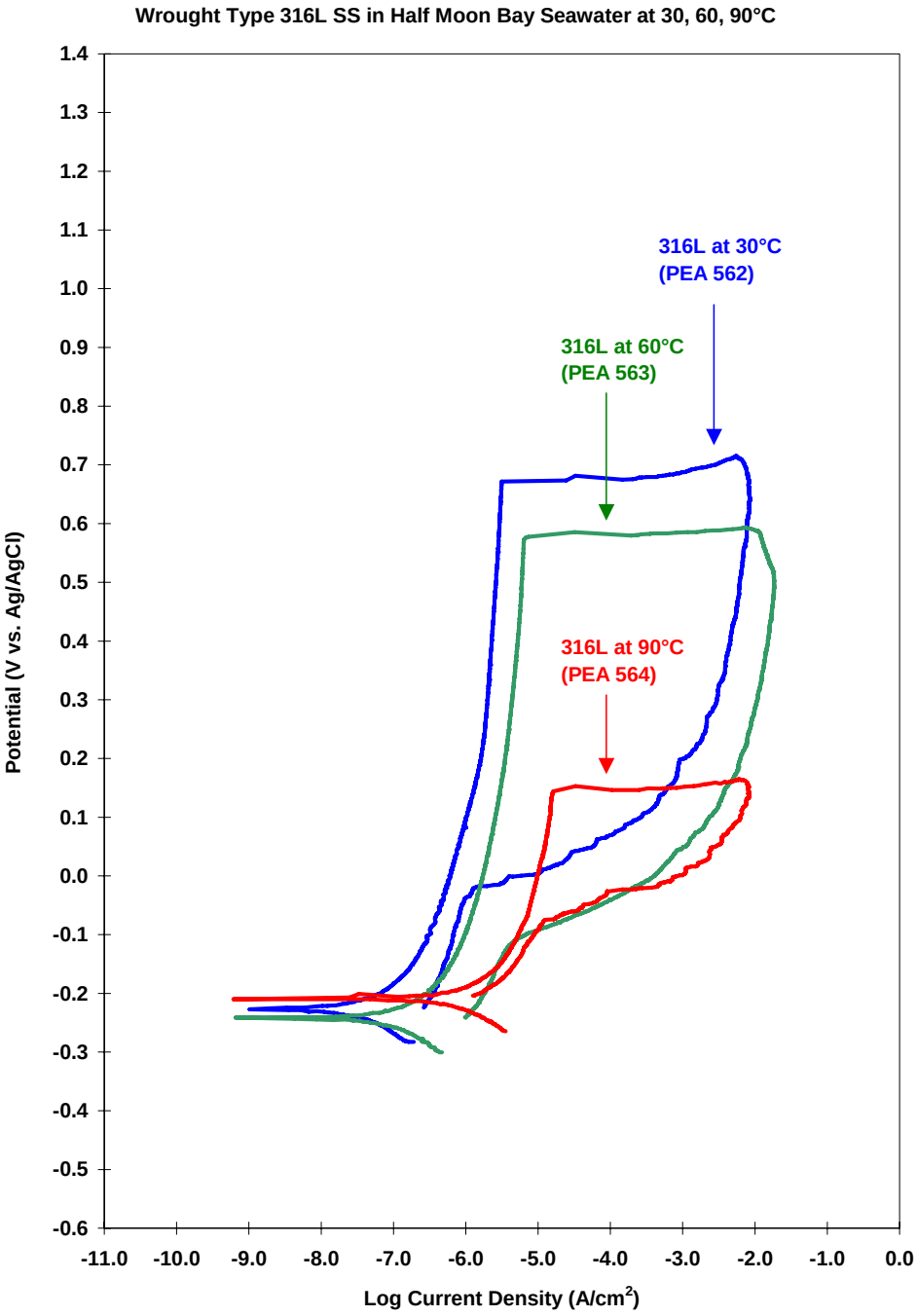

Figure 120 – In contrast to the amorphous metals that are under development, Type 316L stainless steel shows relatively poor resistance to localized corrosion in seawater, even at ambient temperature.

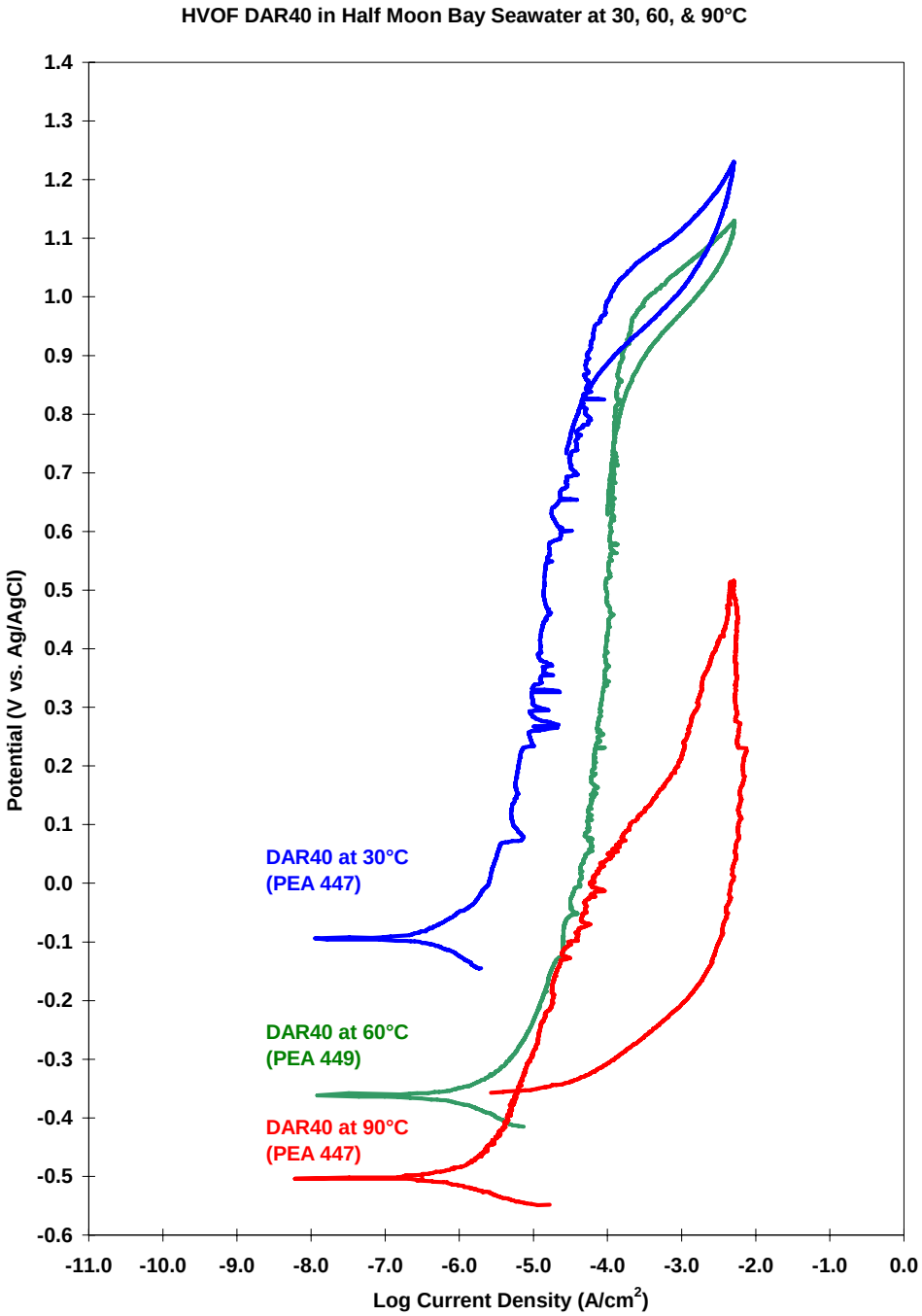

Figure 121 – The corrosion resistance, quantified with cyclic polarization, is temperature dependence. The polarization curves for DAR40 at 30, 60 and 90℃ show outstanding resistance to localized attack at 30 and 60℃, but substantially reduced corrosion resistance at 90℃.

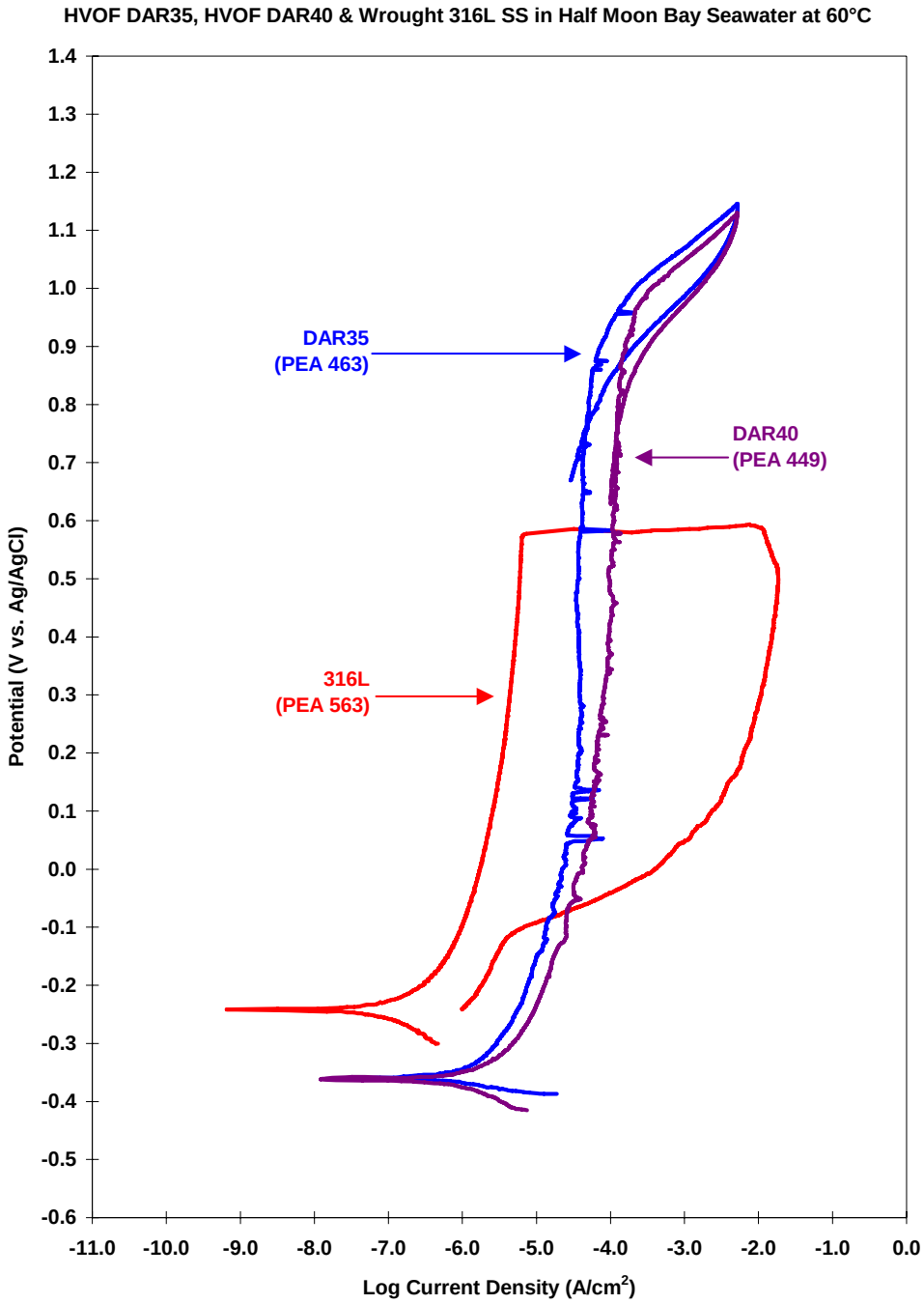

Figure 122 – Cyclic polarization measurements of early DAR35 and DAR40 coatings, deposited with HVOF, showed greater resistance to local corrosion in ambient temperature seawater than wrought, Type 316L stainless steel. The passive film on Type 316L stainless steel experienced catastrophic breakdown at approximately 600 mV relative to a standard Ag/AgCl reference electrode, whereas no breakdown was experienced with DAR35 and DAR40 until the potential was pushed to levels where oxygen evolution occurs.

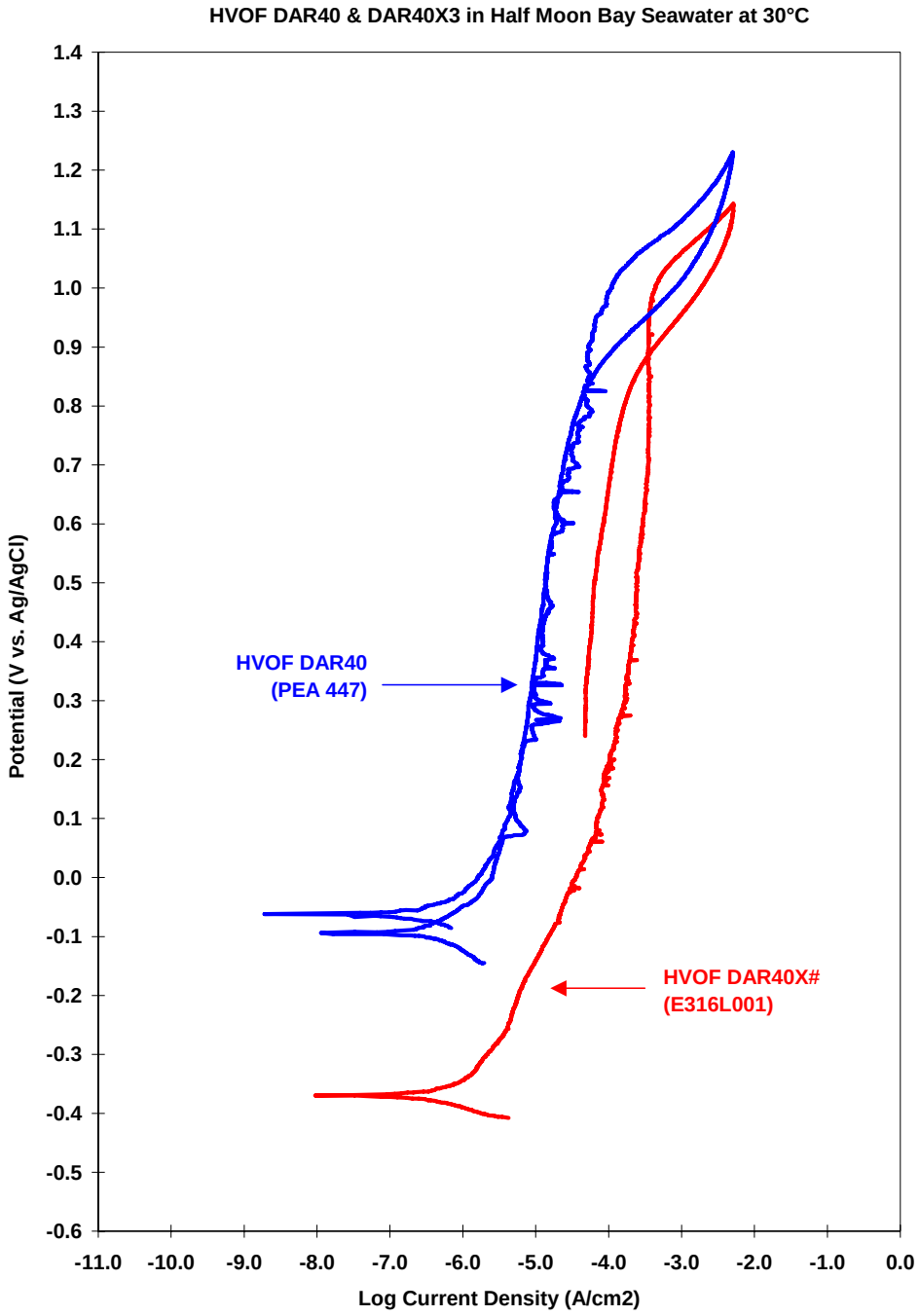

Figure 123 – Comparison of the cyclic polarization curves for DAR40 and DAR40X3 HVOF coatings in Half Moon Bay seawater at ambient temperature. Both coatings have relatively repassivation potentials (~900 mV vs. Ag/AgCl). The differences in apparent current density are attributed to differences in surface roughness.

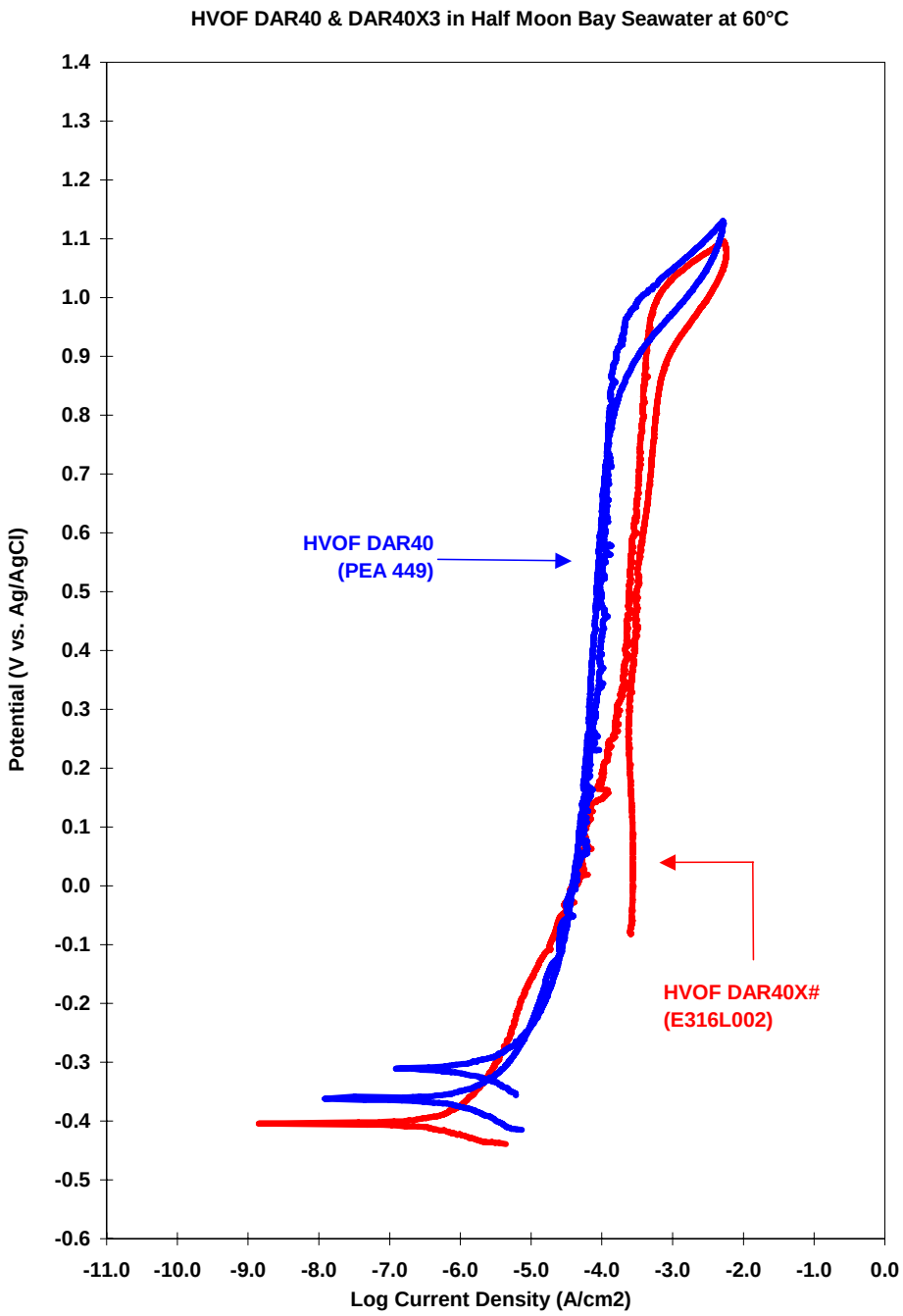

Figure 124 – The data compared in this figure is similar to that compared in Figure 123, with the exception of the test temperature, which was higher in this case.

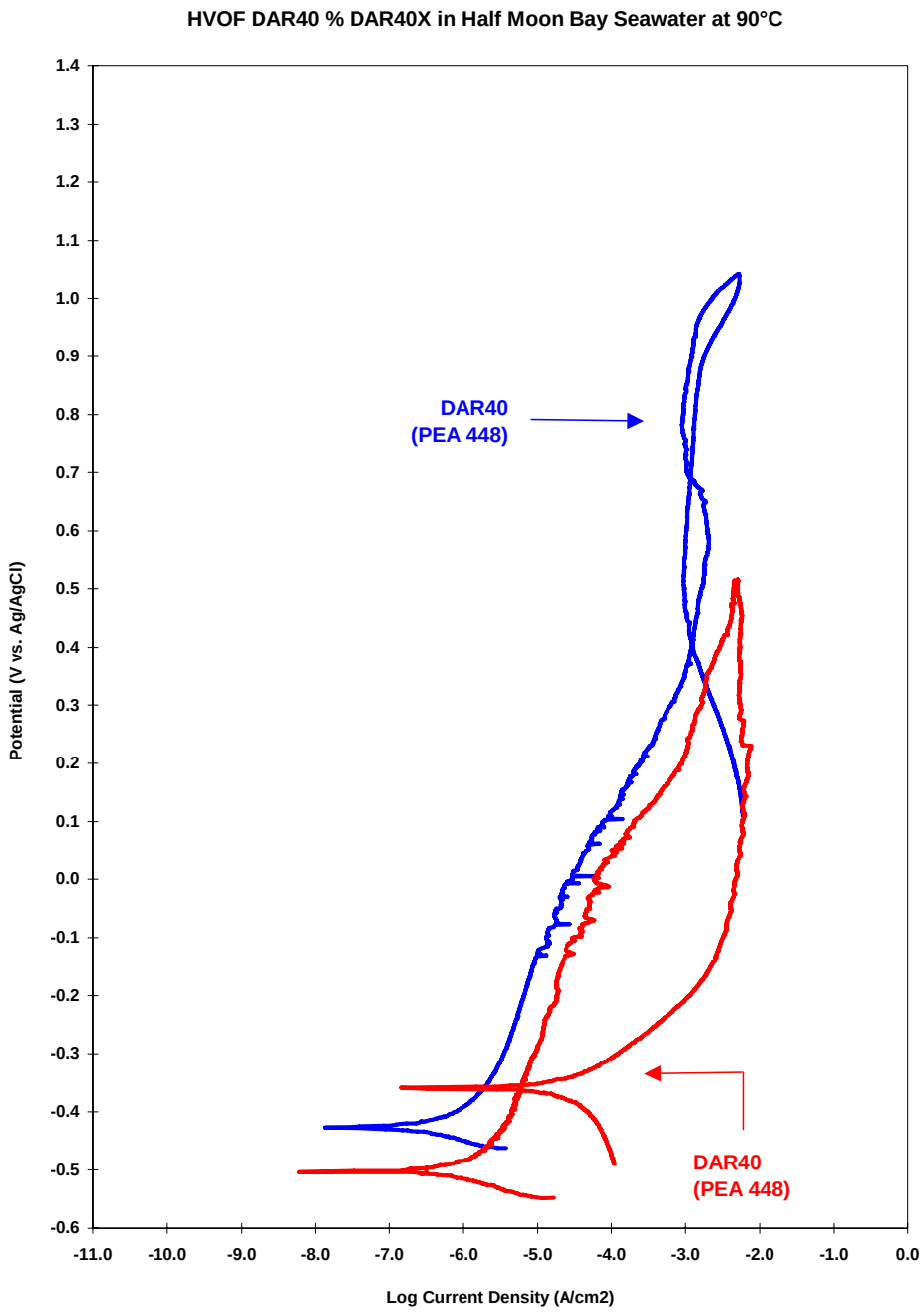

Figure 125 – The data compared in this figure is similar to that compared in Figure 124, with the exception of the test temperature, which was higher in this case.

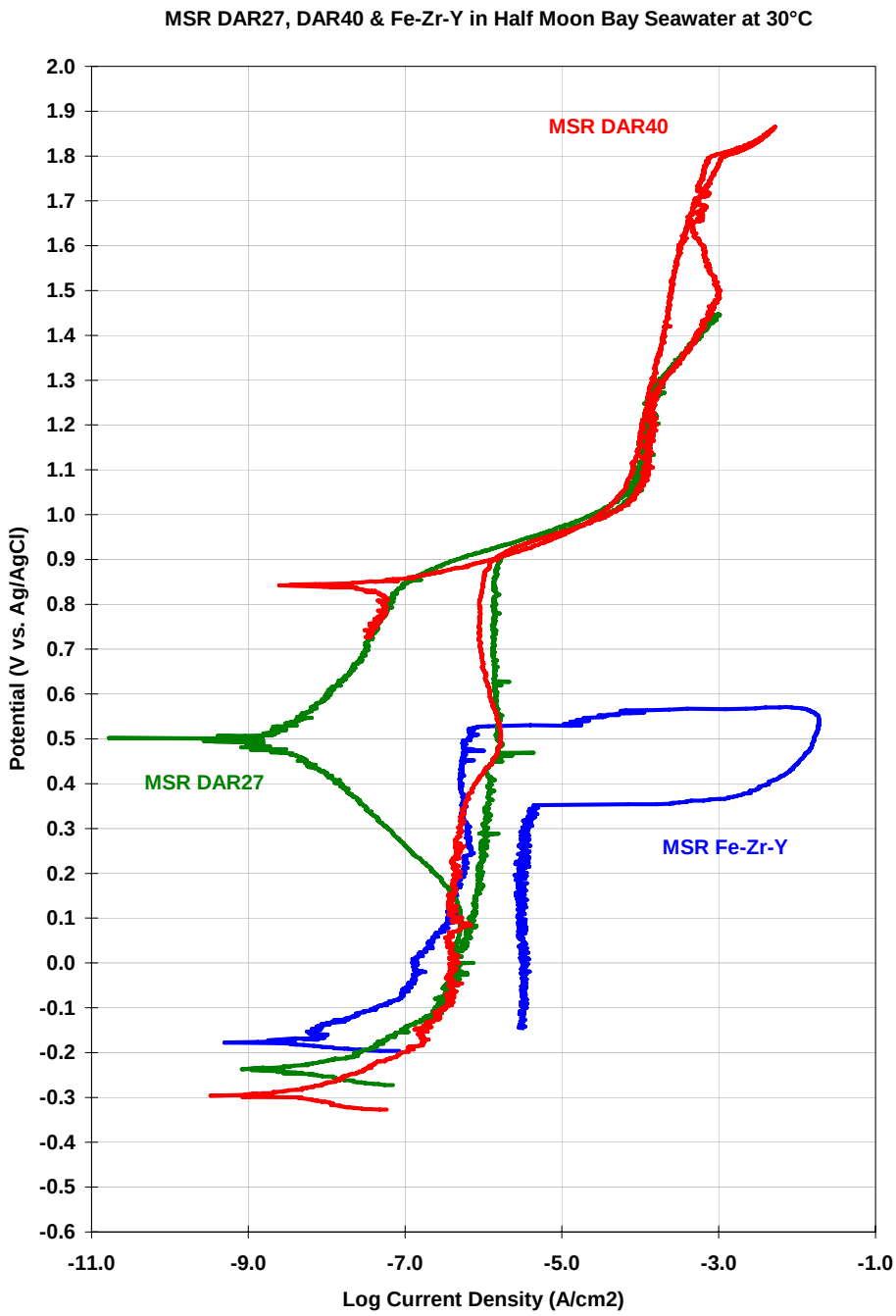

Figure 126 – Cyclic polarization of melt-spun ribbons of DAR27, DAR40 and Fe-Zr-Y amorphous-metal formulations in Half Moon Bay seawater at ambient temperature show no passive film breakdown (or hysteresis loop) with DAR27 and DAR40. However, in the case of the Fe-Zr-Y material, a large excursion in the anodic current density was observed at 500 mV during the forward scan, with the corresponding hysteresis loop evident.

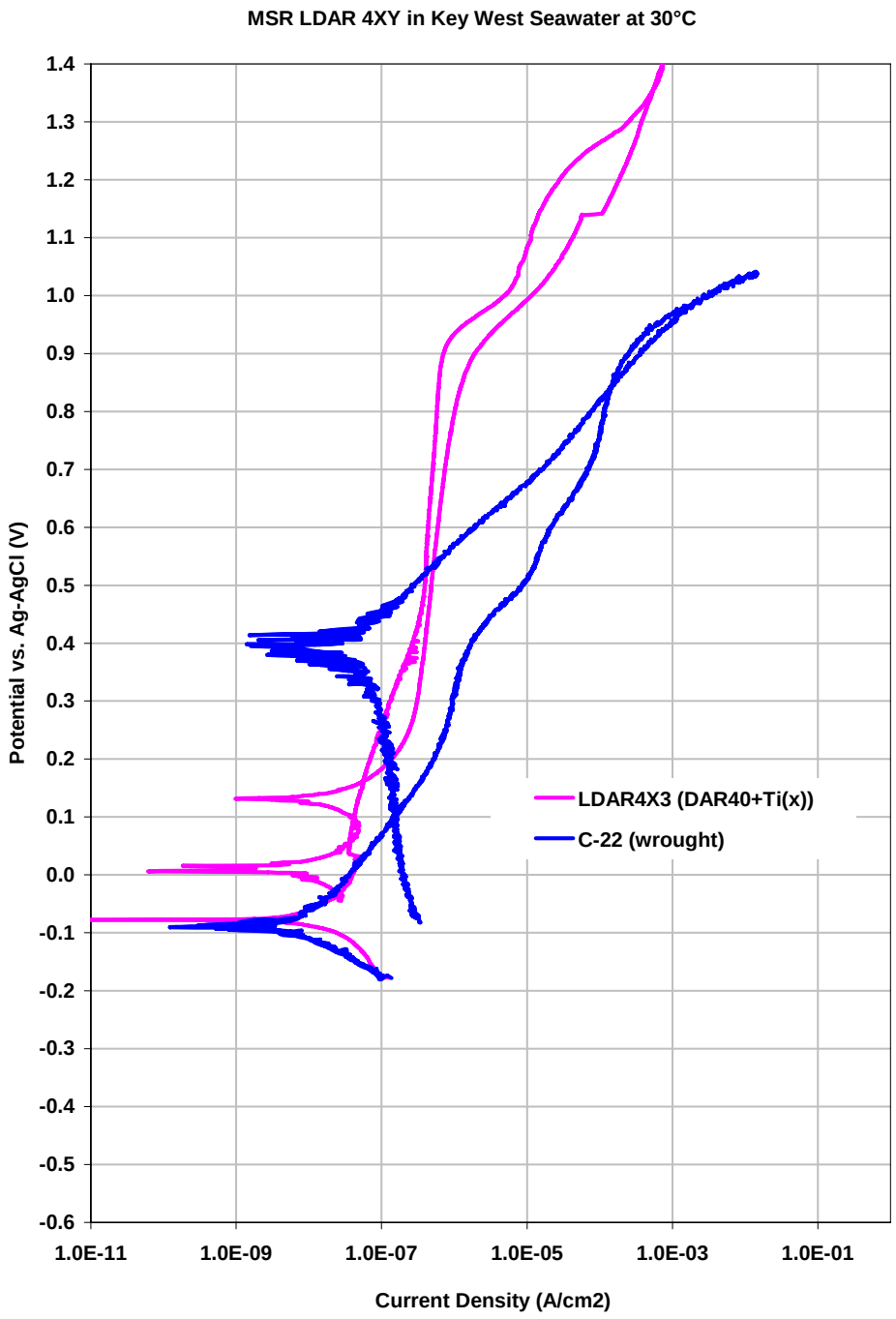

Figure 127 – A comparison of the cyclic polarization curve for LDAR4X3 melt-spun ribbon to that of wrought nickel-based Alloy C-22 in Key West seawater at 30°C shows that the amorphous metal has lower passive current density than Alloy C-22. LDAR4X4 is a variant of DAR40 with a titanium addition of 3 atomic percent. Note that the current density (corrosion rate) of Alloy C-22 is an order-of-magnitude higher than that of the amorphous metal at 400 mV vs. Ag/AgCl.

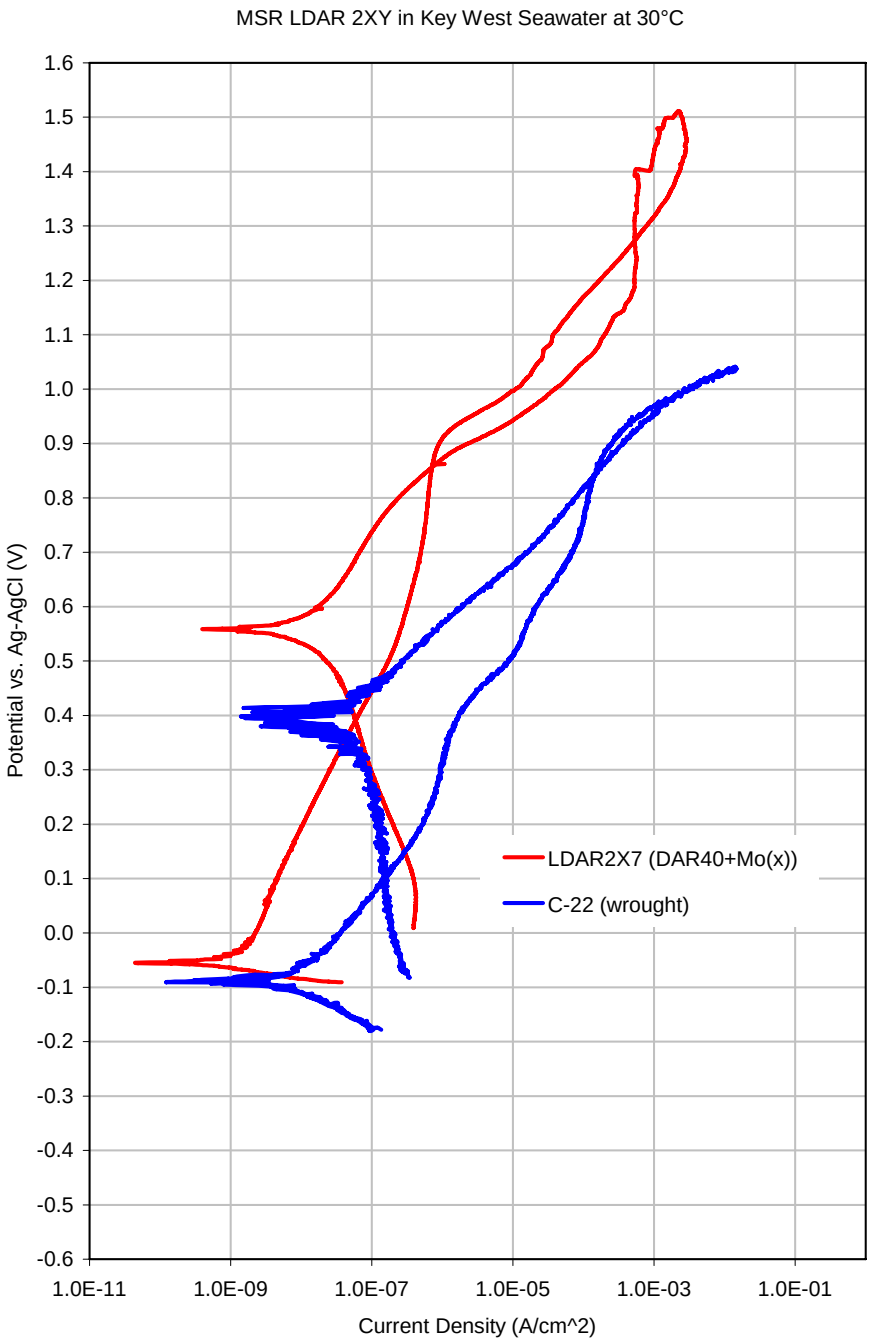

Figure 128 – Comparison of cyclic polarization data for melt-spun ribbon of LDAR2X7 to that of wrought nickel-based Alloy C-22 in Key West seawater at 30°C. Increases in the molybdenum concentration, from 1 to 5 atomic % (not shown) causes a corresponding increase in the amplitude of the anodic oxidation peak, whereas the increase to 7 atomic % causes an overall drop in the passive current density, and associated corrosion rate. Note that the current density (corrosion rate) of Alloy C-22 is almost two orders-of-magnitude higher than that of the amorphous metal at 400 mV vs. Ag/AgC.

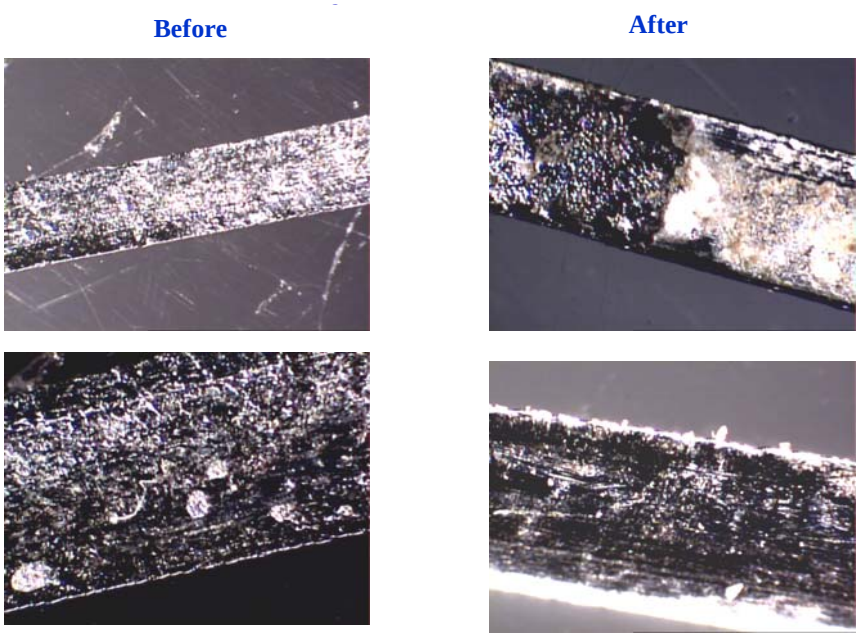

Figure 129 – Macro photographs of melt spun ribbons of LDAR2X1 (only 1 atomic percent molybdenum) after cyclic polarization in seawater from Key West at 30℃. There may be some evidence of corrosion, but at high anodic potential, close to that required for oxygen evolution.

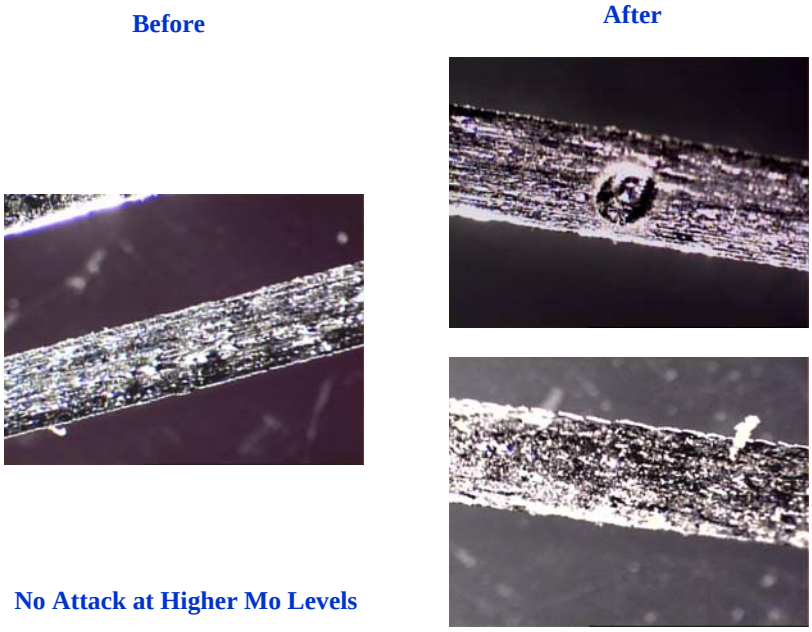

Figure 130 – Macro photographs of melt spun ribbons of LDAR2X3 (3 atomic percent molybdenum) after cyclic polarization in seawater from Key West at 30℃. There is no apparent evidence of corrosion, even after polarization at potentials close to that required for oxygen evolution. It is therefore concluded that a minimum molybdenum concentration of 3 atomic percent is needed in the parent Fe-based amorphous metal to prevent localized corrosion in ambient temperature seawater.

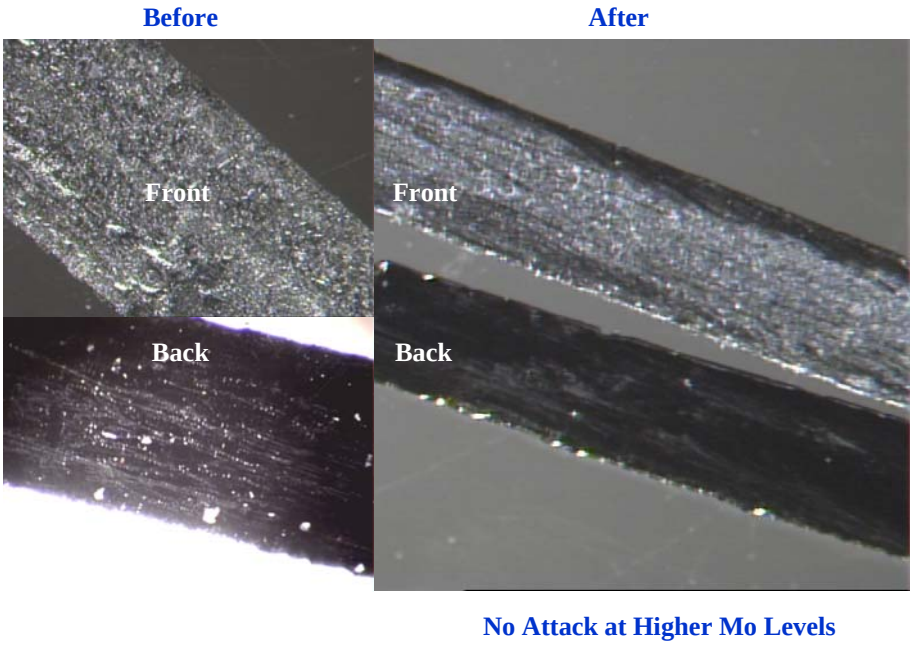

Figure 131 – Macro photographs of melt spun ribbons of LDAR2X7 (7 atomic percent molybdenum) after cyclic polarization in seawater from Key West at 30℃. There is no apparent evidence of corrosion, even after polarization at potentials close to that required for oxygen evolution. The parent Fe-based amorphous metal with an addition of molybdenum at 7 atomic percent performs very well.

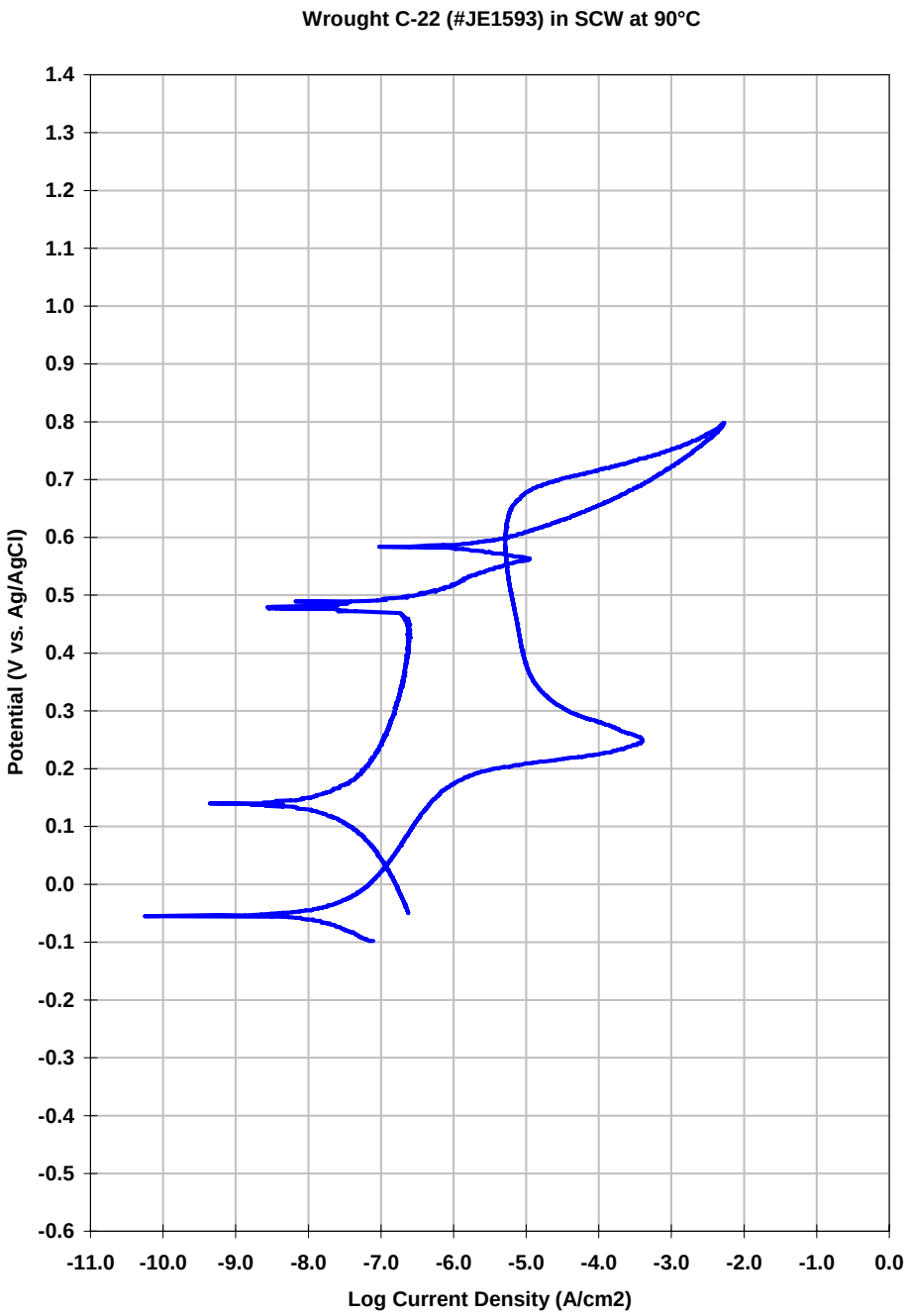

Figure 132 – Cyclic polarization of wrought Alloy C-22 in a standard bicarbonate solution at 90℃. This bicarbonate brine is known as SCW (simulated concentrated water) and used for evaluating alloy performance for repository applications. A small hysteresis loop is observed, indicating breakdown of the passive film. After scan reversal, repassivatioin occurs at 600 mV, a level much higher than the open-circuit corrosion potential. The large anodic oxidation peak between 200 and 300 mV is attributed to the oxidation of molybdenum in the passive film.

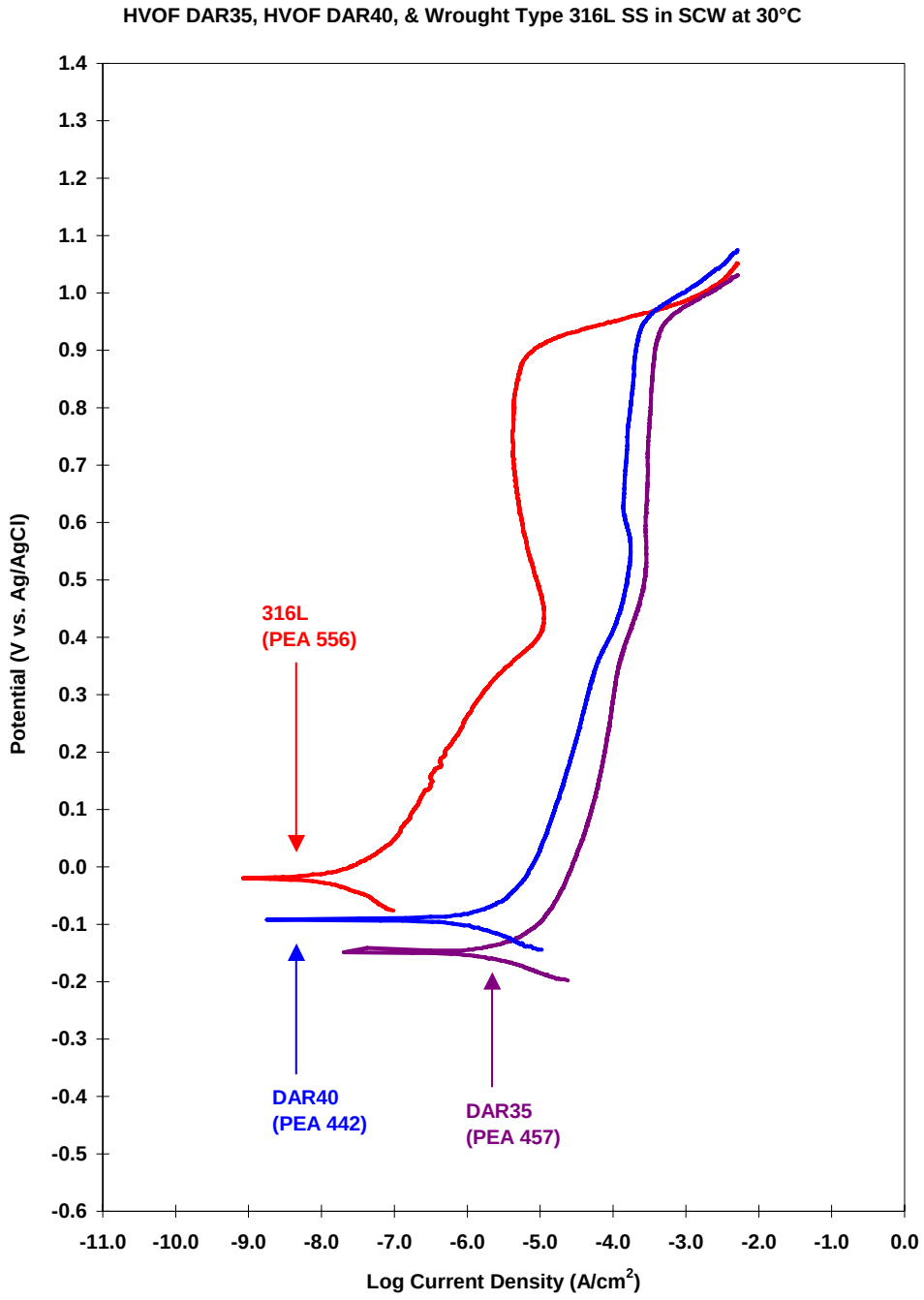

Figure 133 – This figure shows the cyclic polarization curves (positive scans) for early DAR35 and DAR40 HVOF coatings, as well as for Type 316L stainless steel. The tests were conducted in a bicarbonate-brine test solution (SCW) at 30℃. All three materials he amorphous metals have comparable performance (based upon threshold potential) in such benign solutions. The DAR35 and DAR40 HVOF coatings show higher current densities than the fully dense Type 316L stainless steel due to the greater surface roughness of these early coatings.

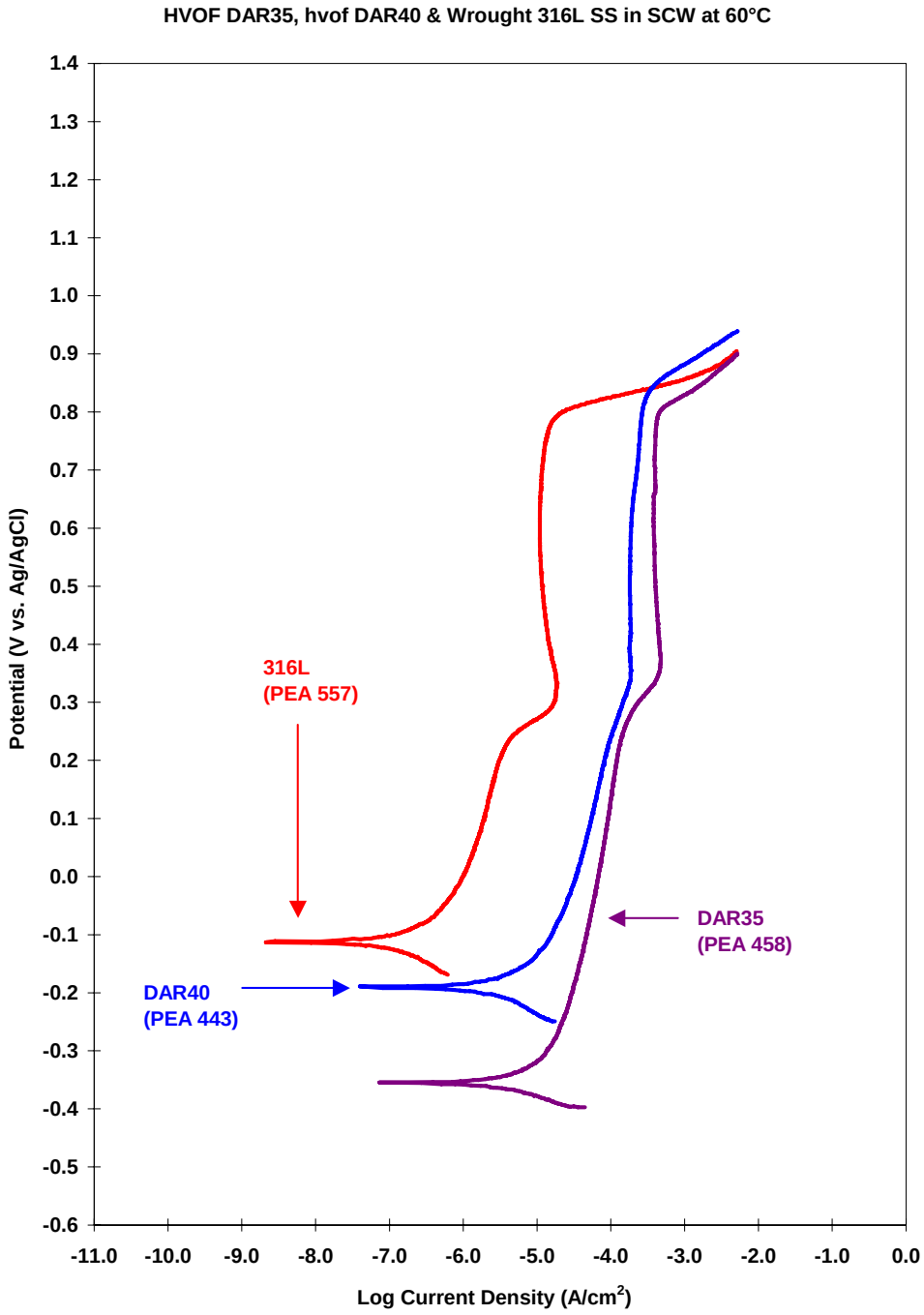

Figure 134 – The data compared in this figure is similar to that compared in Figure 133, with the exception of the test temperature, which was higher in this case.

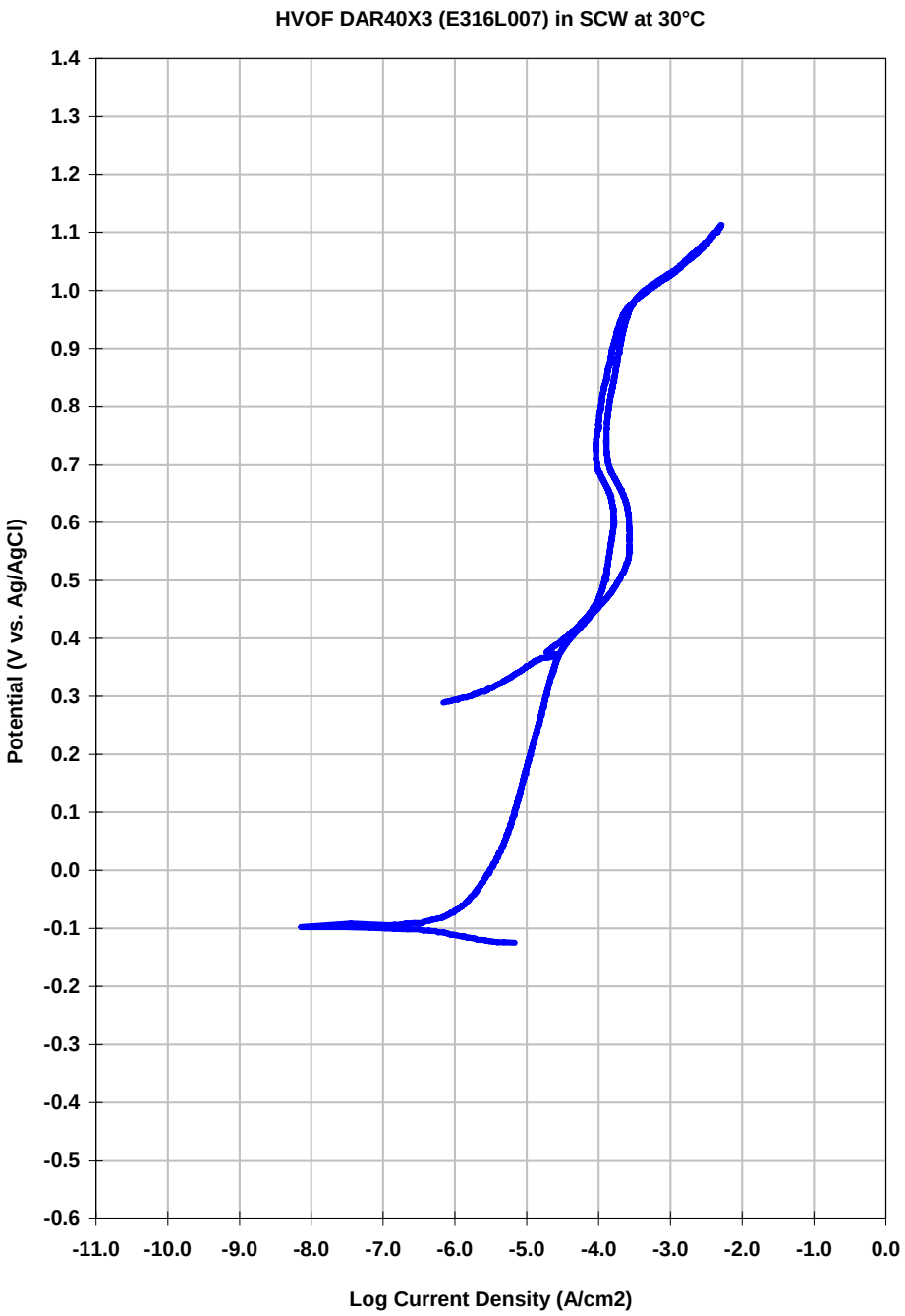

Figure 135 – Cyclic polarization of HVOF DAR40X3 in concentrated bicarbonate test solution (SCW) at 30℃ shows the anodic peak typical of Mo-containing alloys between 400 to 700 mV vs. Ag/AgCl, and no loss of passivity with reversal potentials as high as 1100 mV vs. Ag/AgCl.

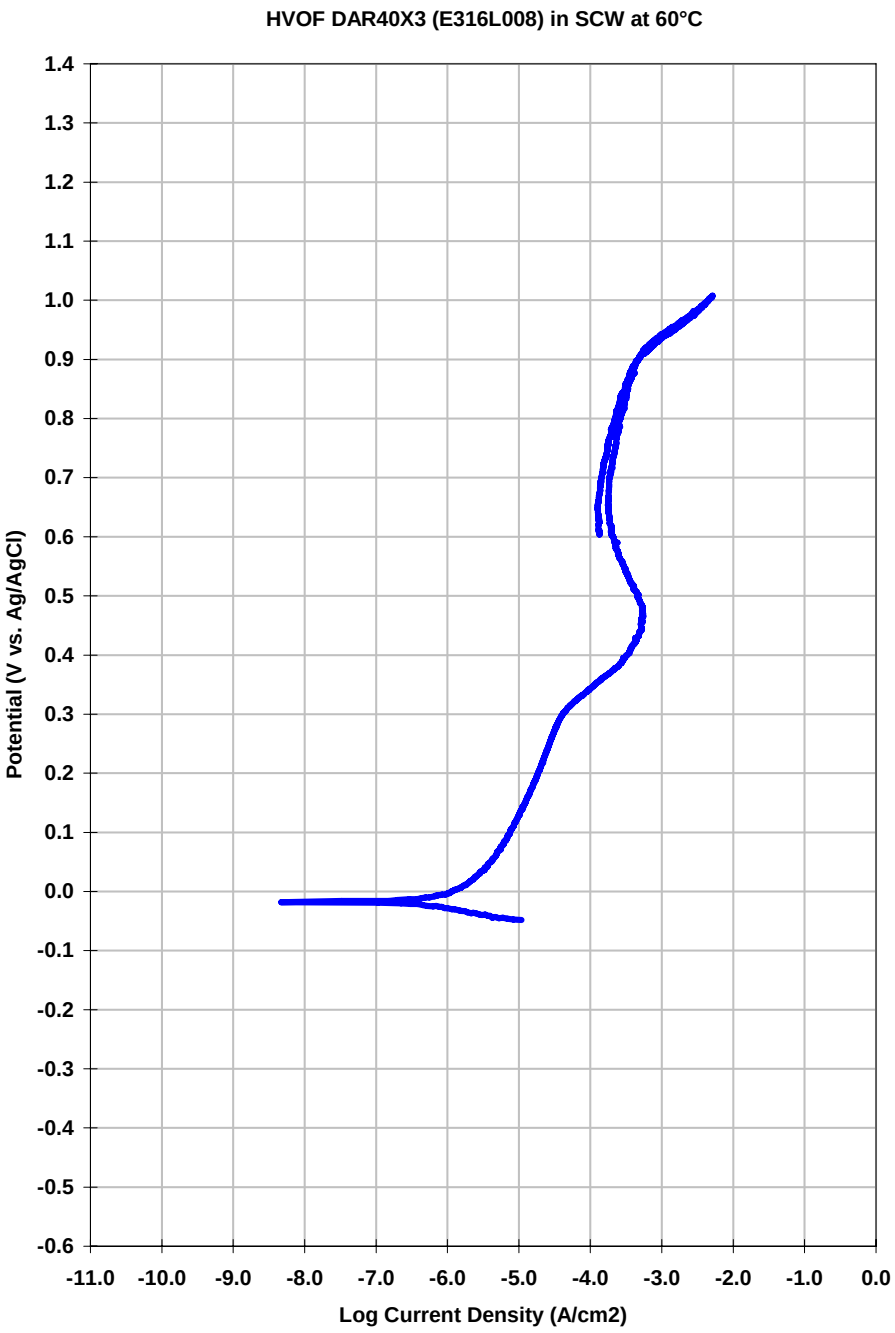

Figure 136 – Cyclic polarization of HVOF DAR40X3 in concentrated bicarbonate test solution (SCW) at 60℃ shows the anodic peak typical of Mo-containing alloys between 300 to 600 mV vs. Ag/AgCl, and no loss of passivity with reversal potentials as high as 1000 mV vs. Ag/AgCl. The anodic oxidation peak is shifted about -100 mV for the first 30℃ increase in temperature.

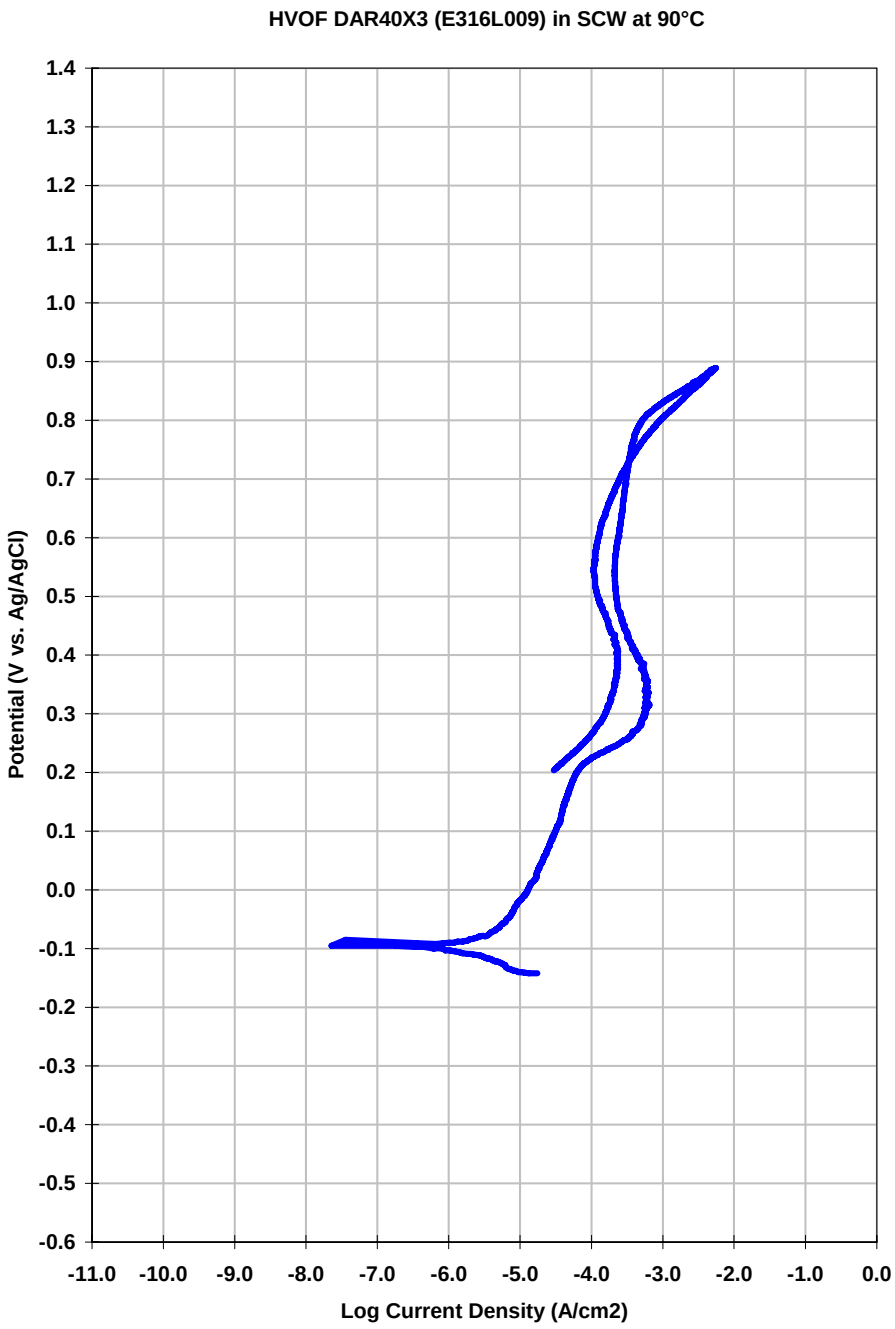

Figure 137 – Cyclic polarization of HVOF DAR40X3 in concentrated bicarbonate test solution (SCW) at 90℃ shows the anodic peak typical of Mo-containing alloys between 200 to 500 mV vs. Ag/AgCl, and no loss of passivity with reversal potentials as high as 900 mV vs. Ag/AgCl. The anodic oxidation peak is shifted about -100 mV for every 30℃ increase in temperature.

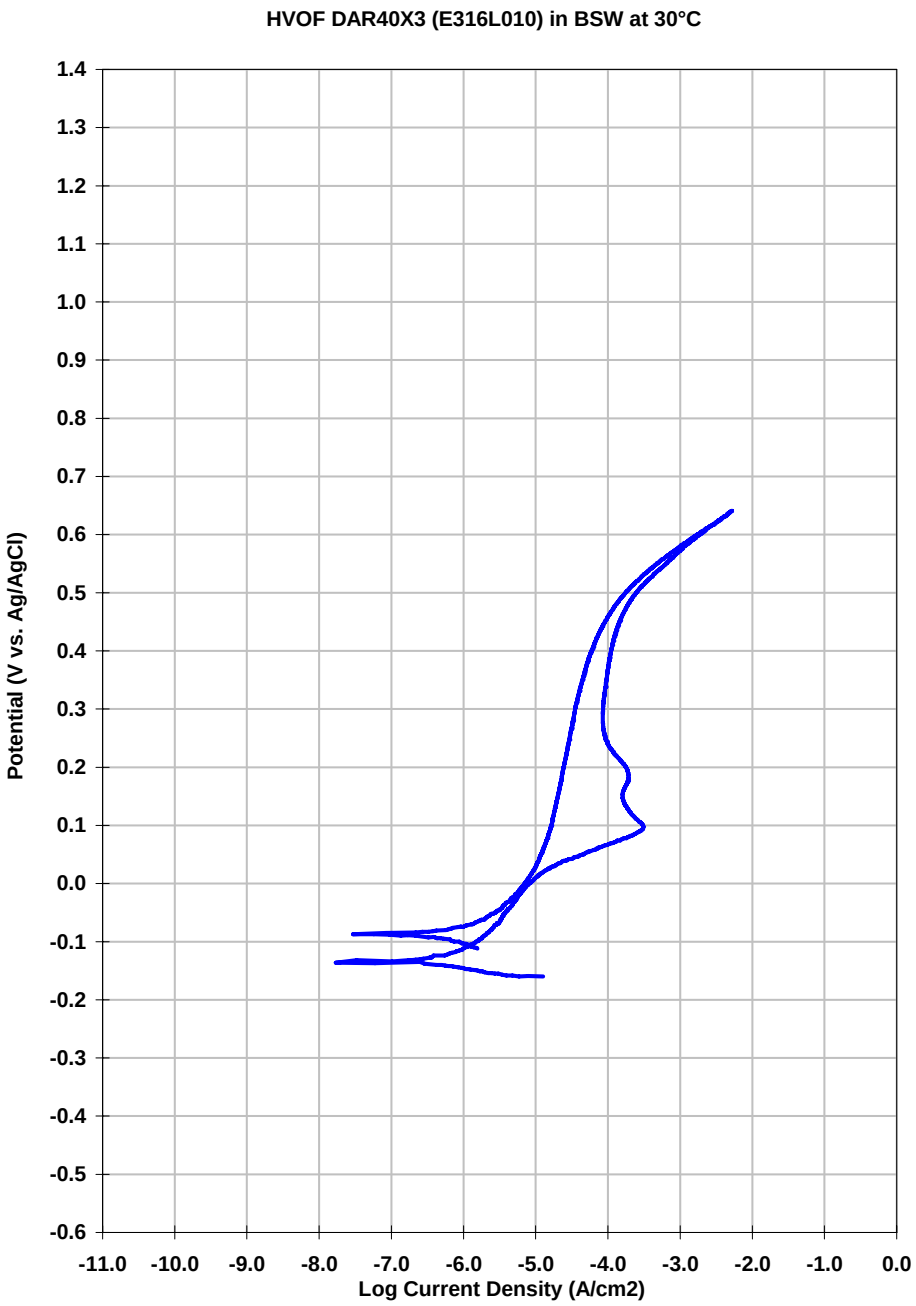

Figure 138 – Cyclic polarization of HVOF DAR40X3 in standard near-saturation bicarbonate test solution (BSW) at 30°C shows two anodic peaks (100 and 200 mV vs. Ag/AgCl) and no loss of passivity with reversal potentials as high as 650 mV vs. Ag/AgCl. At least one of these anodic oxidation peaks may also be associated with the oxidation of Mo in the passive film.

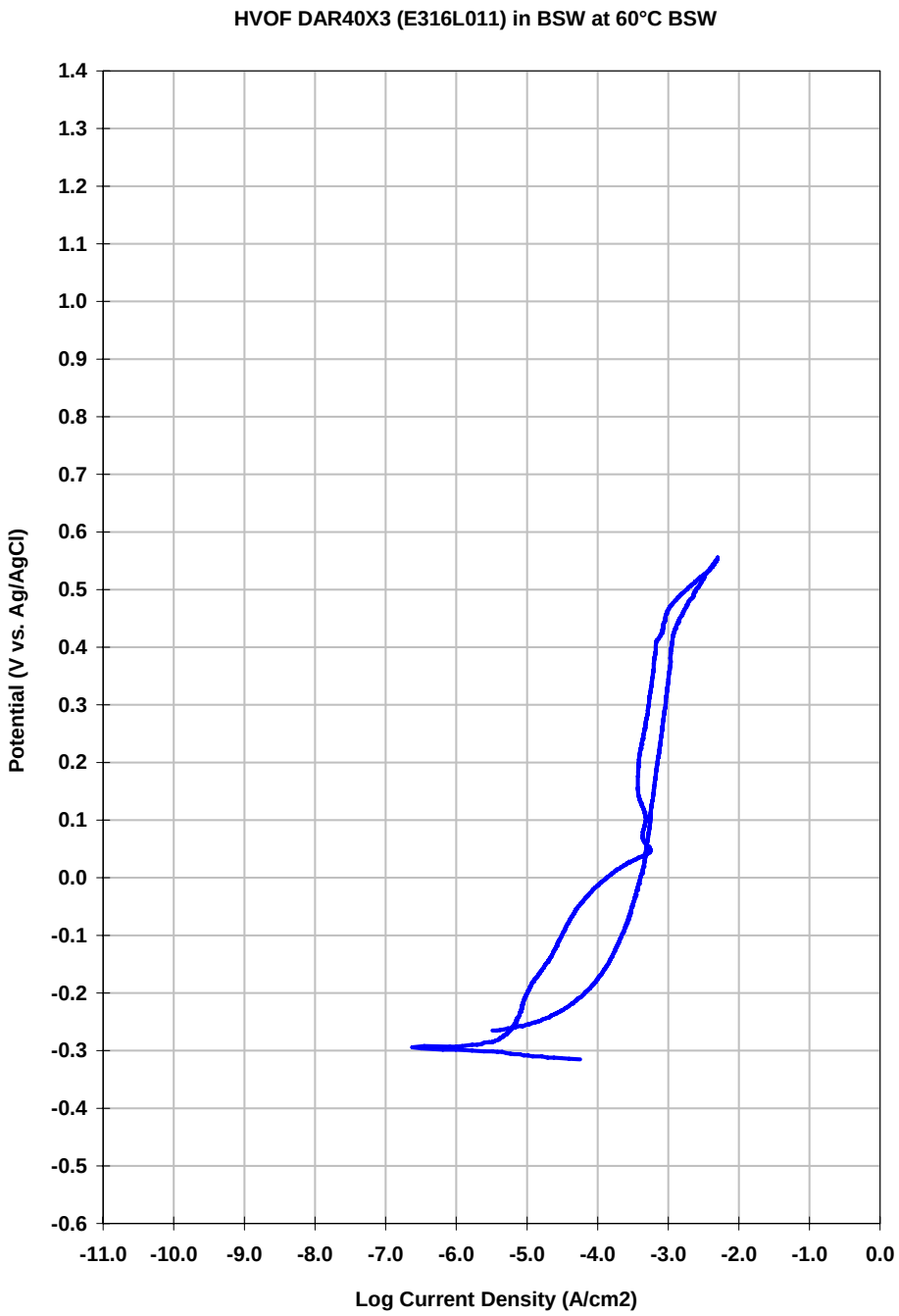

Figure 139 – Cyclic polarization of HVOF DAR40X3 in standard near-saturation bicarbonate test solution (BSW) at 60°C shows two anodic peaks (50 and 100 mV vs. Ag/AgCl). A hysteresis loop is observed, however, a simultaneous loss of passivity has not yet been confirmed. At least one of these anodic oxidation peaks may also be associated with the oxidation of Mo in the passive film.

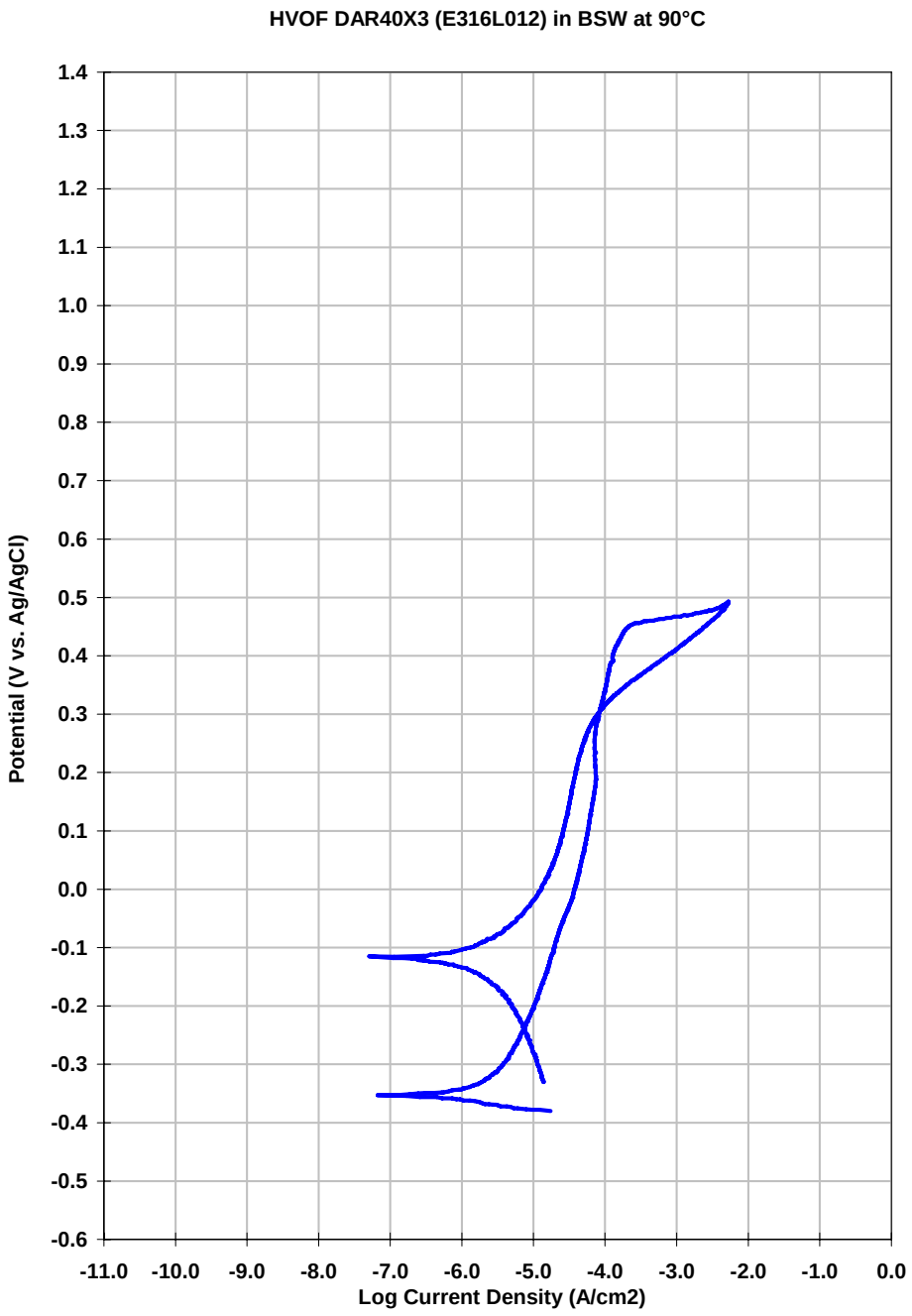

Figure 140 – Cyclic polarization of HVOF DAR40X3 in standard near-saturation bicarbonate test solution (BSW) at 90℃ shows no distinct anodic peak. A hysteresis loop is observed, however, a simultaneous loss of passivity has not yet been confirmed.

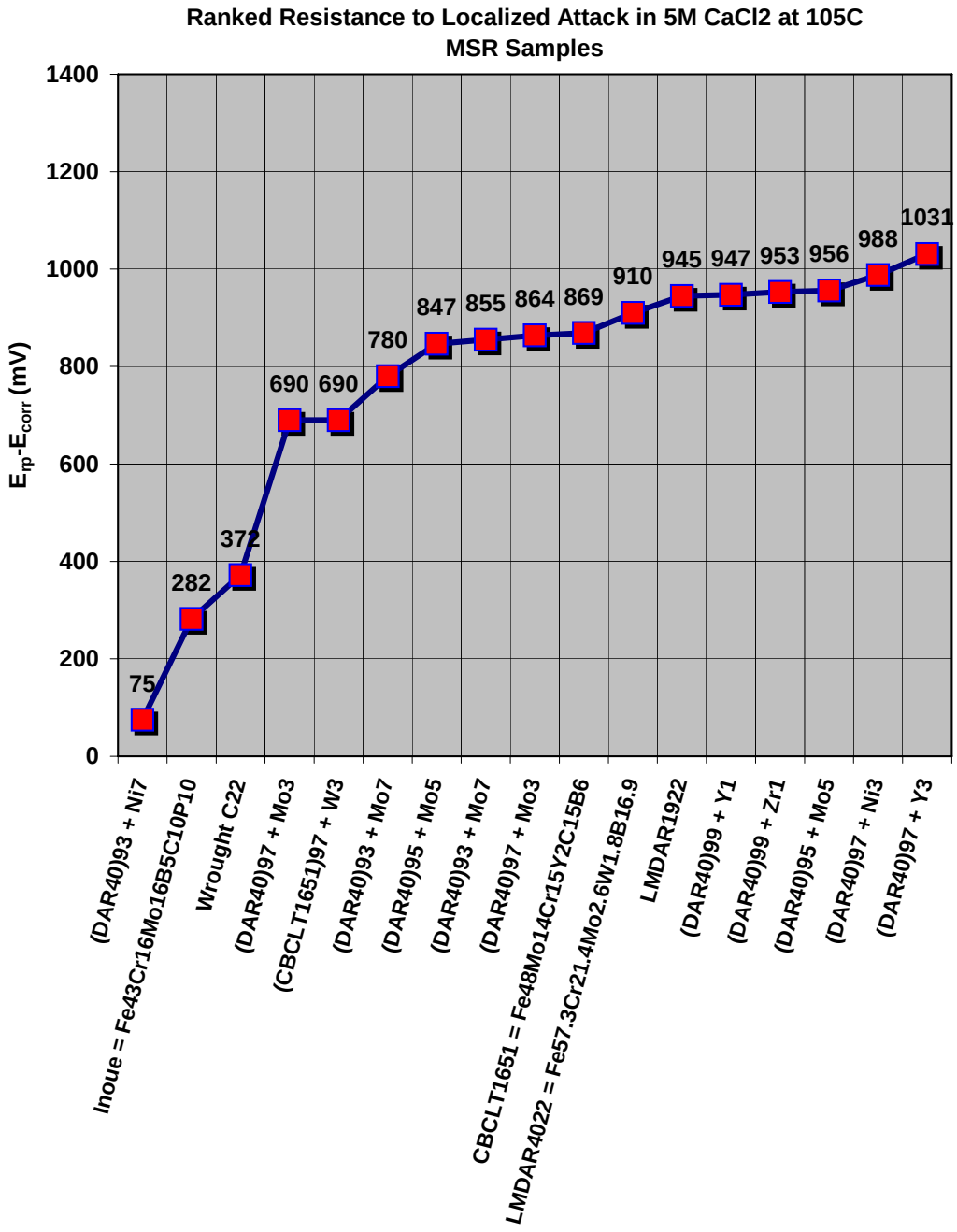

Figure 141 – (a) Various alloy samples, ranked based upon their measured resistance to localized corrosion ($\Delta E=E_{corr}-E_{rp}$) in 5M $CaCl_2$ at 105°C. Most of the amorphous-samples performed very well in this aggressive environment. In contrast, wrought nickel-based Alloy C-22 (N06022) performed relatively poorly, as did the P-containing, Fe-based metallic glass, and the LDAR1X7 with high nickel content (7 atomic percent).

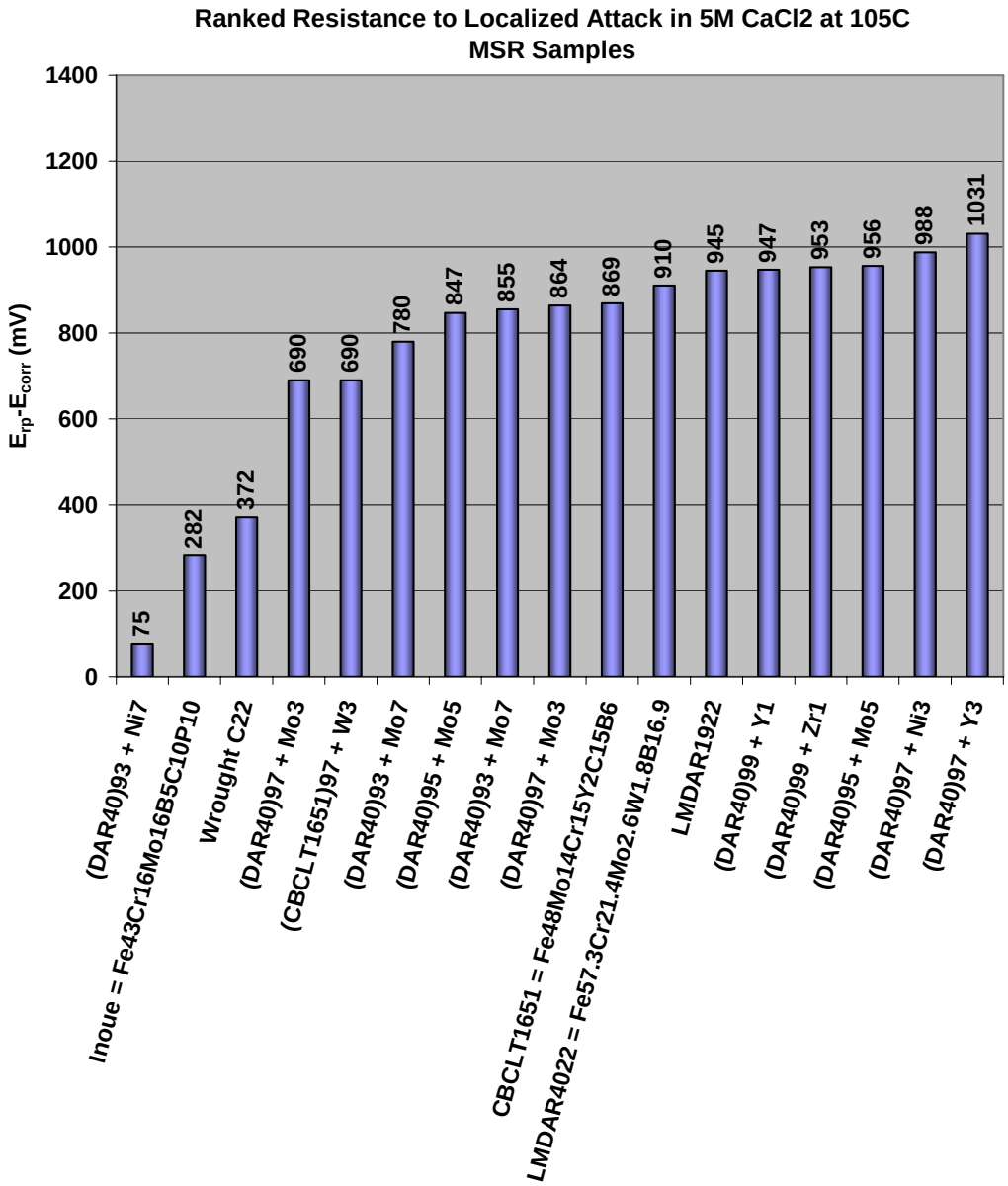

Figure 141 – (b) Various alloy samples, ranked based upon their measured resistance to localized corrosion ($\Delta E=E_{corr}-E_{rp}$) in 5M $CaCl_2$ at 105°C. Most of the amorphous-samples performed very well in this aggressive environment. In contrast, wrought nickel-based Alloy C-22 (N06022) performed relatively poorly, as did the P-containing, Fe-based metallic glass, and the LDAR1X7 with high nickel content (7 atomic percent).

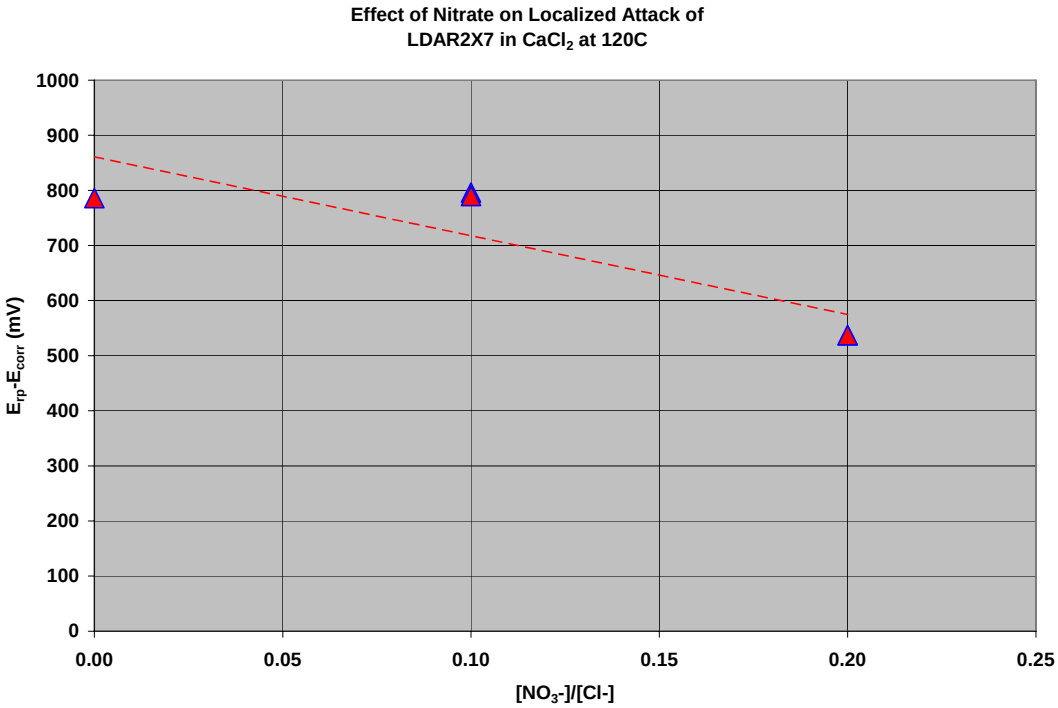

Figure 142 – Nitrate anion serves as an inhibitor to localized attack of nickel-based Alloy C-22 in concentrated calcium chloride solutions. A parametric study was performed to determine the effects of nitrate on the susceptibility of LDAR2X7 (7 atomic percent molybdenum) to localized in concentrated calcium chloride at 120°C. In contrast to the inhibitory effect observed with nickel-based austenitic alloys such as C-22, nitrate additions cause a slight decrease in the the difference between the repassivation and open-circuit corrosion potentials.

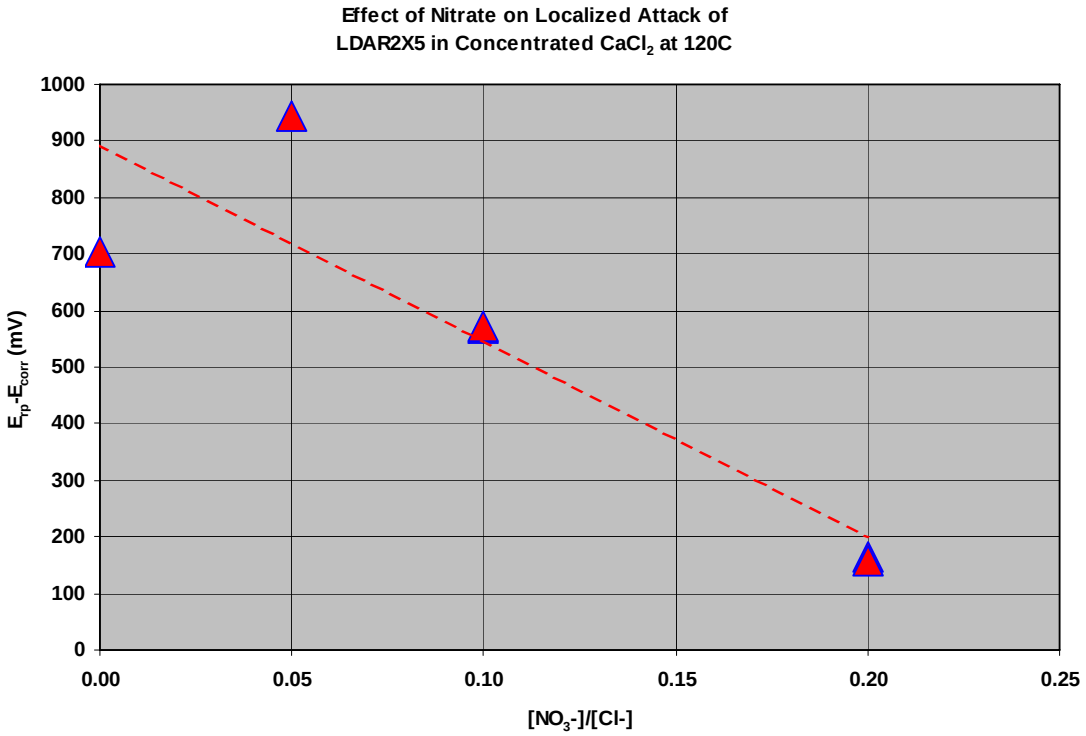

Figure 143 – Nitrate anion serves as an inhibitor to localized attack of nickel-based Alloy C-22 in concentrated calcium chloride solutions. A parametric study was performed to determine the effects of nitrate on the susceptibility of LDAR2X5 (5 atomic percent molybdenum) to localized in concentrated calcium chloride at 120°C. In contrast to the inhibitory effect observed with nickel-based austenitic alloys such as C-22, nitrate additions cause a significant decrease in the difference between the repassivation potential and open-circuit corrosion potential, larger than the decrease observed with LDAR2X7 (7 atomic percent molybdenum).

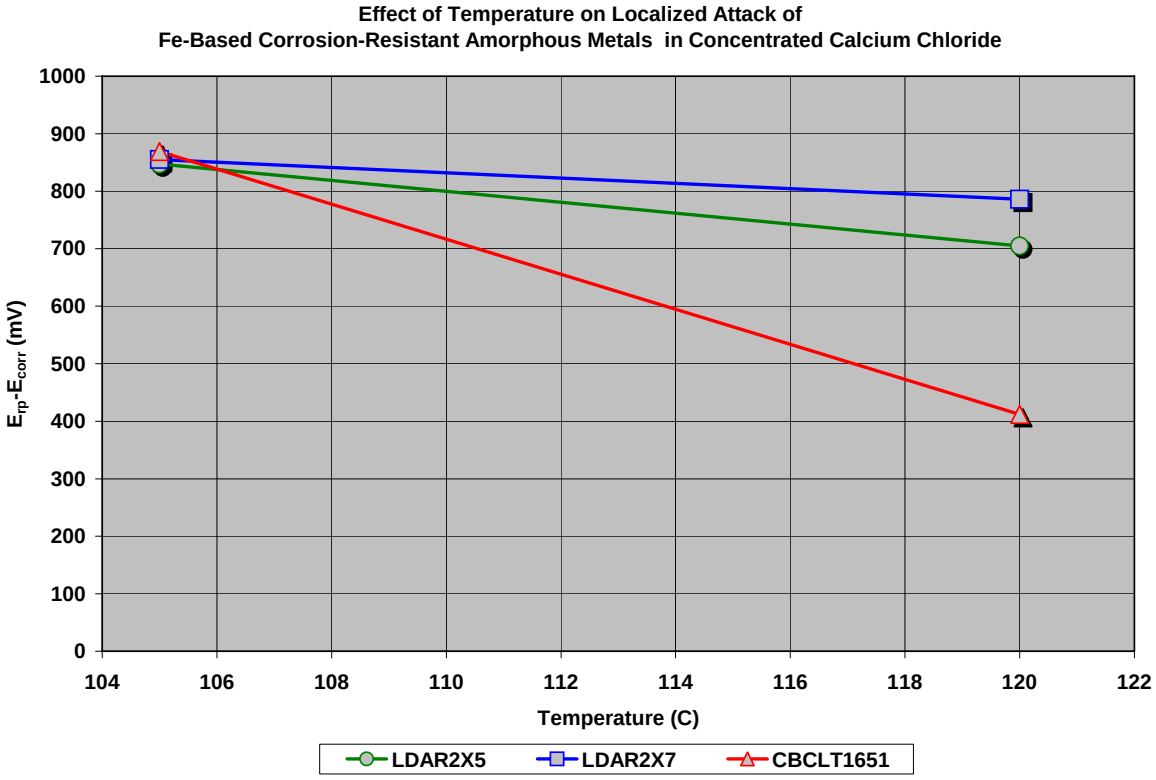

Figure 144 – In general, increases in temperature lower the resistance of an alloy to localized corrosion, with a commensurate decrease in the separation of the open-circuit corrosion potential and the repassivation potential. A parametric study was performed to determine the effects of temperature on the susceptibility of MSR samples of LDAR2X5 (5 atomic percent molybdenum), LDAR2X7 (7 atomic percent molybdenum), and CBCTL1651 (yttrium addition) to localized attack in concentrated calcium chloride. All three materials have comparable performance at 105°C. However, LDAR2X5 and LDAR2X7 have slightly greater resistance to localized attack at 120°C than CBCTL1651.

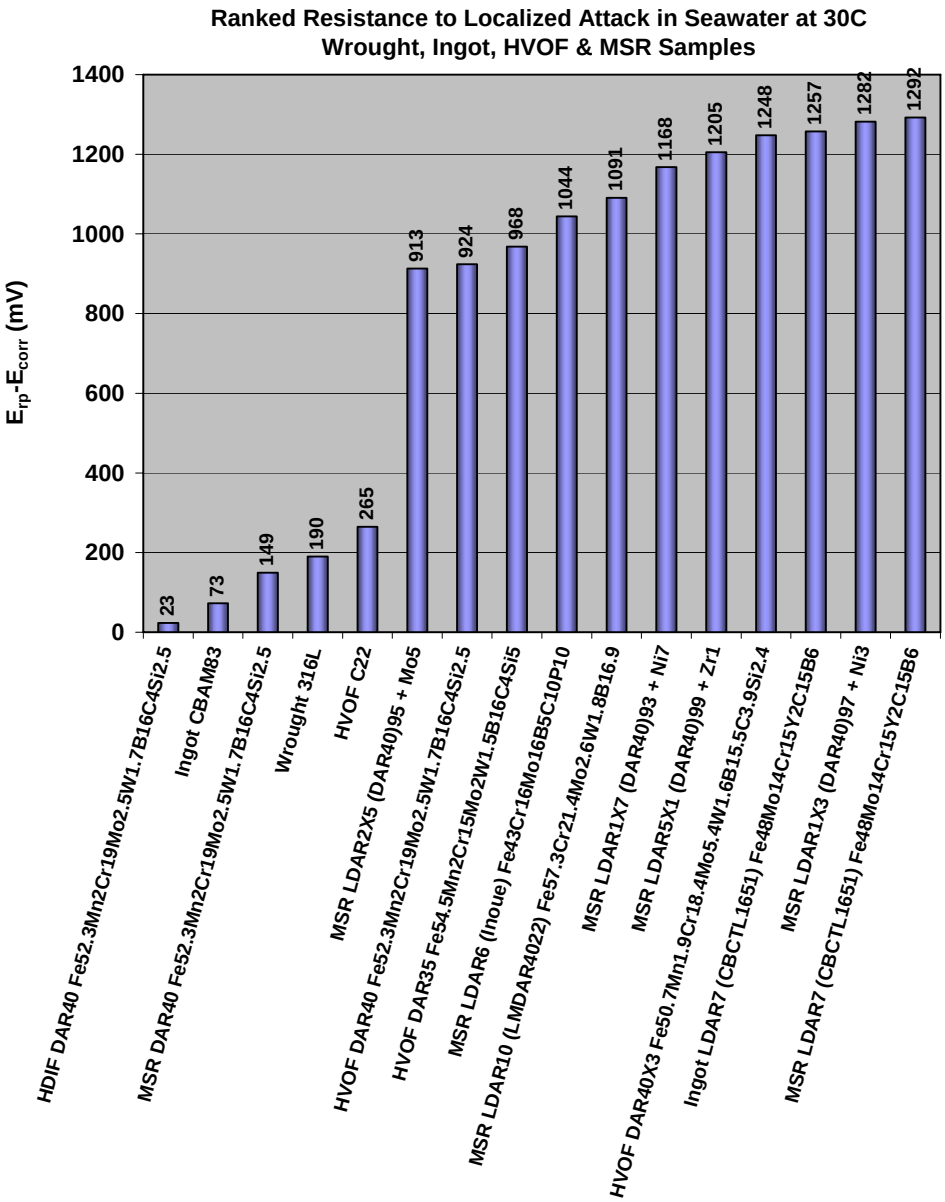

Figure 145 – Various alloy samples, ranked based upon their measured resistance to localized corrosion ($\Delta E=E_{corr}-E_{rp}$) in Half Moon Bay seawater at ambient temperature (30 ℃). Most of the amorphous-samples performed very well, with the arc-melted drop-cast ingot and melt-spun ribbon of CBCTL1651 (also designated as LDAR7) showing the best performance. DAR40X3 coatings deposited with the HVOF process also performed well. A melt-spun ribbon of DAR40 had relatively poor performance, and was the exception. Nickel-based alloy C-22 coatings (N06022) deposited with HVOF performed poorly, as did samples of wrought Type 316L stainless steel, ingots of CBAM83, and HDIF-HVOF samples of DAR40. In this case, the devitrification caused by high-density infrared fusing was detrimental to corrosion resistance.

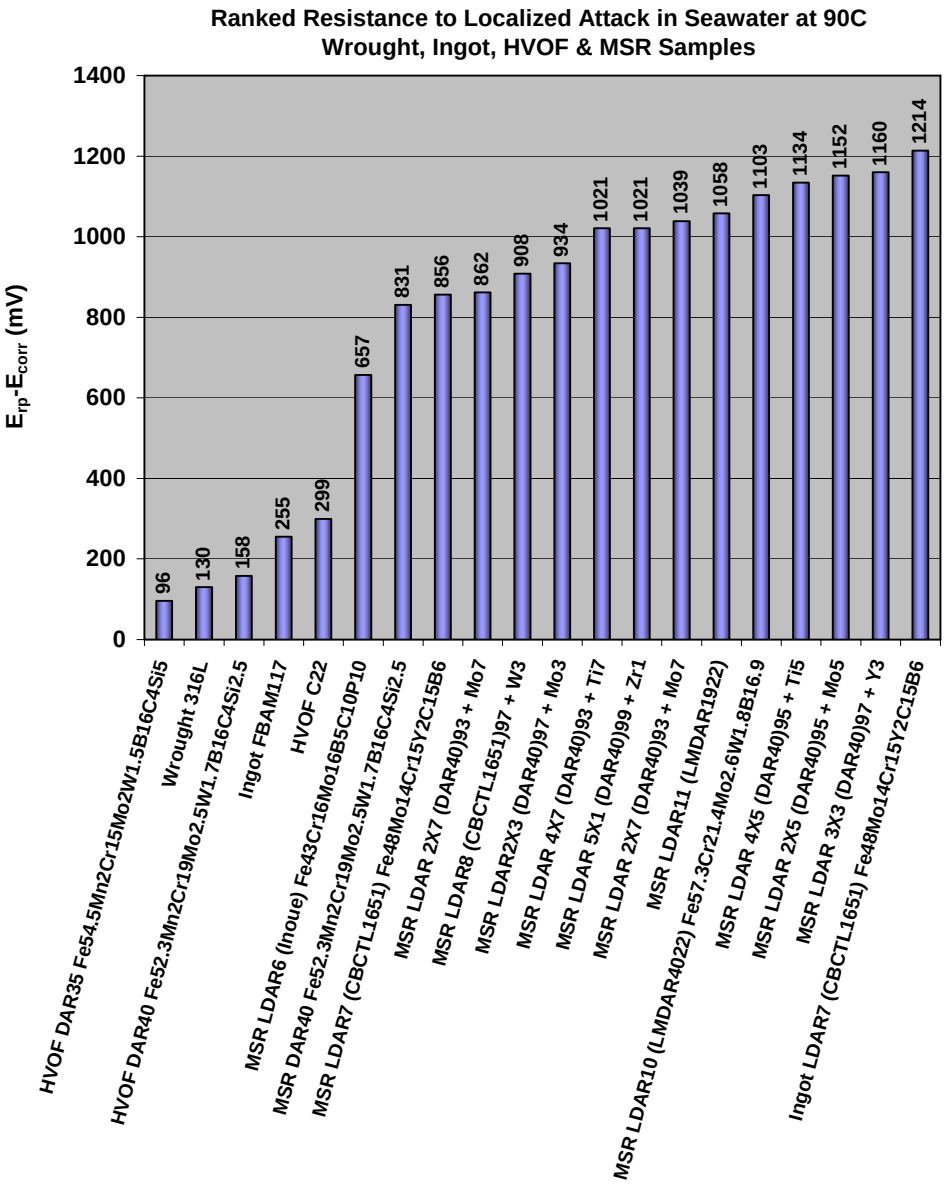

Figure 146 – Various alloy samples, ranked based upon their measured resistance to localized corrosion ($\Delta E=E_{corr}-E_{rp}$) in Half Moon Bay seawater at 90 ℃. Most of the amorphous-samples performed very well, with the arc-melted drop-cast ingot of CBCTL1651 (also designated as LDAR7) showing the best performance. DAR40X3 coatings deposited with the HVOF process also performed well. Nickel-based alloy C-22 coatings (N06022) deposited with HVOF performed more poorly, as did samples of wrought Type 316L stainless steel, ingots of FBAM117, and HVOF DAR35 and DAR40 produced early in the program and reported at the 2004 HPCRM Team Meeting in Key West. HVOF DAR35 and DAR40 have sufficient molybdenum to perform well in seawater at ambient temperature; however, these formulations require modification for good performance at higher temperature.

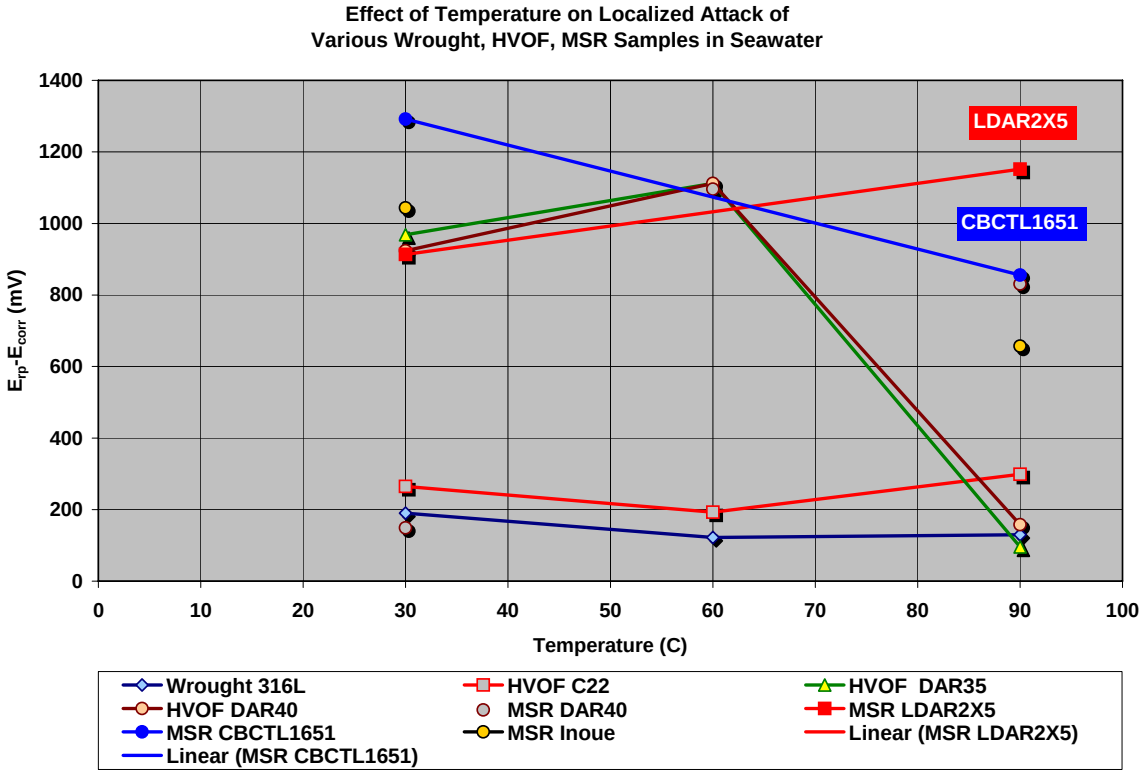

Figure 147 – As discussed in regard cyclic polarization testing in concentrated calcium chloride solutions at various temperature levels, increases in temperature lower the resistance of an alloy to localized corrosion, with a commensurate decrease in the separation of the open-circuit corrosion potential and the repassivation potential. A parametric study was performed to determine the effects of temperature on the susceptibility of numerous alloys to localized attack in seawater at 30, 60 and 90°C. The materials tested include: wrought Type 316L stainless steel; HVOF nickel-based Alloy C-22 (N06022); HVOF DAR35; HVOFDAR40; MSR DAR40; MSR LDAR2X5 (5 atomic percent molybdenum); MSR CBCTL1651 (yttrium addition); and MSR P-containing Fe-based amorphous metal developed by Inoue. Of the tested materials, only two amorphous metal formulations, LDAR2X5 and CBCTL1651, maintained consistently high resistance to localized corrosion (quantified as E_{rp}-E_{corr}) over the entire range of temperature (30 to 90°C), though the P-containing formulation developed by Inoue was close in performance. The HVOF coatings of DAR35 and DAR40 exhibited good resistance to localized attack at 30 and 60°C, but became susceptible to attack at 90°C (E_{rp}-E_{corr} approaching zero). The performance of the wrought Type 316L stainless steel and the HVOF coating of Alloy C-22 was relatively poor over the entire range of potential. In conclusion, corrosion resistant thermal-spray coatings can be produced with powders of Fe-based amorphous metal, but not with powders of Ni-based Alloy C-22 (N06022).

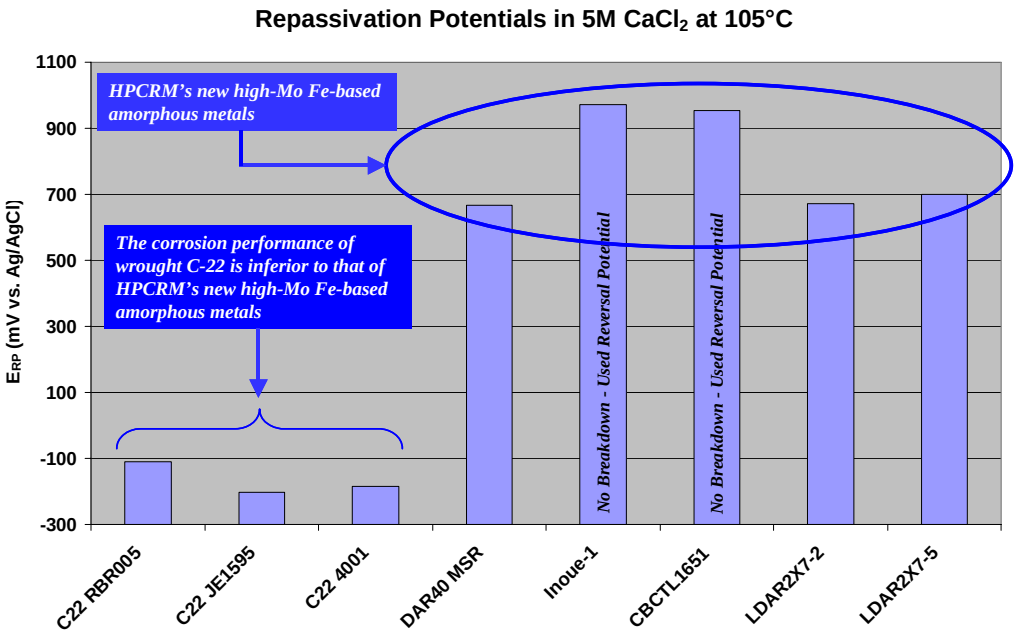

Figure 148 – In addition to ranking the materials based upon the difference between the open-circuit corrosion potential (E_{corr}) and the repassivation potential, a ranking based on the repassivation potential alone has merit, as the open-circuit corrosion potential may be more affected by the instantaneous concentration of oxidants in the electrolyte, including hydrogen peroxide that can be formed by gamma radiolysis. In this ranking, all of the new high-Mo Fe-based amorphous metals under development by the HPCRM Team perform very well in 5M $CaCl_2$ at 105°C, as does the P-containing Fe-based material developed by Inoue. However, several samples of wrought, nickel-based Alloy C-22 (N06022) perform poorly, with very little resistance to localized corrosion in such environments. This finding is consistent with the ranking based upon (E_{rp}-E_{corr}). These data were collected at Lawrence Livermore National Laboratory, and are corroborated by independent measurements at the Naval Research Laboratory in Key West, Florida.

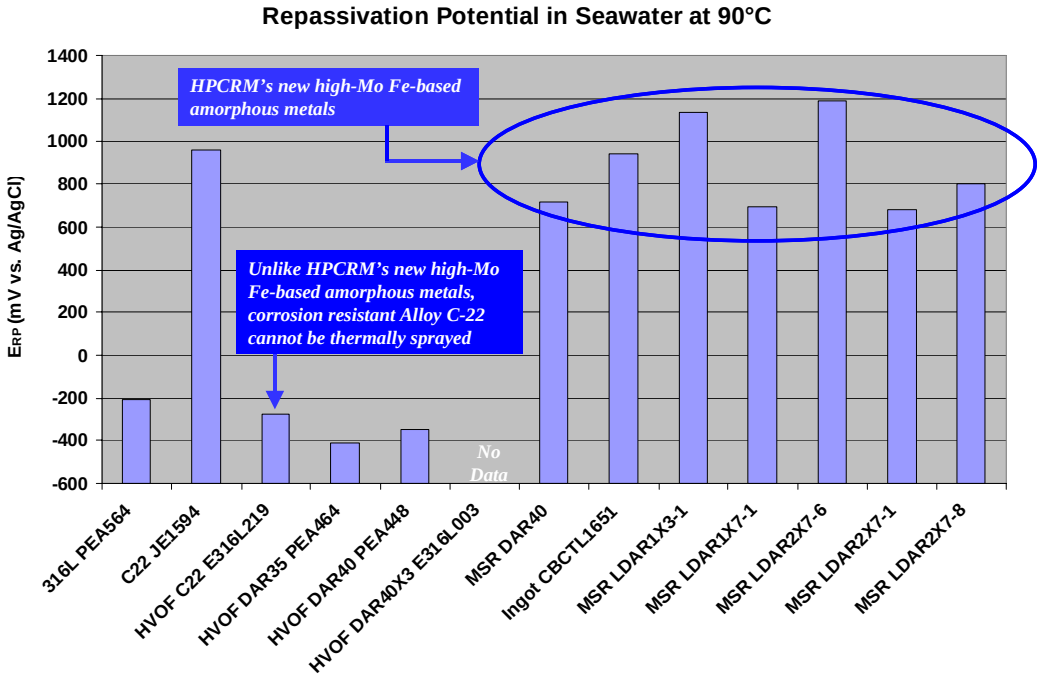

Figure 149 – As previously discussed, in addition to ranking the materials based upon the difference between the open-circuit corrosion potential (E_{corr}) and the repassivation potential, a ranking based on the repassivation potential alone has merit, as the open-circuit corrosion potential may be more affected by the instantaneous concentration of oxidants in the electrolyte, including hydrogen peroxide that can be formed by gamma radiolysis. In this ranking, all of the new high-Mo Fe-based amorphous metals under development by the HPCRM Team perform very well in Half Moon Bay seawater at 90°C, as does the P-containing Fe-based material developed by Inoue. However, several samples of wrought Type 316L stainless steel, wrought and HVOF nickel-based Alloy C-22 (N06022), and HVOF DAR35 and DAR40 perform poorly, with very little resistance to localized corrosion in such environments. It is evident that corrosion-resistant thermal-spray coatings can be produced with Fe-based amorphous metals, but not with Ni-based Alloy C-22. These data were collected at Lawrence Livermore National Laboratory, and are corroborated by independent measurements at the Naval Research Laboratory in Key West, Florida.

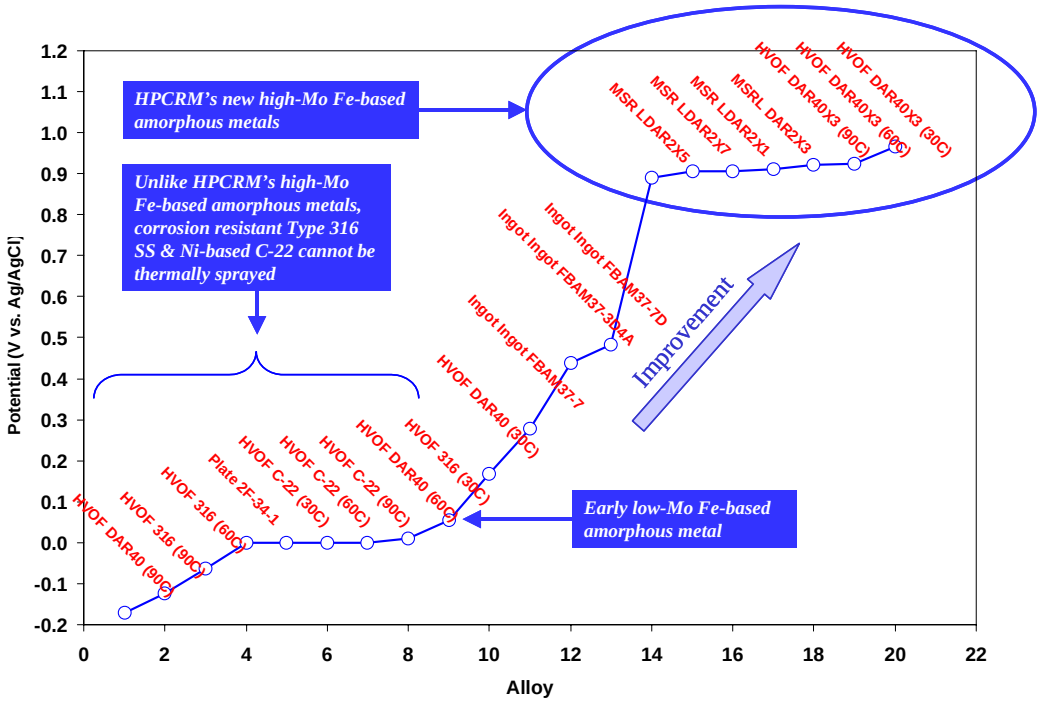

Figure 150 – The Naval Research Laboratory (NRL) at Key West used cyclic polarization to determine the pitting potentials for the materials of interest, and then ranked the alloys based upon the measurements. In this ranking, all of the dense high-Mo Fe-based amorphous metals under development by the HPCRM Team perform very well in Key West seawater. However, many of the early HVOF coatings discussed at the 2004 HPRCRM Team Meeting in Key West, including Type 316L stainless steel, nickel-based Alloy C-22 (N06022), DAR35, and DAR40 perform poorly, with very little resistance to localized corrosion in such environments. It is evident that corrosion-resistant thermal-spray coatings can be produced with Fe-based amorphous metals, but not with Ni-based Alloy C-22. These data were collected at NRL in Key West, and are corroborated by independent measurements at Lawrence Livermore National Laboratory (LLNL).

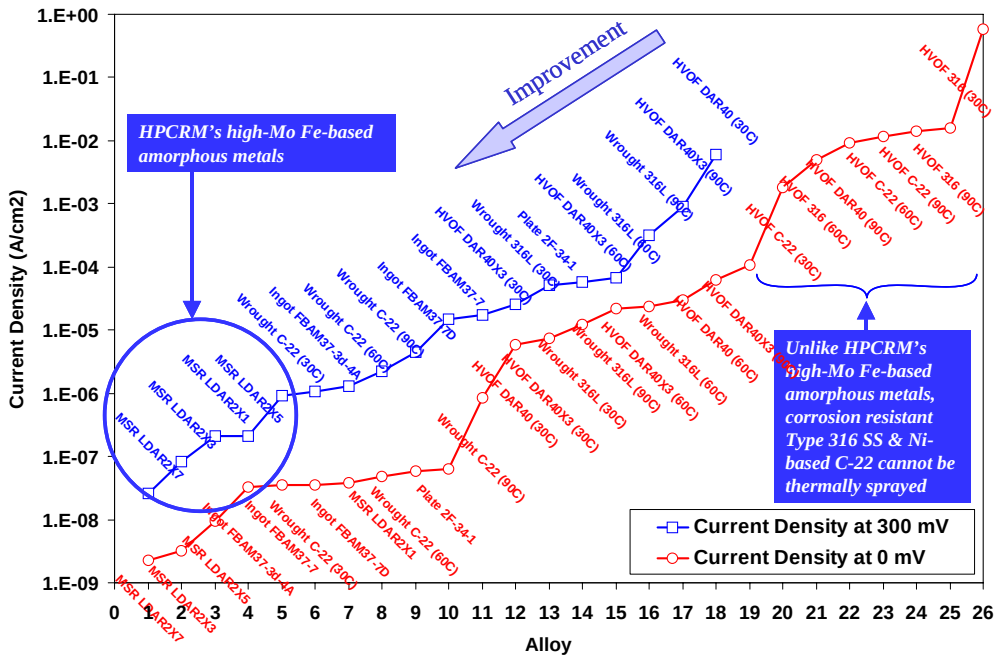

Figure 151 – The Naval Research Laboratory (NRL) at Key West also measured the anodic current density during potentiostatic polarization of 0 and 300 mV vs. Ag/AgCl, and used these measurements as indicators of the instantaneous corrosion rates. The current density measurements were also used as the basis of ranking the dense high-Mo Fe-based amorphous metals under development by the HPCRM Team, and produced by melt spinning. All exhibit low current densities in Key West seawater, and perform very well. However, many of the early HVOF coatings discussed at the 2004 HPRCRM Team Meeting in Key West, including Type 316L stainless steel, nickel-based Alloy C-22 (N06022), DAR35, and DAR40 perform poorly, with relatively high current densities.

(a) External view of salt fog test cabinet. External dimensions are 94"L x 35"W x 56"H.

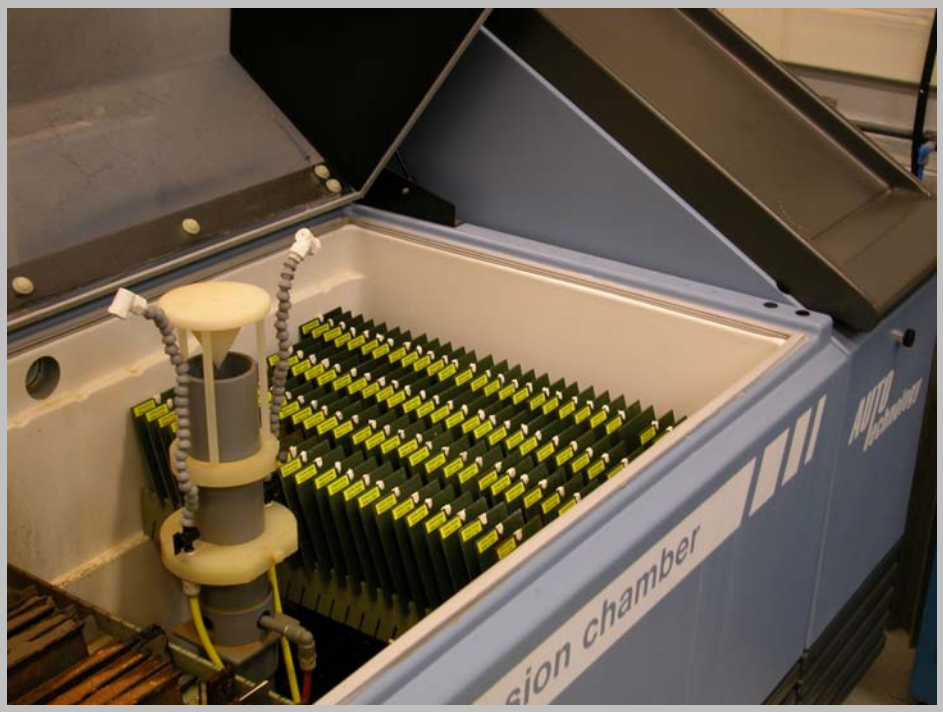

(b) View of internal test section showing a rack of painted specimens test specimens that are not part of this project. Internal test section dimensions are 50"L x 29"W x 25"H.

Figure 152 – Cabinet used for salt-fog testing of HPCRM reference and developmental alloys.

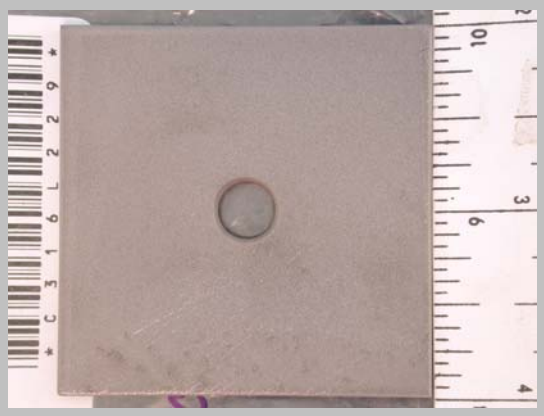

(a) HVOF coating of Alloy C-22 on Type 316L substrate ID# C316L229 (as-received)

(b) HVOF coating of Alloy C-22 on Type 316L substrate ID# C316L229 (after 13 cycles)

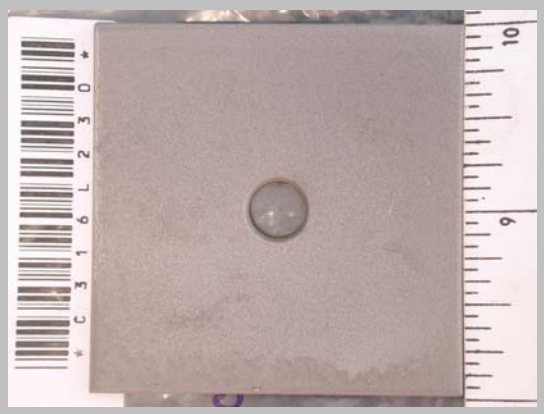

(c) HVOF coating of Alloy C-22 on Type 316L substrate ID# C316L230 (as-received)

(d) HVOF coating of Alloy C-22 on Type 316L substrate ID# C224042 (after 13 cycles)

Figure 153 – Macro photographs of early HVOF coatings of nickel-based Alloy C-22 on Type 316L stainless steel substrate, before and after 13-cycle exposure in the salt-fog chamber at NSWC. There may be some discoloration due to the onset of rusting.

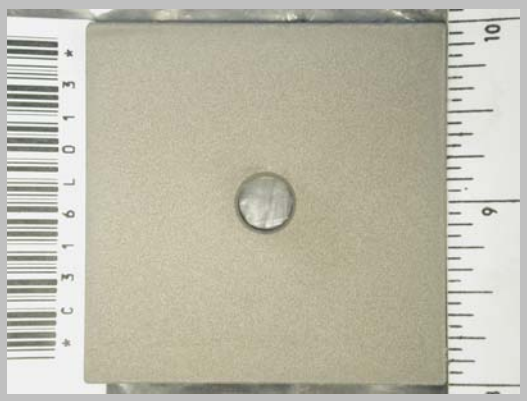

(a) HVOF coating of DAR40 on Type 316L substrate ID# C316L013 (as-received)

(b) HVOF coating of DAR40 on Type 316L substrate ID# C316L013 (after 13 cycles)

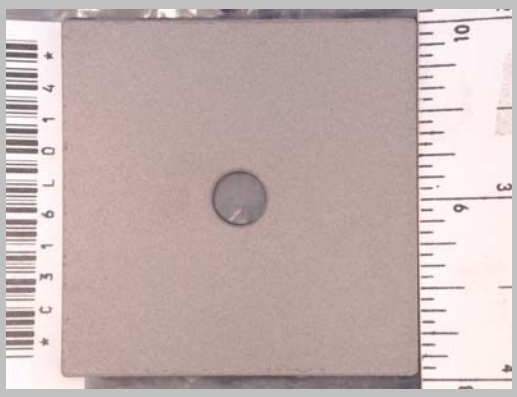

(c) HVOF coating of DAR40 on Type 316L substrate ID# C316L014 (as-received)

(d) HVOF coating of DAR40 on Type 316L substrate ID# C316L014 (after 13 cycles)

Figure 154 – Macro photographs of early HVOF coatings of DAR40 on Type 316L stainless steel substrate, before and after 13-cycle exposure in the salt-fog chamber at NSWC. The rust is attributed to residual porosity and crystalline phases, such as alpha ferrite.

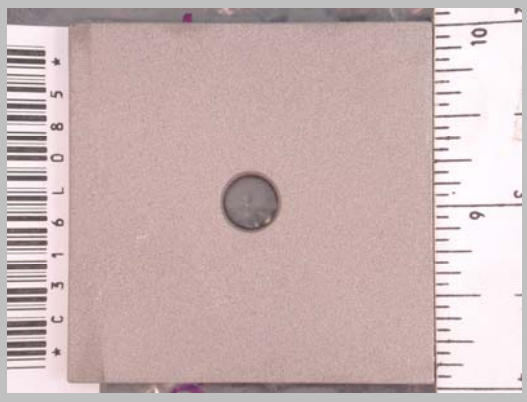

(a) HVOF coating of DAR40X3 on Type 316L substrate ID# C316L085 (as-received)

(b) HVOF coating of DAR40X3 on Type 316L substrate ID# C316L085 (after 13 cycles)

(c) HVOF coating of DAR40X3 on Type 316L substrate ID# C316L087 (as-received)

(d) HVOF coating of DAR40X3 on Type 316L substrate ID# C316L087 (after 13 cycles)

Figure 155 – Macro photographs of early HVOF coatings of DAR40X3 on Type 316L stainless steel substrate, before and after 13-cycle exposure in the salt-fog chamber at NSWC. The rust is attributed to residual porosity and crystalline phases, such as alpha ferrite.

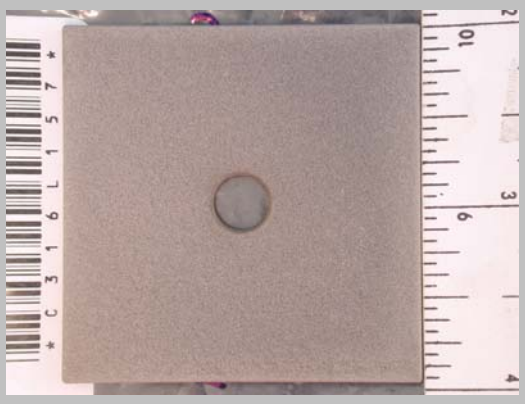

(a) HVOF coating of Type 316L on Type 316L substrate ID# C316L157 (as-received)

(b) HVOF coating of Type 316L on Type 316L substrate ID# C316L157 (after 13 cycles)

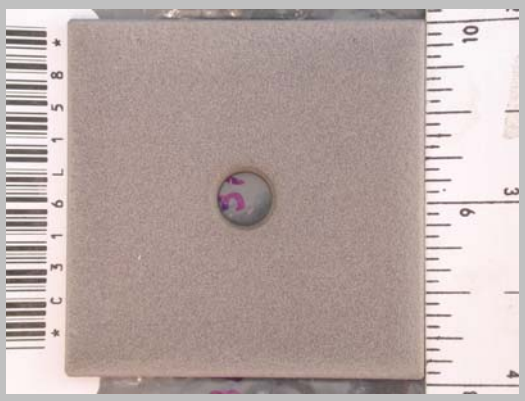

(c) HVOF coating of Type 316L on Type 316L substrate ID# C316L158 (as-received)

(d) HVOF coating of Type 316L on Type 316L substrate ID# C316L158 (after 13 cycles)

Figure 156 – Macro photographs of early HVOF coatings of Type 316L stainless steel on Type 316L stainless steel substrate, before and after 13-cycle exposure in the salt-fog chamber at NSWC. In this case, the micro-structural cause for the observed rusting is not yet fully understood.

(a) Wrought nickel-based Alloy C-22 reference ID# CC-224041 (as-received)

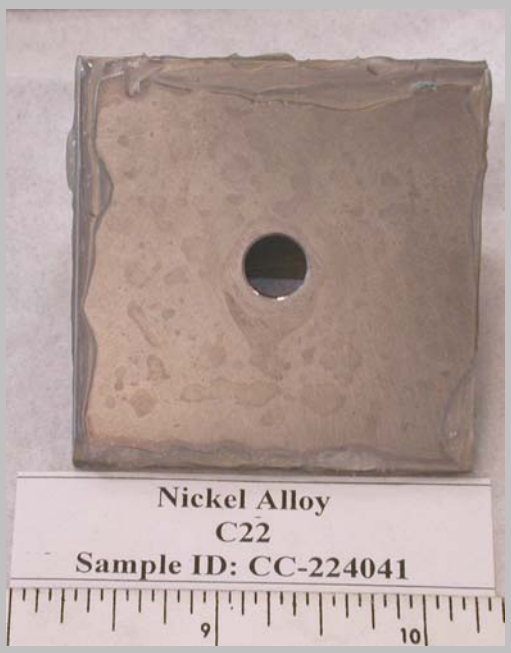

(b) Wrought nickel-based Alloy C-22 reference ID# CC-224041 (after 13 cycles)

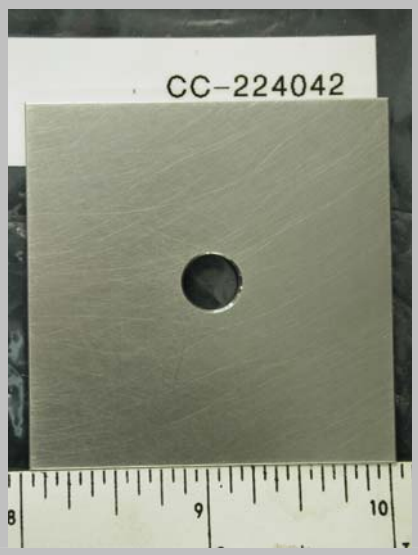

(c) Wrought nickel-based Alloy C-22 reference ID# CC-224042 (as-received)

(d) Wrought nickel-based Alloy C-22 reference ID# CC-224042 (after 13 cycles)

Figure 157 – Macro photographs of wrought, nickel-based Alloy C-22 reference, before and after 13-cycle exposure in the sal- fog chamber at NSWC. The discoloration in the post-exposure photographs is due to water spots and precipitated salts.

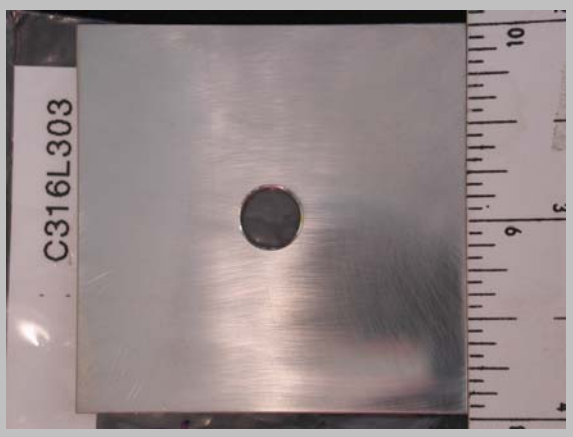

(a) Wrought Type 316L stainless steel reference ID# C316L303 (as-received)

(b) Wrought Type 316L stainless steel reference ID# C316L303 (after 13 cycles)

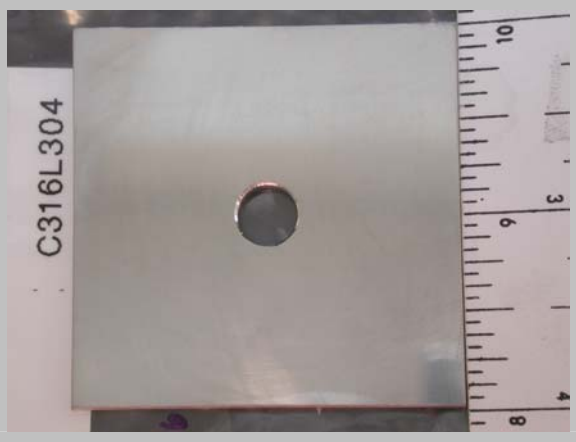

(c) Wrought Type 316L stainless steel reference ID# C316L304 (as-received)

(d) Wrought Type 316L stainless steel reference ID# C316L304 (after 13 cycles)

Figure 158 – Macro photographs of wrought, Type 316L stainless steel reference, before and after 13-cycle exposure in the salt-fog chamber at NSWC. The discoloration in the post-exposure photographs is due to water spots and precipitated salts.

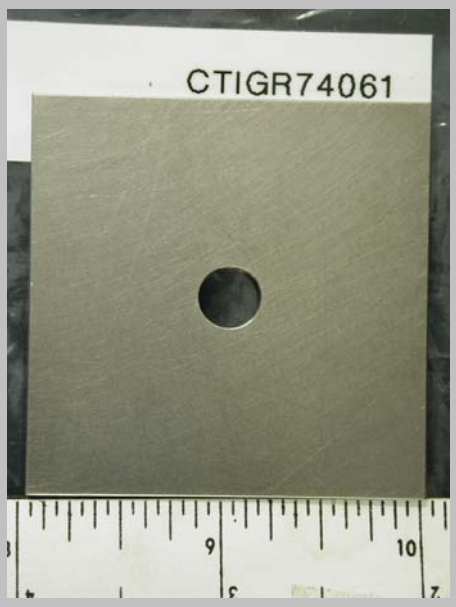

8a. Ti Grade 7, wrought
ID# – CTIGR74061, as-received

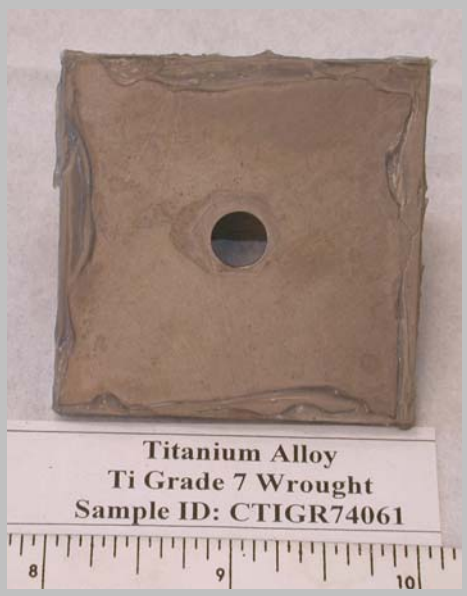

8b. Ti Grade 7, wrought
ID# – CTIGR74061, after 13 cycles

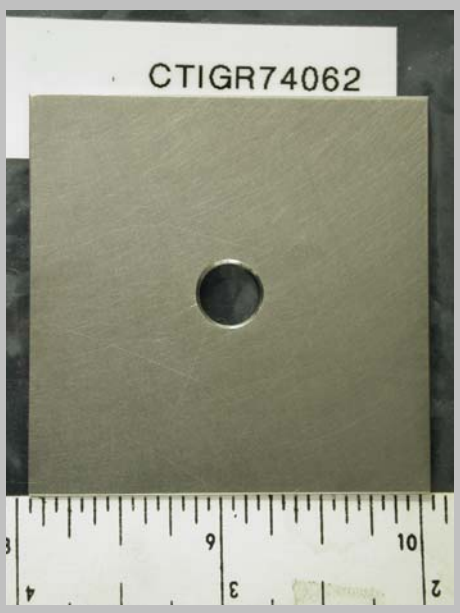

8c. Ti Grade 7, wrought
ID# – CTIGR74062, as-received

8d. Ti Grade 7, wrought
ID# – CTIGR74062, after 13 cycles

Figure 159 – Macro photographs of wrought, Ti Grade 7 reference, before and after 13-cycle exposure in the salt-fog chamber at NSWC. The discoloration in the post-exposure photographs is due to water spots and precipitated salts.

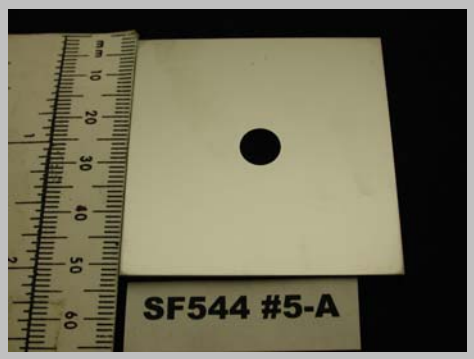

(a) 50Ni50Cr spray-metal formed alloy ID# SF544 #5-A (as-received)

(b) 50Ni50Cr spray-metal formed alloy ID# SF544 #5-A (after 13 cycles)

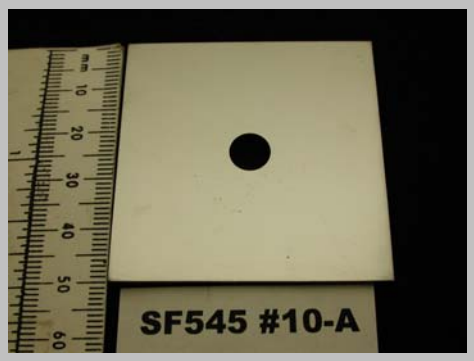

(c) 50Ni50Cr spray-metal formed alloy ID# SF545 #10-A (as-received)

(d) 50Ni50Cr spray-metal formed alloy ID# SF545 #10-A (after 13 cycles)

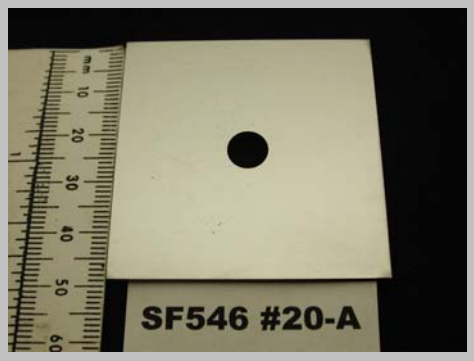

(e) 50Ni50Cr spray-metal formed alloy ID# SF546 #15-A (as-received)

(f) 50Ni50Cr spray-metal formed alloy ID# SF546 #20-A (after 13 cycles)

Figure 160 – Macro photographs of wrought, Ti Grade 7 reference, before and after 13-cycle exposure in the salt-fog chamber at NSWC. The discoloration in the post-exposure photographs is due to water spots and precipitated salts.

Figure 161 – Samples with HVOF coatings are shown in salt fog chamber at the Naval Surface Warfare Center (NSWC).

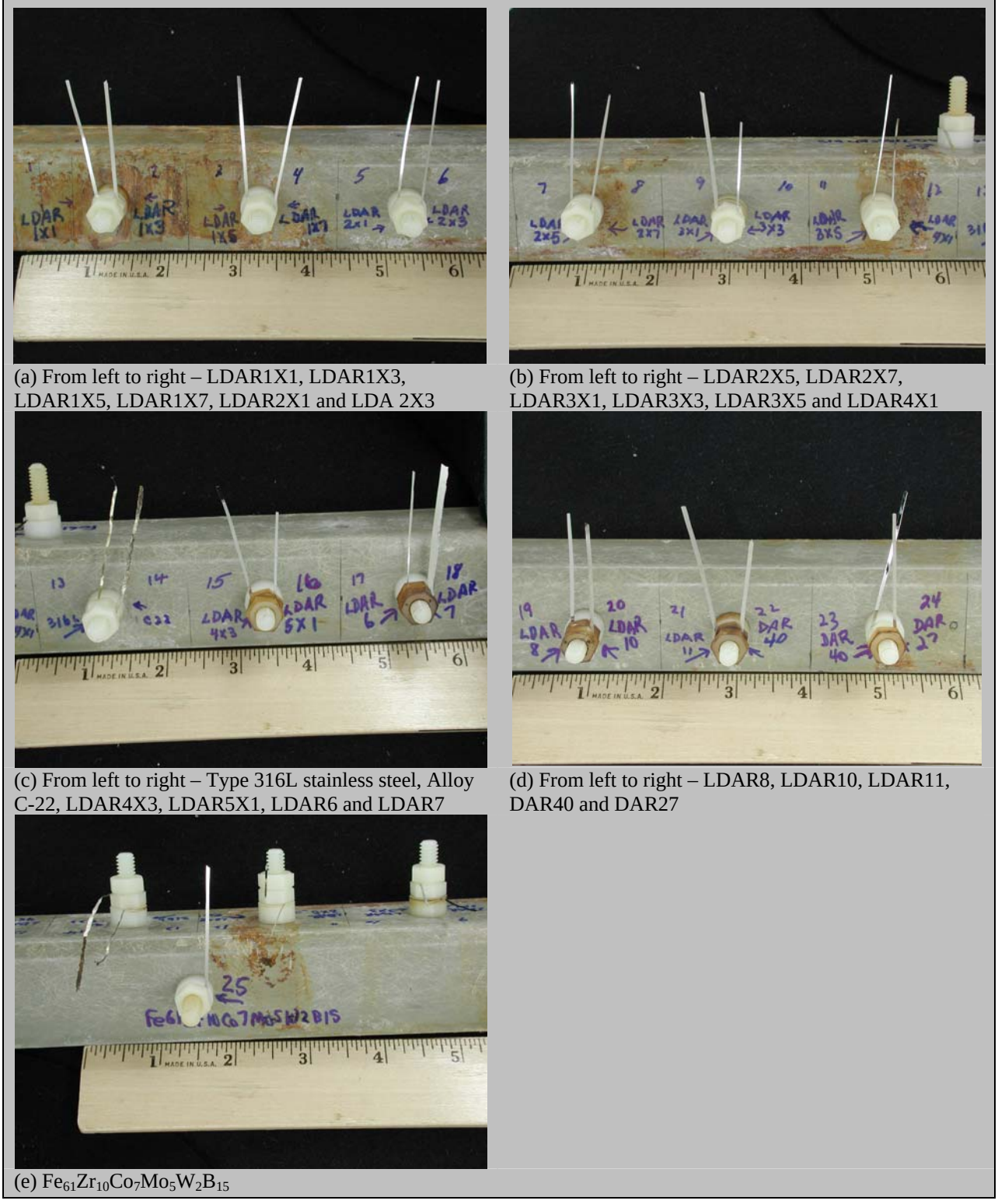

(a) From left to right – LDAR1X1, LDAR1X3, LDAR1X5, LDAR1X7, LDAR2X1 and LDA 2X3

(b) From left to right – LDAR2X5, LDAR2X7, LDAR3X1, LDAR3X3, LDAR3X5 and LDAR4X1

(c) From left to right – Type 316L stainless steel, Alloy C-22, LDAR4X3, LDAR5X1, LDAR6 and LDAR7

(d) From left to right – LDAR8, LDAR10, LDAR11, DAR40 and DAR27

(e) $Fe_{61}Zr_{10}Co_7Mo_5W_2B_{15}$

Figure 162 – Macro photographs of melt-spun ribbons of HPCRM developmental alloys on test fixture before the initial exposure in the salt fog test chamber.

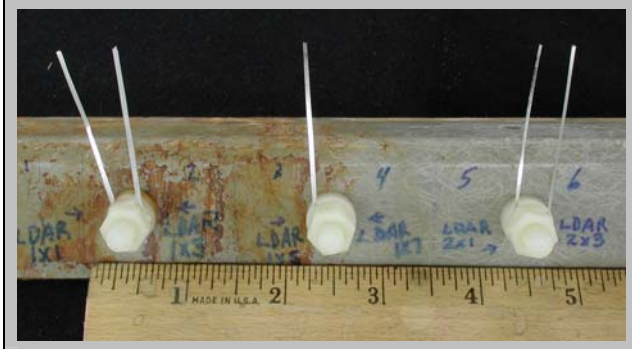

(a) From left to right – LDAR 1x1, LDAR 1x3, LDAR 1x5, LDAR 1x7, LDAR 2x1, and LDAR 2x3

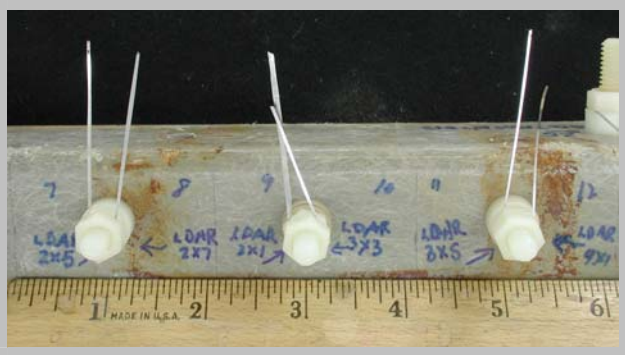

(b) From left to right – LDAR 2x5, LDAR 2x7, LDAR 3x1, LDAR 3x3, LDAR 3x5, and LDAR 4x1

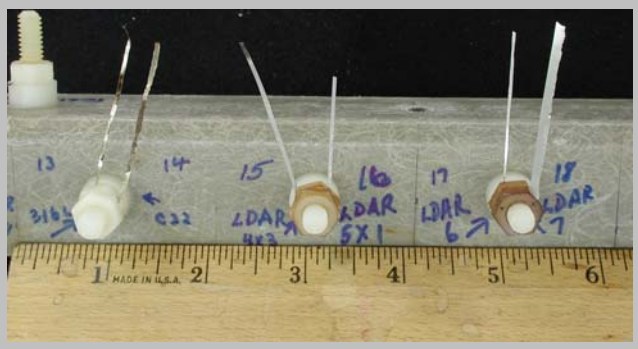

(c) From left to right – SS316L, C22, LDAR 4x3, LDAR 5x1, LDAR 6, and LDAR 7

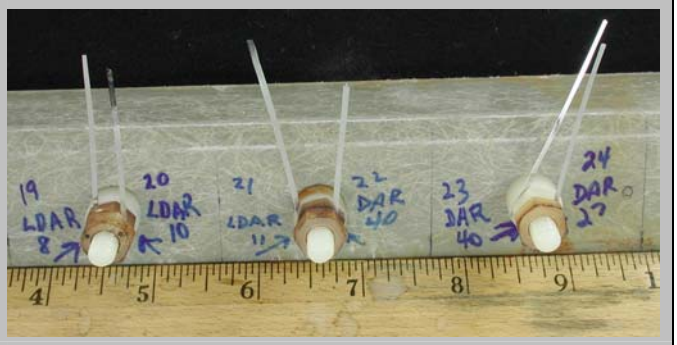

(d) From left to right – LDAR 8, LDAR 10, LDAR 11, DAR40, DAR40, and DAR 27

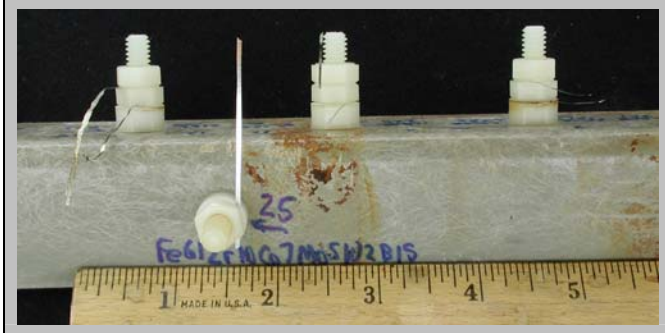

(e) Fe61Zr10Co7Mo5W2B15

Figure 163 – Macrographs of melt-spun ribbons on test fixture after 24 cycles in salt fog test chamber. Some photographs were removed from fixture prior to photograph.

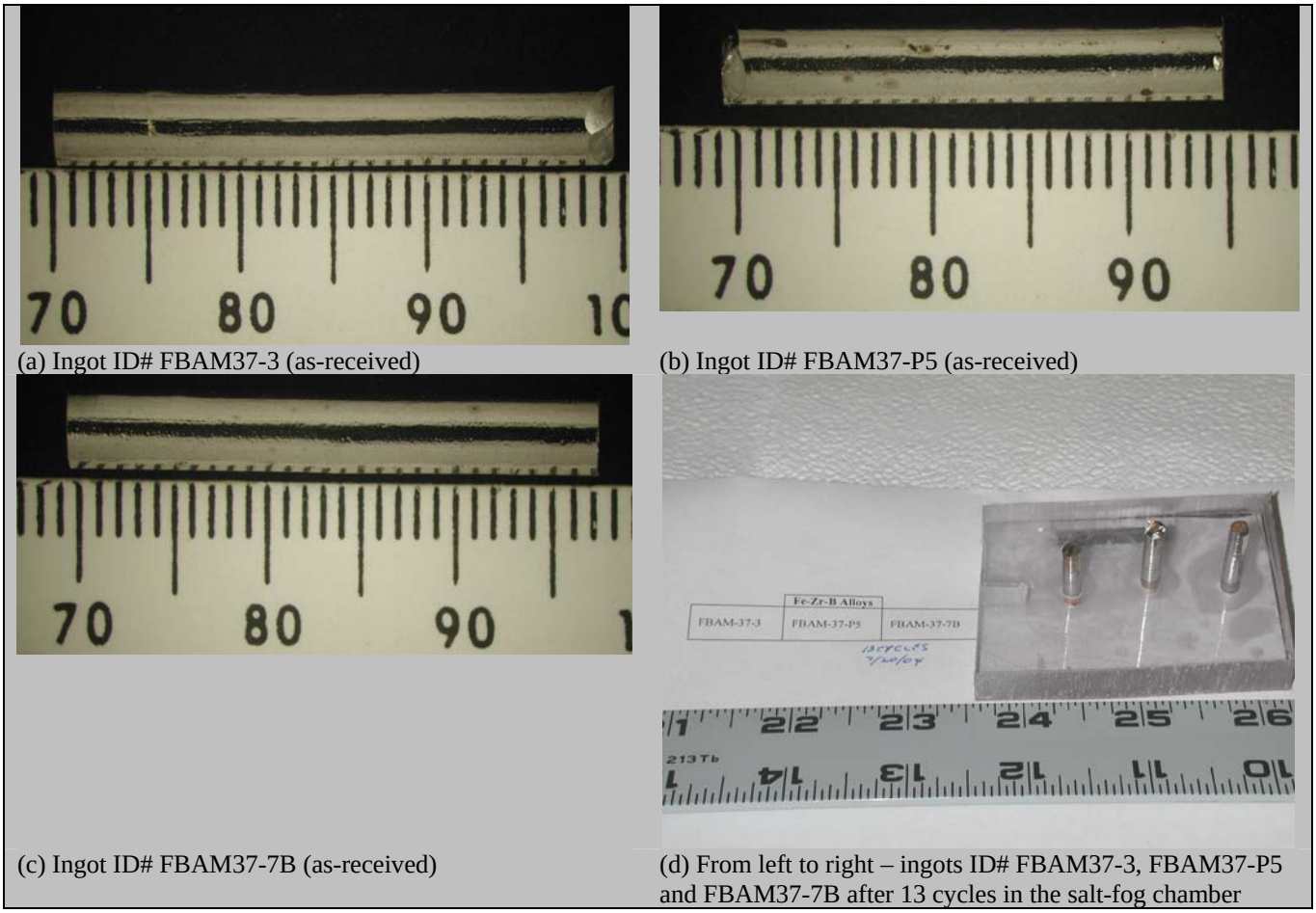

(a) Ingot ID# FBAM37-3 (as-received)

(b) Ingot ID# FBAM37-P5 (as-received)

(c) Ingot ID# FBAM37-7B (as-received)

(d) From left to right – ingots ID# FBAM37-3, FBAM37-P5 and FBAM37-7B after 13 cycles in the salt-fog chamber

Figure 164 – Macro photographs of arc melted, drop-cast ingots (test pins) of FBAM37 before and after exposure in the salt fog chamber. Note that the formula for FBAM37 is $Fe_{61}Y_2Zr_8Co_5Mo_7Cr_2B_{15}$.